



HAL
open science

Development of a MEMS Loudspeaker with Optimized Performance

Romain Liechti

► **To cite this version:**

Romain Liechti. Development of a MEMS Loudspeaker with Optimized Performance. Acoustics [physics.class-ph]. Le Mans Université, 2022. English. NNT : 2022LEMA1037 . tel-03969506

HAL Id: tel-03969506

<https://theses.hal.science/tel-03969506>

Submitted on 2 Feb 2023

HAL is a multi-disciplinary open access archive for the deposit and dissemination of scientific research documents, whether they are published or not. The documents may come from teaching and research institutions in France or abroad, or from public or private research centers.

L'archive ouverte pluridisciplinaire **HAL**, est destinée au dépôt et à la diffusion de documents scientifiques de niveau recherche, publiés ou non, émanant des établissements d'enseignement et de recherche français ou étrangers, des laboratoires publics ou privés.

THÈSE DE DOCTORAT DE

LE MANS UNIVERSITÉ

ÉCOLE DOCTORALE N° 602
Sciences pour l'Ingénieur
Spécialité : Acoustique

Par

Romain LIECHTI

Development of a MEMS Loudspeaker with Optimized Performance

Thèse présentée et soutenue à Le Mans, le 20 décembre 2022

Unité de recherche : Laboratoire d'Acoustique de l'Université du Mans (LAUM, UMR CNRS 6613)

Thèse N° : 2022LEMA1037

Rapporteurs avant soutenance :

Bertrand DUBUS Directeur de Recherche CNRS - IEMN (Lille, France)

Thérèse LEBLOIS Professeure - Université de Bourgogne Franche-Comté (Besançon, France)

Composition du Jury :

Examinateur : Elie LEFEUVRE Professeur - Université Paris-Saclay (Paris, France)

Examinateur : Skandar BASROUR Professeur - Université Grenoble Alpes (Grenoble, France)

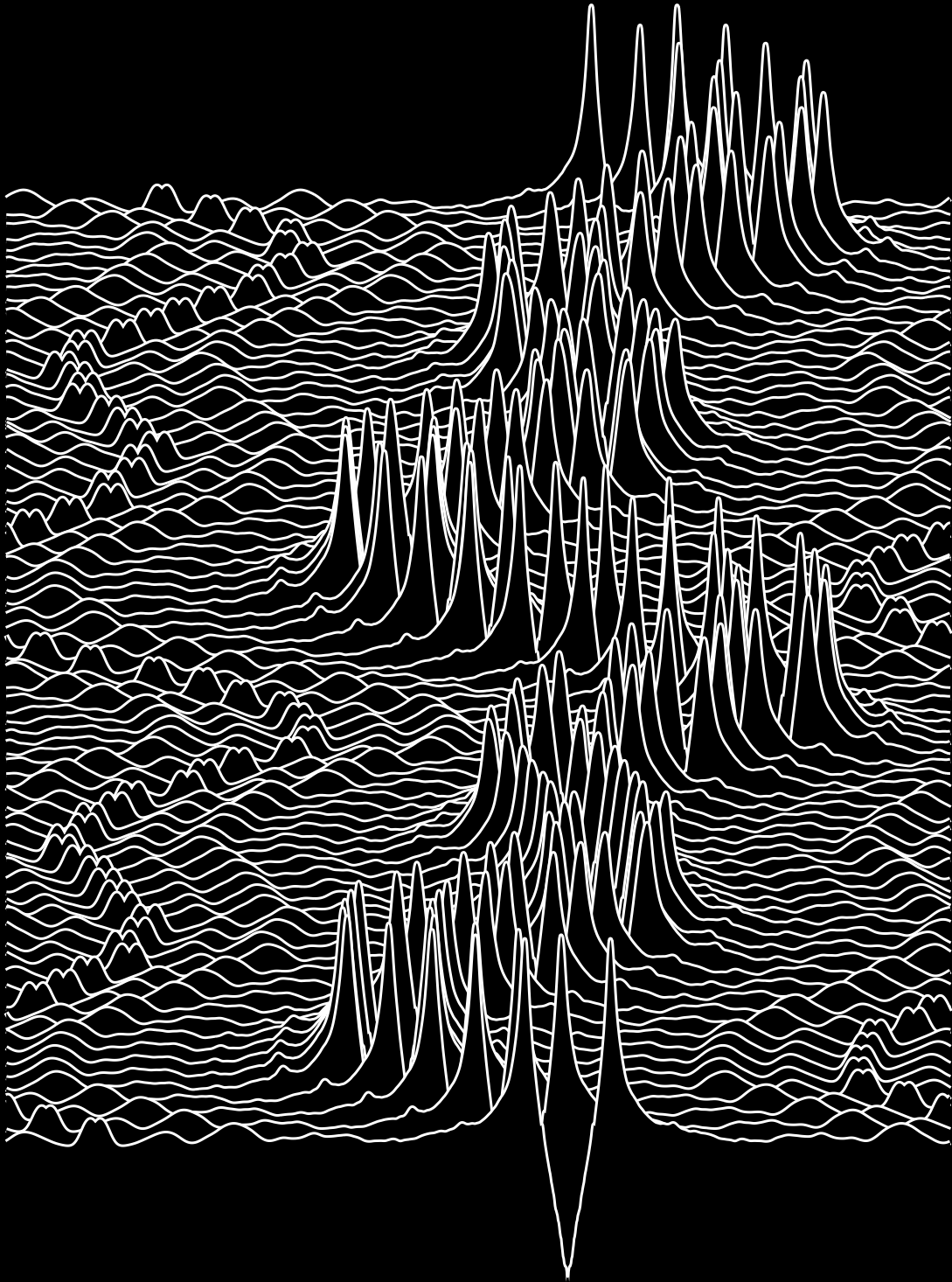
Dir. de thèse : Stéphane DURAND Maître de Conférence HDR - Le Mans Université (Le Mans, France)

Encadrant de thèse : Fabrice CASSET Ingénieur Docteur - CEA Leti (Grenoble, France)

Invité :

Thierry HILT Ingénieur - SOITEC (Bernin, France)

Development of a
MEMS Loudspeaker
with optimized performance



Romain Liechti

Knowledge speaks, but wisdom listens.

Jimi Hendrix

Acknowledgments

The work reported in this manuscript is not limited to the product of my own work only, and countless helpful people need to be acknowledged first. During these three years, I had the privilege to work with enthusiastic and heavily skilled individuals, whom were able to circumvent the most complex issues.

Somewhat logically, I will start to greatly thank Stéphane Durand for directing this thesis from the inception to the writing. Without him, I would probably never have done a thesis. His experience was largely helpful on specific theoretical points, but also for more general matters. Next, I would like to expressively thanks Fabrice Casset for having closely supervised this thesis from the beginning and never failed to be available to suggest a better solution to go into the right direction. His experience concerning MEMS devices was determinant for the successful completion of this project. I'm sorry you endured the correction of hundreds of pages of report on PDFs.

Writing this thesis would probably not be possible without Thierry Hilt. He defended the project in order to obtain funds from the Carnot Institute for the manufacturing of the loudspeakers. He was often using his long experience at CEA to shorten-up some of the delays. He was my supervisor and he was leading the project for the two first years and I would like to thank him for that. Some of his ideas were decisive for some aspects of the design as well.

Some aspects of the project, such as the manufacturing part requires a lot of knowledge, and was mostly handled by Christel Dieppedale. No devices could never have come out of the clean room without her availability, dedication and experience. I would like to thank Greg Enyedi as well for having treated the technically difficult wafers almost one by one for the most critical steps of the process. I would like to thank Gwenaël Le Rhun for the help on everything related to PZT, as well as Hugo and Franklin for evaluating a few of my wafers on the DBLI. And thanks to everyone else that have participated into the risky manufacturing of the loudspeakers.

Year after year, I have been able to rely on people from the lab, thanks to Thierry Verdot for his outlook on the analytical formulations of mechanical structures and problems, thanks to Samer Dagher for his unfailing calmness in the office during my first year, thanks to Marc Sansa Perna for animating the renowned group therapies. Thanks to everybody else for the ambiance, particularly good in our lab.

Early into my thesis, I was not expecting to sign a permanent contract at CEA-Leti three years later, and accordingly I would like to thank Mikaël Colin, head of the laboratory, for his contribution into the

realization of this project, for having trusted me from the beginning, for having involved me in other stimulating projects and for having been, I believe, decisive in my hiring.

Infinite thanks to all the persons from the CEA with whom I discussed, for example Théo Miani, for the fascinating advice on real estate investments. I'm sure he will become a great businessman.

Yeah, we had strong divergences in our political opinions, but we made our office the hardest working one in the building, by having in common a sense of dedication. We also had a common interest for utterly compulsive music buys, thank you Thijs Geurts for the two years in the office.

Without all the other people I have met, my thesis would probably have been less funny, thanks to the enchanting PhD students, Post-Docs and other temporary contracts, Bogdan for our music discussions regarding Black Metal, Fabrice for visiting our office every time he didn't wanted to work, Adrien for establishing the connection with the proteomics lab, Louis for partying hard and Dr Trzпил for la bagarre.

At last, I would like to thanks my family and friends for their psychological support through these laborious years of higher education. Thanks to my parents for their emotional support during these intense years, my elder brother and younger sister for the evenings in Grenoble and Lyon and my younger venerable brother for all the beers. I would also like to thanks to Benja, Juliette, Julien, Laureen, Lucie, ever ready to go to Le Café du Nord and everybody else that I have forgotten to mention here.

Résumé

Introduction

Cette thèse porte sur la conception, la fabrication et la caractérisation d'un haut-parleur MEMS (Système Micro Électro-Mécanique). Dans le premier chapitre, l'état de l'art est passé en revue, et les spécifications permettant de se positionner avantageusement en terme de performances sont définies. Dans le deuxième chapitre le modèle utilisé pour la conception préliminaire du haut-parleur est décrit, et ce même modèle est ensuite utilisé pour définir les paramètres non dimensionnels du haut-parleur. De ces paramètres, la consommation prédite du haut-parleur est calculée, ce qui permet de concevoir l'amplificateur nécessaire à son bon fonctionnement. Dans le troisième chapitre, la conception avancée du haut-parleur, utilisant un modèle en éléments finis ainsi qu'un modèle en espace-état non linéaire est décrite. Dans le quatrième et dernier chapitre, le procédé de fabrication utilisé pour la fabrication du haut-parleur est décrit étape par étape et la caractérisation de ces haut-parleurs est présentée.

État de l'art et spécifications

Un haut-parleur est un transducteur électro-acoustique reproduisant un signal acoustique dans la bande de fréquences audibles. Dans le cas d'un haut-parleur large bande, celui-ci doit reproduire les signaux avec une amplitude égale, de 20 Hz à 20 kHz. Cette large bande de fréquences est généralement reproduite à l'aide de plusieurs haut-parleurs différents, dont les signaux d'entrée sont préalablement filtrés. Dans un souci de miniaturisation, les appareils portables ne disposent en général que d'un seul haut-parleur, et leur bande passante est donc réduite. A cela s'ajoute le fait qu'un haut-parleur en champ libre ne rayonne efficacement qu'à partir de sa fréquence de résonance. Les dimensions étant réduites la fréquence de résonance augmente mécaniquement, ce qui réduit davantage la bande passante du haut-parleur. La réduction des dimensions du haut-parleur est donc peu compatible avec la reproduction des basses fréquences et avec de hauts niveaux de pression acoustique. De plus, les haut-parleurs sont un des seuls composants des appareils multimédias portables à ne pas avoir été adapté aux procédés de micro-fabrication. Cette adaptation permettrait d'en réduire l'épaisseur, de faciliter leur intégration et, à terme, de réduire les coûts de fabrication. Pour se rendre compte de la réponse en fréquences des haut-parleurs intégrés dans les smartphones, la réponse moyennée de plusieurs haut-parleurs récents du commerce est représentée sur la Figure 1. La réponse de ces haut-parleurs est mesurée sur un baffle, en conditions anéchoïques avec une cavité arrière de 1 cm^3 . De cette figure, la réponse typique de tels haut-parleurs est identifiée comme étant celle d'un système dont l'amortissement est légèrement inférieur

à un amortissement critique, avec une fréquence de résonance d'environ 1 kHz avec une cavité à l'arrière, et un niveau de pression acoustique légèrement supérieur à $90 \text{ dB}_{\text{SPL}}$.

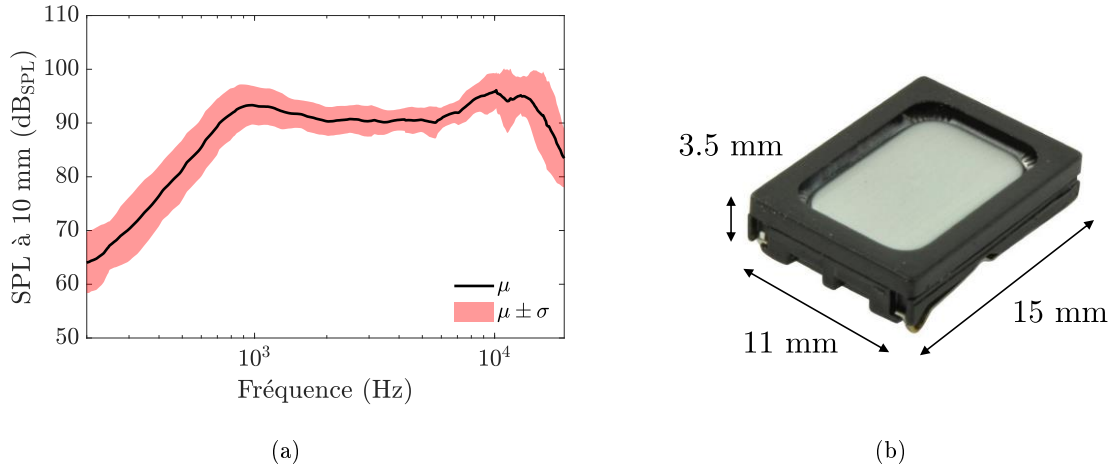


Figure 1: Réponses en fréquence moyennées de douze haut-parleurs du commerce ainsi que l'écart type (a) et photo d'un haut-parleur typique mesurant $11 \times 15 \times 3.5 \text{ mm}^3$ tiré de [1] (b)

Depuis un certain nombre d'années, entraînés par le développement d'appareils portables de plus en plus fins, les chercheurs tentent de rendre le haut-parleur compatible avec les techniques de micro-fabrication dans le but de réduire leur épaisseur, leur consommation et de les intégrer plus facilement. Malgré de multiples architectures, types de transduction et matériaux, les haut-parleurs micro-fabriqués ne permettent pas de remplacer avantageusement les haut-parleurs non MEMS à ce jour. Sur la Figure 2, dix-neuf haut-parleurs MEMS récents sont comparés. La comparaison porte sur la pression rayonnée par ces haut-parleurs à 1 kHz et à 10 cm, en fonction de leur surface active.

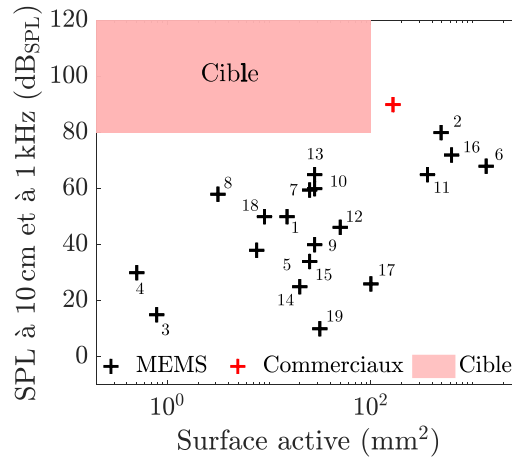


Figure 2: Pression acoustique à 10 cm et à 1 kHz des haut-parleurs MEMS des publications récentes en fonction de leur surface active

D'après les performances des haut-parleurs MEMS récents, les performances cibles sont fixées comme étant une pression minimale rayonnée de $80 \text{ dB}_{\text{SPL}}$ à 1 kHz ou en dessous, pour une surface active inférieure ou égale à 100 mm^2 . Après quelques simulations préliminaires et après une inspection des publications, la méthode choisie pour atteindre ces performances est basée sur un haut-parleur ayant des actionneurs

flexibles piézoélectriques à base de titano-zirconates de plomb (PZT). Le haut-parleur est un haut-parleur linéaire (opposé à un haut-parleur digital ou à d'autres techniques de reproduction non linéaires), et l'application visée est celle des haut-parleurs rayonnant en champ libre.

Modélisation en petits signaux et design préliminaire

Le fonctionnement complet du haut-parleur est d'abord décrit pour permettre la compréhension du modèle en constantes localisées présenté ensuite. Le haut-parleur est composé de deux wafers, l'un d'eux comprenant les actionneurs flexibles piézoélectriques et le second comprenant une plaque rigidifiée pouvant se déplacer librement le long de l'axe z . Sur la Figure 3(a), le haut-parleur complet est représenté. Sur cette figure, on voit le quadrillage des raidisseurs de la plaque mobile, et les deux encoches permettant de voir les contacts électriques nécessaires à l'actionnement du haut-parleur.

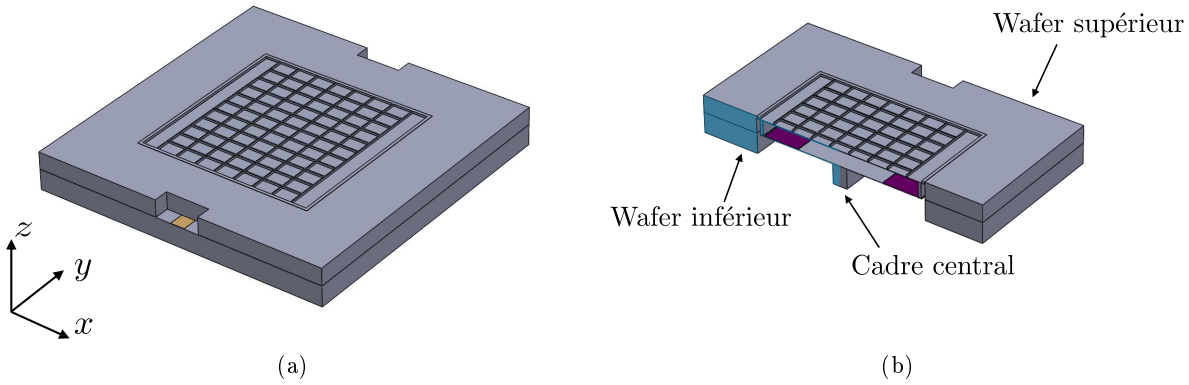


Figure 3: Vue 3D (a) et vue 3D en coupe (b) du haut-parleur dans Solidworks®

Sur la Figure 3(b), la vue en coupe laisse apparaître en violet les actionneurs piézoélectriques et la demi coupe, représentée schématiquement sur la Figure 4 est surlignée en bleu. Le cadre central, attaché par ses extrémités sur le cadre extérieur se trouve au milieu du haut-parleur et est visible sur la vue en coupe. Sur la Figure 4, les actionneurs de longueur L sont couverts sur la moitié de leur longueur par un matériau piézoélectrique, entre deux électrodes de platine. Grâce à la symétrie du dispositif en $x = 0$, l'extrémité de l'actionneur est guidée et est solidement fixée sur la plaque mobile qui ne peut se déplacer que le long de l'axe z . Sous l'effet du champ électrique créé par la différence de potentiel entre l'électrode supérieure et l'électrode inférieure (respectivement en dessous et au dessus de la couche piézoélectrique), une contrainte longitudinale apparaît le long de l'axe x . La couche piézoélectrique d'épaisseur t_p étant solidement attachée à une couche flexible de silicium d'épaisseur t_m , celle-ci se déforme et adopte une déformation encastree-guidée, du fait de ses conditions aux limites. La force F_{bl} est la force générée par l'actionneur piézoélectrique flexible lorsque l'extrémité de celui-ci est bloquée. Le déplacement δ_0 est le déplacement statique maximum de la plaque lorsque aucune force n'est appliquée sur la plaque.

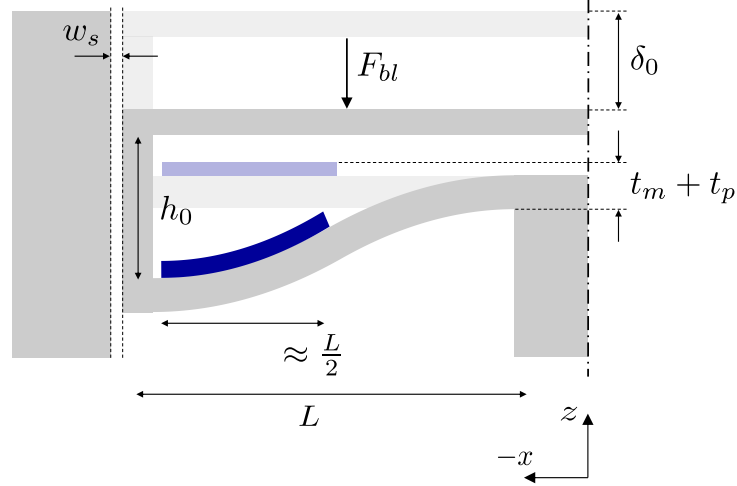


Figure 4: Vue en demi-coupe du principe de fonctionnement du haut-parleur avec les dimensions importantes qui le régissent

Le haut-parleur pouvant être assimilé à un résonateur du premier ordre, il est modélisé par un circuit électrique équivalent, qui est principalement composé d'une capacité C_{ms} représentant sa souplesse apparente et d'une inductance M_{ms} représentant la masse mobile de son circuit mécanique. A ce circuit mécanique viennent s'ajouter en amont un transformateur représentant le matériau piézoélectrique (agissant comme transducteur électro-mécanique) et en aval un transformateur représentant la plaque mobile agissant comme un transducteur mécano-acoustique. Le transducteur électro-mécanique est composé d'une résistance R_g , représentant les pertes électriques dans les conducteurs acheminant le courant jusqu'au matériau piézoélectrique, d'une capacité C_p représentant l'effet capacitif dû au matériau isolant piézoélectrique entre les deux électrodes et un transformateur de ratio γ représentant le facteur de transduction de la tension vers la force. Pour le transducteur mécano-acoustique, le facteur de transduction est égal à la surface mobile S_d du haut-parleur. Tous les paramètres sont déterminés par des calculs analytiques ou directement sur la base des dessins assistés par ordinateurs lorsqu'il s'agit de surfaces et de volumes. Le circuit complet est représenté sur la Figure 5.

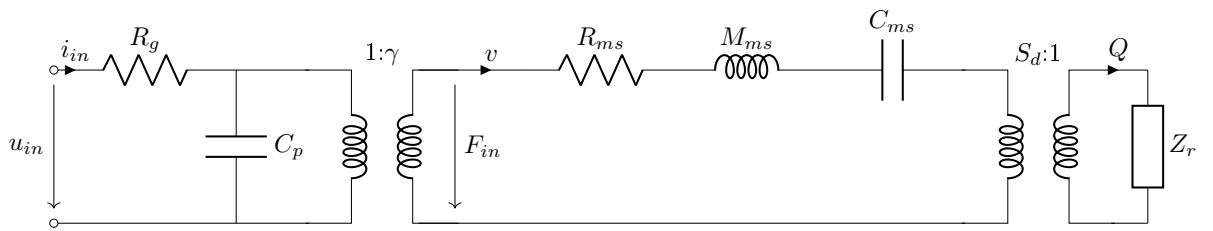


Figure 5: Schéma électrique équivalent du haut-parleur

De ce circuit équivalent, la réponse en fréquence du haut-parleur peut s'écrire comme étant

$$p(r, \omega) = -j\rho_0 c_0 S_d \frac{F_{in}}{R_{ms} + j\omega M_{ms} + \frac{1}{j\omega C_{ms}} + Z_r S_d^2} \frac{e^{jk_0 r}}{2\pi r} \quad (1)$$

avec $p(r, \omega)$ la pression évaluée à une distance r du centre de la plaque, ρ_0 la densité de l'air à température ambiante, c_0 la célérité des ondes acoustiques dans un fluide de densité ρ_0 à température ambiante, S_d

la surface de la partie mobile du haut-parleur, F_{in} la force d'entrée du circuit mécanique, égale à la force bloquée F_{bl} générée par les actionneurs et k_0 le vecteur d'onde. Dans cette équation, la souplesse apparente C_{ms} est déterminée via un modèle des actionneurs et dépend principalement de leur longueur L et de leur épaisseur t_m . Les parties supérieure et inférieure du haut-parleur étant de taille identique pour pouvoir être assemblées, la longueur L est liée à la surface de la plaque mobile S_d . De cette équation, la réponse en fréquence est calculée pour plusieurs valeurs de surface S_d et pour plusieurs valeurs de l'épaisseur de la partie élastique des actionneurs t_m .

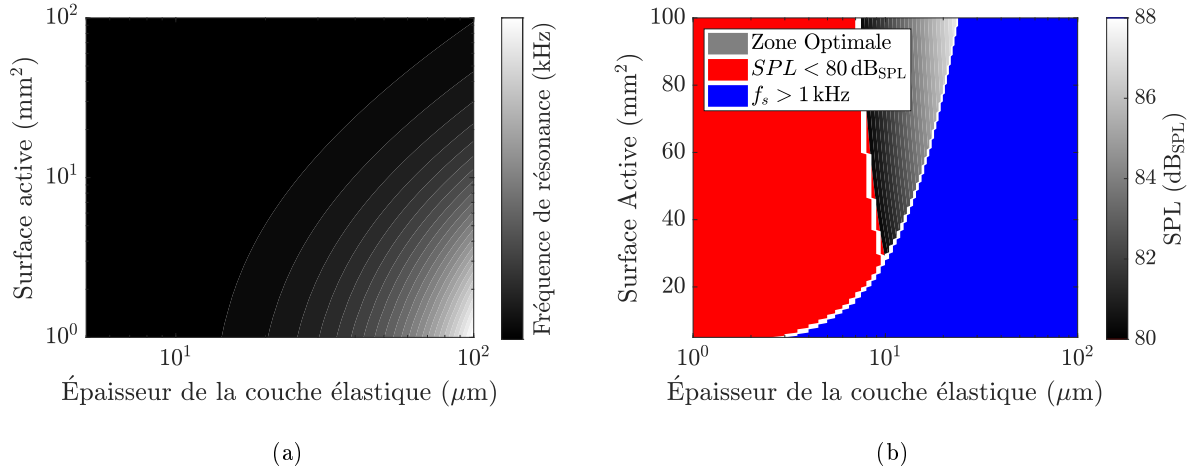


Figure 6: Fréquence de résonance du haut-parleur en fonction de l'épaisseur de la couche élastique t_m et en fonction de la surface active S_d (a) et pression acoustique générée par le haut-parleur en fonction des mêmes paramètres (b)

D'après ces deux figures, une épaisseur t_m de 12 μm et une surface active de 36 mm^2 sont choisies pour la version principale du haut-parleur. Elles correspondent à une pression dans la bande passante d'environ 78 dB_{SPL} , avec une fréquence de résonance d'environ 1 kHz. Le facteur de qualité Q_{ms} dépend ensuite de la dissipation dans le circuit mécanique R_{ms} . La réponse en fréquences du haut-parleur, calculée pour trois valeurs du facteur de qualité Q_{ms} arbitrairement choisies (0.1, 1 et 10), est représentée sur la Figure 7(a). La pression acoustique étant proportionnelle à l'accélération de la partie mobile du haut-parleur, elle est similaire à celle d'un filtre passe-haut, dont la fréquence de coupure correspond à la fréquence de résonance f_s . La valeur du facteur de qualité affecte largement la réponse en fréquence du haut-parleur et ne peut pas être déterminée simplement en utilisant les modèles analytiques. Les dissipations semblent cependant limitées, et un facteur de qualité supérieur à dix est attendu. A partir du circuit électrique équivalent, l'impédance électrique du haut-parleur peut être calculée également. L'impédance électrique est représentée sur la Figure 7(b). Elle est principalement complexe et correspond majoritairement à l'impédance d'un condensateur, hormis le pic dû à la résonance mécanique, aux alentours de 1 kHz. Pour une tension d'alimentation $u_{in} = 30 \text{ V}$, la puissance nécessaire au fonctionnement du haut-parleur peut donc être estimée à environ 1.8 W à 20 kHz. Fort de ce constat, un amplificateur est conçu pour permettre d'actionner le haut-parleur.

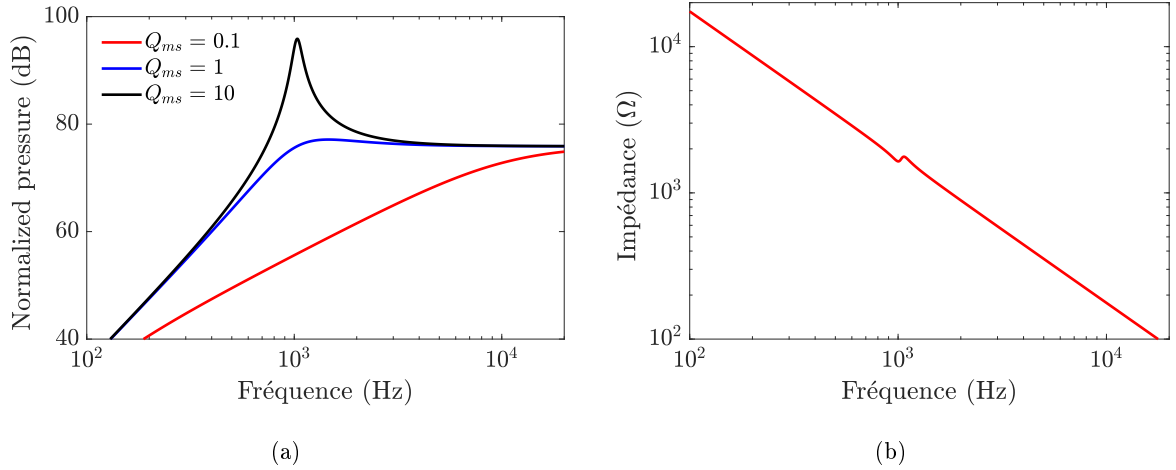


Figure 7: Réponses en fréquences du haut-parleur pour différentes valeurs arbitraires de facteur de qualité Q_{ms} (a) et impédance électrique du haut-parleur pour un facteur de qualité $Q_{ms} = 10$ (b)

Modélisation et design avancé

A partir des dimensions définies dans le chapitre précédent, un modèle en éléments finis du haut-parleur est construit dans COMSOL[®]. Il est composé de quatre physiques et de quatre couplages multi-physiques. La première physique permet la simulation de l'élément piézoélectrique et utilise un couplage électromécanique pour interagir avec la partie mécanique. La partie mécanique interagit avec l'acoustique via un couplage mécano-acoustique. Dans l'interstice autour de la plaque mobile du haut-parleur une physique acoustique thermo-visqueuse est utilisée et est couplée au domaine acoustique et au domaine mécanique via deux autres couplages. Sur la Figure 8(a), le modèle électro-mécanique du haut-parleur tel qu'il est construit dans COMSOL[®] est représenté. En violet, les actionneurs piézoélectriques sont à la fois dans la physique mécanique et dans la physique électrique. Les électrodes ne sont pas simulées, car leur épaisseur est trop faible pour influencer significativement la raideur apparente du haut-parleur.

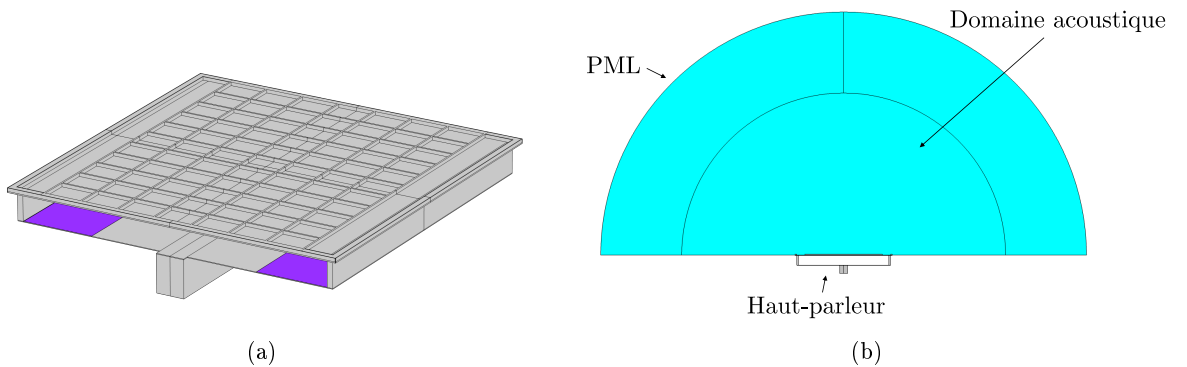


Figure 8: Haut-parleur en vue 3D (a) et modèle complet comprenant la partie acoustique (b) dans COMSOL[®]

Le haut-parleur est disposé dans un domaine acoustique hémisphérique, dont les surfaces extérieures sont considérées rigides dans la physique acoustique. Une couche absorbante parfaitement adaptée (PML) est ensuite ajoutée entre la surface hémisphérique rigide et le domaine acoustique. Elle permet de simuler

une condition de Sommerfeld. La partie circulaire simule un baffle plan infini. La partie arrière du haut-parleur n'est pas couplée au domaine acoustique. En disposant un point dans le domaine acoustique à une distance de 10 mm, la pression acoustique en dB_{SPL} peut être évaluée en fonction de la fréquence. Cette pression est ensuite comparée avec celle calculée par le modèle en constantes localisées. La comparaison des deux courbes est présentée sur la Figure 9(a).

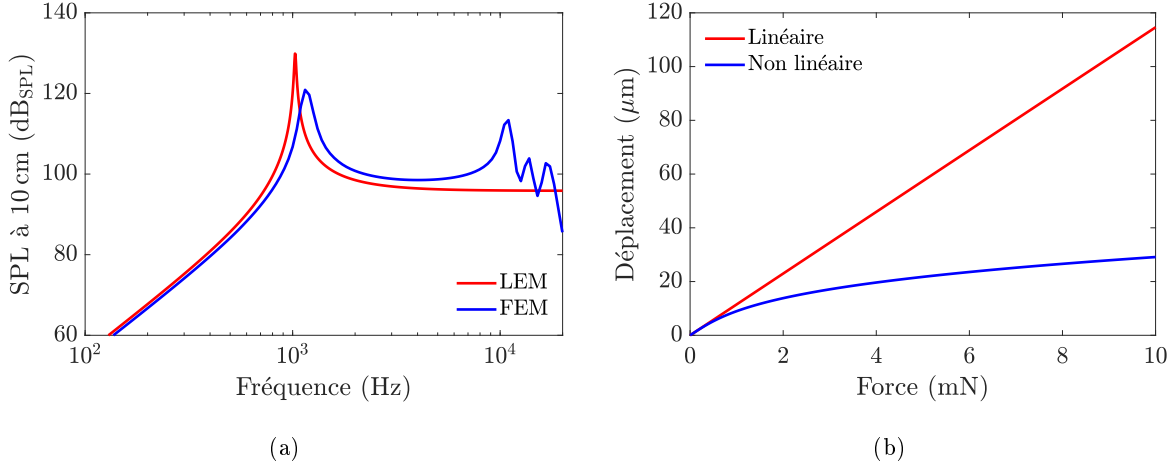


Figure 9: Comparaison entre la pression acoustique calculée à l'aide du modèle en constantes localisées et avec le modèle en éléments finis (a) et non linéarité géométrique dues aux contraintes longitudinales dans les couches élastiques de la partie d'actionnement du haut-parleur (b)

Les résultats des modèles en éléments finis (FEM, pour Finite Element Modeling) et en constantes localisées (LEM, pour Lumped Element Modeling) sont en adéquation dans leur bande passante de validité, c'est à dire autour de la fréquence de résonance. Après une évaluation approfondie des paramètres linéaires du haut-parleur, les simulations portent sur les non-linéarités géométriques du haut-parleur, qui sont principalement liées aux conditions aux limites des actionneurs. Lors de la déformation d'une plaque encastree-guidée, un effet d'étirement de la plaque s'ajoute à la déformation de celle-ci, rendant la plaque de plus en plus rigide lors de sa déformation. Cet effet peut être observé sur la Figure 9(b).

Pour pallier ces non-linéarités géométriques qui résulteraient en une diminution du déplacement de la partie mobile du haut-parleur, et donc en une importante dégradation des performances, un pseudo degré de liberté supplémentaire est ajouté au système. Une vue en coupe de la structure mécanique est présentée sur la Figure 10(a). Ce degré de liberté supplémentaire est ajouté via une deuxième plaque déformable, dont l'extrémité est liée au bloc de couplage de hauteur h_0 . La force F_{nl} , due à la différence entre la longueur de la partie flexible des actionneurs projetée sur l'axe x avant et après sa déformation, déforme la structure supérieure de longueur L_{ls} intégrée dans la plaque mobile, via un moment M_{ls} . Cette force F_{nl} utilise la hauteur h_0 comme bras de levier.

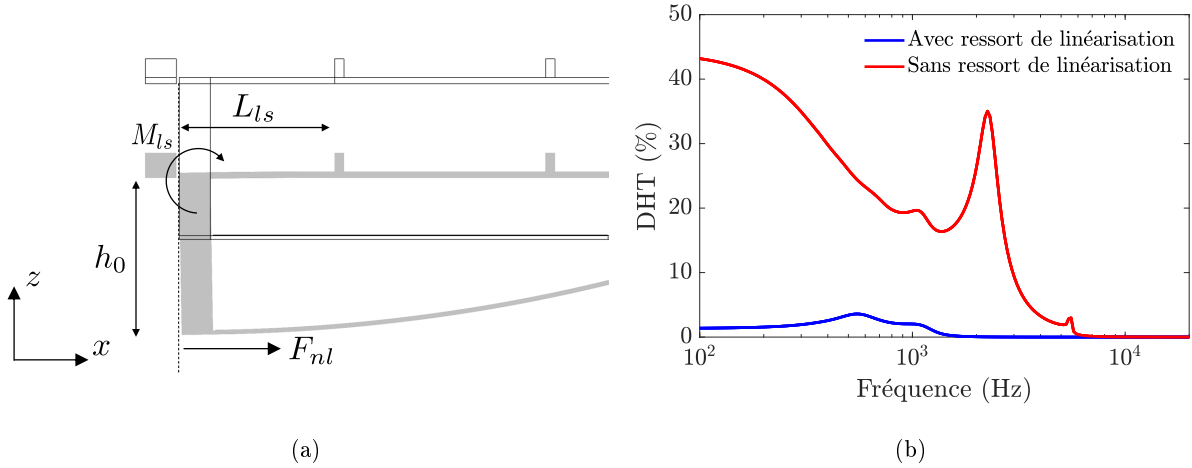


Figure 10: Vue en coupe partielle du ressort de linéarisation et de l'extrémité de l'actionneur (a) et distorsion harmonique totale simulée du haut-parleur avec et sans ressort de linéarisation (b)

Via un modèle espace-état, le gain sur la distorsion harmonique totale (THD) peut être calculé en écrivant les équations temporelles du circuit équivalent présenté sur la Figure 5. Ce calcul montre l'avantage du ressort de linéarisation et donne des valeurs indicatives pour le niveau de distorsion attendu du haut-parleur. À un actionnement de 1.5 V, le taux de distorsion harmonique attendu est situé aux alentours de 1 % et atteint son maximum un octave sous la fréquence de résonance du haut-parleur, à environ 500 Hz.

Fabrication et caractérisation

Les haut-parleurs sont fabriqués sur la ligne 200 mm du CEA-Leti. La fabrication commence par le wafer inférieur, dont la base est un wafer silicium sur isolant (SOI, pour Silicon On Insulator), dont la couche dispositif mesure 12 μm d'épaisseur, et la couche support mesure 675 μm d'épaisseur. Une couche de 500 nm de SiO_2 est déposée sur la couche dispositif, et est durcie à 800 $^\circ\text{C}$. Ensuite, l'empilement platine/PZT/platine est déposé et gravé. Après une vérification de l'intégrité du matériau à l'aide d'un diffractomètre à rayons X, une couche de passivation est déposée et gravée pour laisser un accès aux électrodes inférieures et supérieures. Sur ces accès, des contacts électriques en or sont déposés et gravés. Une fois les contacts électriques fonctionnels, le bon fonctionnement du matériau piézoélectrique est vérifié à l'aide d'un AixACCT TF Analyzer 2000 et d'un double interféromètre laser (DBLI). Un masque dur d'oxyde de silicium est alors déposé et gravé sur la face arrière du wafer. Ensuite, la couche dispositif est gravée pour préparer la libération de la partie flexible des actionneurs. Après cela, la couche de SINR utilisée pour coller le wafer supérieur sur le wafer inférieur est déposée et gravée. L'empilement technologique du wafer inférieur après cette étape est représenté sur la Figure 11(a). Le procédé de fabrication du second wafer (un deuxième wafer SOI, dont les couches dispositif et support mesurent 80 μm et 500 μm d'épaisseur respectivement) commence par le dépôt et la gravure d'un masque dur sur la face arrière. Un second masque dur est ensuite déposé et gravé sur la face avant du wafer. Subséquemment, une gravure partielle est effectuée avec un second masque sur la face avant. Celle-ci a été chronométrée et calibrée préalablement sur des wafers de test. Une gravure profonde est ensuite effectuée dans toute l'épaisseur de la couche support. Après cette étape, le wafer supérieur, représenté sur la Figure 11(b) est collé sur le wafer inférieur avec une pression de 2 kN et un vide partiel de 500 mbar. Finalement, la

seconde gravure partielle permettant de graver les renforts sur le côté dispositif du wafer supérieur est réalisée et une gravure profonde est effectuée sur la face du wafer support. Les deux couches d'oxyde, comprises entre les couches dispositifs et support des deux wafers SOI sont ensuite gravées, ce qui libère la structure mobile du haut-parleur. L'empilement technologique du haut-parleur terminé est représenté sur la Figure 11(c).

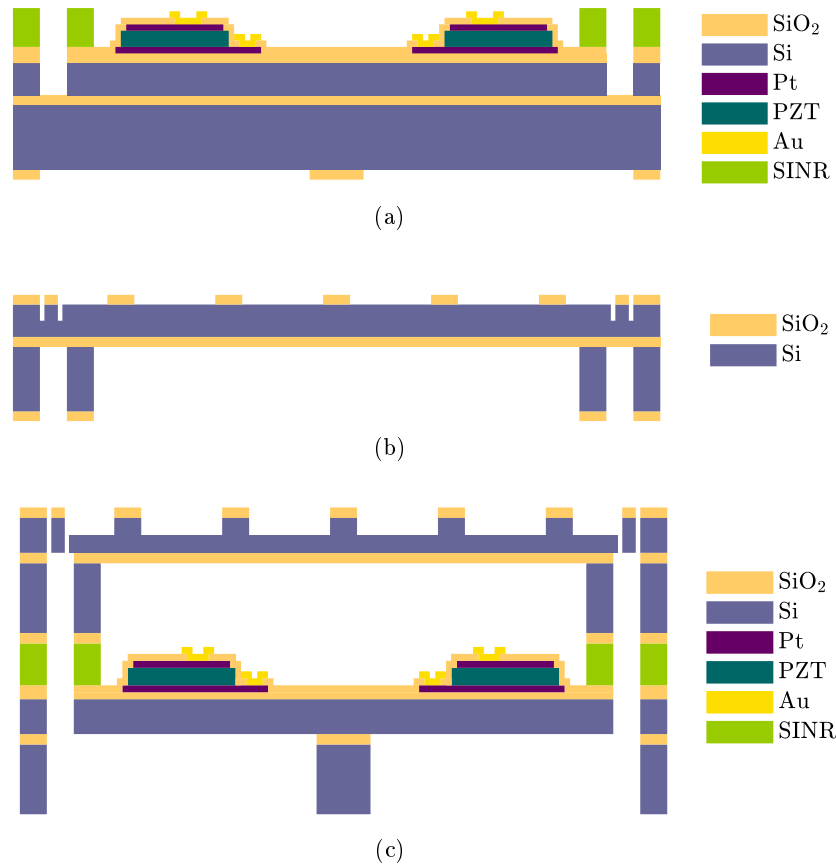


Figure 11: Empilement technologique simplifié montrant le wafer inférieur après dépôt et gravure de la colle SINR (a), le wafer supérieur après la gravure de la cavité arrière (b) et le haut-parleur après collage des deux wafers et gravures de libération (c)

Une fois fabriqués, les haut-parleurs sont séparés les uns des autres en utilisant une amorphisation laser. Ils sont ensuite individuellement soudés sur des PCB spécifiques, qui sont eux-même montés sur un baffle plan carré de 200 mm de côté, permettant d'éviter les interférences acoustiques entre les ondes avant et arrière du haut-parleur. Le baffle est ensuite disposé dans une chambre anéchoïque (G.R.A.S. AL0030) permettant la mesure acoustique du haut-parleur. Un microphone (G.R.A.S. 46 BE) est ensuite disposé à une distance de 10 mm de la surface de la plaque mobile du haut-parleur. Connecté à un amplificateur le haut-parleur est alimenté par un sinus à fréquence variable d'une amplitude comprise entre 0 V et 30 V, et la réponse en fréquences est ensuite calculée et lissée avec un filtre par fraction d'octave. Sur la Figure 12(a), une photo d'un haut-parleur découpé et soudé est représentée. Sur la Figure 12(b), la réponse en fréquences mesurée est comparée avec celle calculée en utilisant le modèle en constantes localisées. Une incertitude est calculée en tenant compte des incertitudes dimensionnelles du haut-parleur, ainsi que des incertitudes imputables aux appareils de mesure.

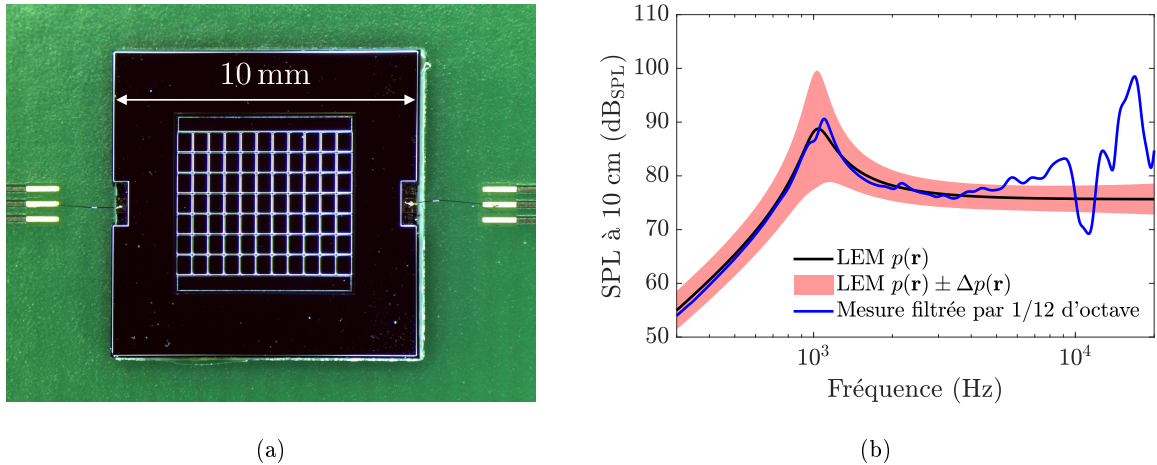


Figure 12: Photo d'un haut-parleur découpé et soudé sur un PCB, vu de dessus (a) et réponse en fréquence mesurée, lissée au douzième d'octave et comparée avec la réponse en fréquence calculée avec le modèle en constantes localisées ainsi que l'incertitude sur celle-ci (b)

Il y a une bonne adéquation entre la réponse en fréquences mesurée et la réponse calculée avec le modèle en constantes localisées, dans la bande de fréquences où celui-ci est valide, c'est à dire autour de la fréquence de résonance du haut-parleur. La fréquence de résonance ainsi que le niveau sont correctement estimés. Plus haut en fréquences, aux alentours de 5 kHz, les deux réponses divergent, ce qui est dû au comportement modal du haut-parleur, dont le modèle en constantes localisées ne tient pas compte. Aussi, les non-linéarités semblent déformer la réponse mesurée autour de la résonance.

Conclusion

Un haut-parleur MEMS innovant, basé sur un procédé de fabrication utilisant deux wafers séparés a été modélisé, fabriqué et mesuré avec succès. Il permet d'atteindre des performances supérieures aux haut-parleurs MEMS présentés dans la littérature récente. L'épaisseur de seulement 1.2 mm peut permettre l'intégration de ce haut-parleur dans des appareils portables dont l'épaisseur ne permet pas l'intégration de dispositif non-MEMS, tels que les montres connectées ou les écouteurs intra-auriculaires sans fil. La résonance pourrait être atténuée par filtrage ou par contrôle actif pour rendre la réponse du haut-parleur plus plate. Des filtres peuvent également être utilisés pour permettre de corriger la réponse accidentée du haut-parleur, plus haut en fréquence.

Abstract

In pursuance of making loudspeakers compatible with very large scale integration (VLSI) processes, research has been carried out on the development of MEMS loudspeaker, from nearly as early as the first MEMS device and recently arouses a gain of interest due to the thinning of portable multimedia devices. Despite interesting performance for in-ear loudspeaker, where high resonance frequencies and small displacements can generate significant sound pressure level, no solution was found to advantageously replace non-MEMS loudspeakers for free field applications. To widen the frequency range of MEMS loudspeaker, an innovative geometry based on an assembly of two wafers is proposed, in order to separate the electro-mechanical transducer from the mechano-acoustics transducer, with the aim of reaching a better optimization target. In this thesis, the working principle of the loudspeaker, as well as the models used for the design and the optimization are presented and detailed. The innovative custom manufacturing process with which the loudspeaker is manufactured in the CEA-Leti clean rooms is then detailed, and the measured frequency response is compared with the simulated ones. The loudspeaker is able to radiate a pressure of $110 \text{ dB}_{\text{SPL}}$ at 10 mm and at 1 kHz, the resonance frequency of the loudspeaker, which is above the state of the art for MEMS loudspeaker with these dimensions. More than radiating high sound pressure level at relatively low frequencies, the loudspeaker is generating a frequency response flatter than what is observed in the recent literature, with a pressure of $98 \text{ dB}_{\text{SPL}} \pm 3 \text{ dB}$ at 10 mm from 1410 Hz to 7980 Hz. The total harmonic distortion of the loudspeaker is also estimated and measured, and values below 5% for the usable bandwidth of the loudspeaker and for reasonably high sound pressure level are reported. By using digital signal processing, as well as a dedicated packaging with specific acoustical couplings, this loudspeaker could replace the secondary loudspeaker of smartphones.

Contents

Acknowledgments	i
Résumé	iii
Introduction	iii
État de l’art et spécifications	iii
Modélisation en petits signaux et design préliminaire	v
Fabrication et caractérisation	viii
Fabrication et caractérisation	x
Conclusion	xii
Abstract	xiii
List of Figures	xxii
List of Tables	xxx
Introduction	1
1 State of the Art and Specifications	3
1.1 Chapter Introduction	3
1.2 Single Degree of Freedom Loudspeaker	4
1.3 Distortion	6
1.4 Free Field	7
1.4.1 Electrodynamic	7
1.4.2 Piezoelectric	10
1.4.3 Electrostatic	15
1.4.4 Digital	17
1.4.5 Other Types of Transduction	19
1.5 In-Ear	20
1.6 Specifications and Design Choices	27
1.7 Chapter Conclusion	31
2 Small Signal Modeling and Design	33
2.1 Design Methodology	34
2.2 Lumped Element Modeling	35
2.2.1 General Structure	35
2.2.2 Equivalent Electrical Circuit	37
2.2.3 Actuators	37

2.2.4	Residual Stress	39
2.2.5	Electrical Circuit	41
2.2.6	Damping	42
2.2.7	Squeeze Film	44
2.2.8	Radiation	45
2.2.9	In-Ear	49
2.2.10	Back Cavity	50
2.2.11	Electrical behavior	50
2.2.12	Sensitivity and Efficiency	51
2.3	Optimization of the Performance	53
2.3.1	Dimensions	53
2.3.2	Height of the Coupling Blocks	56
2.3.3	Width of the Air Interstice	56
2.4	Dedicated Driving Board	57
2.4.1	Amplifier	57
2.4.2	Notch Filter	63
2.4.3	Printed Circuit Board	66
2.5	Chapter Conclusion	68
3	Advanced Design	69
3.1	Chapter Introduction	70
3.2	Finite Element Modeling	70
3.2.1	Physics and Geometry	70
3.2.2	Mesh	73
3.2.3	Static Simulation	74
3.2.4	Modal Analysis	75
3.2.5	Perfectly Matched Layer	79
3.2.6	Acoustic Pressure	79
3.2.7	In-Ear	82
3.2.8	Stress	83
3.2.9	Geometric Nonlinearities	84
3.3	Linearization Spring	86
3.3.1	General Structure	86
3.3.2	Static Modeling	86
3.3.3	Dynamic Modeling	89
3.4	State Space Modeling	90
3.4.1	Free Field	91
3.4.2	In-Ear	95
3.4.3	Loudspeaker Design Summary	98
3.5	Chapter Conclusion	101
4	Technological Realization & Characterization	103
4.1	Chapter Introduction	104
4.2	Technological Realization	104
4.2.1	Bottom Wafer (Electromechanical Wafer)	104
4.2.2	Top Wafer (Mechanoacoustical Wafer)	111

4.2.3	Wafer Bonding	114
4.3	Mechanical Characterization	117
4.3.1	Stiffness	117
4.4	Electrical Characterization	118
4.4.1	Impedance	118
4.4.2	Amplifier	119
4.5	Acoustical Characterization	120
4.5.1	Pressure Response on Wafer	120
4.5.2	Pressure Response in Anechoic Chamber	122
4.5.3	Directivity	124
4.6	Non Linearities	124
4.6.1	Frequency Response	124
4.6.2	Transduction Factor	125
4.6.3	Total Harmonic Distortion	126
4.7	Chapter Conclusion	127
Conclusion		129
Appendices		143
A	State Space Modeling	145
B	Horn	146
C	Cumulative Error Calculation	150
C.1	Moving Mass	150
C.2	Compliance	150
C.3	Blocked Force	151
C.4	Radiating Surface	151
C.5	Total	152
D	CAD Plans	153
D.1	Wafer 1	153
D.2	Wafer 2	154
D.3	Assembly	155
E	Power Supply Filters	156
F	Printed Circuit Board	158
F.1	Top Layer	158
F.2	Bottom Layer	158
G	Altium Circuits	159
G.1	Top Level	159
G.2	Amplifier 1	160
G.3	Amplifier 1	161
G.4	Precision Rectifier	162
G.5	Nocth Filter	163
H	Cover	164

List of Symbols

Symbol	Description	Unit	Page
F_{in}	Input force of the equivalent mechanical circuit	N	4
Z_m	Equivalent mechanical impedance	N s m^{-1}	4
v	Velocity	m s^{-1}	4
δ	Displacement	m	4
α	Acceleration	m s^{-2}	4
p_{out}	Output pressure	Pa	4
S_d	Effective radiating surface of the loudspeaker	m^2	4
F_{out}	Force at the output of the mechanical circuit	N	4
R_{ms}	Equivalent viscous damping of the moving structure	N s m^{-1}	4
M_{ms}	Equivalent mass of the moving structure	kg	4
C_{ms}	Apparent compliance of the moving structure	m N^{-1}	4
ω	Pulsation	rad s^{-1}	6
t	Time	s	6
\mathbf{F}	Force generated by an electromagnetic circuit	N	8
ℓ	Length of coil immersed in a magnetic field	m	8
\mathbf{B}	Intensity of magnetic field inside the air interstice	T	8
u_{in}	Input voltage	V	8
i_{in}	Input current	A	8
R_e	Equivalent electrical resistance of a coil	Ω	8
L_e	Equivalent electrical inductance of a coil	H	8
S_p	Strain in the p direction in the piezoelectric material	1	10
D_i	Electric displacement in the i direction in a piezoelectric material	C m^{-2}	10
T_q	Stress in the q direction in a piezoelectric material	Pa	10
E_k	Electric field in the k direction in a piezoelectric material	V m^{-1}	10
s_{pq}^E	Compliance at constant electric field E in a piezoelectric material	m N^{-1}	10

continues on next page

c_{pq}^E	Stiffness at constant electric field E in a piezoelectric material	N m^{-1}	??
ε_{ik}^T	Dielectric constant for a constant strain	F m^{-1}	10
d_{kp}	Piezoelectric constant	V m^{-1}	10
T_p	Strain at constant electric field ion the p direction	1	10
P_r	Remanent polarization	C m^{-2}	13
E_c	Coercive field in a ferroelectric material	V m^{-1}	13
C_p	Capacitance of the piezoelectric layer	F	13
C_0	Capacitance of a electrostatic actuator	F	15
ε_0	Vacuum permittivity	F m^{-1}	15
ε	Relative permittivity	1	15
V_{DC}	Direct Current bias voltage	V	16
R_g	Equivalent generator and connectors resistance	Ω	16
ϕ	Transduction factor of an electrostatic transducer	N V^{-1}	16
R_2, R_4	Equivalent acoustical dissipation in a 60318-4 ear-occluded coupler	Pa s m^{-3}	22
$C_1 - C_5$	Equivalent acoustical compliance in a 60318-4 ear-occluded coupler	Pa m^{-3}	22
$L_1 - L_5$	Equivalent acoustical mass in a 60318-4 ear-occluded coupler	$\text{Pa s}^2 \text{m}^{-3}$	22
L	Length of the flexible part of the actuators	m	36
t_p	Thickness of the piezoelectric layer	m	36
t_m	Thickness of the electric part of the actuators	m	36
F_{bl}	Blocked force generated by the actuators	N	36
δ_0	Free displacement of the actuators	m	36
w_s	Width of the air interstice around the rigid plate	m	36
Z_r	Radiation impedance of the loudspeaker	Pa s m^{-3}	37
EI_n	Equivalent Young's modulus times the inertial moment of beam n	kg N	38
W	Width of the actuators	m	38
e_{31}	Reduced piezoelectric coefficient	C V^{-1}	38
σ_0	Residual stress	N m^{-2}	40
t_o	Thickness of the equivalent layer carrying the residual stress	m	40
A_p	Surface of piezoelectric material	m^2	41
R_s	Electrical losses during conduction of the piezoelectric layer	Ω	41
μ	Dynamic viscosity of air	Pa s	42
p	Acoustic pressure	Pa	42
t_{pl}	Total thickness of the moving plate	m	43
l_s	Perimeter of the moving plate	m	43
v_i	Fluid velocity in the viscous layer	m s^{-1}	43
ρ_0	Air density at ambient temperature	kg m^{-3}	43

continues on next page

F_{sf}	Reaction force caused by the viscous damping	N	44
c_0	Sound velocity in air at ambient temperature	m s^{-1}	45
k_0	Wavenumber	rad m^{-1}	45
r	Source to evaluation point distance	m	46
Z_0	Characteristic acoustical impedance	kg s m^{-3}	47
f_s	Resonance frequency	Hz	48
Q_{ms}	Mechanical Quality Factor	1	48
R_{le}	Equivalent acoustic leak resistor	Pa s m^{-3}	49
C_b	Acoustic compliance created by a sealed back cavity	Pa m^{-3}	50
Z_e	Electrical impedance of the loudspeaker	Ω	50
P_e	Dissipated electrical power	W	51
Q_e	Reactive electrical power	var	51
κ	Sensitivity of the loudspeaker	dB_{SPL} at 1 mW at 2 kHz	51
η	Electroacoustical efficiency of the loudspeaker	1	52
h_0	Height of the coupling block	m	53
σ_{max}	Maximum stress in the elastic part of the actuators	Pa	54
k	Safety factor for stress concentration in the elastic part of the actuators	1	55
γ	Electro-mechanical transduction factor	N V^{-1}	37
n_x	Number of stiffeners of the plate in the x direction	1	75
n_y	Number of stiffeners of the plate in the y direction	1	75
L_p	Length of the moving plate	m	76
W_p	Width of the moving plate	m	76
L_{ls}	Length of the linearization spring	m	76
W_{ls}	Width of the linearization spring	m	76
L_{fpn}	Width of the plain frame around the moving plate in the n direction	m	76
w_r	Width of the stiffeners of the moving plate	m	76
t_{pp}	Thickness of the plain part of the moving plate	m	76
L_{rr}	Length of the rectangle created by the stiffeners of the moving plate	m	76
W_{rr}	Width of the rectangle created by the stiffeners of the moving plate	m	76
M_{ls}	Bending torque at the end of the linearization spring	N m	87
t_{ls}	Thickness of the linearization spring	m	88

List of Acronyms

Acronym	Description	Page
VLSI	Very Large Scale Integration	1
MEMS	Micro Electro-Mechanical System	1
FEM	Finite Element Model	2
THD	Total Harmonic Distortion	7
SPL	Sound Pressure Level	8
CAD	Computer-Aided Design	9
PZT	Lead Zirconate Titanate	11
IEC	International Electrotechnical Commission	20
SOI	Silicon On Insulator	25
DBLI	Double Beam Laser Interferometer	106
SEM	Scanning Electron Microscope	108
DRIE	Deep Reactive Ion Etching	113

List of Figures

1	Réponses en fréquence moyennées de douze haut-parleurs du commerce ainsi que l'écart type (a) et photo d'un haut-parleur typique mesurant $11 \times 15 \times 3.5 \text{ mm}^3$ tiré de [1] (b) . . .	iv
3	Vue 3D (a) et vue 3D en coupe (b) du haut-parleur dans Solidworks®	v
4	Vue en demi-coupe du principe de fonctionnement du haut-parleur avec les dimensions importantes qui le régissent	vi
5	Schéma électrique équivalent du haut-parleur	vi
6	Fréquence de résonance du haut-parleur en fonction de l'épaisseur de la couche élastique t_m et en fonction de la surface active S_d (a) et pression acoustique générée par le haut-parleur en fonction des mêmes paramètres (b)	vii
7	Réponses en fréquences du haut-parleur pour différentes valeurs arbitraires de facteur de qualité Q_{ms} (a) et impédance électrique du haut-parleur pour un facteur de qualité $Q_{ms} = 10$ (b)	viii
8	Haut-parleur en vue 3D (a) et modèle complet comprenant la partie acoustique (b) dans COMSOL®	viii
9	Comparaison entre la pression acoustique calculée à l'aide du modèle en constantes localisées et avec le modèle en éléments finis (a) et non linéarité géométrique dues aux contraintes longitudinales dans les couches élastiques de la partie d'actionnement du haut-parleur (b)	ix
10	Vue en coupe partielle du ressort de linéarisation et de l'extrémité de l'actionneur (a) et distorsion harmonique totale simulée du haut-parleur avec et sans ressort de linéarisation (b)	x
11	Empilement technologique simplifié montrant le wafer inférieur après dépôt et gravure de la colle SINR (a), le wafer supérieur après la gravure de la cavité arrière (b) et le haut-parleur après collage des deux wafers et gravures de libération (c)	xi
12	Photo d'un haut-parleur découpé et soudé sur un PCB, vu de dessus (a) et réponse en fréquence mesurée, lissée au douzième d'octave et comparée avec la réponse en fréquence calculée avec le modèle en constantes localisées ainsi que l'incertitude sur celle-ci (b)	xii
13	Number of publications about MEMS loudspeaker per year	2
1.1	Block diagram of the main transductions in a loudspeaker	4
1.2	Equivalent electrical circuit of a mechanical oscillator	4
1.3	Normalized velocity, acceleration and displacement of	5
1.4	First order approximation of the frequency response of a loudspeaker radiating in free field (a) and in a sealed cavity (b)	5
1.5	Normalized linear and nonlinear transfer functions (a) and output signals resulting from the transfer through the linear and nonlinear transfer functions, normalized to the maximum amplitude of the linear signal (b)	6

1.6	Pure sine (a) and sum of pure sines (b) after being transferred through a linear and a nonlinear function in the frequency domain (b)	7
1.7	Schematic representation of an electrodynamic loudspeaker motor	8
1.8	Equivalent electrical circuit of an electromagnetic transducer using a coil and a magnet	8
1.9	Averaged frequency response of twelve commercial loudspeakers with the standard deviation (a) and picture of a typical $11 \times 15 \text{ mm}^2$ of the loudspeaker described in [1] (b)	9
1.10	Frequency response (a) and 3D CAD drawing (b) of the loudspeaker presented in [15]	10
1.11	Representation of cuboid subjected to three three dimensional stresses in the three orthogonal directions	11
1.12	Schematic of a piezoelectric cantilever with an non-deformable free end	12
1.13	Cubic structure of PZT below (a) and tetragonal structure of PZT above (b) Curie transition temperature adapted from [25]	13
1.14	Simplified polarization P of a ferroelectric material subjected to an electric field E represented by sigmoid functions	13
1.15	Equivalent electrical circuit of a bending piezoelectric transducer	14
1.16	Frequency response (a) and schematic of the concept (b) of the loudspeaker presented in [38]	14
1.17	Frequency response (a) and picture (b) of the Usound UTP-2018 loudspeaker, whose characteristics are detailed in [40]	15
1.18	Schematic of two plates polarized to a different potential	16
1.19	Equivalent electrical circuit of a electrostatic transducer	16
1.20	Frequency response (a) and schematic of the concept (b) of the loudspeaker presented in [38]	17
1.21	Schematic of an array of speaklets (a) and sequence of acoustic pulse reproducing a period of a sine wave (b)	18
1.22	Velocity response of a damped oscillator to a square voltage impulse	18
1.23	Frequency response (a) and picture (b) of the loudspeaker presented in [56]	19
1.24	Schematic of thermoacoustic transduction effect, adapted from [62]	19
1.25	Frequency response (a) and picture (b) of the loudspeaker presented in [63]	20
1.26	Transfer function of 3 commercial head and torso mannequin measured in [67] (a) and picture of the B&K 4128	21
1.27	Transfer function of a G.R.A.S. standardized artificial ear (a) and picture of this artificial ear (b)	21
1.28	Lumped equivalent network of the ear-occluded IEC 60318-4 coupler	22
1.29	Harman target curve adapted from [68] (a) and impedance on a IEC 60318-4 ear-occluded coupler calculated using the equivalent electrical circuit of Figure 1.28 (b)	23
1.30	Frequency response of the microloudspeaker in a 2 cm^3 cavity (a) and picture of this microloudspeaker (b) taken from [70]	24
1.31	Frequency response of the microloudspeaker in an IEC 60318-4 coupler (a) and picture of this microloudspeaker (b) adapted from [76]	25
1.32	Frequency response of the loudspeaker in an IEC 60318-4 coupler (a) and picture of this microloudspeaker (b) adapted from [82]	26
1.33	Frequency response of the loudspeaker in an IEC 60318-4 coupler (a) and a drawing of a cross section of the loudspeaker mounted on the coupler (b) taken from [93]	27
1.34	Sound pressure level at 10 cm and 1 kHz of MEMS loudspeakers of the literature whose performance are recalled in Table 1.2	28

1.35	Sound pressure level at 100 Hz radiated in a coupler of MEMS loudspeakers of the literature whose performance are recalled in Table 1.3	30
1.36	Choice of methods for sound reproduction using a MEMS loudspeaker	31
2.1	Design loop where the optimisation of the linear parameters appears in blue, and the optimization using finite element modeling and state space modeling appears in red	34
2.2	3D (a) and 3D cross-section (b) views of the main version of the designed loudspeaker	35
2.3	Half cross section sketch of the principle of the designed loudspeaker in which the light gray and light blue parts represent the undeformed structure	36
2.4	Strain resulting from an applied input electric field on a ferroelectric material (a) and output signals for a symmetric and asymmetric input sinusoidal signals applied to such a material (b)	36
2.5	Linear lumped equivalent network of the loudspeaker	37
2.6	Bottom part of the loudspeaker manufactured in the wafer 1	38
2.7	3D schematic of a cantilever	38
2.8	Deflection profile of a clamped-guided (a) and clamped-clamped (b) beam, actuated with a piezoelectric layer	39
2.9	Deflection of a cantilever with and without residual stress in an oxide layer (a) and cross section sketch of a cantilever with residual stress in one layer (b)	41
2.10	3D schematic of a microfabricated metallic conductor	41
2.11	Equivalent electrical circuit of the electrical connections and of the piezoelectric layer	42
2.12	3D schematic (a) and zoom on the 3D view of Figure 2.2 (b) showing the thin interstice between the mobile plate and the fixed frame of the loudspeaker	42
2.13	Critical thickness of the viscous layer, in which the velocity in the layer is entirely determined by the velocity of the plate (a) and profile of the velocity of the fluid inside the interstice for different frequencies (b)	44
2.14	Sketch of the squeeze film effect (a) and squeeze film impedance for different gap height (b)	44
2.15	Geometric representation of the Rayleigh integral	45
2.16	Pressure relative to the low frequency pressure as a function of the angle θ for $\phi = 0$ (a) and $\phi = \pi/4$ (b)	46
2.17	Real (a) and imaginary (b) part of the radiation impedance for a circular rigid plate, a square rigid plate and a rectangular rigid plate with an aspect ratio of 10 and of same surface S_d , flush-mounted in an infinite baffle	47
2.18	Influence of the radiation impedance calculated with Equation 2.31 on the velocity of a typical microloudspeaker such as the one reviewed in Section 1.4.1 (a) and frequency response of a loudspeaker calculated using Equation 2.27 for different quality factor Q (b)	48
2.19	Pressure at the coupler for arbitrary values of C_{ms} and M_{ms} (a), and for different leak resistors R_{le} (b)	49
2.20	Schematic of a loudspeaker with a back cavity (a) and pressure radiated by a loudspeaker with different sizes of back cavities (b)	50
2.21	Real and imaginary parts of the impedance (a) and active and reactive power (b) of the piezoelectric loudspeaker on a arbitrary scale, and as a function of a normalized frequency	51
2.22	Sensitivity (a) and electromechanical efficiency (b) of a piezoelectric bending actuators loudspeaker	53
2.23	Normalized Resonance frequency and sound pressure level as a function of the elastic layer thickness and the active area	54

2.24	Displacement of the moving plate for different loudspeaker dimensions S_d (a) and maximum stress in a clamed-guided beam as a function of the displacement of the guided end for different beam thicknesses t_m (b)	54
2.25	Frequency response of the loudspeaker for three different radiating surfaces S_d with a fixed actuator thickness $t_m = 12 \mu\text{m}$ (a) and for three different actuator thicknesses with a fixed surface $S_d = 36 \text{mm}^2$ (b)	55
2.26	Pressure response for different heights h_0 with $R_{ms} = 0$ and $S_d = 36 \text{mm}^2$ (a) and pressure response for different radiating surfaces S_d (b)	56
2.27	Frequency response of the loudspeaker for different interstice widths w_i (a) and for different plate thicknesses t_{pl} , considering the change of moving mass M_{ms} (b)	57
2.28	Impedance of the loudspeaker (a) and power drawn by the loudspeaker for a 30 V input signal (b)	58
2.29	Current gain output stage	59
2.30	Non Inverting Operational Amplifier	59
2.31	Offset adder and low pass filter	60
2.32	Transfer function of the circuit depicted in figure 2.31 from V_+ to u_{out} (a) and from u_{in} to u_{out} (b)	61
2.33	Frequency response of the complete circuit simulated using LTspice (a) and input and output time domain signal at 1 kHz of the amplifier at maximum gain (b)	62
2.34	Time signal at the output of the amplifier for different amplifier gain simulated with LTspice (a) and THD of the amplifier as a function of gain (b)	62
2.35	Instantaneous and RMS power dissipated in the NPN and the PNP transistors (a) and equivalent thermal circuit of the transistor junction to ambient air (b)	63
2.36	Schematic of the notch filter circuit	64
2.37	Frequency responses of the notch filter for different values of R_2 and R_3 (a) and for different values of R_7 (b)	65
2.38	Frequency response of the notch filter for different values of R_4 (a) and frequency response of the loudspeaker corrected by the notch filter (b)	66
2.39	Routing of the Printed Circuit Board	67
2.40	3D view of the loudspeaker amplifier printed circuit board (a) and 3D view of the loudspeaker printed circuit board (b)	67
3.1	3D mechanical part of the loudspeaker (a) and same loudspeaker coupled to a hemispherical air domain (b) in COMSOL®	71
3.2	Thermoacoustics domain around the moving plate of the loudspeaker (a) and view of the circular hard boundary wall disc around the loudspeaker (b) in COMSOL®	71
3.3	3D view of the skewness of the mechanical part of the model (a) and zoom on the linearization spring (b) represented from red (poor quality) to green (good quality)	73
3.4	Histogram of the skewness for the total number of elements of the model (a) and skewness of elements in a cross section of the complete model represented as red (poor quality) to green (good quality) (b)	74
3.5	3D view (on scale) (a) and cross section view (not on scale) (b) of the loudspeaker deformed under an input voltage $u_{in} = 30 \text{V}$	75
3.6	Deflection profile of the actuators calculated with the finite element model and with the analytical model (a) and deflection profile calculated along the width of the actuator (b)	75

3.7	First eigenmode of the moving plate as a function of the number of stiffeners (a) and pressure response of the loudspeaker for different number of stiffeners (b)	76
3.8	Dimensions of the moving plate on a 3D view (a) and dimensions of the plate on a partial cross section of the plate (cross section A) not on scale (b)	77
3.9	Geometry of the plate with $n_x = n_y = 3$ (a), modal shape of the plate with $n_x = n_y = 3$ (b), geometry of the plate with $n_x = n_y = 10$ (c) and modal shape of the plate with $n_x = n_y = 10$ (d)	77
3.10	Modal shape of the mechanical part in the loudspeaker for the 16 modes in the audio bandwidth	78
3.11	Sound pressure level in the air domain and in the PML for a PML with 5 elements of mesh (a) and for a PML with 15 elements of mesh (b)	79
3.12	Comparison of the sound pressure level computed with the finite element and lumped element models for different loudspeakers dimensions (a) and 3D view of the loudspeaker radiating in air in COMSOL® (b)	80
3.13	Total thermoviscous losses in the interstice surrounding the plate and acoustic pressure in the air domain	80
3.14	Sound pressure level on axis as a function of the width of the air interstice w_s around the moving plate (a) and pressure field simulated with a simple moving plate with a simple acoustic domain around the plate (on the left) and with a thermoviscous domain around the plate (on the right) with an arbitrary scale (b)	81
3.15	Directivity normalized to the pressure at $\theta = 0$ of the loudspeaker for four frequencies (a) and SPL field radiated by the loudspeaker at $f = 50$ kHz	82
3.16	3D view of the loudspeaker in the coupler in Comsol Multiphysics (a) and frequency response of this model (b)	83
3.17	3D view of Von Mises stress in the actuators (a) and zoomed around the location of the maximum Von Mises stress (b)	84
3.18	Schematic cross section of a clamped-rotation locked cantilever, highlighting the change of projected length ΔL (a) and deflection of the actuators, with and without considering the geometrical nonlinearities in the finite element model (b)	85
3.19	Linear and nonlinear stiffness of a clamped-guided silicon beam with a thickness of $12 \mu\text{m}$, a width W of 5.8 mm and a length L of 2.641 mm (a) and Von Mises stress in a clamped-guided cantilever without (on top) and with (on bottom) nonlinearities considered (b) in COMSOL® (not on scale)	85
3.20	Working principle of the linearization spring represented as hinges and rigid bodies	86
3.21	Linear and nonlinear stiffnesses of a clamped-guided silicon beam with a thickness of $12 \mu\text{m}$, a width W of 5.8 mm and a length L of 2.641 mm (a) and cross section schematic of the coupling block of height h_0 attached to a linearization spring (b)	87
3.22	Analytical nonlinear stiffness without and with the linearization spring for different parameters t_{ls} , L_{ls} and h_0 (a) and simplified semi lumped cross section view of a nonlinear beam attached to the linearization spring (b)	88
3.23	Cross section schematic of the piezoelectric actuator linked to the plate of the loudspeaker by an apparent stiffness k_{lsz} (a) and working curves of the actuators crossing the different stiffnesses at different working points (b)	89
3.24	Lumped equivalent network of the loudspeaker with a linearization spring	89

3.25 Pseudo rigid half cross section of the loudspeaker (a) and pressure radiated by this model in free field (b)	90
3.26 Block schematic representation of a state space model	91
3.27 Linear lumped equivalent network of the loudspeaker	92
3.28 Pressure response calculated with the state space model and with the lumped model (a) and input multitone signal and the resulting displacement $x(t)$ computed with the State Space model (b)	93
3.29 Nonlinear theoretical $C_{ms}(x)$ function (a) and nonlinear $\gamma(u_c)$ fitted from measurements (b)	93
3.30 Nonlinear capacitance $C_p(u_c)$ fitted to a measurement (a) and total harmonic distortion calculated with the nonlinear model for the loudspeaker with and without linearization spring (b)	94
3.31 Total harmonic distortion at $u_{in} = 1.5$ V independently for each parameters (a) and for different input levels u_{in} (b)	95
3.32 Lumped equivalent network of the loudspeaker inside a IEC 711 coupler	96
3.33 Pressure response calculated with the state space model for different sampling frequencies F_s and with the lumped model (a) and input multitone signal and the displacement $x(t)$ computed with the state space model (b)	97
3.34 Total harmonic distortion at $u_{in} = 1.5$ V independently for each parameters (a) and for different input levels u_{in} (b)	98
3.36 Frequency responses of the different variants of the loudspeaker simulated using the lumped element circuit of Section 2.2 (a), 3D CAD view of the 3×3 variant (b) and of the 8×8 variant (c)	100
3.37 Mapping of the loudspeakers on the wafer	101
4.1 Bottom wafer	104
4.2 Bottom wafer after deposition and etching of the PZT stack layers	104
4.3 XRD measurement of the piezoelectric stack showing the desired orientation (100) of the PZT lattice (a) and planes (100), (110) and (111) for a tetragonal structure (PZT) and plane (111) for a face-centered cubic structure such as the one of platinum (b)	105
4.4 Bottom wafer after etching of the hard mask on the handle wafer side	105
4.5 Bottom wafer after etching of the PZT stack	106
4.6 Polarization as a function of the electric field (a) and capacitance as a function of the input voltage (b) on test devices on the manufactured PZT	106
4.7 Displacement as a function of the electric field on a test device (a) and expected pressure response of the loudspeaker with the $e_{31,f}$ estimated from the electromechanical measurements (b)	107
4.8 Bottom wafer after deposition and etching of the passivation layer	107
4.9 Bottom wafer after deposition and etching of the metal pads	108
4.10 Microscope picture of the connection between the top electrode and the gold conductor (a), zoom on the gold connector connecting the top electrode (b) after the etching of the gold pads and location of the pictures on a 2D view of a loudspeaker (c)	108
4.11 SEM picture of the device layer of the bottom wafer (a) and zoom on the PZT stack (b)	109
4.12 Bottom wafer after the pre-release of the structure in the device layer	109
4.13 Microscope picture of the connection between the top electrode and the gold conductor (a), zoom on the gold connector connecting the top electrode (b) after the etching of the gold pads and locations of the pictures on a 2D view of a loudspeaker (c)	110

4.14	Picture of the bottom wafer after the etching of the device layer (a) and zoom on the wafer (b)	110
4.15	Bottom wafer after the deposition and patterning of the SINR glue	110
4.16	Top wafer after hard mask deposition on the handle wafer side	111
4.17	Schematic technology stack after the etching of the back hard mask	111
4.18	Top wafer after etching of the hard mask on the device layer	111
4.19	Microscope picture of the hard mask of the device layer on the top wafer after etching on a complete moving plate (a) and zoom on the interstice (b)	112
4.20	Test silicon wafer with a hard mask for the frame and the stiffeners (a), after the partial etch of the interstice around the plate and the linearization spring (b) and after the second etch (c)	112
4.21	SEM picture of the calibration of the partial etching in the device layer of the top wafer at the periphery of the plate (a) and on a stiffener (b)	113
4.22	Top wafer after the partial etching around the linearization spring and the moving plate	113
4.23	Microscope picture of a device after the partial etching of the periphery of the plate (a) and zoom around the periphery of the plate (b)	113
4.24	Top wafer after the back cavity etching	114
4.25	Top and bottom wafers after bonding	114
4.26	Infrared microscope picture of a 3×4 device after bonding (a) and same device as designed in Solidworks® (b)	115
4.27	Wafer 1 and 2 after etching of the stiffeners on the device side of the top wafer	115
4.28	Microscope picture of the top wafer after the etching of the stiffeners (a) and zoom around the linearization spring (b)	116
4.29	Wafer 1 and 2 after full sheet etching of the back cavity on back side 1 and etching of remaining oxides	116
4.30	Picture of a diced 6×6 loudspeaker on a one euro coin (a) and picture of a wafer after the dicing process (b)	117
4.31	Schematic cross section of a nanoindenter (a) and stiffness measured and simulated on two loudspeakers (b)	117
4.32	Impedance of the loudspeaker (a) and reactive power of the loudspeaker calculated using the measured impedance (b)	118
4.33	Picture of the amplifier	119
4.34	Frequency response measured and simulated (a) and input and output time domain signals (b) of the amplifier	119
4.35	Total harmonic distortion as a function of frequency (a) and transfer function of the active peak filter for different settings of R_{12} , R_{15} and R_{17} (b)	120
4.36	Measurement setup of the wafer on the prober	121
4.37	Frequency response of the loudspeaker calculated with the lumped element model and compared to the one measured on twelve loudspeakers (a) and position of the twelve loudspeakers on the wafer (b)	121
4.38	Schematic of the measurement setup	122
4.39	Cross section of a 3D drawing of the loudspeaker mounted on the PCB and on the baffle (a) and binocular magnifier picture of a 6×6 loudspeaker mounted on the PCB (b)	122

4.40	Picture of the measurement setup inside the anechoic chamber (a) and measured pressure response smoothed at 1/12 octave compared to the frequency response calculated with the lumped element model (b)	123
4.41	Schematic of the measurement setup	123
4.42	Schematic of the measurement setup (a) and measured directivity (b)	124
4.43	Twenty frequency responses of the loudspeaker with an input voltage before the amplifier from 50 mV to 1000 mV referenced to the pressure at 2 kHz (a) and increase of the level of the response for different frequencies (b)	125
4.44	Acoustic pressure as a function of the input voltage for different frequencies (a) and for different input voltages (b)	126
4.45	Simulated and measured frequency response of the loudspeaker at $u_{in} = 100$ mV (a) and simulated and measured THD (b)	127
B.1	Horn shape and discretized tubes (a) and simple acoustical quadripole element	146
B.2	Linear lumped equivalent network of the loudspeaker radiating into a horn	147
B.3	Imaginary and real part of the acoustical impedance of the horn (a) and pressure radiated by the loudspeaker with and without horn (b)	147
B.4	3D CAD view of the horn in Solidworks [®] (a) and cross section 3D view of the horn mounted on the PCB on which the loudspeaker is bonded (b)	148
B.5	Acoustic simulation of the horn using COMSOL [®]	148
B.6	Real and imaginary part of the acoustical impedance of the horn calculated using the two port model and COMSOL [®] (a) and pressure response of the horn at 10 cm calculated with the two port model and with COMSOL [®] (b)	149
E.1	Equivalent Electrical Circuit of a Ferrite Bead	156
E.2	Electrical impedance of a ferrite beam with a series decoupling capacitor (a) and transfer function of the power supply filter (b)	157
H.1	Frequency response using a patch (a) and mirrored repeated and shifted frequency response (b)	164
H.2	Frequency responses with patch iteratively shifted by a sine (a) and noisy shifting sum of sine used in the cover (b)	164

List of Tables

1.1	Parameters of the equivalent circuit of the IEC 60318-4 ear-occluded coupler	23
1.2	Sound pressure level and footprint of MEMS loudspeakers of the literature for free field applications	28
1.2	Sound pressure level and footprint of MEMS loudspeakers of the literature for free field applications	29
1.3	Sound pressure level in coupler and footprint of MEMS loudspeakers of the literature for in-ear applications	30
3.1	Main linear and isotropic parameters of the materials used in the COMSOL® model . . .	72
3.2	Main dimensions of the nine different variants of the loudspeaker (mm)	99

Introduction

Loudspeakers are electroacoustic transducers, used in most consumer devices to convert an electrical signal into an audible acoustic signal. The first embodiment of the loudspeaker was invented by Edward W. Kellogg and Chester W. Rice in 1925 and patented in its electrodynamic form, which is still the most widely used today. Despite some advanced materials and geometrical optimizations, the working principle is still the same today. Depending on the application, loudspeakers have a large range of dimensions, ranging from millimeters for portable devices, to meters for sound reinforcement systems.

A loudspeaker should reproduce all audible frequencies, from 20 Hz to 20 kHz with the same sound pressure level. It essentially means that if the loudspeaker is represented by a single input single output linear time invariant system, the transfer function should be equal to one in the audio frequency range. Undoubtedly and due to numerous physical limitations and wave behavior this is achievable only for specific conditions, frequency bands, and by neglecting the time of propagation of the wave from the source to the sensor. Despite a few remaining flaws, bulky loudspeakers designed for home or studio use can achieve incredibly flat frequency responses, with a very small alteration of the reproduced signal.

During the past decades, an exponentially growing interest for connected portable multimedia devices was observed worldwide, and the electrodynamic loudspeaker was adapted in order to be integrated into these devices. Due to the physical limitations such as the wavelength of low frequencies, a lot of compromises were made in order to shrink the size of the loudspeaker down. Despite the extreme reduction of the size of the loudspeaker, down to approximately 500 mm^3 , no real breakthrough occurred, and these loudspeakers are still working on the same century-old principle and are still manufactured individually.

More than being based on an ancient transduction principle, the loudspeaker is one of the only components that is not compatible with the micromanufacturing Very Large Scale Integration (VLSI) processes. During the past few years, the interest for Micro Electro-Mechanical Systems (MEMS) loudspeakers has significantly grown, as it can be seen by displaying the number of publications on the topic in the recent years. As it can be seen in Figure 13, MEMS loudspeakers have been developed as early as three years after the introduction of the term “MEMS”. During the first decade, the number of publications was very low and linked to the poor performance of these loudspeakers. The recent increase of interest for this technology since 2005 could be linked to the advent of portable multimedia devices, and the need to reduce the size of loudspeakers in order to integrate them into the aforementioned apparatuses.

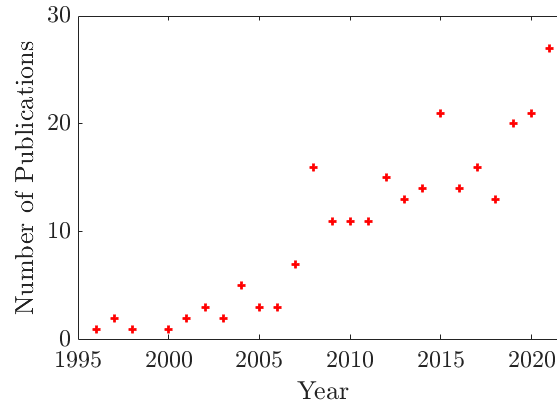


Figure 13: Number of publications about MEMS loudspeaker per year

In view of these recent developments and based on the strength of its long experience in the design and manufacturing of MEMS actuators, especially using thin film piezoelectric materials, CEA Leti has undertaken the development of MEMS loudspeakers in order to widen its range of skills on the side of electroacoustics transducers operating in the audio band.

As it will be described in more detail in the first chapter, the recent development on MEMS loudspeakers are compatible with in-ear applications but are not reaching ideal performance for free field applications yet. Through an exhaustive literature review, performance targets are defined at the end of the first chapter, in order to advantageously place the designed loudspeaker among the results reached in recent publications. From the same literature review, the choice of the transduction for the electromechanical and for the mechanoacoustical conversion as well as the application and the sound reproduction method are defined. In the second chapter, the small signal model of the loudspeaker is detailed and derived. This simple model is then used to define linear small signal parameters of the loudspeaker requisite to reach the previously defined performance target. In the third chapter two more advanced models are described. The first one is the complete Finite Element Model (FEM) of the loudspeaker built in COMSOL[®] and the second model is the large signal pseudo-nonlinear model of the loudspeaker, based on the state space formulation. Based on these models, the performance of the loudspeaker is more precisely defined, and nonlinear aspects, as well as the modal behavior of the loudspeaker are investigated. Concurrently to these aspects and with the help of the three dimensions finite element model, the manufacturing process used to manufacture the loudspeaker is designed. The fourth and last chapter describes the manufacturing process and the characterization of the loudspeaker, in which the measurements are also compared with the simulations.

Chapter 1

State of the Art and Specifications

Contents

1.1 Chapter Introduction	3
1.2 Single Degree of Freedom Loudspeaker	4
1.3 Distortion	6
1.4 Free Field	7
1.4.1 Electrodynamic	7
1.4.2 Piezoelectric	10
1.4.3 Electrostatic	15
1.4.4 Digital	17
1.4.5 Other Types of Transduction	19
1.5 In-Ear	20
1.6 Specifications and Design Choices	27
1.7 Chapter Conclusion	31

1.1 Chapter Introduction

This first chapter describes succinctly the linear working principle of loudspeakers in Section 1.2, in order to better explain the performance of loudspeakers of the literature. It then describes why nonlinearities are important to take care of in loudspeaker design in Section 1.3. Then, electrodynamic commercial loudspeakers are reviewed to determine the required performance for smartphone use in Section 1.4. In the same section, MEMS loudspeakers using electrodynamic, piezoelectric, electrostatic, digital and other types of transductions are successively reviewed, for free field applications. MEMS loudspeakers of the literature are then reviewed for in-ear applications in Section 1.5. Performance of loudspeakers are compared for both applications and depicted in a figure of merit in Section 1.6, leading to a choice of the

working principle of the loudspeaker to design and giving the performance to reach.

1.2 Single Degree of Freedom Loudspeaker

For a better understanding of the involved physical quantities and limitations, a theoretical background is needed. This part does not claim to be exhaustive and more details on the modeling of the loudspeakers are given in Chapter 2. To perform an electric to acoustic transduction, most loudspeakers use two transducers. One being the electromechanical transducer, converting the electrical energy into mechanical energy and the other one being the mechanoacoustical one, converting the mechanical energy into acoustical energy. In most cases, the mechanoacoustical transducer is a rigid element, attached to a single degree of freedom mechanical oscillator, actuated by an electromechanical transducer. This chain is represented in Figure 1.1 and displays the main quantities involved.

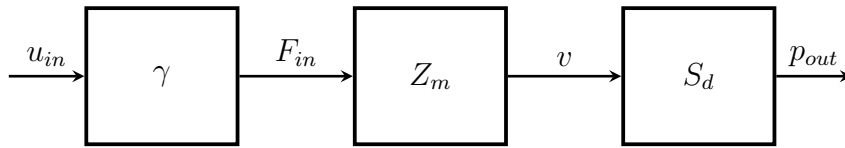


Figure 1.1: Block diagram of the main transductions in a loudspeaker

The conversion of the force F_{in} into a velocity v , that can be differentiated or integrated in order to compute respectively the displacement δ or the acceleration α , is performed via the impedance Z_m , representing the frequency dependent behavior of the mechanical oscillator. In most cases, the mechanical oscillator is designed to approach the behavior of a single degree of freedom oscillator. Generally, a rigid moving surface S_d is actuated at the velocity v and converts then the mechanical movement into a pressure p_{out} . To represent the electromechanical system, an equivalent electrical circuit is used and depicted in Figure 1.2. For more details on the simulation of electroacoustic circuits using lumped element models see [2].

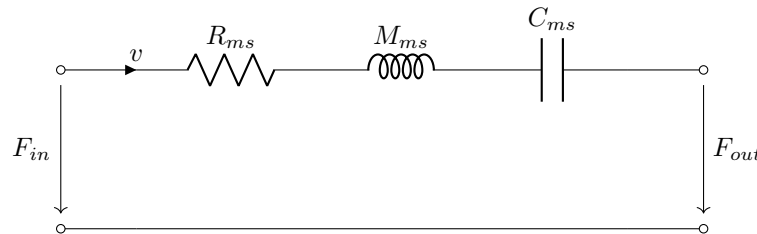


Figure 1.2: Equivalent electrical circuit of a mechanical oscillator

The force F_{out} is determined by the acoustical impedance seen by the radiating element of the loudspeaker. As a first approximation, this impedance can be seen as a capacitance for an in-ear loudspeaker, and as a mass for a loudspeaker radiating in free field. By neglecting the force F_{out} , the velocity of the moving mass of the mechanical oscillator can be written as the ratio between the input force F_{in} and the total impedance of the mechanical circuit, which is composed of the sum of the impedance created by the viscous damping R_{ms} , the equivalent mass M_{ms} and the apparent compliance C_{ms} . From the velocity v , the acceleration α and the displacement δ are obtained respectively by multiplying and dividing v by $j\omega$.

$$v = \frac{F_{in}}{R_{ms} + j\omega M_{ms} + \frac{1}{j\omega C_{ms}}} \tag{1.1}$$

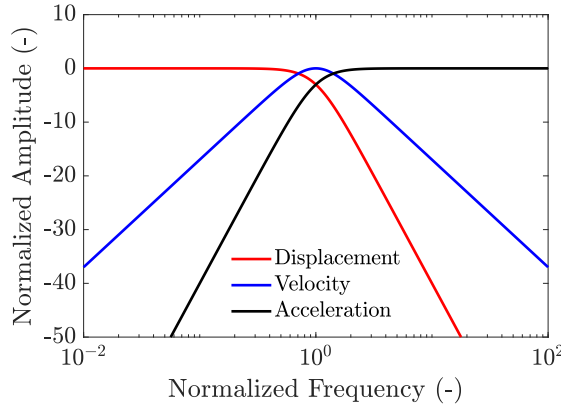


Figure 1.3: Normalized velocity, acceleration and displacement of

The three curves of the acceleration, the velocity and the displacement for a critically damped single order mechanical oscillator as a function of frequency are presented in Figure 1.3. It can be shown from the fundamental equations of acoustics, that a rigid plate flush mounted in an infinite baffle will radiate a sound pressure proportional to the acceleration of the moving plate in free field, and that a rigid plate oscillating into a cavity will radiate a sound pressure proportional to the displacement as it is depicted respectively in Figures 1.4(a) and 1.4(b). Thus, the frequency response of a loudspeaker radiating in free field is similar to the one of a high pass filter, with the resonance frequency being the lowest frequency at which the loudspeaker is efficiently generating sound pressure. When radiating in a cavity, the frequency response is similar to a low pass filter, with the resonance frequency being the highest frequency at which the loudspeaker is efficiently generating sound pressure. This major difference is responsible for the differences in design for the two configurations.

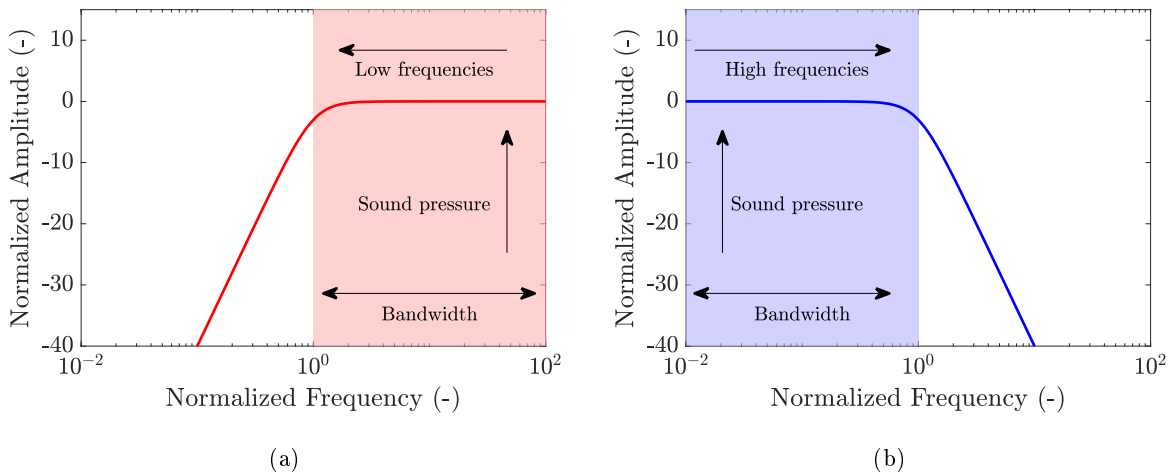


Figure 1.4: First order approximation of the frequency response of a loudspeaker radiating in free field (a) and in a sealed cavity (b)

1.3 Distortion

Once the needed bandwidth and level are reached, the design should consider the nonlinearities, in order to accurately reproduce the input signal. For a linear system, the amplitude of the output signal is proportional to the amplitude of the input signal. This property is called homogeneity and is usually written as

$$y(t) = A(\omega) \cos(\omega t + \varphi(\omega)) \quad (1.2)$$

where ω is the pulsation, $A(\omega)$ is the pulsation dependent gain of the loudspeaker and $\varphi(\omega)$ is the pulsation dependent phase shift of the loudspeaker. For a non linear system, the gain is amplitude dependent, which makes Equation 1.2 and the superposition theorem invalid. In a typical nonlinear system, the gain is reduced for larger amplitudes of the input signal, as presented in Figure 1.5(a). In this case, even after correcting the phase shift $\varphi(\omega)$ and the gain $A(\omega)$, signals are different in shape, as depicted in Figure 1.5(b).

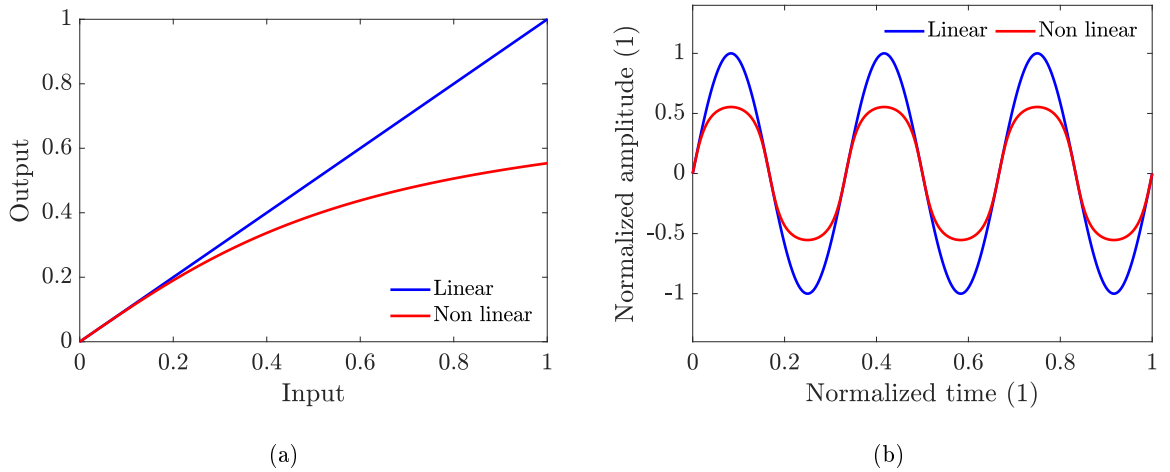


Figure 1.5: Normalized linear and nonlinear transfer functions (a) and output signals resulting from the transfer through the linear and nonlinear transfer functions, normalized to the maximum amplitude of the linear signal (b)

In the frequency domain, nonlinearities are responsible for unwanted frequencies in the output signal. In a simple case of a sine compressed by a function such as the one depicted in Figure 1.5(a), that could be approximated by a simple second order polynomial

$$y(t) = x(t) + x^2(t) \quad (1.3)$$

with t the time vector and $x(t) = \cos(\omega t)$. After using trigonometric identities, the output could be rewritten

$$y(t) = \frac{1}{2} + \cos(\omega t) + \frac{1}{2} \cos(2\omega t) \quad (1.4)$$

which makes clearly appear an offset (null frequency component) and a 2ω term. This simple test can be generalized to nonlinearities to order n , and since real systems usually behave as higher order polynomials, they generates a broadband of odd harmonics if the system is symmetric around zero, as shown in Figure

1.6(a), and a broadband of all harmonics if the system is asymmetric. If the input signal is a sum of multiple signals $x(t) = \cos(\omega_1 t) + \cos(\omega_2 t)$, the output $y(t)$ can be rewritten as

$$y(t) = 1 + \frac{1}{2} \cos(2\omega_1 t) + \frac{1}{2} \cos(2\omega_2 t) + 2 \cos(\omega_1 + \omega_2) + 2 \cos(\omega_1 - \omega_2), \quad (1.5)$$

which clearly shows an offset, the first order harmonic of both input signal, and two components whose pulsations are the sum and the difference of the input pulsations. This can be generalized for higher order, and it usually creates a wide band of nonharmonic content in the output signal, as depicted in Figure 1.6(b). This kind of distortion is called Inter Modulation Distortion (IMD), and contrarily to harmonic distortion, it can generate frequency components with a lower frequency than the ones of the input signals. Figures 1.6(a) and 1.6(b) also show the reduction of amplitude of the fundamental frequencies, due to the diminution of the gain for higher amplitudes.

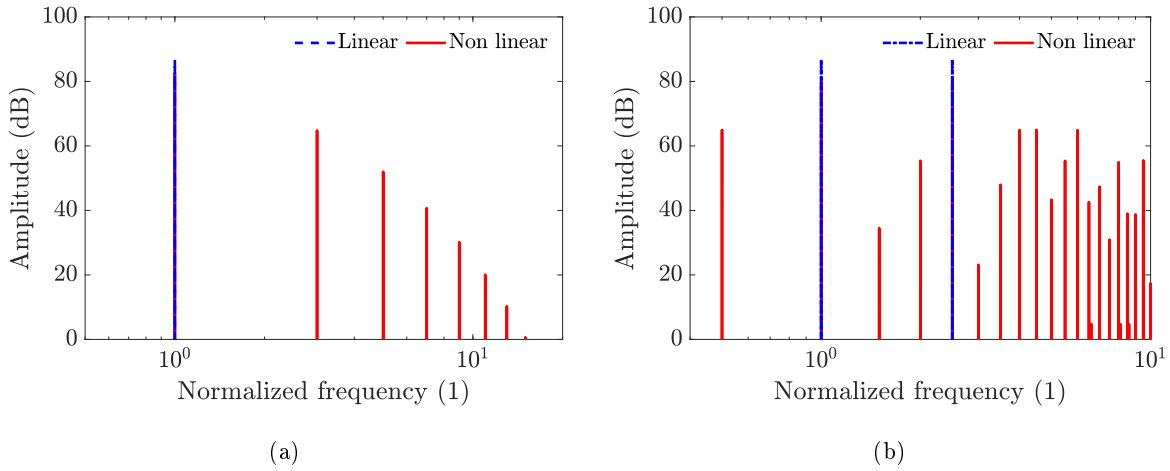


Figure 1.6: Pure sine (a) and sum of pure sines (b) after being transferred through a linear and a nonlinear function in the frequency domain (b)

The human ear sensitivity to distortion is rather complex, and the importance of distortion widely depends on the frequencies. To be able to quickly evaluate the linearity of a system, Total Harmonic Distortion (THD) was introduced. The THD is the ratio between the sum of effective values of the harmonics and the effective value of the fundamental harmonic and other harmonics and is calculated using

$$\text{THD} = 100 \cdot \frac{\sqrt{\sum_{h=2}^H v_h^2}}{\sqrt{\sum_{h=1}^H v_h^2}}. \quad (1.6)$$

This indicator only evaluates the linearity of the system through harmonic distortion, but it's safe to say that a low THD would suggest a low intermodulation distortion. Studies have shown that depending on the order of the harmonics, the human ear can be sensitive to a THD as low as 0.1% [3–6].

1.4 Free Field

1.4.1 Electrodynamic

Electrodynamic loudspeakers rely on the Laplace force that writes

$$\mathbf{F} = q \mathbf{E} + q \mathbf{v} \times \mathbf{B}. \quad (1.7)$$

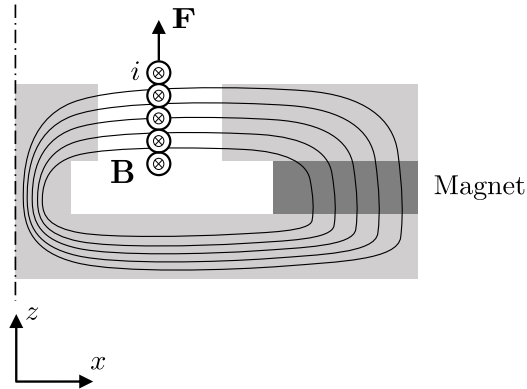


Figure 1.7: Schematic representation of an electrodynamic loudspeaker motor

A solenoid coil of length ℓ , that can freely move along z is immersed in a magnetic field whose magnetic flux density is noted B . Due to the Lorentz force experienced by each electric charge moving in the current carrying coil, a macroscopic force \mathbf{F} is generated. This force can be written

$$\mathbf{F} = i \int d\mathbf{l} \times \mathbf{B}. \quad (1.8)$$

The magnetic field in the air interstice in which the coil can freely move is usually conducted from a magnet using pole pieces that are organized as a magnetic circuit. By assuming a constant magnetic flux intensity in the air interstice \mathbf{B} , a rectilinear current carrying wire of length ℓ and by neglecting edge effects, the Lorentz force writes

$$\mathbf{F} = i\mathbf{l} \times \mathbf{B}. \quad (1.9)$$

As loudspeakers are designed to maximize the transduction factor, it is usually simply written as $\mathbf{B}\ell$, and the force F is proportional to the input current i . This transduction is usually represented as a gyrator in the lumped element circuit, as the transduction is non-reciprocal. The input current gives a force, and the output velocity is proportional to the voltage. As the coil is inductive and resistive, the equivalent electrical circuit is represented as a series inductor and resistor. The equivalent circuit is represented in Figure 1.8, where u_{in} is the input voltage, i_{in} is the input current, R_e is the equivalent electrical resistance of the coil, L_e is the equivalent inductance of the coil and e_m is the back counter-electromotive force.

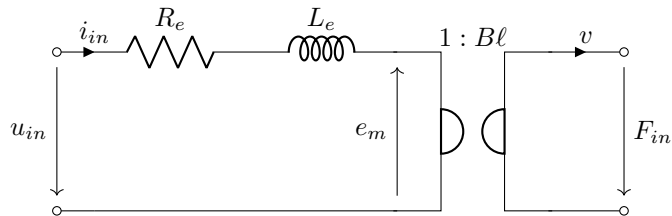


Figure 1.8: Equivalent electrical circuit of an electromagnetic transducer using a coil and a magnet

In order to have a reference for what to expect as the frequency response for a miniature loudspeaker, commercial loudspeakers are used as an example. Present miniature loudspeakers used in smartphones and other portable multimedia devices usually have a nearly critically damped frequency response, with a radiating sound pressure level as high as $90 \text{ dB}_{\text{SPL}}$ (where SPL stands for Sound Pressure Level), from 1 kHz to 20 kHz, with a back cavity of 1 cm^3 . Figure 1.9 shows the averaged frequency response of twelve commercial loudspeakers, as well as the standard deviation of the used samples. These loudspeakers are usually used with specific packaging in smartphones, in order to increase the sound pressure level in the middle of the audio bandwidth, while avoiding the acoustic short-circuit without using a completely sealed back cavity.

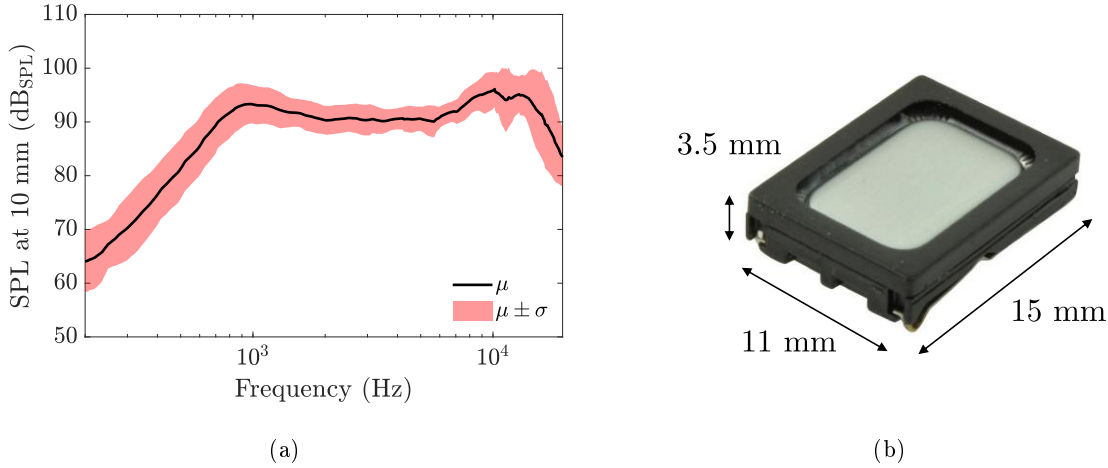


Figure 1.9: Averaged frequency response of twelve commercial loudspeakers with the standard deviation (a) and picture of a typical $11 \times 15 \text{ mm}^2$ of the loudspeaker described in [1] (b)

Non-MEMS loudspeakers are still being studied in order to reduce their thickness [7], extend their frequency bandwidth in the low frequency range [8] and modeled to improve their acoustic performance [7, 9–14]. Very few articles describe the manufacturing and the measurement of MEMS loudspeaker using electromagnetic transduction for free field applications. This could be attributed to the fact that permanent magnets are difficult to adapt to microfabrication processes. In multiple articles [15–19], a MEMS loudspeaker using a heterogeneously assembled permanent magnet and an electrochemically deposited copper coil, on a stiffened silicon circular plate was presented. This MEMS loudspeaker provides a flat frequency response, depicted in Figure 1.10(a), and a radiated sound pressure level of around $80 \text{ dB}_{\text{SPL}}$ at 10 cm in a wide frequency band. A 3D Computer-Aided Design (CAD) cross section view of the loudspeaker is depicted in Figure 1.10(b). Despite the acoustic response in phase with the requirements, the loudspeaker is bulky and requires an heterogeneously assembled magnet and a polymer suspension to avoid an acoustic short-circuit between the front and rear sides of the membrane. This makes this loudspeaker difficult to adapt to industrial applications, such as the integration in smartphones.

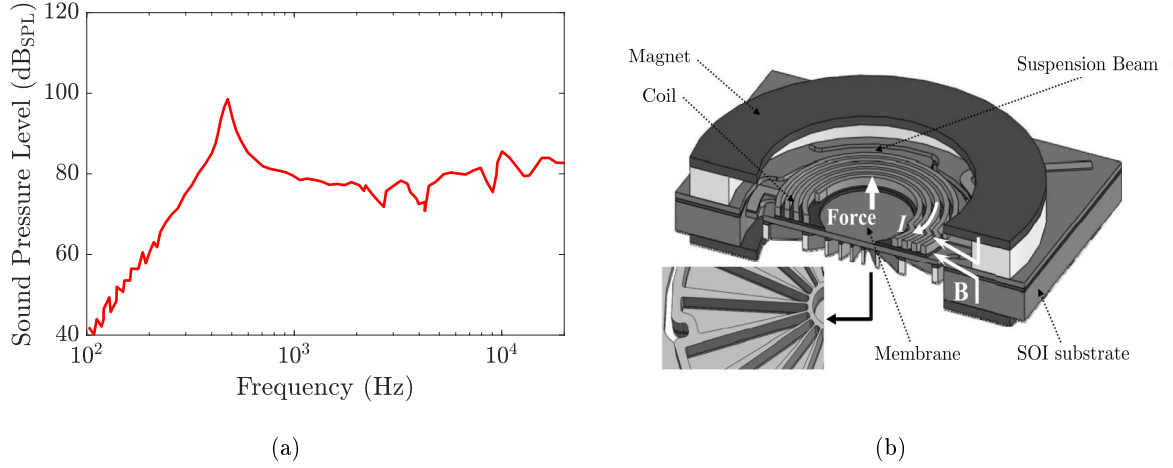


Figure 1.10: Frequency response (a) and 3D CAD drawing (b) of the loudspeaker presented in [15]

1.4.2 Piezoelectric

Piezoelectric loudspeakers mostly rely on piezoelectric cantilevers or deformable structures using thin piezoelectric materials. Piezoelectricity is a property of a material that linearly links the electric field and the strain of a material. The piezoelectric effect comes from the polarization of deformed crystalline structure of the piezoelectric material. The main equation, in the stress-charge form is a superposition of the Hooke Law and the piezoelectric effect which is formalized in the IEEE standard, and is presented in Equation 1.10

$$\begin{cases} S_p = s_{pq}^E T_q + d_{kp} E_k \\ D_i = d_{iq} T_q + \varepsilon_{ik}^T E_k \end{cases} \quad (1.10)$$

with S_p the strain in the p direction, D_i the electric displacement in the i direction, T_q the stress in the q direction, E_k the electric field in the k direction, s_{pq}^E the compliance at constant electric field, ε_{ik}^T the dielectric constant for a constant stress, d_{kp} the piezoelectric constant and T_p the stress for a constant electric field in the p direction.

Usually, indices of the stresses are reduced with $(11) = 1, (22) = 2, (33) = 3, (32) = (23) = 4, (13) = (31) = 5$ and $(12) = (21) = 6$. Considering an orthotropic material whose elastic properties are different along the three dimensions, the complete stiffness tensor of the material can then be written as

$$\begin{bmatrix} S_1 \\ S_2 \\ S_3 \\ S_4 \\ S_5 \\ S_6 \end{bmatrix} = \begin{bmatrix} s_{11} & s_{12} & s_{13} & s_{14} & s_{15} & s_{16} \\ s_{12} & s_{22} & s_{23} & s_{24} & s_{25} & s_{26} \\ s_{13} & s_{23} & s_{33} & s_{34} & s_{35} & s_{36} \\ s_{14} & s_{24} & s_{34} & s_{44} & s_{45} & s_{46} \\ s_{15} & s_{25} & s_{35} & s_{45} & s_{55} & s_{56} \\ s_{16} & s_{26} & s_{36} & s_{46} & s_{56} & s_{66} \end{bmatrix} \begin{bmatrix} T_1 \\ T_2 \\ T_3 \\ T_4 \\ T_5 \\ T_6 \end{bmatrix}. \quad (1.11)$$

This tensor is the elastic material constant tensor in the piezoelectric Equation 1.10. In the case of an isotropic material, $s_{14} = s_{15} = s_{16} = s_{24} = s_{25} = s_{26} = s_{34} = s_{35} = s_{36} = s_{45} = s_{46} = s_{56} = 0$, and the

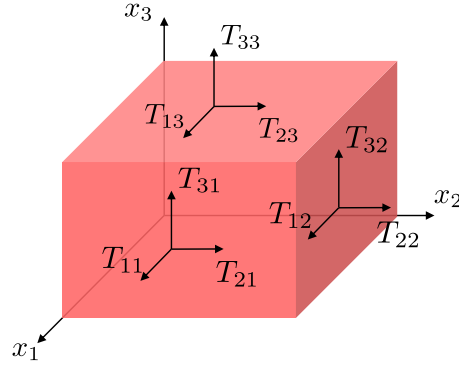


Figure 1.11: Representation of cuboid subjected to three three dimensional stresses in the three orthogonal directions

tensor can be expressed as a function of the Young modulus and the Poisson ratio [20]. The piezoelectric effect is also described as a tensor, whose parameters are axis dependent. Using three dimensions tensors, Equation 1.10 can be rewritten

$$\begin{bmatrix} D_1 \\ D_2 \\ D_3 \end{bmatrix} = \begin{bmatrix} d_{11} & d_{12} & d_{13} & d_{14} & d_{15} & d_{16} \\ d_{21} & d_{22} & d_{23} & d_{24} & d_{25} & d_{26} \\ d_{31} & d_{32} & d_{33} & d_{34} & d_{35} & d_{36} \end{bmatrix} \begin{bmatrix} T_1 \\ T_2 \\ T_3 \\ T_4 \\ T_5 \\ T_6 \end{bmatrix} + \begin{bmatrix} \varepsilon_{11} & \varepsilon_{12} & \varepsilon_{13} \\ \varepsilon_{12} & \varepsilon_{22} & \varepsilon_{23} \\ \varepsilon_{13} & \varepsilon_{23} & \varepsilon_{33} \end{bmatrix} \begin{bmatrix} E_1 \\ E_2 \\ E_3 \end{bmatrix}. \quad (1.12)$$

Lead Zirconate Titanate (PZT), which is the most widely used piezoelectric material for microfabricated actuators, have an orthorhombic crystal structure, and Equation 1.12 can be rewritten using $d_{11} = d_{12} = d_{13} = d_{14} = d_{16} = d_{21} = d_{22} = d_{23} = d_{25} = d_{26} = d_{34} = d_{35} = d_{36} = 0$ and $\varepsilon_{12} = \varepsilon_{13} = \varepsilon_{23} = 0$. Equations 1.11 and 1.12 are usually assembled into a single tensor and writes

$$\begin{bmatrix} S_1 \\ S_2 \\ S_3 \\ S_4 \\ S_5 \\ S_6 \\ D_1 \\ D_2 \\ D_3 \end{bmatrix} = \begin{bmatrix} s_{11}^E & s_{12}^E & s_{13}^E & 0 & 0 & 0 & 0 & 0 & d_{31} \\ s_{21}^E & s_{22}^E & s_{23}^E & 0 & 0 & 0 & 0 & 0 & d_{31} \\ s_{31}^E & s_{32}^E & s_{33}^E & 0 & 0 & 0 & 0 & 0 & d_{33} \\ 0 & 0 & 0 & s_{44}^E & 0 & 0 & 0 & d_{15} & 0 \\ 0 & 0 & 0 & 0 & s_{55}^E & 0 & d_{15} & 0 & 0 \\ 0 & 0 & 0 & 0 & 0 & s_{66}^E & 0 & 0 & 0 \\ 0 & 0 & 0 & 0 & d_{15} & 0 & \varepsilon_{11}^T & 0 & 0 \\ 0 & 0 & 0 & d_{15} & 0 & 0 & 0 & \varepsilon_{11}^T & 0 \\ d_{31} & d_{31} & d_{33} & 0 & 0 & 0 & 0 & 0 & \varepsilon_{33}^T \end{bmatrix} \begin{bmatrix} T_1 \\ T_2 \\ T_3 \\ T_4 \\ T_5 \\ T_6 \\ E_1 \\ E_2 \\ E_3 \end{bmatrix}. \quad (1.13)$$

were the piezoelectric constant matrix and the transposed piezoelectric constant matrix are highlighted in blue, the isotropic stiffness matrix is highlighted in red and the electrical permittivity appears in black. Most MEMS loudspeakers use a thin piezoelectric layer, between two electrodes, firmly attached to a passive elastic layer, as it is represented in Figure 1.12.

In this specific case, the potential difference between the two electrodes creates an electric field of magnitude E along the direction 3, and since dimensions along y and x are large compared to the dimensions along z , edges effects can be neglected. In this configuration, the stresses along the direction 3 can be

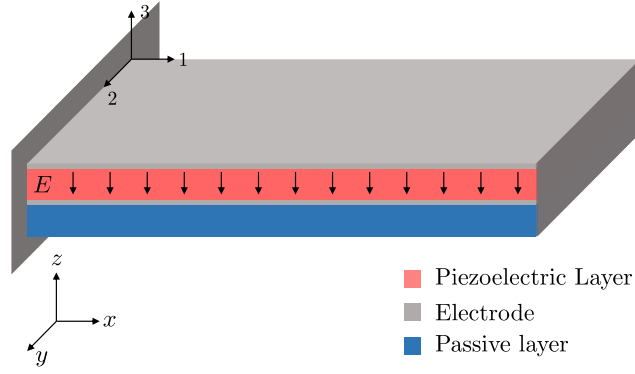


Figure 1.12: Schematic of a piezoelectric cantilever with an non-deformable free end

neglected, as the related deformation is very small. Due to the same geometric characteristics, transverse shear stress is neglected as well, and equation can be rewritten using $T_3 = T_4 = T_5 = 0$ [21]

$$\begin{bmatrix} S_1 \\ S_2 \\ S_6 \\ D_3 \end{bmatrix} = \begin{bmatrix} s_{11}^E & s_{12}^E & 0 & d_{31} \\ s_{12}^E & s_{11}^E & 0 & d_{31} \\ 0 & 0 & s_{66}^E & 0 \\ d_{31} & d_{31} & 0 & \varepsilon_{33}^T \end{bmatrix} \begin{bmatrix} T_1 \\ T_2 \\ T_6 \\ E_3 \end{bmatrix}. \quad (1.14)$$

If the width of the plate is small compared to its length, the plate can be considered as a thin beam and the stress T_2 along the direction 2 and the shear stress T_6 can be neglected as well. This simplification can also be used in the case of a cantilever with a larger width but whose boundary conditions avoid large deformations along the width direction. This simplification leads to

$$\begin{bmatrix} S_1 \\ D_3 \end{bmatrix} = \begin{bmatrix} s_{11}^E & d_{31} \\ d_{31} & \varepsilon_{33}^T \end{bmatrix} \begin{bmatrix} T_1 \\ E_3 \end{bmatrix}. \quad (1.15)$$

Equation 1.15 gives a simple model to evaluate performance of the piezoelectric material. s_{11}^E is used to predict the bending stiffness of the piezoelectric layer, ε_{33}^T is used to predict the electrical behavior and d_{31} is used to predict the stress generated by the piezoelectric layer. Coupled to a mechanical model of the passive layer, this equation can be used to predict mechanical output from electrical input. Piezoelectricity is a nearly linear reciprocal effect. Unfortunately, purely piezoelectric materials have poor d_{31} coefficients, and thus are not converting electrical energy to mechanical energy efficiently. The most widely used piezoelectric material in MEMS actuators is the PZT ($\text{PbZr}_x\text{Ti}_{1-x}\text{O}_3$ ($0 \leq x \leq 1$)) showing the highest piezoelectric coefficient and is compatible with the microfabrication processes [22]. Due to the non-centrometric crystal structure, PZT belongs to the pyroelectric and more specifically to the ferroelectric class of piezoelectric materials [23]. This material was first synthetised in the 50s [24]. The ferroelectric behavior, by analogy to the ferromagnetic behavior, is mainly defined by the ability of the material to have a remanent polarization that can be reversed by an external electric field. This effect comes from the electric dipole of the PZT lattice below the Curie temperature, as shown in Figure 1.13. Due to the ceramic arrangement in domain, hysteretic behavior occurs (Figure 1.14).

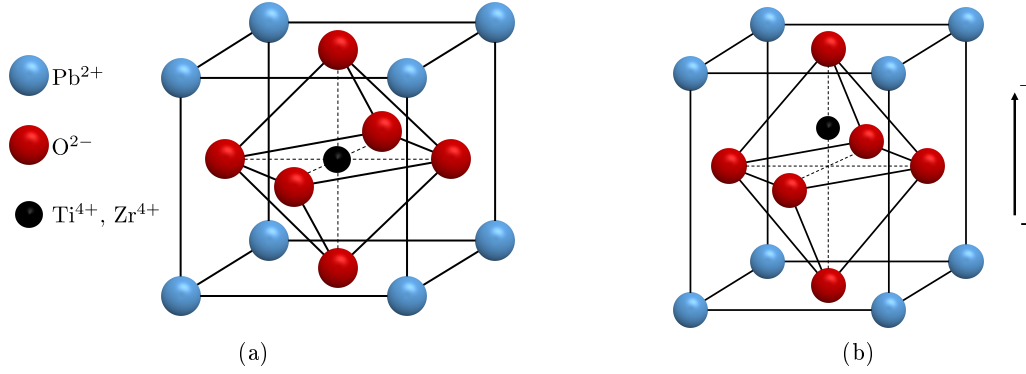


Figure 1.13: Cubic structure of PZT below (a) and tetragonal structure of PZT above (b) Curie transition temperature adapted from [25]

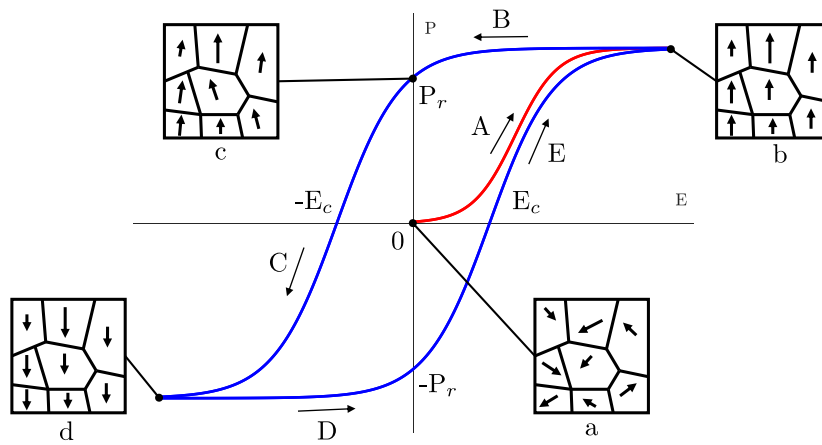


Figure 1.14: Simplified polarization P of a ferroelectric material subjected to an electric field E represented by sigmoid functions

After manufacturing the material has a randomly distributed ferroelectric domains orientation (Figure 1.14 a), and the resulting macroscopic polarization is null. When the material is subjected to an electric field, dipoles in the ferroelectric domain switch until their macroscopic dipoles are aligned with the electric field direction (Figure 1.14 b), initially following path A. When the electric field is reduced, polarization follows path B, and does not decrease as fast as it increased, to reach the remanent polarization P_r when the electric field is null and dipoles are randomly distributed (Figure 1.14 c). If a negative electric field is applied, the structure is unpolarized, down to the negative coercive field $-E_c$, to randomly spatially distributed dipoles, with a null polarization. By reducing further the electric field, the material is polarized in the opposite direction through path C, similarly to path A. At the negative saturation field, all dipoles are aligned to the electric field. When the electric field is increased back, the material is depolarized to $-P_r$, the negative remanent polarization. By increasing the electric field and similarly to path B, the coercive field which correspond to a null polarization is reached and the loop is closed at the saturation polarization. Because the polarization is linked to piezoelectric coefficients through Equation 1.10, the transduction is also highly non linear and hysteretic. Also, piezoelectric parameters of thin film PZT depend on film thickness [26], stress and frequency [27] and multiple other parameters [28]. For small signals, piezoelectric materials are considered linear, and the transduction can be represented by a simple coefficient. The piezoelectric effect being reciprocal, it is usually represented as a transformer in the

electrical equivalent circuit. Due to the piezoelectric material being dielectric, the electrical part of the transduction is usually represented as a capacitor C_p , as depicted in Figure 1.15. As the piezoelectric layer adds a bending stiffness to the mechanical structure, it also contributes to the apparent compliance C_{ms} of the mechanical equivalent circuit.

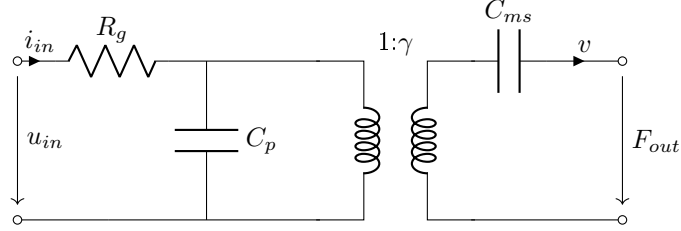


Figure 1.15: Equivalent electrical circuit of a bending piezoelectric transducer

Piezoelectric materials have been integrated into MEMS devices since the early 1990s [29–31] and more specifically into MEMS loudspeaker since the mid 1990s [32]. Most notable recent performance were reached by the loudspeaker presented in different declinations in [33–37]. The loudspeaker is based on a released silicon oxide circular membrane on which a high piezoelectric constant piezoceramic is bonded and a picture is presented in Figure 1.16(b).

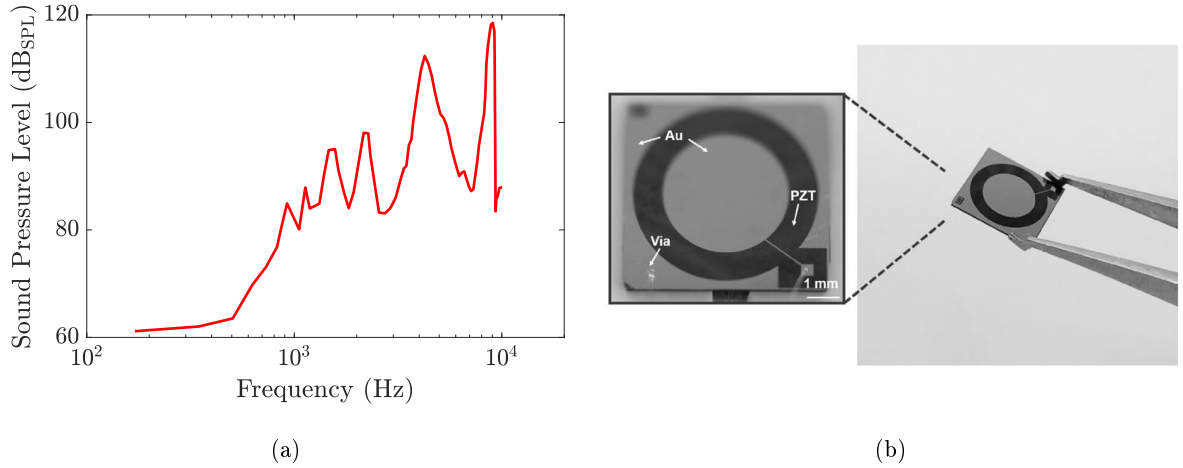


Figure 1.16: Frequency response (a) and schematic of the concept (b) of the loudspeaker presented in [38]

The radiated sound pressure measured at 10 mm is depicted in Figure 1.16(a) and shows an accidented response, with a very low sound pressure level in low frequencies. The measurement is also far from being in agreement with the models, and the pressure was measured with a sound level meter, which might evaluates the total harmonic distortion into the frequency response.

A piezoelectric loudspeaker, based on thin film PZT cantilevers and an heterogeneously assembled membrane, integrated in the packaging is already commercialized. Although the design mainly aims for in-ear applications, this loudspeaker could be used in near field applications as well. The frequency response of the loudspeaker in free field, as well as a picture of the loudspeaker are presented in Figure 1.17. A equivalent model of this loudspeaker is presented in [39].

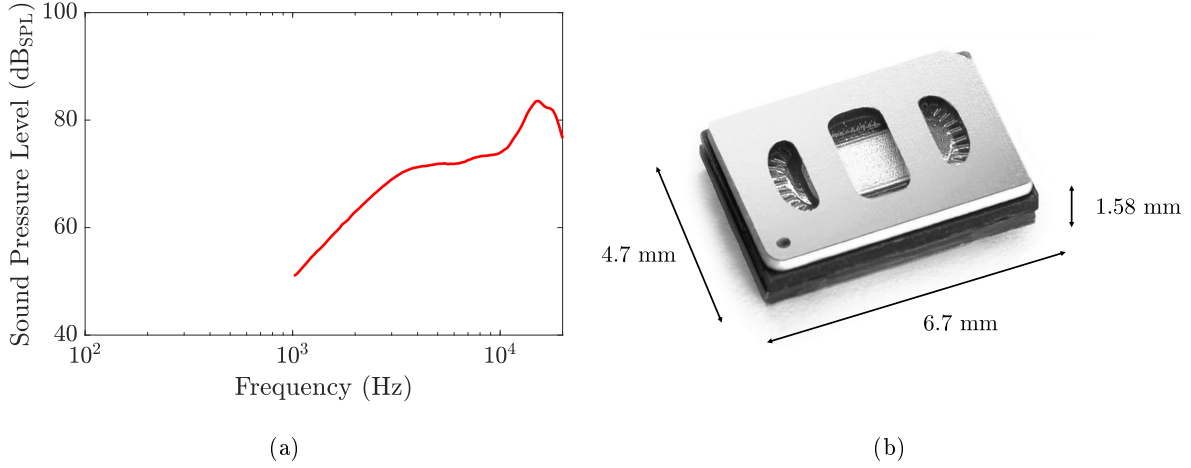


Figure 1.17: Frequency response (a) and picture (b) of the Usound UTP-2018 loudspeaker, whose characteristics are detailed in [40]

Although the frequency response of the loudspeaker is reasonably flat between 3 kHz and 10 kHz, the level is not high enough to fulfill free field application requirements. Also, the resonance frequency of the loudspeaker is higher than 3 kHz and this results in a lack of sound pressure level in the lower frequencies. In [41], a microloudspeaker using ZnO on a SiN membrane is reported. It generates an acoustic pressure of 60 dB_{SPL} from 1 kHz and a very irregular response, due to the modal behavior of the membrane. Using thin film PZT on a polyimide membrane, pressure as high as 79 dB_{SPL} at 1 kHz was reported in [42]. In [43], a reasonably flat frequency response starting at 450 Hz, with a sound pressure level of 90 dB_{SPL} at 1 cm for a microloudspeaker of $18 \times 20 \text{ mm}^2$ was reported. In [44] finite element and lumped element model of a microloudspeaker actuated by piezoelectric bending actuator predict a pressure of 100 dB_{SPL} at 15 kHz and at 1 cm, which is very high in frequency. In [45], a concentric microloudspeaker using thin film PZT on a deformable silicon structure is simulated, predicting sound pressure level of more than 90 dB_{SPL} at frequencies lower than 1 kHz. Measurement results have not been presented yet. In [46], a microloudspeaker using AlN thin film on a low stress silicon nitride deformable membrane with a surface of $4 \times 4 \text{ mm}^2$ generates a sound pressure level of approximately 80 dB_{SPL} at a frequency of 10 kHz and at a distance of 3 mm, which is an order of magnitude lower in pressure and frequency than what is expected for smartphones.

1.4.3 Electrostatic

Electrostatic transduction is the oldest type of transduction and was used in the first MEMS devices in the mid 1960s [47]. The electrostatic transduction relies on the electrostatic force created between two charges. In Figure 1.18, two plates of surface S separated by a distance d are represented. Considering dimensions along x and y are way larger than the distance d , edges effects can be neglected. The capacitance C_0 created by the two plates and the dielectric can be written

$$C_0 = \varepsilon_0 \varepsilon \frac{S}{d} \quad (1.16)$$

where ε_0 is the vacuum permittivity and ε is the dielectric permittivity. From Coulomb's theorem, the static force as a function of the input voltage can be written

$$F_{in} = \frac{\varepsilon\varepsilon_0 S V_{DC}^2}{2 d^2}. \quad (1.17)$$

As deduced from Equation 1.17, the relation between the force and the input voltage is non linear. By considering an input signal composed of a DC voltage V_{DC} , large compared to the input signal u_{in} , and by considering that the variation of the capacitance C_0 due to the variation of the distance d is negligible, the variation of the static force generated by the electrostatic transducer can be written as

$$F = \varepsilon\varepsilon_0 S \frac{V_{DC} u_{in}}{d^2}. \quad (1.18)$$

Equation 1.18 shows the limitation of the electrostatic transducer for loudspeaker actuation. Firstly, a high polarization voltage is needed in order to tend to a linear working principle, and this is limited by the breakdown voltage in the dielectric between the two plates. The force is also inversely proportional to the distance between the two plates, which limits the maximum displacement.

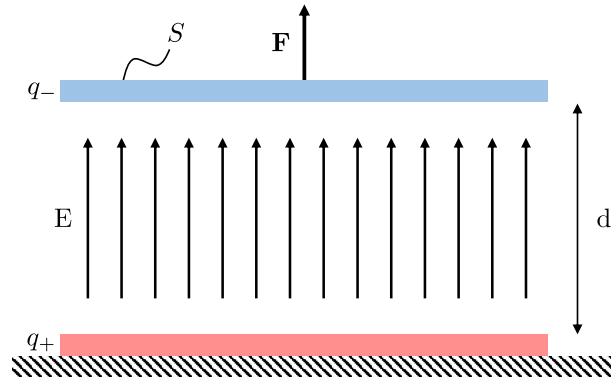


Figure 1.18: Schematic of two plates polarized to a different potential

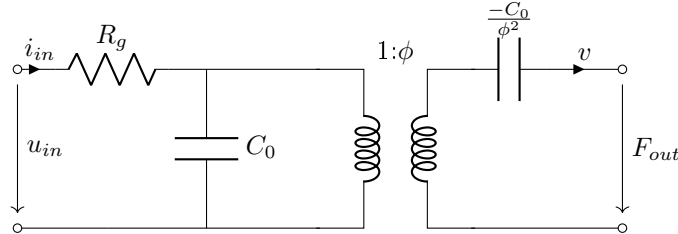


Figure 1.19: Equivalent electrical circuit of an electrostatic transducer

Figure 1.19 represents the equivalent electrical circuit of an electrostatic transducer. The resistor R_g represents the output resistor of the generator, as well as the resistance created by the electrical connections. A negative compliance is also induced in the mechanical domain due to the transduction. The negative compliance value is the value of the electrical capacitance transposed in the mechanical domain through the squared transduction factor ϕ . Equations and equivalent electrical circuits are adapted from [48]. Very few loudspeakers using electrostatic transduction for free field applications were described. This could be due to the low displacement generated by the transduction, that doesn't allow this type of loudspeaker to generate high sound pressure level at low frequencies. An interesting design was presented in [38], showing a circular electrostatic MEMS loudspeaker, actuated only peripherally. The design only

uses silicon and silicon oxide, which makes it convenient to manufacture. The frequency response and a schematic view of the loudspeaker are presented in Figure 1.20.

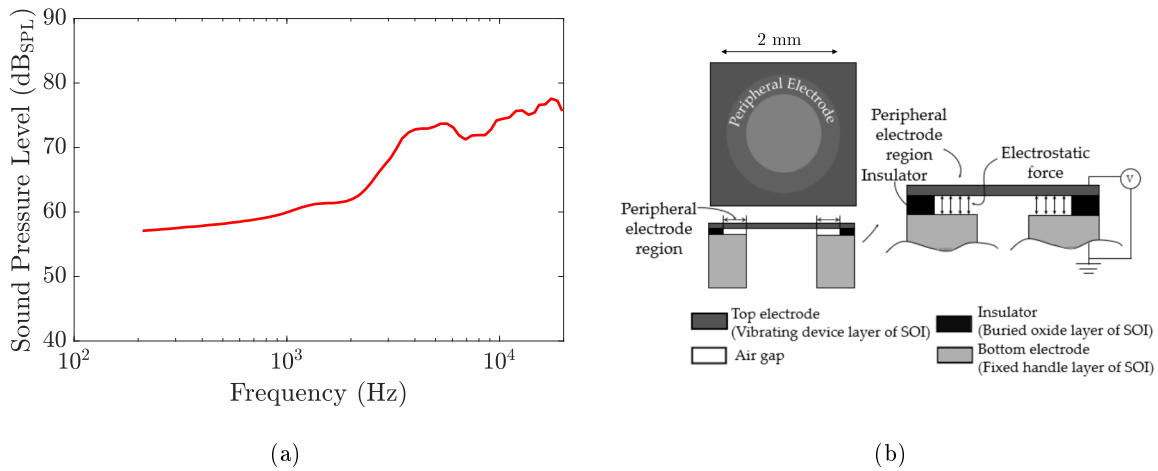


Figure 1.20: Frequency response (a) and schematic of the concept (b) of the loudspeaker presented in [38]

The loudspeaker with a diameter of 2 mm and measured at a 1 mm distance produces a very low sound pressure level below 1 kHz when actuated at $30 V_{DC} + 30 V_{AC}$. The actuation voltage being equal to the bias voltage, the loudspeaker might show very high total harmonic distortion. Other loudspeakers are using push-pull electrostatic transduction and a flexible membrane [49], or silicon flexible elements to obtain a pistonic motion of the vibrating element [50], using a corrugated structure to decrease the stiffness of the membrane [51], using a poly-SiC membrane [52], or using a membrane bonding [53], but show similar low sound pressure levels at low frequencies, with high distortion and high polarization voltages.

1.4.4 Digital

Independently of the transduction principle, sound can theoretically be reproduced in air using a digital loudspeaker. Instead of converting linearly the harmonic displacement of a rigid surface to produce a sound pressure, digital loudspeakers are using a digital signal to feed a matrix of transducers, that reconstruct the analog signal directly in air, with the combination of a high number of independent smaller loudspeakers, often called speaklets. A schematic of the principle of the digital loudspeaker is depicted in Figure 1.21(a).

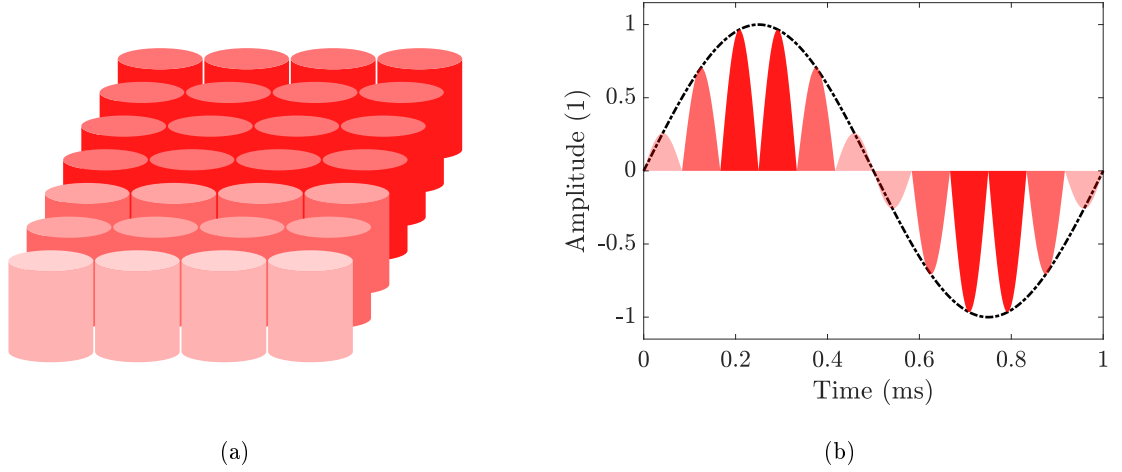


Figure 1.21: Schematic of an array of speaklets (a) and sequence of acoustic pulse reproducing a period of a sine wave (b)

Groups of different numbers of speaklets are actuated successively, to reproduce pulses with different amplitudes. If the length of the pulse corresponds to a frequency much higher than the maximum frequency of the audio band, this system could theoretically reproduce any frequency without the need of a low resonance frequency. Two major difficulties rely on the reproduction of a perfect air pulse and on the small variation of characteristics from one speaklet to another. These issues were investigated in [54]. For a resonating MEMS, simulated using a simple mechanical oscillator, the air pulse generated usually have the shape of the impulse response of an under-damped impulse response, as depicted in Figure 1.22. The difference between the perfect rectangular pulse and the response of a second oscillator is responsible for the limitations of this system in the lower frequencies.

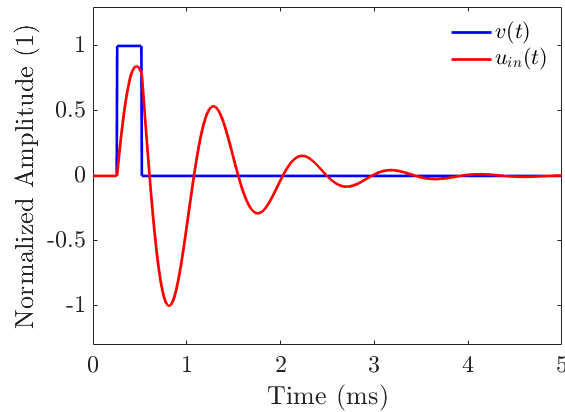


Figure 1.22: Velocity response of a damped oscillator to a square voltage impulse

A proof of concept of a digital loudspeaker was built and measured in [55, 56], using piezoelectric transduction, whose performance is presented in Figure 1.23. Other proof of concept were demonstrated in [57] and [58].

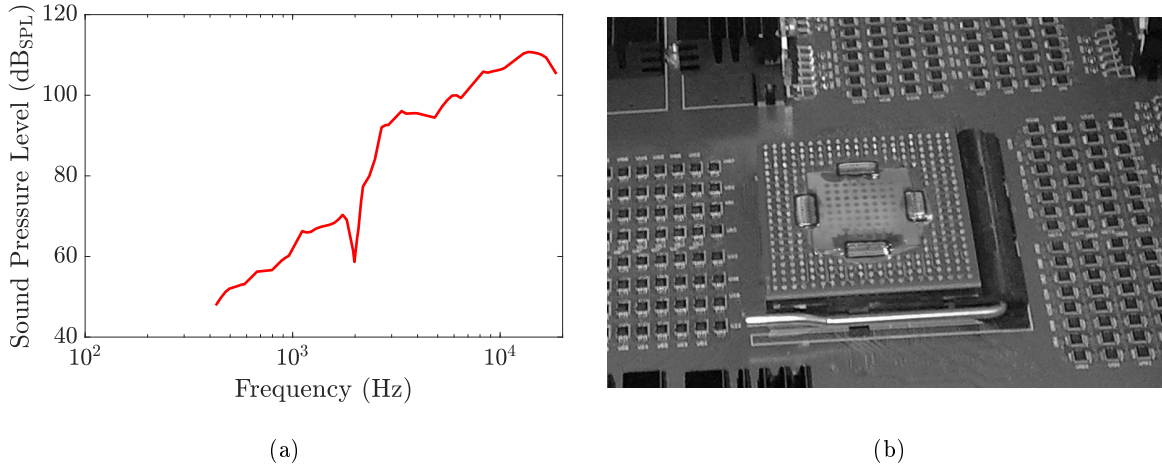


Figure 1.23: Frequency response (a) and picture (b) of the loudspeaker presented in [56]

The frequency response of the loudspeaker shows a low sound pressure in low frequencies and is not flat in the audio bandwidth. This response is similar to the one of other piezoelectric loudspeakers using analog transduction techniques, for loudspeaker smaller and without complex electronic circuitry. This could mainly be attributed to the inability of single speaklets to reproduce sharp peaks of acoustic pressure, and to the disparities between the characteristic of the speaklets. Research is still ongoing to improve the intrinsic performance of the individual speaklets [59, 60], or to find new techniques of digital signal reconstruction [61], but no competitive frequency response with a low total harmonic distortion was presented to date, and performance are at least an order of magnitude under to required ones.

1.4.5 Other Types of Transduction

A few others loudspeakers of the literature are using different transduction techniques, such as the thermoacoustic transduction. This transduction relies on the expansion of air and solid through a change of temperature. The change of the temperature of the solid is generally achieved with an alternative current, creating a sinusoidal change of temperature of the resistive solid through the joule effect.

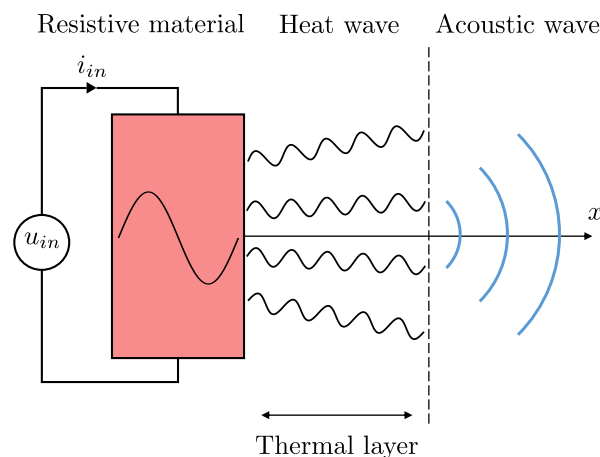


Figure 1.24: Schematic of thermoacoustic transduction effect, adapted from [62]

Under a sinusoidal electrical current, the resistive solid experiences a pseudo-sinusoidal change of temperature. As the sign of the input current i_{in} does not affect the temperature change, a current at a pulsation ω generates a change of temperature at a pulsation 2ω . The sinusoidal change of temperature is then conducted through air via the air to solid interface and this change of temperature is creating sound waves. As other types of transductions, this transduction is highly non linear and requires a polarization voltage.

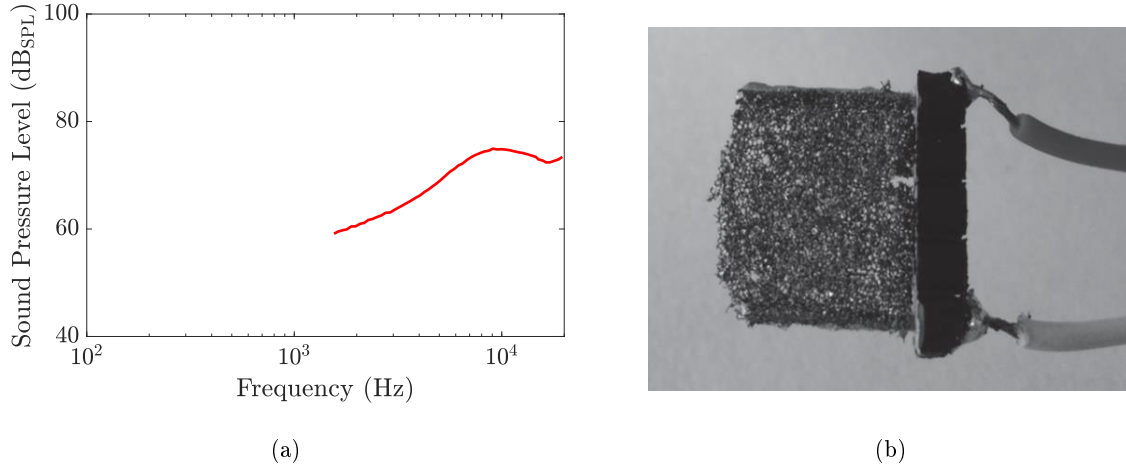


Figure 1.25: Frequency response (a) and picture (b) of the loudspeaker presented in [63]

The frequency response and a picture of the loudspeaker presented in [63] are depicted in Figure 1.25. A sound pressure level of approximately 70 dB_{SPL} is reached at 10 kHz and at 10 cm. A few others loudspeakers compatible with microfabrication processes and featuring a thermoacoustic transduction are described in the literature [64–66] and are showing similar low sound pressure levels at low frequencies.

1.5 In-Ear

The target frequency behavior for a loudspeaker is a flat frequency response in the audible frequency range. When an in-ear loudspeaker is used, the influence of the head, torso and external ear is short-circuited by the geometrical configuration. In order to make the music sound natural, the effect needs to be introduced in the frequency response of the loudspeaker. To reproduce the frequency response of the average human body, measurements were carried out on large number of people and measurements tools were designed. These tools are mainly artificial ears, following the International Electrotechnical Commission (IEC) 60318-4 standard, and artificial mannequins, following the IEC 60318-7 standard. The transfer functions of different head and torso mannequins as well as a picture of one of these mannequins is presented in Figure 1.26 and the transfer function and the picture of an artificial ear are presented in Figure 1.27.

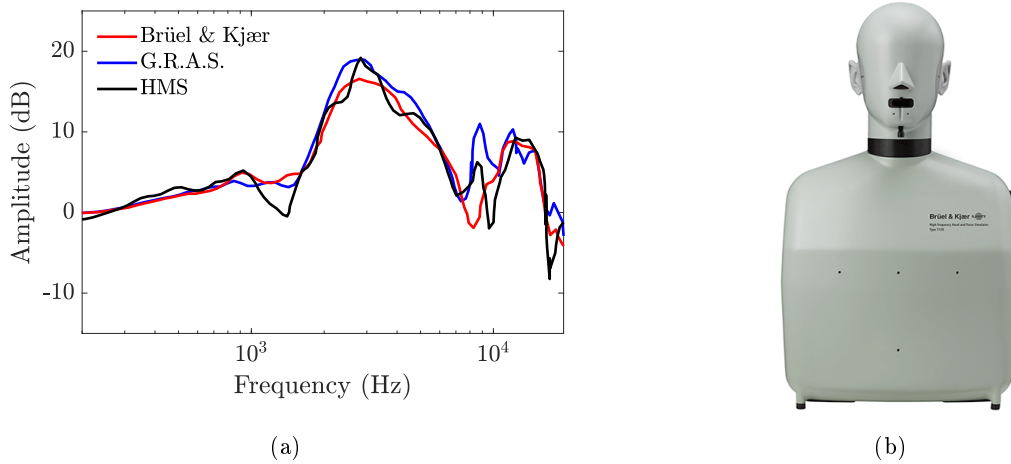


Figure 1.26: Transfer function of 3 commercial head and torso mannequin measured in [67] (a) and picture of the B&K 4128 (b)

The transfer function in Figure 1.26(a) represents the transfer function from a perfect source in front of the mannequin to the microphones placed inside the dummy ear canals. Researches on the topic have found that listeners prefer a slightly different curve, often referenced to as the Harman curve [68]. This curve has a similar behavior and amplifies frequencies between 2 and 6 kHz, as depicted in Figure 1.29(a). Although this curve is very important at the design stage, some corrections can be made with acoustical resonators in the packaging, and publications often do not aim at this particular curve.

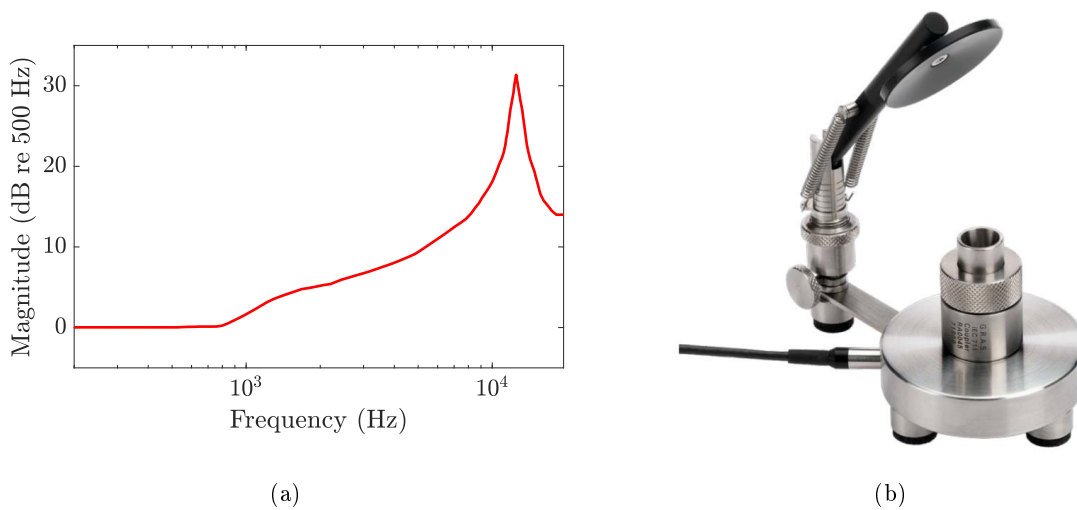


Figure 1.27: Transfer function of a G.R.A.S. standardized artificial ear (a) and picture of this artificial ear (b)

The curve presented in Figure 1.27(a) is the measured transfer function of ear-occluded depicted in Figure 1.27(b). It shows a sharp resonance peak at around 10 kHz, due to a resonance of the ear canal. A significant increase of the level from 1 kHz is observed as well. For simulation purpose, the coupler is often simulated using an equivalent acoustical circuit, that can be found in [69]. This circuit predicts the acoustical behavior of the coupler in the audio range, and allows to predict the sound pressure level at

the microphone integrated in the coupler, which represents the tympan of the user.

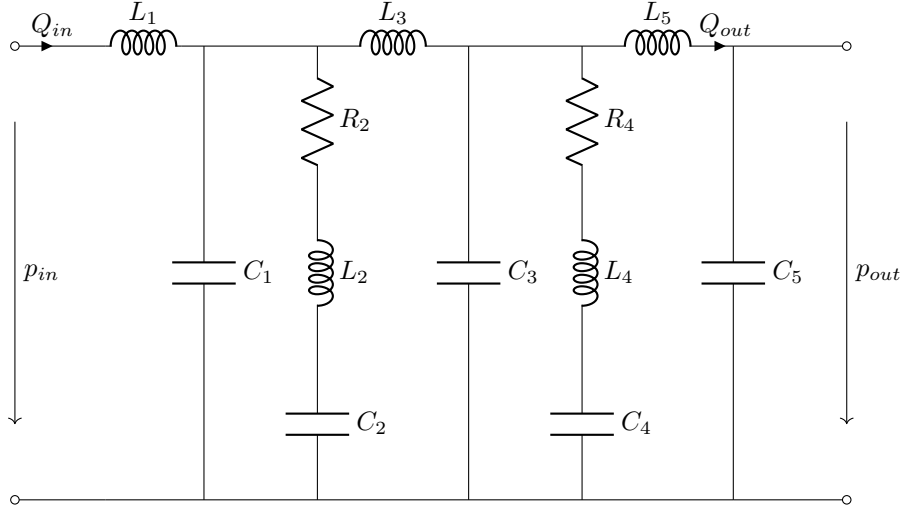


Figure 1.28: Lumped equivalent network of the ear-occluded IEC 60318-4 coupler

From the schematic presented in Figure 1.28, the equivalent impedance of the coupler writes

$$Z_c = j\omega L_1 + \frac{1}{j\omega C_1 + \frac{1}{Z_2} + \frac{1}{j\omega L_3 + \frac{1}{j\omega C_3 + \frac{1}{Z_4} + \frac{1}{Z_5}}}} \quad (1.19)$$

with $Z_2 = j\omega L_2 + \frac{1}{j\omega C_2} + R_2$, $Z_4 = j\omega L_4 + \frac{1}{j\omega C_4} + R_4$ and $Z_5 = \frac{1}{j\omega C_5} + j\omega L_5$ where R_2 and R_4 are representing the equivalent acoustical dissipation of the coupler, $C_1 - C_5$ are the equivalent acoustical compliances of the coupler and where $L_1 - L_5$ are the equivalent acoustical masses of the coupler. The transfer function from p_{in} to p_{out} can then be written

$$T_f = \frac{\frac{1}{\frac{1}{j\omega C_3} + \frac{1}{Z_4} + \frac{1}{Z_5}}}{j\omega L_3 + \frac{1}{\frac{1}{j\omega C_3} + \frac{1}{Z_4} + \frac{1}{Z_5}}} \frac{Z_c - j\omega L_1}{Z_c} \frac{1}{j\omega C_5 Z_5}. \quad (1.20)$$

The impedance of the coupler is depicted in Figure 1.29(b), and the parameters are given in Table 1.1.

Table 1.1: Parameters of the equivalent circuit of the IEC 60318-4 ear-occluded coupler

Parameter	Value	Unit
L_1	82.9	$\text{Pa s}^2 \text{m}^{-3}$
L_2	9400	$\text{Pa s}^2 \text{m}^{-3}$
L_3	130.3	$\text{Pa s}^2 \text{m}^{-3}$
L_4	983.8	$\text{Pa s}^2 \text{m}^{-3}$
L_5	133.4	$\text{Pa s}^2 \text{m}^{-3}$
C_1	$1 \cdot 10^{-12}$	Pa m^{-3}
C_2	$1.9 \cdot 10^{-12}$	Pa m^{-3}
C_3	$1.5 \cdot 10^{-12}$	Pa m^{-3}
C_4	$2.1 \cdot 10^{-12}$	Pa m^{-3}
C_5	$1.517 \cdot 10^{-12}$	Pa m^{-3}
R_2	$50.6 \cdot 10^6$	Pa s m^{-3}
R_4	$31.1 \cdot 10^6$	Pa s m^{-3}

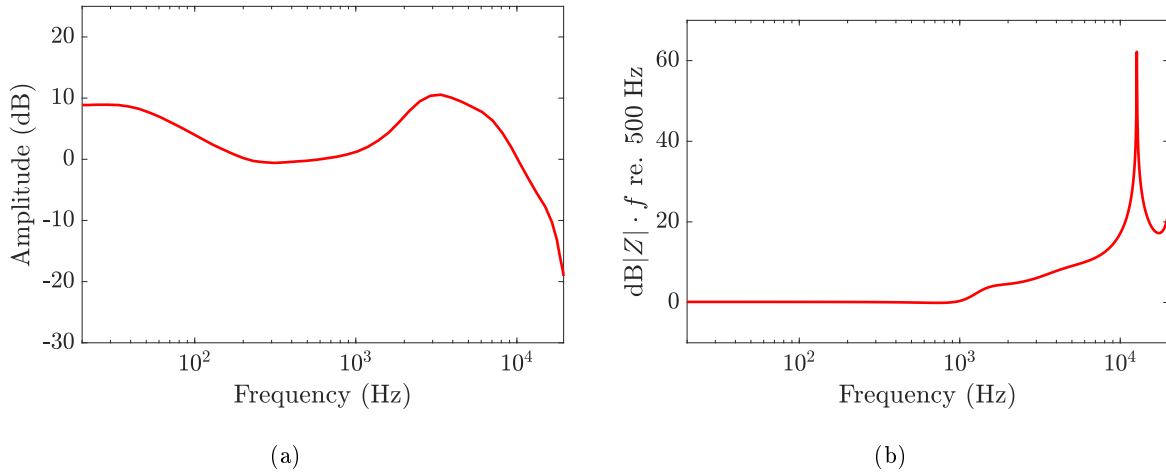


Figure 1.29: Harman target curve adapted from [68] (a) and impedance on a IEC 60318-4 ear-occluded coupler calculated using the equivalent electrical circuit of Figure 1.28 (b)

As discussed in Section 1.2, the needed displacement for in ear loudspeaker can be orders of magnitude below the required one for free field applications. It makes MEMS more adapted for this use. This is translated by an abundance of devices in the literature. As early as in 2003, the feasibility of MEMS loudspeaker was demonstrated using electromagnetic transduction with an assembly of a glass substrate and permanent magnets with a silicon substrate featuring a polymer suspended membrane with an electrochemically deposited copper coil. The loudspeaker radiates $90 \text{ dB}_{\text{SPL}}$ at 5 kHz for a footprint of approximately 25 mm^2 . Due to an important leak, the sound pressure level in the low frequencies is very low. The overall level radiated by the loudspeaker is too low to fulfill industry requirements. The frequency response and a picture of this MEMS loudspeaker are presented in Figure 1.30.

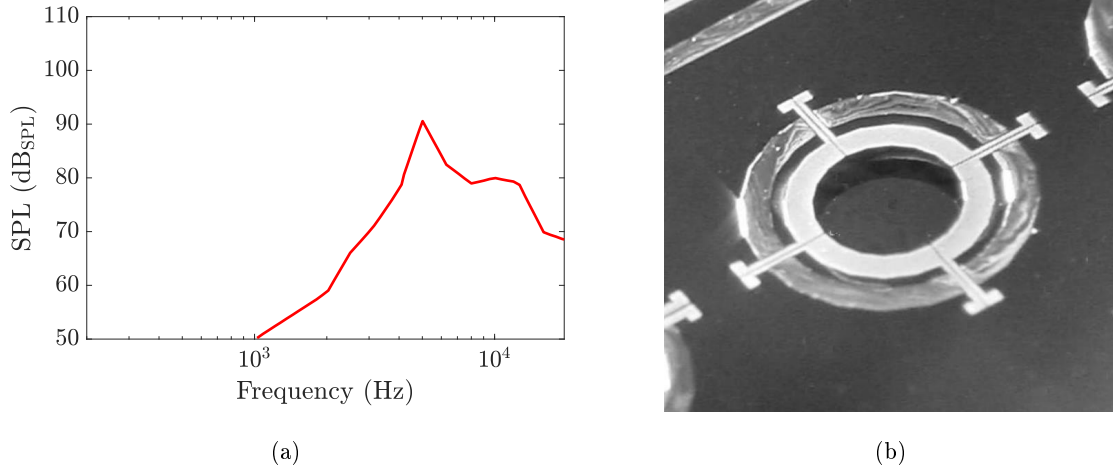


Figure 1.30: Frequency response of the microloudspeaker in a 2 cm³ cavity (a) and picture of this microloudspeaker (b) taken from [70]

Other electromagnetic loudspeakers are presented in the literature such as the one with a Cu-Ni nanocomposite coils described in [71] showing a rather low sound pressure level of 70 dB_{SPL} at 2 kHz. Another one based on an integrated wax-bonded Nd-Fe micro-magnet [72] shows a low displacement of less than 1 μm and no measurement of the acoustic pressure generated in the coupler was made. Another loudspeaker, based on a single turn micro-coil integrated on a polyimide diaphragm with a permanent Nd-Fe-B magnet [73] gave a high sound pressure level in lower frequencies (105 dB_{SPL} at 100 Hz) but the loudspeaker was unfortunately not measured in a standard ear-occluded coupler. Another loudspeaker with an optimized magnetic circuit using soft magnets [74] generated a low displacement of less than 1 μm. Lastly a loudspeaker with a PDMS membrane [75] generated a sound pressure level of 110 dB_{SPL} at 1.5 kHz but of only 70 dB_{SPL} at 125 Hz.

For the electrostatic transduction, interesting results were obtained using a new type of geometry, based on an in-plane displacement of deformable silicon beams [76–78]. Due to the use of an in-plane displacement, as opposed to out-of-plane displacement, the footprint of the device is reduced as the depth of these membranes increases the effective radiation area. The use of electrostatic transduction makes the device easy to manufacture using classical microfabrication processes.

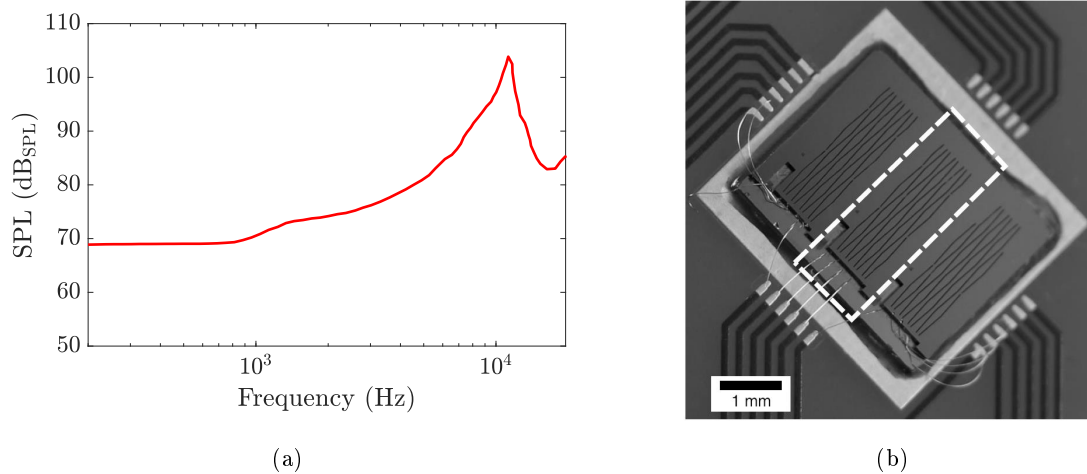


Figure 1.31: Frequency response of the microloudspeaker in an IEC 60318-4 coupler (a) and picture of this microloudspeaker (b) adapted from [76]

As it can be observed in Figure 1.31(a), the frequency response of the loudspeaker is close to the frequency response of the coupler presented in Figure 1.27(a) which would suggest the loudspeaker is behaving as an equivalent piston in the whole frequency range. Despite the correct behavior of the device in the whole audio range, the acoustic pressure in the low frequencies is not sufficient and due to the inherent nonlinear behavior of the electrostatic transduction, a high THD of more than 30% an octave below the resonance of the coupler is observed. The use of multiple cells should increase sufficiently the sound pressure level, and based on the nonlinear models [79, 80] the THD could be corrected. Another loudspeaker using a metal membrane with a polymer seal is showing similar sound pressure levels [81], but due to the sealing polymer, the loudspeaker is not compatible with CMOS processes.

For piezoelectric transduction, an abundance of notable results are presented in the literature. Based on a simple manufacturing process using a Silicon On Insulator (SOI) wafer and using the thermoviscous layer as the sealing between four triangular actuators, a pressure of 110 dB_{SPL} was reached at 1 kHz with an actuation voltage of 20 V. Unfortunately, the pressure at 20 V was equalized to flat, and only the sound pressure level at 2 V is presented. It shows a pressure of more than 130 dB_{SPL} at the resonance of the coupler. The overall pressure is around 105 dB_{SPL} in the whole frequency range. As the previous loudspeaker, the similarity between the curve and the transfer function of the coupler depicted in Figure 1.27(a) suggests that the loudspeaker behaves as a piston in the audio range. The decrease of the level in the lower frequencies could be attributed to an acoustic leak in the measurement setup, or due to the thin interstice of the membrane.

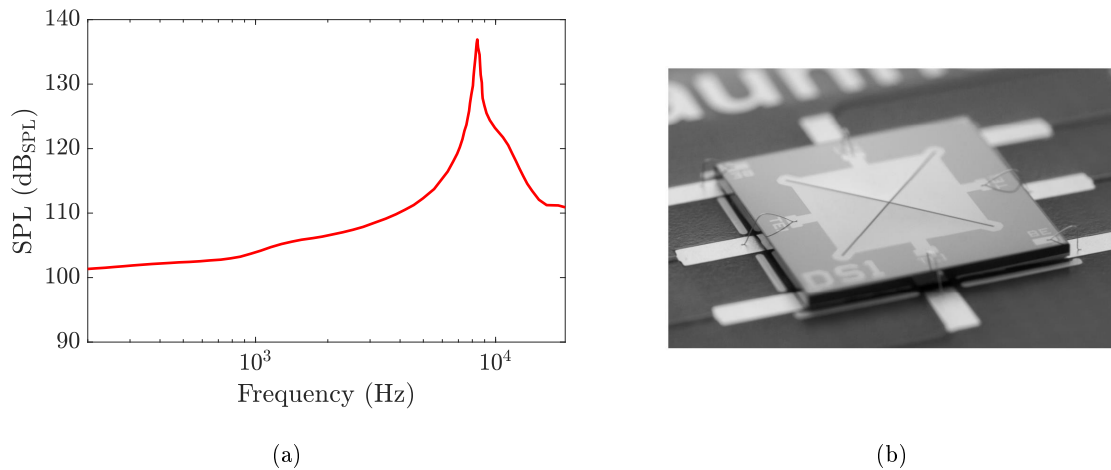


Figure 1.32: Frequency response of the loudspeaker in an IEC 60318-4 coupler (a) and picture of this microloudspeaker (b) adapted from [82]

A very similar loudspeaker using AlN was presented in [83]. Similar loudspeakers, with different shapes, using bending piezoelectric actuators and a thin interstice as the sealing were presented in [84, 85]. Using meandering piezoelectric bending actuators and a rigid radiating element, a pressure of 80 dB_{SPL} around 1 kHz was demonstrated [86]. In [87] a pressure of 120 dB_{SPL} at 4.2 kHz was generated by a loudspeaker manufactured using a Si-parylene composite diaphragm and a PZT actuator. Others loudspeakers with meandering and a rigid radiating element have shown the feasibility of piezoelectric MEMS loudspeaker for in-ear applications [88–91]. Commercial piezoelectric MEMS loudspeakers are already available, such as the UT-P 2018 manufactured by Usound and presented in [92]. It uses two bending actuators facing each other and pushing an heterogeneously assembled rigid membrane, guided out of the plane with a polymer suspension. The loudspeaker is very similar in shape as the one depicted in Figure 1.17(b). The frequency response of the loudspeaker inside a standard coupler is presented in Figure 1.33(a), as well as a mechanical drawing of a cross-section of the loudspeaker inside the ear-occluded coupler in Figure 1.33(b).

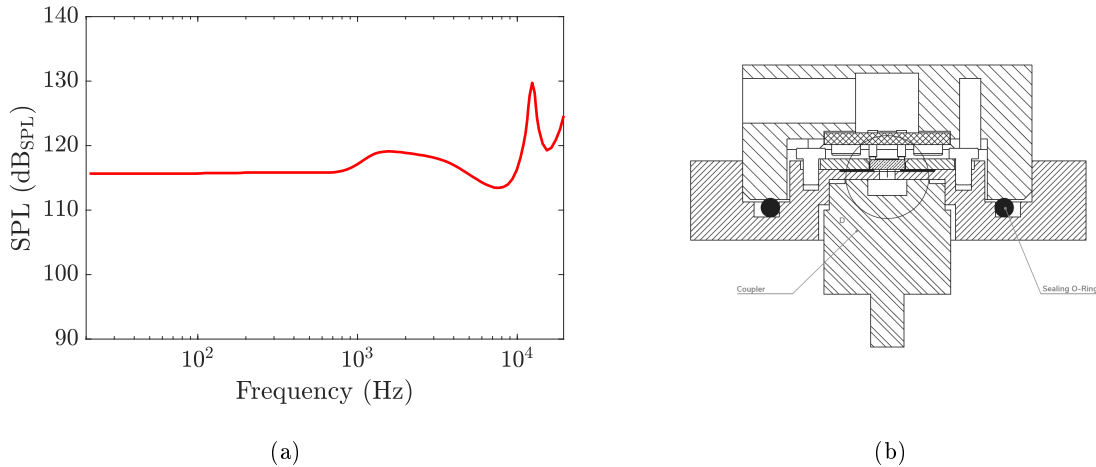


Figure 1.33: Frequency response of the loudspeaker in an IEC 60318-4 coupler (a) and a drawing of a cross section of the loudspeaker mounted on the coupler (b) taken from [93]

The resonance of the loudspeaker can be observed in the audio range, around 3 kHz. Although having a resonance in the audio range is not recommended, the displacement and force generated by piezoelectric bending actuators is linked by their stiffness and a simple way of increasing the latter is to reduce the resonance frequency. The decrease of the radiated sound pressure above the resonance frequency predicted with the one dimensional model of Figure 1.4 is compensated by the modes of the coupler, and the loudspeaker radiates more than 110 dB_{SPL} in the whole audio bandwidth.

1.6 Specifications and Design Choices

From the loudspeakers presented in Section 1.5 and 1.4, a single value to characterize the performance of micro-loudspeaker is chosen. The comparison of all frequency responses of the loudspeaker shows that the resonance frequency of MEMS loudspeakers are very rarely below 1 kHz. At this frequency, only one loudspeaker of the literature radiates at least 80 dB_{SPL}. As loudspeakers behave as high pass filters in free field and the critical lowest frequency for the smartphone market seems to lean around 1 kHz with a back cavity of 1 cm³, the target is fixed as a pressure of at least 80 dB_{SPL} starting at 1 kHz. For smartphone use, the industry standard for footprint is approximately 165 mm². To reduce the manufacturing cost and make loudspeakers compatible with smaller devices, such as smartwatches, the chosen upper limit for the footprint is 100 mm². The pressure radiated by loudspeakers of the literature in free field, as well as the targeted zone is summarized as the radiated sound pressure level at 1 kHz at 10 cm as a function of the footprint in Figure 1.34.

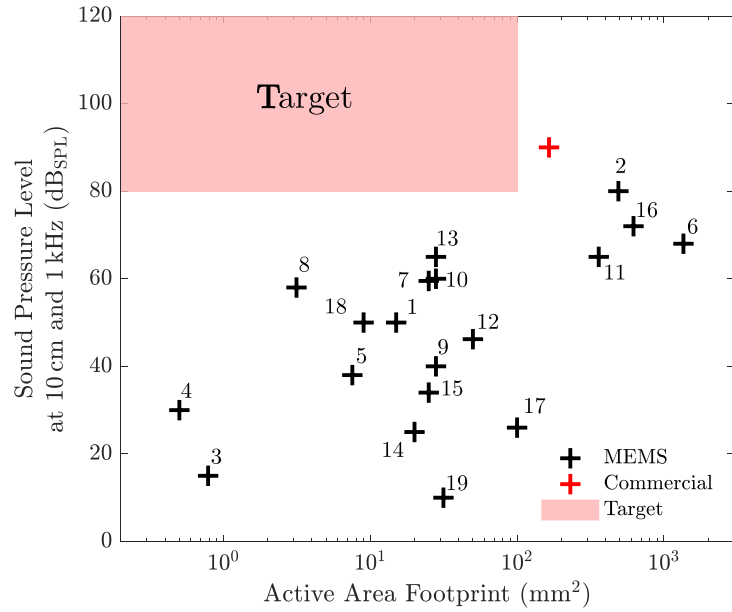


Figure 1.34: Sound pressure level at 10 cm and 1 kHz of MEMS loudspeakers of the literature whose performance are recalled in Table 1.2

Table 1.2: Sound pressure level and footprint of MEMS loudspeakers of the literature for free field applications

Reference	Number	Transduction	Date	SPL at 1 kHz at 10 cm (dB _{SPL})	Footprint (mm ²)
<i>continues on next page</i>					

Table 1.2: Sound pressure level and footprint of MEMS loudspeakers of the literature for free field applications

[15]	1	Electromagnetic	2012	80	490
[49]	2	Electrostatic	2015	50	15
[51]	3	Electrostatic	2014	15	0.785
[52]	4	Electrostatic	2007	30	0.5
[38]	5	Electrostatic	2020	38	7.5
[56]	6	Piezoelectric	2015	68	1359
[41]	7	Piezoelectric	2005	59.5	25
[42]	8	Piezoelectric	2009	58	3.14
[36]	9	Piezoelectric	2019	40	28
[33]	10	Piezoelectric	2020	60	28
[43]	11	Piezoelectric	2009	65	360
[94]	12	Piezoelectric	2015	46	50
[35]	13	Piezoelectric	2021	65	28
[95]	14	Piezoelectric	2009	25	20
[96]	15	Piezoelectric	2000	34	25
[63]	16	Thermoacoustic	2014	26	100
[97]	17	Piezoelectric	2014	72	621
[93]	18	Piezoelectric	2019	50	12
[98]	19	Thermoacoustic	2013	10	31

Similarly, the pressure generated by loudspeakers at 100 Hz in ear-occluded couplers is presented in Figure 1.35. The comparison is more difficult, due to the lack of standardization in the measurement setups, and only eight loudspeakers are compared. Some sound pressure levels are extrapolated from the available data. This comparison shows that no MEMS loudspeaker is able to radiate more than 120 dB_{SPL}. Although this acoustic pressure could cause damage to the human ear at some frequencies, the human ear is not so sensitive to lower frequencies, as it can be observed on the Fletcher-Munson curves [99]. Also, since the sixties, the frequency content in the lower frequency range has significantly increased [100], thus the need to have a high level of pressure in the lower frequencies of the audio range. Finally, reaching a higher level of pressure could result in a lower THD at lower levels.

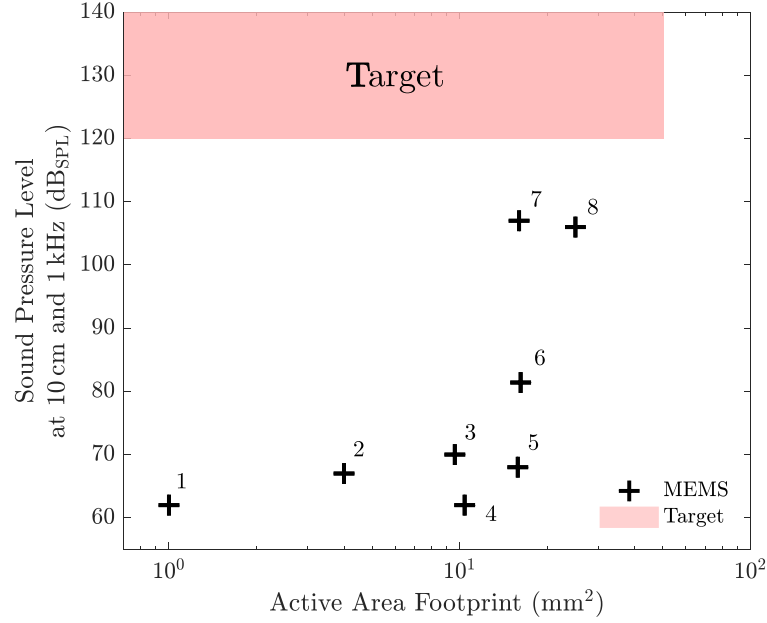


Figure 1.35: Sound pressure level at 100 Hz radiated in a coupler of MEMS loudspeakers of the literature whose performance are recalled in Table 1.3

Table 1.3: Sound pressure level in coupler and footprint of MEMS loudspeakers of the literature for in-ear applications

Reference	Number	Transduction	Date	SPL at 100 Hz in a coupler (dB _{SPL})	Footprint (mm ²)
[88]	1	Piezoelectric	2020	62	1
[37]	2	Piezoelectric	2021	67	4
[75]	3	Electromagnetic	2011	70	9.6
[34]	4	Piezoelectric	2021	62	10.4
[76]	5	Electrostatic	2019	68	15.9
[89]	6	Piezoelectric	2020	81.4	16.2
[82]	7	Piezoelectric	2018	107	16
[73]	8	Electromagnetic	2017	106	25

The design is focused on the free field characteristic presented in Figure 1.34, as it is harder to obtain a high sound pressure level at a low frequency, and because loudspeaker designed for free field applications can be adapted to be used for in-ear applications, contrarily to the opposite.

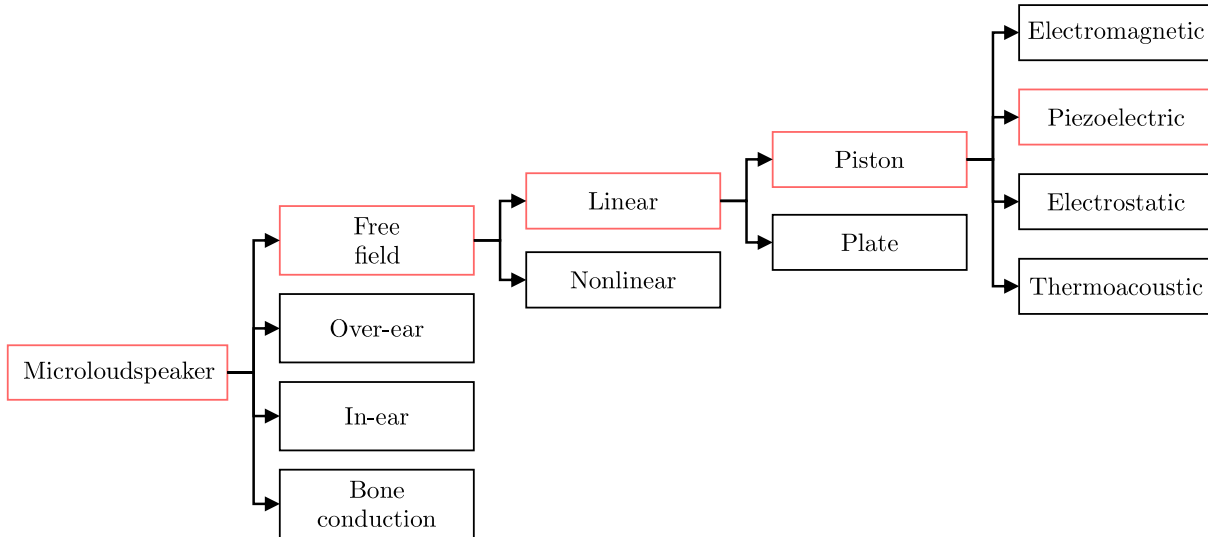


Figure 1.36: Choice of methods for sound reproduction using a MEMS loudspeaker

After an exhaustive review of the recent literature, the application and the working principle of the loudspeaker is defined. A few MEMS loudspeakers are already commercialized for in-ear and over-ear applications, and if good performance for free field applications are reached, it would be beneficial for in-ear applications as well, as the frequency response of the loudspeaker can be acoustically modified to fulfill the requirements. Bone conduction is too difficult to characterize, and although the displacement and force reached by MEMS devices could be compatible with this type of sound reproduction, the perceived sound quality would need to be estimated through psychoacoustic studies, as there is no guideline for this type of sound reproduction devices. Loudspeakers based on nonlinear transduction and more precisely digital loudspeaker are not exhibiting encouraging results in the recent literature. For other nonlinear sound reproduction principles, such as the parametric array, the required level for the nonlinear propagation in air is not compatible with the small size of MEMS devices. Piezoelectric transduction is chosen, mainly because of its great compatibility with microfabrication processes. Electrodynamics MEMS loudspeakers show great performance, but permanent magnet are difficult to manufacture. Electrostatic loudspeaker do not provide sufficient displacement and sound pressure level. Thermoacoustics loudspeaker do not provide a sufficient sound pressure level and have usually a poor efficiency. The chosen loudspeaker is a linear loudspeaker, with a piston motion, actuated by bending piezoelectric actuators.

1.7 Chapter Conclusion

In this chapter, the pioneer and recent research for the development of MEMS loudspeaker was reviewed, for free field and in-ear applications. From this review, the performance for both applications were summarized into the pressure radiated at respectively 100 Hz and 1 kHz as a function of the active area. This classification highlighted that no MEMS loudspeakers were able to radiate 120 dB_{SPL} or more at 100 Hz for an active surface smaller than 40 mm², and able to radiate 80 dB_{SPL} or more at 1 kHz, for an active surface of less than 100 mm². By observing the geometry used for the best performing loudspeakers in this review, the method for the transduction is chosen to be piezoelectric bending actuators.

Chapter 2

Small Signal Modeling and Design

Contents

2.1	Design Methodology	34
2.2	Lumped Element Modeling	35
2.2.1	General Structure	35
2.2.2	Equivalent Electrical Circuit	37
2.2.3	Actuators	37
2.2.4	Residual Stress	39
2.2.5	Electrical Circuit	41
2.2.6	Damping	42
2.2.7	Squeeze Film	44
2.2.8	Radiation	45
2.2.9	In-Ear	49
2.2.10	Back Cavity	50
2.2.11	Electrical behavior	50
2.2.12	Sensitivity and Efficiency	51
2.3	Optimization of the Performance	53
2.3.1	Dimensions	53
2.3.2	Height of the Coupling Blocks	56
2.3.3	Width of the Air Interstice	56
2.4	Dedicated Driving Board	57
2.4.1	Amplifier	57
2.4.2	Notch Filter	63
2.4.3	Printed Circuit Board	66
2.5	Chapter Conclusion	68

2.1 Design Methodology

In this chapter the design of the loudspeaker firstly based on a lumped element model is detailed.

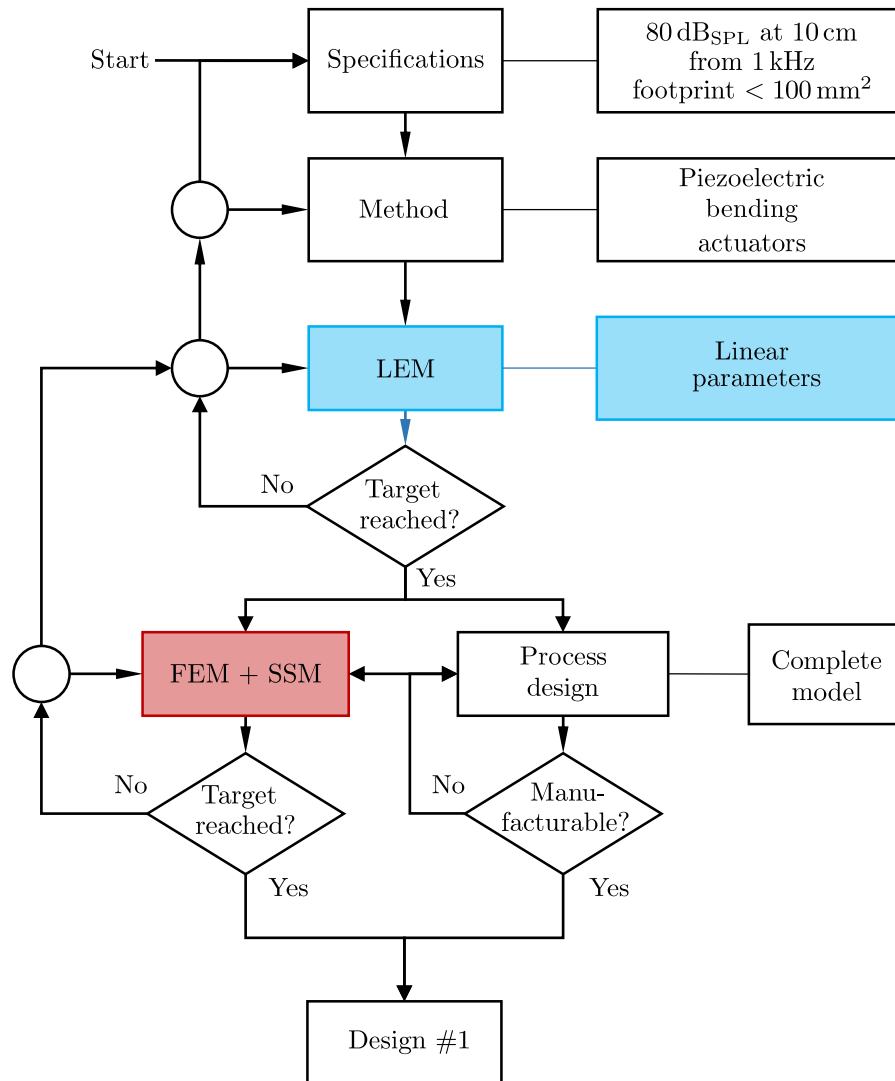


Figure 2.1: Design loop where the optimisation of the linear parameters appears in blue, and the optimization using finite element modeling and state space modeling appears in red

In Figure 2.1, the design loop used for the conception of the loudspeaker is presented. It starts with the choice of specifications and the choice of the method for sound reproduction, as defined in Section 1.6 after the literature review of the recent development concerning MEMS loudspeakers. This review gives a sound pressure level of at least 80 dB_{SPL} at 1 kHz for a footprint of less than 100 mm². The method of sound reproduction, also defined in Section 1.6 is by using a linear transduction and piezoelectric bending actuators. From the specifications and the method, the lumped element model whose elements are described one by one in Section 2.2 is used to define the required linear characteristics of the loudspeaker, such as the maximum displacement, the size of the radiating surface, the dimensions, the actuation voltage and the thickness of the bending actuators in Section 2.3. This optimization process is looped

until the targeted performance is reached. If the targeted performance is not attained after multiple trials, the method or the target might be reevaluated. If the target is reached, a combination of finite element method and state space modeling, described in Sections 3.2 and 3.4 respectively, is used to evaluate the modal behavior, the linearity, the stress and other more complex aspects of the loudspeaker. During this second design phase, performance are usually revised downwards and a revision of the linear parameters defined by the lumped element model could be reassessed. If after a few iterations the performance are not reached, the method and the target could be modified again. The manufacturing process, presented in Chapter 4, is defined concurrently to the nonlinear and three-dimensional model of the loudspeaker, until a complete manufacturable and high-performance design is reached.

2.2 Lumped Element Modeling

2.2.1 General Structure

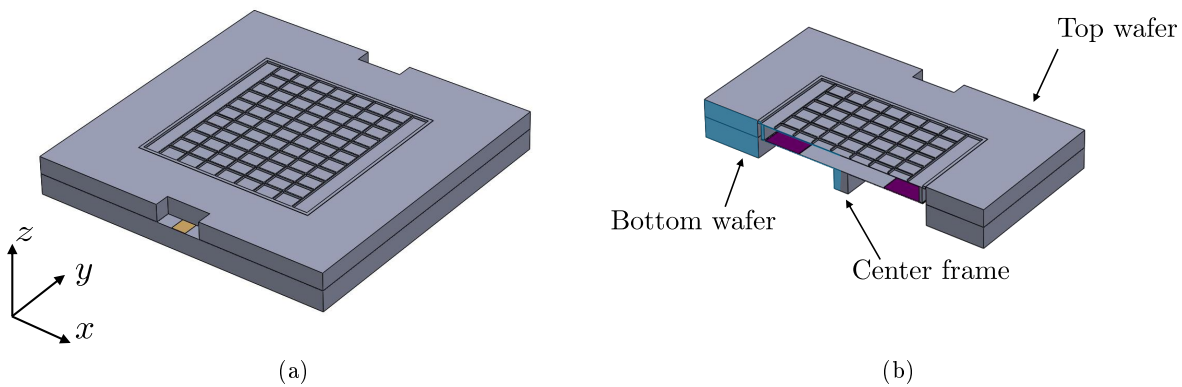


Figure 2.2: 3D (a) and 3D cross-section (b) views of the main version of the designed loudspeaker

As it is shown in Figures 2.2(a) and 2.2(b), the loudspeaker is composed of a central square rigid stiffened plate, a square frame, and lateral openings on the sides for the contacts to the electrodes. The loudspeaker is composed of two wafers, a wafer featuring the actuators and a wafer featuring the moving plate. A sketch of the principle of the loudspeaker, which is highlighted in blue the cut view of Figure 2.2(b) is shown in Figure 2.3.

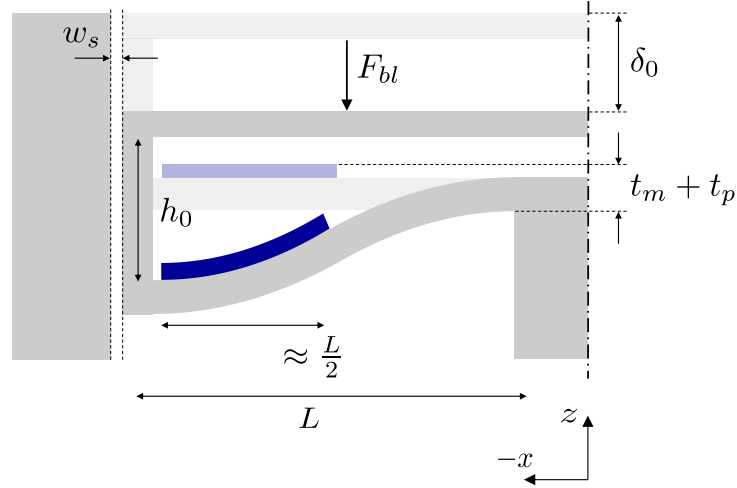


Figure 2.3: Half cross section sketch of the principle of the designed loudspeaker in which the light gray and light blue parts represent the undeformed structure

Flexible layers of silicon of length L are covered with approximately half their length with a piezoelectric layer. Due to symmetry on the x axis at $x = 0$, the tip of the cantilever is guided, carrying a rigid plate that can only move along z . Under the electric field created by the potential difference between the top electrode, above the piezoelectric layer, and the bottom electrode, below the piezoelectric layer, a strain appears along the x axis, inside the piezoelectric layer. The latter of thickness t_p being firmly attached to the elastic layer of thickness t_m , the actuator bends, adopting a clamped-guided shape along x . The force F_{bl} is the force needed to block the plate when the actuators are subjected to the maximum admissible voltage. The resulting displacement δ_0 is the maximum displacement of the plate with no external load, along the z axis. Instead of using a classical surround to avoid the rear acoustic waves to interact with the front acoustic waves, the plate moves in a frame, whose dimensions are $2w_s$ wider than the plate, to avoid the back acoustic waves to interact with the front acoustic ones.

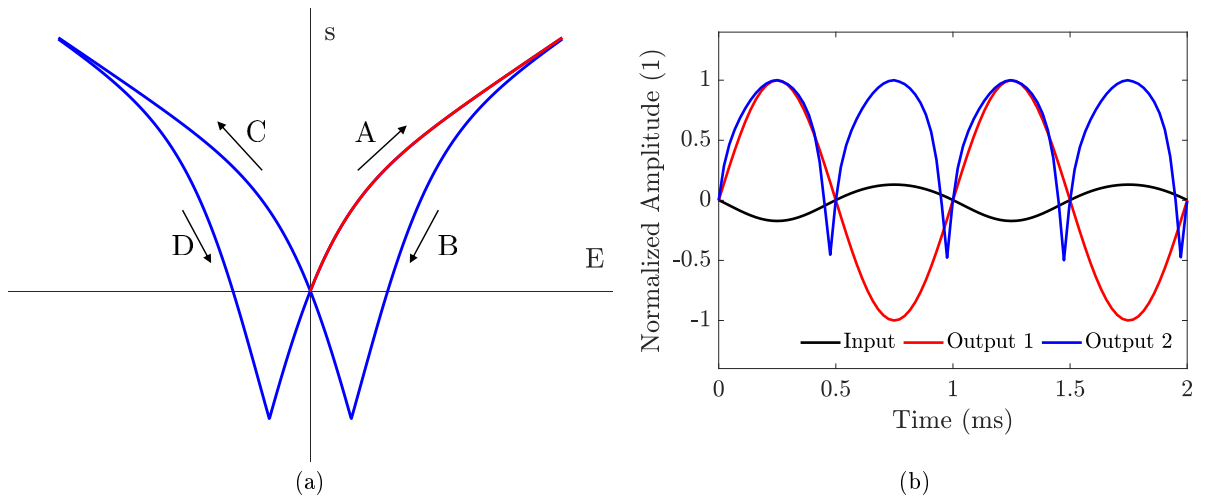


Figure 2.4: Strain resulting from an applied input electric field on a ferroelectric material (a) and output signals for a symmetric and asymmetric input sinusoidal signals applied to such a material (b)

The piezoelectric material used is ferroelectric and the relation between the input electric field E and the resulting longitudinal strain s is highly hysteretic and nonlinear. Figure 2.4(a) shows the typical ferroelectric loop of the piezoelectric material, which is linked to the material behavior described in Section 1.4.2 in Figure 1.14. For small electric fields, the material behaves as a piezoelectric material, and the input signal, depicted in red in Figure 2.4(b) is correctly reproduced. For larger electric fields, the material is successively polarized and unpolarized and the output strain signal is strongly altered, with the negative part reversed. This shifts the pulsation ω of the input signal to a pulsation 2ω in the output signal. To circumvent this effect, an offset of half the input dynamic is used, and the path A is used, highlighted in red in Figure 2.4(a). Figure 2.4(b) depicts a sinusoidal signal as the input signal and the output 1 signal is the output signal for a low input voltage, such as the material behaves as a piezoelectric material, and output 2 is the output strain signal for a high input electric field, with the negative part of the input signal reverted similarly to the output of a rectifier bridge.

2.2.2 Equivalent Electrical Circuit

The loudspeaker mainly behaves as a second order oscillator, actuated with a piezoelectric actuator, and the behavior of such a loudspeaker can be predicted using an assembly of the equivalent electrical circuits depicted in Figures 1.15 and 1.2, on which a rigid plate of surface S_d , represented as a transformer of the same ratio is added. The counter-force acting on the plate due to the air is represented as the complex impedance Z_r . The complete schematic is represented in Figure 2.5.

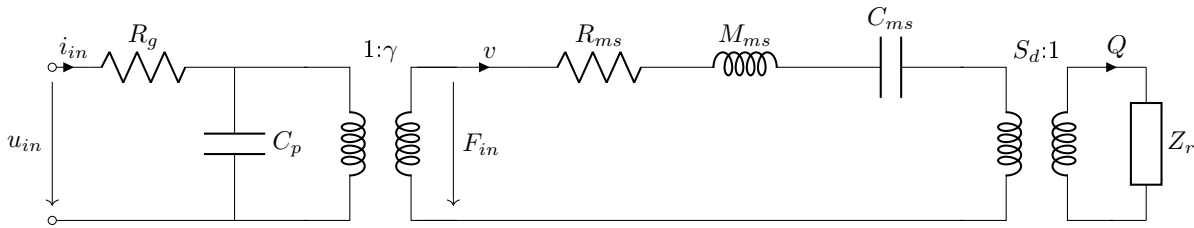


Figure 2.5: Linear lumped equivalent network of the loudspeaker

From the equivalent circuit depicted in Figure 2.5, the mechanical impedance of the moving part, seen from the electromechanical transducer can be expressed as

$$Z_m = R_{ms} + j\omega M_{ms} + \frac{1}{j\omega C_{ms}} + Z_r S_d^2 \quad (2.1)$$

and the velocity of the moving part of the loudspeaker is calculated using

$$v = \frac{F_{in}}{Z_m}. \quad (2.2)$$

2.2.3 Actuators

The capacitor C_p , the apparent compliance C_{ms} and the transduction factor γ are determined using a model of the piezoelectric bending actuators, based on Bernoulli's equation. Contrarily to what's depicted in Figure 2.6, and due to the symmetry of the loudspeaker, the cantilever end is guided. Due to the boundary conditions, the actuators are considered as cantilevers.

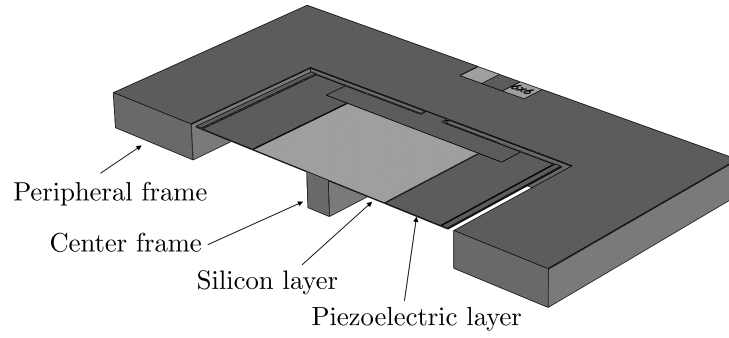


Figure 2.6: Bottom part of the loudspeaker manufactured in the wafer 1

Only a part of the length of the actuators is covered with piezoelectric material. Figure 2.7 schematically represents the actuators of the loudspeaker. L is the length of the actuator and F_{bl} is the force needed to prevent the tip from moving. The plate is analytically represented as two different beams, connected together at a length $= -\beta L$.

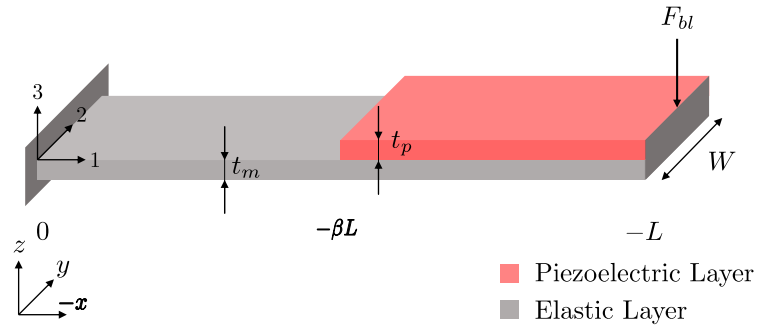


Figure 2.7: 3D schematic of a cantilever

Both beams follow the Bernoulli beam integral, and the following equations can be written

$$M_1(x) = -EI_1 \frac{\partial^2 w_1}{\partial x^2} + z_p \text{ and} \quad (2.3)$$

$$M_2(x) = -EI_2 \frac{\partial^2 w_2}{\partial x^2} \quad (2.4)$$

with EI_1 the equivalent Young modulus times the moment of inertia for the first beam section, w_1 the displacement profile of the first section of the beam and $z_p = zWe_{31}$ the electromechanical coupling of the piezoelectric layer and considering the simplification described in Equation 1.15, with W the width of the beam, z the distance from the middle of the piezoelectric layer to the neutral axis of the elastic beam and the piezoelectric layer and e_{31} the transverse piezoelectric constant. Using the relevant boundary conditions for the guided and clamped ends, and the continuity relations between the two section of the beams, the displacement profile can be expressed as a function of x

$$w_1(\beta) = -\frac{L^2 u_{in} z_p (-1 + \beta)^2 (-1 - 3\tau + 8\beta\tau)}{2EI_1 (1 + 14\tau + \tau^2)} \text{ and} \quad (2.5)$$

$$w_2(\beta) = -\frac{L^2 u_{in} z_p \beta^2 (-5 + 8\beta + \tau)}{2EI_1 (1 + 14\tau + \tau^2)}, \quad (2.6)$$

with $\tau = EI_1/EI_2$. The deflection profile for a clamped-guided cantilever is depicted in Figure 2.8(a) and for a clamped end in Figure 2.8(b) for different normalized input voltages.

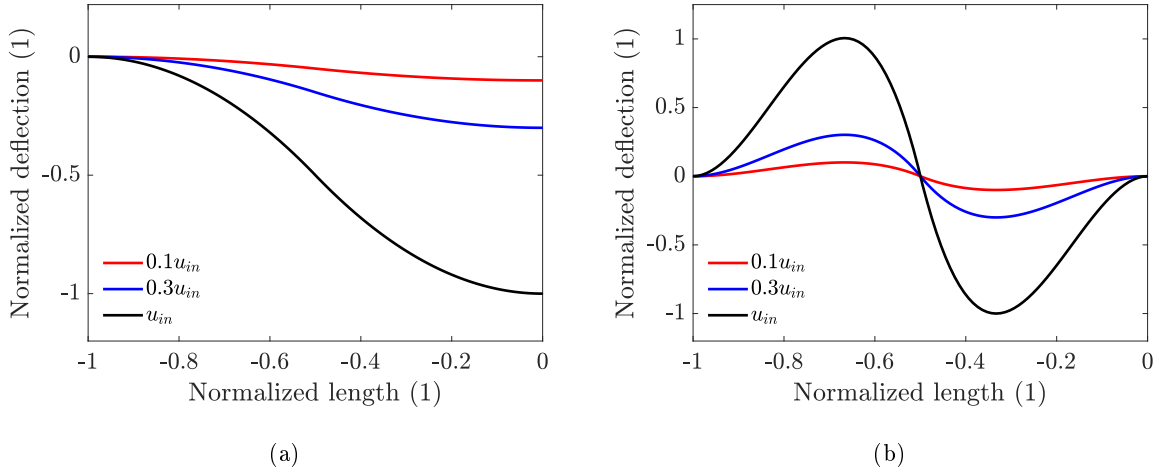


Figure 2.8: Deflection profile of a clamped-guided (a) and clamped-clamped (b) beam, actuated with a piezoelectric layer

As it can be observed from Figure 2.8(b), the difference of bending stiffness of the beam is not significantly influenced by the piezoelectric layer, as long as the piezoelectric layer thickness is small compared to the thickness of the elastic layer. Using the equation of the clamped-clamped beam, the blocked force is determined and can be expressed as

$$F_{bl} = -\frac{24z_p\tau u_{in}}{L(1+14\tau+\tau^2)}. \quad (2.7)$$

Using all the different possible combinations of boundary conditions, the electromechanical coupling of the beam can be written in a matrix form, linking the output force F and torque M , with the angular displacement θ and the displacement δ of the beam along y and u_{in} the input voltage, applied to the piezoelectric layer such as

$$\begin{bmatrix} F \\ M \end{bmatrix} = \begin{bmatrix} \frac{96EI_1\tau(1+\tau)}{L^3(1+14\tau+\tau^2)} & \frac{24EI_1\tau(1+3\tau)}{L^2(1+14\tau+\tau^2)} \\ \frac{24EI_1\tau(1+3\tau)}{L^2(1+14\tau+\tau^2)} & \frac{8EI_1\tau(1+7\tau)}{L(1+14\tau+\tau^2)} \end{bmatrix} \begin{bmatrix} \delta \\ \theta \end{bmatrix} + \begin{bmatrix} -\frac{24z_p\tau}{L(1+14\tau+\tau^2)} \\ \frac{z_p(-5+\tau)\tau}{1+14\tau+\tau^2} \end{bmatrix} u_{in}. \quad (2.8)$$

Using the blocked force F_{bl} and the free displacement δ_0 , the apparent compliance of the beam can be written as

$$C_{ms} = \frac{\delta_0}{2F_{bl}}. \quad (2.9)$$

The limitation of this model is discussed in Section 3.2.9.

2.2.4 Residual Stress

An important point in MEMS manufacturing is the presence of residual stress in materials. This effect is significative for thermal oxide layers. For the actuators, the existence of residual stress in the oxide

layer influences their apparent stiffness. Due to the thicknesses of the different layers (given in Chapter 4), the effect of the residual stress of the oxide layer is considered the most important. From the model of the piezoelectric actuator in Section 2.2.3, an additional term describing the moment created by the residual stress along the beam is added into Equations 2.3 and 2.4 and they are rewritten such as

$$M_1(x) = -EI_1 \frac{\partial^2 w_1(x)}{\partial x^2} + z_p + Nw_1(x) \quad (2.10)$$

and

$$M_2(x) = -EI_2 \frac{\partial^2 w_2(x)}{\partial x^2} + Nw_2(x) \quad (2.11)$$

with $N = \sigma_0 W t_o$, σ_0 being the residual stress, W being the width of the actuator and t_o being the thickness of the layer carrying the residual stress. Solving this equation for the two sections of the beam and applying the continuity conditions between the two beams, and the correct boundary conditions, the profile of the beam can be computed and writes

$$w_1(x) = \frac{e^{-\frac{L\sqrt{N}\beta}{\sqrt{EI_1}}} \left(e^{\frac{L\sqrt{N}}{\sqrt{EI_1}}} - e^{\frac{L\sqrt{N}\beta}{\sqrt{EI_1}}} \right)^2 Lz_p}{2 \left(-1 + e^{-\frac{2L\sqrt{N}}{\sqrt{EI_1}}} \right) \sqrt{EI_1} \sqrt{N}} \quad (2.12)$$

and

$$w_2(x) = \frac{1}{8 \left(-1 + e^{\frac{2L\sqrt{N}}{\sqrt{EI_1}}} \right) EI_1 \sqrt{N}} e^{-\frac{L\sqrt{N}\beta}{\sqrt{EI_1}}} Lz_p \quad (2.13)$$

$$\left(4e^{\frac{2L\sqrt{N}}{\sqrt{EI_1}}} + 4e^{\frac{2L\sqrt{N}}{\sqrt{EI_1}}} - 8e^{\frac{L\sqrt{N}(1+\beta)}{\sqrt{EI_1}}} L\sqrt{N}(1-2\beta)^2 - e^{\frac{L\sqrt{N}(2+\beta)}{\sqrt{EI_1}}} L\sqrt{N}(1-2\beta)^2 \right).$$

These equations allow to display the bending profile of the actuators with respect to the internal residual stress of an equivalent layer. As expected, the apparent stiffness of the actuators changes with the residual stress, as it can be seen in Figure 2.9. The performance are directly affected by the residual stress because it decreases the free displacement of the cantilevers. Although the effect of the residual stress might be overestimated compared to the results of finite element models, it shows that the residual stress has an influence on the behavior of the actuators and need to be taken into account.

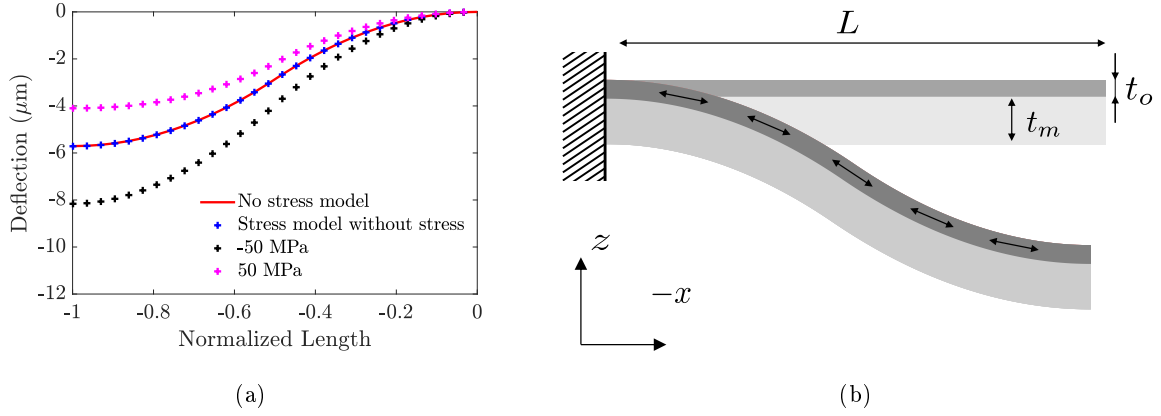


Figure 2.9: Deflection of a cantilever with and without residual stress in an oxide layer (a) and cross section sketch of a cantilever with residual stress in one layer (b)

2.2.5 Electrical Circuit

The electrical parameters of the equivalent circuit are determined from dimensions and materials properties. The resistor R_g represents the resistance in the conductive path from the output of the amplifier to the piezoelectric actuators. The resistance of a homogeneous conductor can be calculated using

$$R_c = \frac{\rho_{Au} L_c}{W_c t_c} \quad (2.14)$$

with ρ_{Au} the resistivity of gold, L_c the length of the conductor, W_c the width of the conductor and t_c the thickness of the conductor, as described in Figure 2.10.

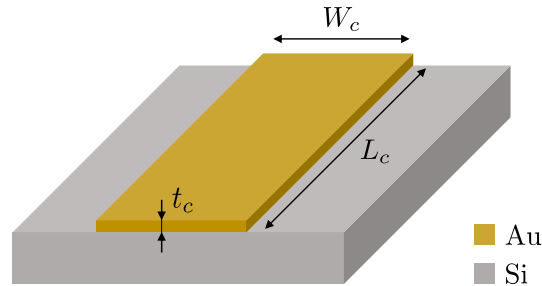


Figure 2.10: 3D schematic of a microfabricated metallic conductor

The capacitance C_p is determined by the dielectric constant of the piezoelectric material and the dimensions of the electrodes. The permittivity of the piezoelectric material is found in the reduced Equation 1.15. The capacitance writes

$$C_p = \epsilon_r \epsilon_0 \frac{A_p}{t_p} \quad (2.15)$$

with ϵ_r^S the relative permittivity of the dielectric material, ϵ_0 the vacuum permittivity, $A_p = L_c W_c$ the surface of piezoelectric material and t_p the thickness of the piezoelectric layer. The full electrical circuit includes a parallel resistor as well, representing the leakage current from the top electrode to the bottom electrode. The value of the resistance is difficult to determine analytically [101]. The complete

electrical circuit is presented in Figure 2.11, including a series resistor R_s , representing the losses in the dielectric material during the conduction of the capacitor. A Zener diode is also included, representing the breakdown voltage of the piezoelectric material, above which a current with a null frequency can flow through the dielectric material.

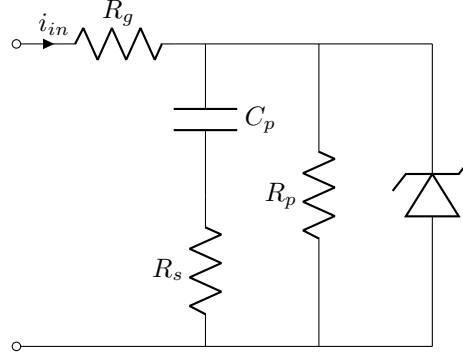


Figure 2.11: Equivalent electrical circuit of the electrical connections and of the piezoelectric layer

2.2.6 Damping

The damping taken into account in this section is the dissipative phenomena occurring between the moving plate and the frame of the loudspeaker. The slit between the moving plate and the frame as well as the physical relevant physical quantities are represented in Figure 2.13(a).

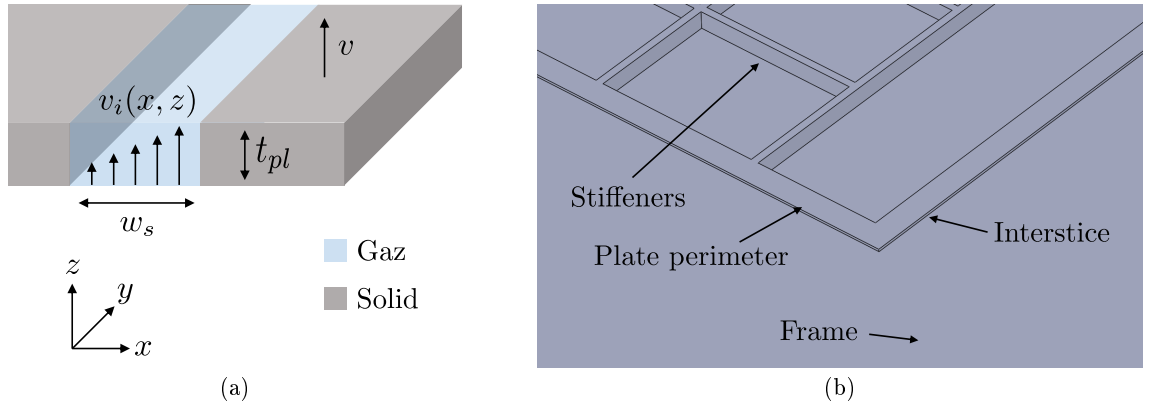


Figure 2.12: 3D schematic (a) and zoom on the 3D view of Figure 2.2 (b) showing the thin interstice between the mobile plate and the fixed frame of the loudspeaker

The air being a viscous fluid, the harmonic translation of the plate along z creates a shear stress in the fluid. This shear stress is creating a force, opposed to the displacement of the plate. This damping is known to be a viscous damping. Considering a viscous fluid, the reaction force can be determined using the reduced Navier-Stokes equation for a Couette flow such as

$$\mu \frac{\partial^2 v_i(x, z)}{\partial x^2} = \frac{\partial p}{\partial z} \quad (2.16)$$

with $v_i(x, z)$ the out-of-plane fluid velocity inside the interstice, p the pressure inside the interstice and μ the dynamic viscosity coefficient of the fluid. By neglecting the pressure gradient created by the

displacement of the plate inside the air interstice, the velocity of the fluid inside the interstice can be assumed to be a linear function of x . Using the boundary conditions $v_z(x = 0, z) = 0$ and $v_z(x = w_s, z) = v$, the force created by the viscosity of the fluid in the interstice and acting on the plate can be written as [102]

$$F_i = \frac{\mu t_{pl} l_s}{w_s} v \quad (2.17)$$

with t_{pl} the thickness of the plate, l_s the perimeter of the plate and w_s the width of the interstice, indicating that the force is proportional to the velocity of the plate, which leads to an equivalent resistor R_{ms} representing the viscous damping written as

$$R_{ms} = \frac{\mu t_{pl} l_s}{w_s}. \quad (2.18)$$

This effect also avoids the acoustic short-circuit between the front and the back side of the plate, as the velocity field of the volume of air between the plate and the frame is determined by the boundary conditions and the velocity of the plate due to the viscous effect. The velocity of the fluid surrounding a plate moving with a harmonic velocity $v = v_0 e^{j\omega t}$ in the z direction can be determined starting from the expression of the shear stress in the interstice determined as

$$\chi(x) = \mu \frac{\partial v}{\partial x} \quad (2.19)$$

where χ is the shear stress in the fluid. Equation 2.19 describes the proportionality between the variation of the velocity along the x axis and the resulting shear stress. They are linked by the dynamic viscosity coefficient of the fluid μ . The total drag force is then the integration of the shear stress of Equation 2.19 over the axis x such as

$$\chi(x) - \chi(x + dx) = -\frac{\partial \chi}{\partial x} dx. \quad (2.20)$$

By replacing χ by its expression, the equation for the x axis becomes

$$\rho \frac{\partial v}{\partial t} = \mu \frac{\partial^2 v}{\partial x^2}. \quad (2.21)$$

By solving this second order homogeneous differential equation, the profile of the velocity along x can be determined and writes [103]

$$v_i = v e^{\frac{-x}{\delta_\nu}} e^{\frac{jx}{\delta_\nu}} \quad (2.22)$$

with $\delta_\nu = \sqrt{\frac{\rho_0 \omega}{2\mu}}$, with ρ_0 the air density at ambient temperature. In Figure 2.13(b), the velocity profile of the fluid at different frequencies is presented. At the vicinity of the boundary, the fluid and the plate have the same velocity. Under a certain interstice dimension, the interstice has the same velocity as the plate, and so, no acoustic short-cut occurs. The size of the layer is frequency dependent and can be plotted against frequency, as depicted in Figure 2.13(a).

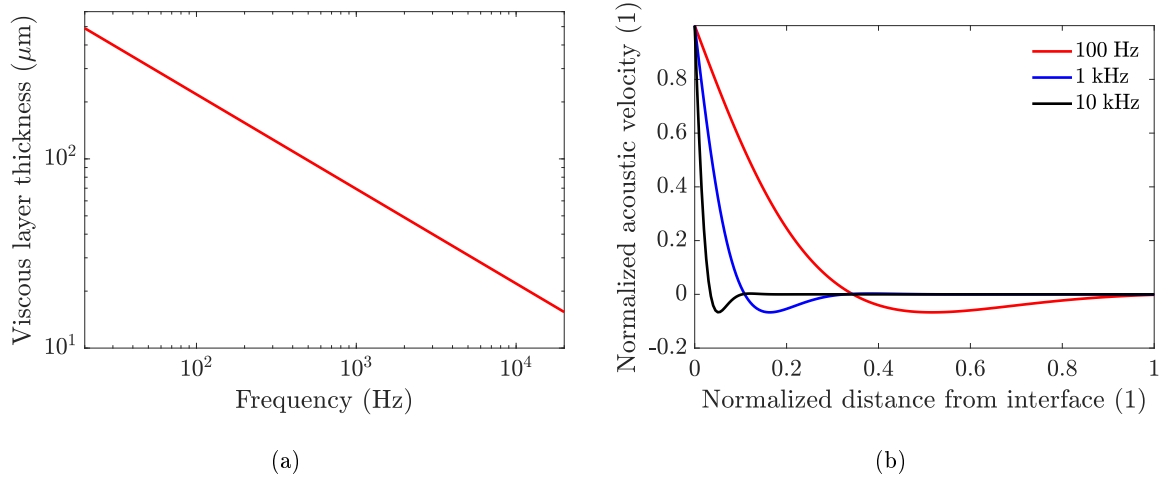


Figure 2.13: Critical thickness of the viscous layer, in which the velocity in the layer is entirely determined by the velocity of the plate (a) and profile of the velocity of the fluid inside the interstice for different frequencies (b)

2.2.7 Squeeze Film

The second part of the damping considered in the model is the damping due to the squeeze film effect behind the moving structure of the loudspeaker. The squeeze film effect is an effect occurring in thin layers of air trapped between moving structures. It is widely studied in MEMS, because it is determinant in structures that need a high quality factor [104]. In the case of a macroscopic structure such as the present loudspeaker, the effect might be negligible, but can degrade the performance around the resonance. A sketch describing the effect is presented in Figure 2.14(a).

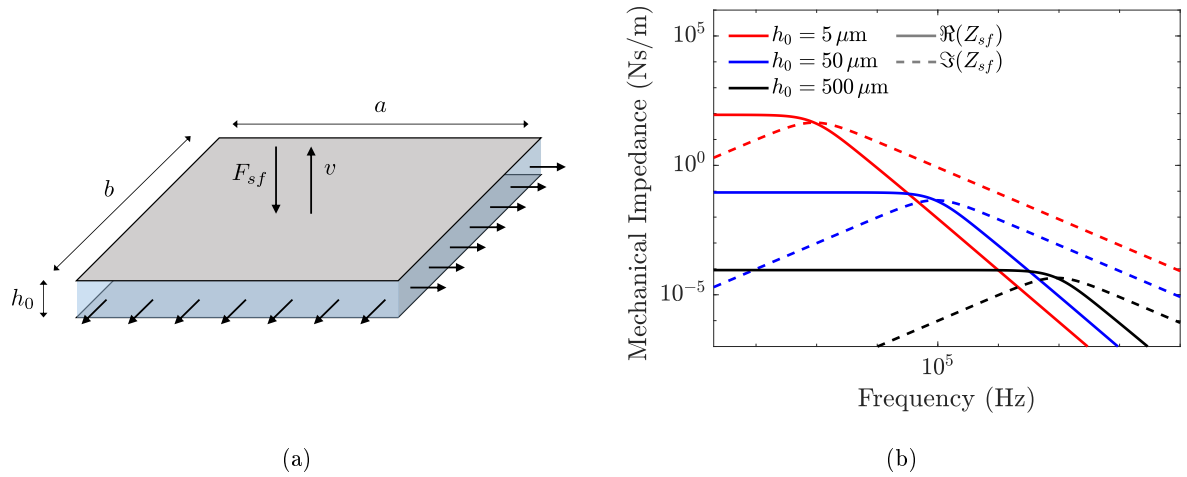


Figure 2.14: Sketch of the squeeze film effect (a) and squeeze film impedance for different gap height (b)

The model derived in [105] for the case of two parallel plates with an open perimeter writes

$$F_{sf} = abP_0 \sum_{m,n=odd} \frac{64}{\pi^2 m^2 n^2} \frac{-j\sigma\eta}{j\sigma + m^2\pi^2 + \beta^2 n^2\pi^2} \frac{h}{h_0} e^{j\omega t} \quad (2.23)$$

with F_{sf} the reaction force acting on the moving plate, β the ratio between the width and the length of

the plate, h the amplitude of the displacement, h_0 the gap height between the two plates, and σ a non dimensional number defined by

$$\sigma = \frac{12\mu a^2 \omega}{\rho h_0^2 P_0} \quad (2.24)$$

with μ the viscous coefficient of the fluid trapped between the plates, $\rho = 1$ for an isothermal process and P_0 the static pressure. Using the expression of the velocity, and replacing the expression of the displacement, the squeeze film impedance experienced mechanically by a plate of surface $ab = 100 \text{ mm}^2$ can be plotted as a function of frequency, for different gap heights. As it can be seen in Figure 2.26, two frequency ranges can be identified. The first frequency range is dominated by the resistance effect. The fluid has a sufficient amount of time to escape and the shear stress creates a pure resistive load on the plate. A critical frequency can be seen, at which the real and imaginary parts of the impedance are equal. Above this frequency, the fluid is not escaping the interstice between the moving structure and the frame and this adds a spring load to the plate. For the expected dimensions of the loudspeaker which are a surface of approximately 100 mm^2 , and a thickness below 1 mm , the critical frequency is far above the audio range, and the effect observed is mainly resistive, thus mainly affecting the damping in the system.

2.2.8 Radiation

To approximate the sound pressure level generated by the moving plate, the loudspeaker is assumed to be flush mounted inside an infinite baffle, and the plate is assumed to be a rigid body. A schematic of a rigid rectangular plate is depicted in Figure 2.15. The irregular gray shape represents an infinite surface of coordinates $(x, y, 0)$, within which an infinitesimal surface $dx'dy'$ moves with a velocity $v(x', y', z')$ normal to the plane. The pressure at the point (x, y, z) , whose position to the origin is characterized by the difference between vector \mathbf{r} and the vector \mathbf{r}' is noted $p(x, y, z)$.

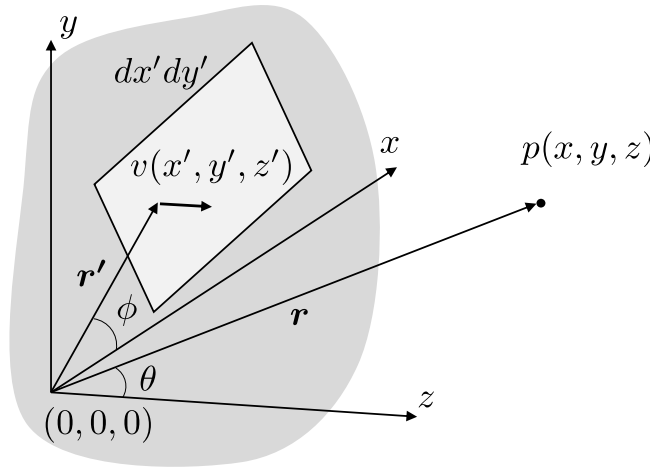


Figure 2.15: Geometric representation of the Rayleigh integral

The pressure at the point of coordinates (x, y, z) , generated by the plane surface S_d can be evaluated using Rayleigh integral such as

$$p(x, y, z) = \frac{-j\rho_0 c_0 k_0}{2\pi} \iint_{S_d} v(x', y', 0) \frac{e^{jk_0 |\mathbf{r} - \mathbf{r}'|}}{|\mathbf{r} - \mathbf{r}'|} dx' dy' \quad (2.25)$$

with c_0 the acoustic velocity at ambient temperature and k_0 the wavenumber. Considering the far field condition, such as $|\mathbf{r} - \mathbf{r}'| \gg \sqrt{S_d}$, using $k_0 c_0 = \omega$ and considering a rigid surface, the Rayleigh integral reduces to [106]

$$p(r) = -j\omega\rho_0 v S_d k_0 \frac{e^{jk_0 r}}{2\pi r} \quad (2.26)$$

with $r = |\mathbf{r} - \mathbf{r}'|$, the distance between the source and the evaluation point. This makes the acceleration $\alpha = j\omega v$ appears and confirms that the radiated acoustic pressure is proportional to the acceleration, as described in Section 1.2. This allows to compute the pressure field generated by the surface S_d . From the equivalent electrical circuit of the loudspeaker and by adding the directivity term, this leads to

$$p(r, \theta, \phi, \omega) = -j\omega\rho_0 S_d \frac{F_{in}}{R_{ms} + j\omega M_{ms} + \frac{1}{j\omega C_{ms}} + Z_r S_d^2} \frac{\sin \frac{\theta a}{2} \sin \frac{\phi b}{2} e^{jk_0 r}}{\theta \phi a b} \frac{1}{2\pi r} \quad (2.27)$$

The second term is the variation of the sound pressure level as a function of the angle for a rectangular plate [107]. For loudspeakers with dimensions in the millimeter range, the directivity only creates a significant effect for frequencies above the audio frequency range, as depicted in Figure 2.16.

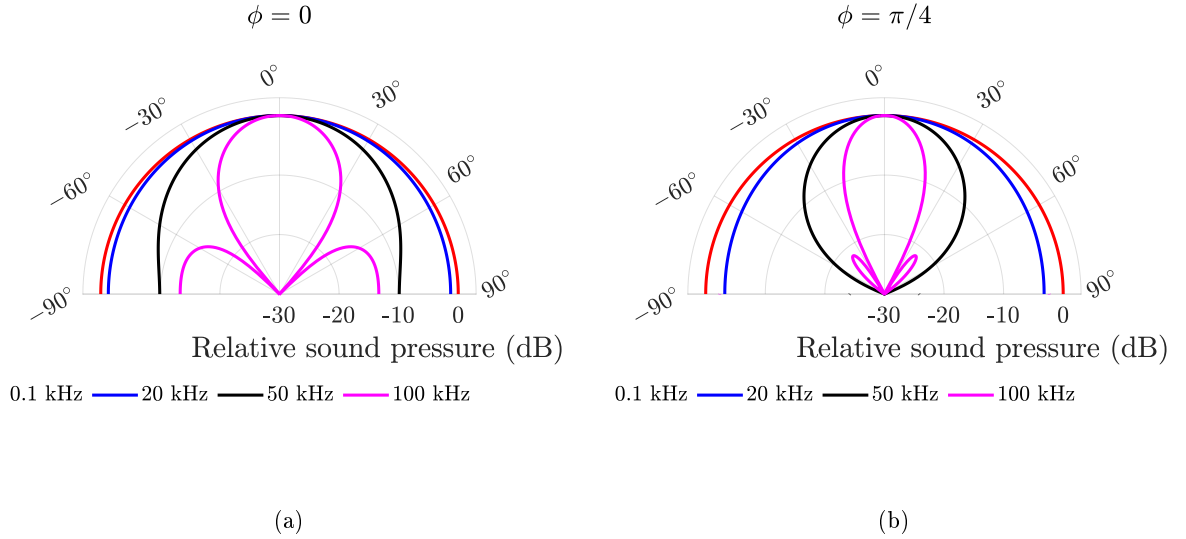


Figure 2.16: Pressure relative to the low frequency pressure as a function of the angle θ for $\phi = 0$ (a) and $\phi = \pi/4$ (b)

No rear coupling of the loudspeaker is considered, in order to compare the lumped element model with the finite element model and decreasing the computational cost of this latter. It is also demonstrated later that the squeeze film effect is not significantly affecting the radiated sound pressure generated by the loudspeaker. The normalized radiation impedance of a rectangular plate flush-mounted into an infinite baffle can be written [108]

$$\frac{Z_r}{Z_0} = \Theta + jX \quad (2.28)$$

with

$$\Theta = 1 - \frac{2}{\pi k_0^2 ab} \left(1 + \cos k_0 \sqrt{a^2 + b^2} + k_0 \sqrt{a^2 + b^2} \sin k_0 \sqrt{a^2 + b^2} - \cos k_0 a - \cos k_0 b \right) + \frac{2}{\pi} \left(\int_1^{\sqrt{1+(b/a)^2}} \sqrt{1 - \frac{1}{x^2}} \cdot \cos x k_0 a dx + \int_1^{\sqrt{1+(a/b)^2}} \sqrt{1 - \frac{1}{x^2}} \cdot \cos x k_0 b dx \right) \quad (2.29)$$

and

$$X = \frac{2}{\pi k_0^2 ab} \left(k_0(a + b) + \sin k_0 \sqrt{a^2 + b^2} - k_0 \sqrt{a^2 + b^2} \cos k_0 \sqrt{a^2 + b^2} - \sin k_0 a - \sin k_0 b \right) + \frac{2}{\pi} \left(\int_1^{\sqrt{1+(b/a)^2}} \sqrt{1 - \frac{1}{x^2}} \cdot \sin x k_0 a dx + \int_1^{\sqrt{1+(a/b)^2}} \sqrt{1 - \frac{1}{x^2}} \cdot \sin x k_0 b dx \right) \quad (2.30)$$

with a and b the length and width of the plate respectively and $Z_0 = c_0 \rho_0$ the characteristic impedance of air at ambient temperature.

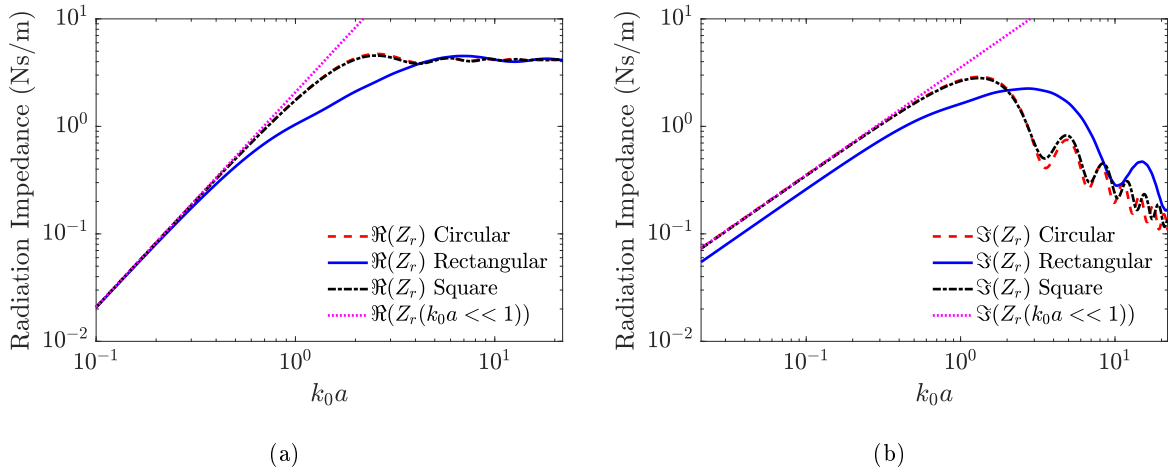


Figure 2.17: Real (a) and imaginary (b) part of the radiation impedance for a circular rigid plate, a square rigid plate and a rectangular rigid plate with an aspect ratio of 10 and of same surface S_d , flush-mounted in an infinite baffle

Figure 2.17 shows the similarity between the radiation impedance of a square plate and a circular plate of the same surface. A significant difference appears only for rectangles with a higher aspect ratio. The computational cost of the model can be reduced by using the radiation impedance of a circular plate with the same surface that writes

$$\frac{Z_r}{Z_0} = S_d \left(1 - \frac{J_1(2ka)}{ka} + j \frac{H_1(2ka)}{ka} \right) \quad (2.31)$$

with J_1 the Bessel function of the first order and of the first kind and H_1 the Hankel function of the first kind. The theoretical calculation can be found in [109]. To further reduce the computational cost of the model, a low frequency approximation can be made. If $k_0 a \ll 1$, the radiation impedance can be approximated by [110]

$$\frac{Z_r}{Z_0} = \frac{S_d}{2} k_0^2 a^2 + j \frac{8S_d}{3\pi} k_0 a. \quad (2.32)$$

The imaginary part and the real parts are presented in Figure 2.17 as well. They can be separated and simulated in the equivalent circuit as a resistor and an inductor, translating into an added damping and an added mass in the behavior of the loudspeaker. For microloudspeakers whose membrane dimension is 10 mm, this approximation is reasonable up to 5 kHz. For a microloudspeaker with average characteristics, the radiation impedance of the membrane is not significantly influencing the velocity, as depicted in Figure 2.18(a). The radiation impedance influences the velocity of the loudspeaker around the resonance only for surfaces of around 0.05 m^2 .

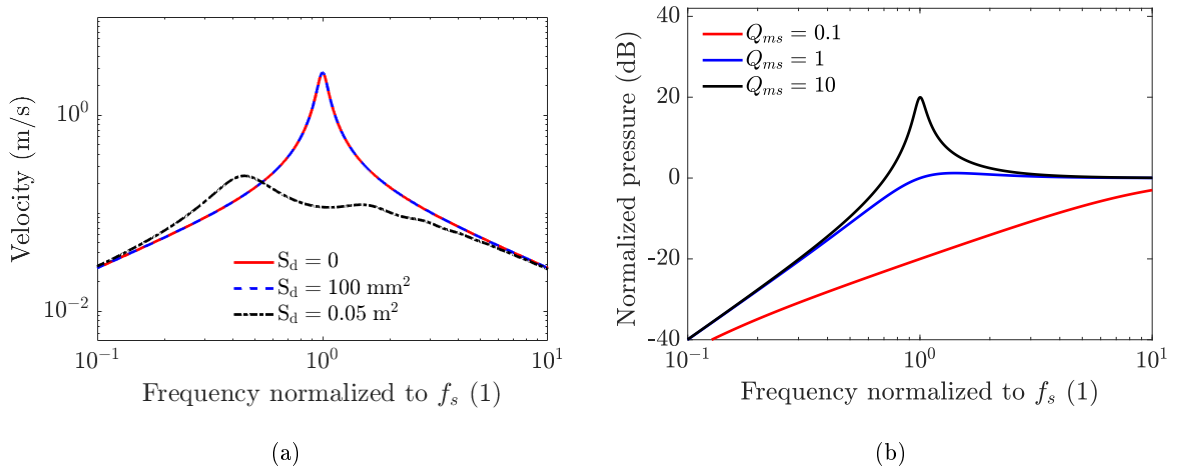


Figure 2.18: Influence of the radiation impedance calculated with Equation 2.31 on the velocity of a typical microloudspeaker such as the one reviewed in Section 1.4.1 (a) and frequency response of a loudspeaker calculated using Equation 2.27 for different quality factor Q (b)

Using Equation 2.27, the pressure generated by a loudspeaker whose parameters C_{ms} and M_{ms} are arbitrarily chosen and for which R_{ms} is calculated from the mechanical quality factor Q_{ms} such as

$$R_{ms} = \frac{1}{Q_{ms}} \sqrt{\frac{M_{ms}}{C_{ms}}} \quad (2.33)$$

with the quality factor value set to $Q_{ms} = 10$, which corresponds approximately to the value observed in the literature for millimetric MEMS loudspeakers, and the figure is normalized to the resonance frequency of the mechanical oscillator f_s that is defined as

$$f_s = \frac{1}{2\pi \sqrt{C_{ms} M_{ms}}}. \quad (2.34)$$

The loudspeaker mainly behaves as a second order high pass filter, because the electrical impedance and the radiation impedance do not influence the mechanical behavior of the system. Figure 2.18(b) depicts the frequency response, normalized in frequency and amplitude of a piezoelectric loudspeaker simulated with the equivalent circuit of Figure 2.5. It shows the influence of the mechanical quality factor on the

pressure response, and that the ideal damping should critically damp the oscillator, in order to have a flat frequency response. This frequency response is the starting point of the design, and gives the radiated sound pressure level in the bandwidth and the resonance frequency that needs to be optimized while keeping a small footprint, in order to place the design in the target of Figure 1.34.

2.2.9 In-Ear

For a loudspeaker radiating in a coupler, the radiation impedance Z_r of the circuit depicted in Figure 2.5 can be replaced by the equivalent circuit of the coupler presented in Figure 1.28. By using Equation 2.1 and Equation 2.2, the velocity of the moving plate of the membrane of the loudspeaker can be calculated and the pressure at the microphone of the coupler is estimated using the transfer impedance of the coupler derived in Equation 1.20. The pressure can be expressed as

$$p_{out} = S_d v Z_c T_f. \quad (2.35)$$

The frequency response of a loudspeaker radiating in a IEC ear-occluded coupler is calculated for three different loudspeakers and is depicted in Figure 2.19.

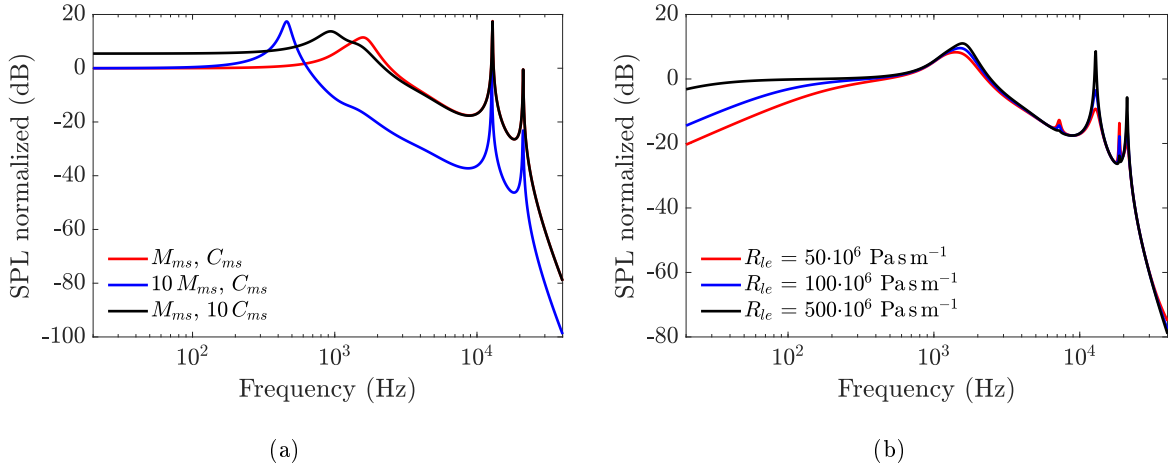


Figure 2.19: Pressure at the coupler for arbitrary values of C_{ms} and M_{ms} (a), and for different leak resistors R_{le} (b)

In Figure 2.19(a), the pressure inside the coupler is calculated for arbitrary pairs of parameters C_{ms} and M_{ms} . Both resonances of the coupler, at approximately 11.2 kHz and 21 kHz are not affected by the parameters of the loudspeaker. As described in Section 1.2, the overall shape of the pressure is similar to a low pass filter, whose cut-off frequency is determined by the resonance frequency of the loudspeaker in the coupler, that can be simplified by the resonance frequency of the loudspeaker, stiffened by the main cavity of the coupler, represented by C_1 . In reality, it is very difficult to obtain a perfect seal between the loudspeaker and the coupler, and the acoustic leak is generally represented as a resistor R_{le} , in parallel with the coupler. Modifying the transfer function and the impedance of the coupler leads to

$$Z_{cl} = \frac{Z_c R_{le}}{Z_c + R_{le}}. \quad (2.36)$$

The modification of Z_c also leads to a modification of the transfer function T_f as well. The frequency response of a loudspeaker inside the coupler is depicted in Figure 2.19(b). Due to the leak, the frequency

response is not flat in the lower frequency range. For lower values of acoustic resistance, the quality factor of the resonances of the coupler is affected. A slight shift of the resonance frequency of the loudspeaker inside the couple, around 1 kHz is also observed. A lower value of R_{le} also creates two additional resonances at 7.2 kHz and 18.7 kHz.

2.2.10 Back Cavity

Although most loudspeaker performance are measured on an infinite baffle setup, it is interesting to see the effect of a sealed back cavity on the frequency response, which is more representative of the conditions of use of a loudspeaker. Figure 2.20(a) represents a loudspeaker mounted in an enclosure.

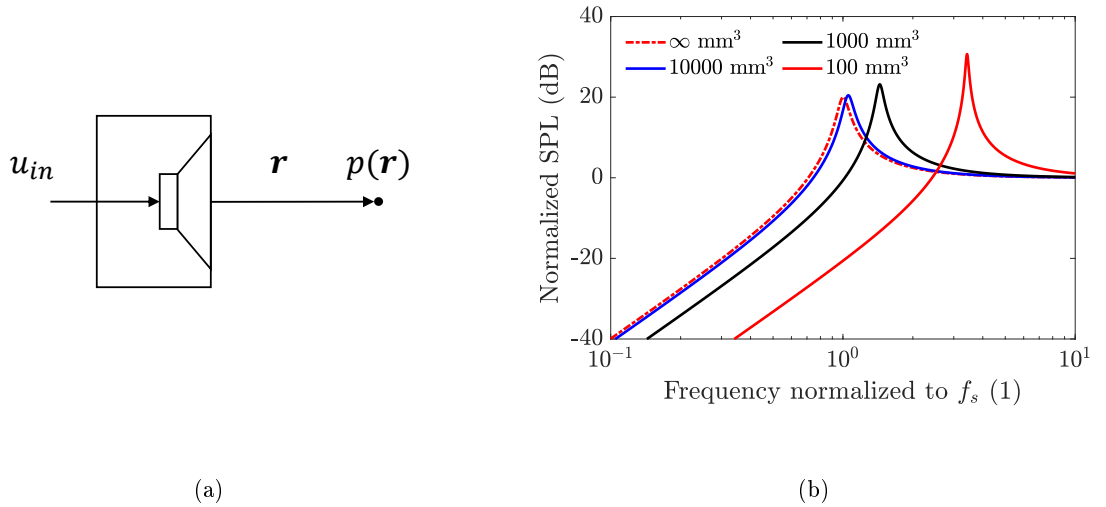


Figure 2.20: Schematic of a loudspeaker with a back cavity (a) and pressure radiated by a loudspeaker with different sizes of back cavities (b)

Neglecting the diffraction effect created by the finite front baffle, the back cavity mainly stiffens the loudspeaker, and the effect can be approximated by adding an equivalent compliance in the equivalent circuit of Figure 2.5. The equivalent compliance created by a perfectly sealed volume of air C_b , harmonically compressed by a piston of surface S_d can be written

$$C_b = \frac{V_b}{\rho c_0^2 S_d^2} \quad (2.37)$$

and the total equivalent compliance of the loudspeaker with the back cavity can be written

$$C_{tot} = \frac{C_b C_{ms}}{C_b + C_{ms} S_d^2} \quad (2.38)$$

The resulting radiated sound pressure is presented in Figure 2.20(b), with different back cavity volumes. Smaller volumes shift the resonance frequency to higher frequencies, and thus reduce the bandwidth. With a stiffer loudspeaker, the back cavity has less influence on the radiated sound pressure level.

2.2.11 Electrical behavior

From the complete equivalent circuit, the electrical impedance of the loudspeaker Z_e , which is the input voltage over the input current can be written

$$Z_e = \frac{u_{in}}{i_{in}} \quad (2.39)$$

It contains the acoustical impedance converted through the mechanical domain and the mechanical impedance converted through the electrical domain.

$$Z_e = R_g + \frac{Z_m}{j\omega C_p Z_m + \gamma^2} \quad (2.40)$$

The dissipated electrical power P_e can be written as the ratio of the input voltage squared over the real part of the electrical impedance such as

$$P_e = \frac{u_{in}^2}{\Re(Z_e)} \quad (2.41)$$

and Q_e , the reactive electrical power writes

$$Q_e = \frac{u_{in}^2}{\Im(Z_e)}. \quad (2.42)$$

The real and imaginary parts of the impedance Z_e are depicted in Figure 2.21(a). In low frequencies, below the mechanical resonance of the system, the electrical impedance is dominated by the imaginary capacitive impedance of the piezoelectric layer. Around the resonance, often referred to as the viscous damping region, the dissipation due to the mechanical resistor R_{ms} is more significant. Above the resonance, the real part of the impedance decreases due to the behavior of the mechanical circuit. Considering a constant voltage over the whole frequency range, the real and active power can be computed and are depicted in Figure 2.21(b). On the real power, the decrease of the real impedance is translated by a higher electrical power dissipation above the resonance frequency.

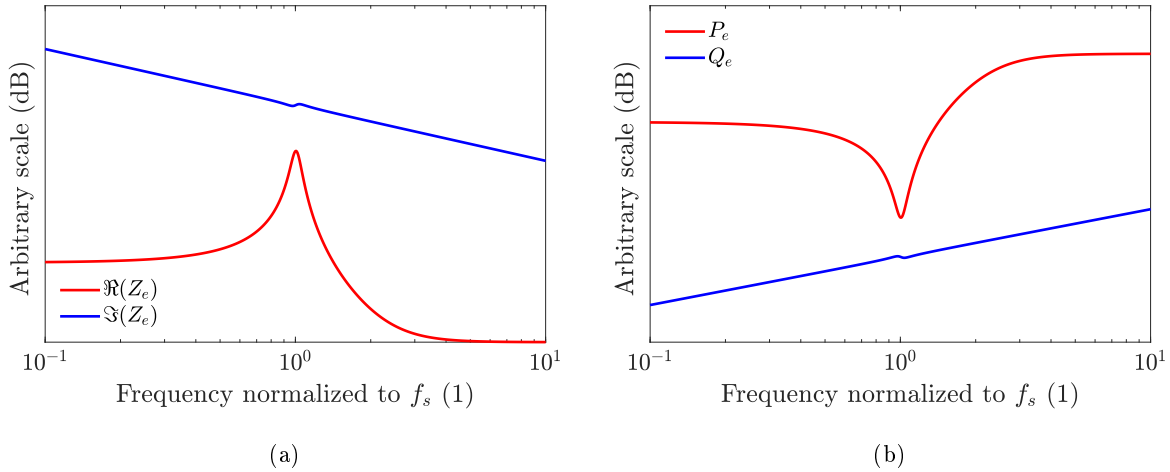


Figure 2.21: Real and imaginary parts of the impedance (a) and active and reactive power (b) of the piezoelectric loudspeaker on an arbitrary scale, and as a function of a normalized frequency

2.2.12 Sensitivity and Efficiency

From the radiated sound pressure level and the input electrical power, the sensitivity of the loudspeaker can be derived. The sensitivity for a macroscopic loudspeaker is usually written as the radiated sound

pressure level, in dB_{SPL} at 1 m for 1 W of input power. For this loudspeaker, the sensitivity is expressed as the radiated sound pressure level in dB_{SPL} , at a distance of 10 cm for an input power of 1 mW at 2 kHz. The sensitivity κ is a frequency dependent parameter and can be calculated for an arbitrary loudspeaker radiating a pressure $p(\mathbf{r})$ such as

$$\kappa = \frac{20 \log_{10} \left(\frac{p(\mathbf{r})}{p_0} \right) \Re(Z_e)}{u_{RMS}^2}. \quad (2.43)$$

For an input signal u_{in} with an offset to circumvent the ferroelectric effect, the root mean square value writes

$$u_{in,RMS} = \sqrt{\frac{1}{T} \int_0^T (a_0 + a_1 \sin(\omega t))^2 dt}, \quad (2.44)$$

with a_0 the amplitude of the DC offset and a_1 the amplitude of the input sinusoidal voltage. This leads to

$$u_{in,RMS} = \sqrt{a_0^2 + \frac{a_1^2}{2}}. \quad (2.45)$$

For a loudspeaker whose frequency response is similar to the one depicted in Figure 2.18(b), with a quality factor $Q = 10$ (as it is detailed in Section 2.2.8), the sensitivity of the loudspeaker is calculated in the audio frequency range and depicted in Figure 2.22(a). For very low frequencies and as the radiated sound pressure is proportional to the acceleration of the mobile assembly of the loudspeaker, the sensitivity is very low. The sensitivity of the loudspeaker is maximum at the resonance for a quality factor of $Q = 10$ due to the maximum acceleration at this frequency. For higher frequencies, the sensitivity drops to a very low level due to the decrease of the impedance Z_e , leading to a higher current i_{in} .

The efficiency is the ratio between the radiated acoustic power and the input electrical power. The acoustic power P_a can be expressed as the surface integral of the acoustic intensity such as

$$P_a = \iint_S I_a dS \quad (2.46)$$

Using both the far field and the low frequency assumptions, the source is assumed to radiate hemispherical waves and the equation reduces to the surface of the hemisphere at the point of estimation and the acoustical power writes

$$P_a = \frac{2\pi r^2 p(r)^2}{\rho_0 c_0} \quad (2.47)$$

and the electroacoustical efficiency η is then

$$\eta = \frac{2\pi r^2 p(r)^2 \Re(Z_e)}{\rho_0 c_0 u_{in}^2}. \quad (2.48)$$

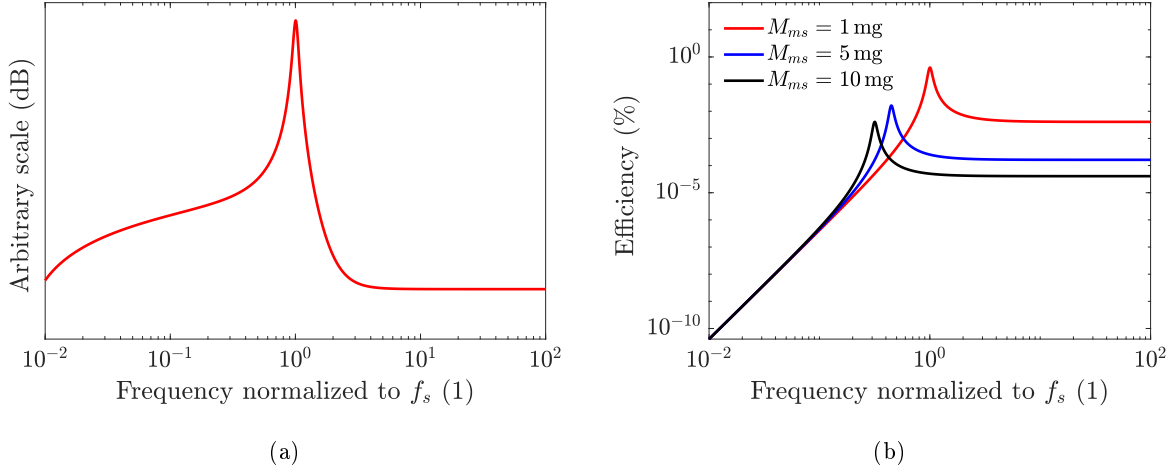


Figure 2.22: Sensitivity (a) and electromechanical efficiency (b) of a piezoelectric bending actuators loudspeaker

The electroacoustic efficiency of a piezoelectric bending loudspeaker is depicted in Figure 2.22(b) for different values of moving mass M_{ms} . The electroacoustic efficiency is expected to be lower than 1% in the bandwidth. The shape is similar to the one of the acceleration of the loudspeaker. A decrease of the moving mass is advantageous to increase the efficiency of the loudspeaker.

2.3 Optimization of the Performance

2.3.1 Dimensions

In this section, the main parameters of the loudspeaker, determining the apparent compliance C_{ms} , the moving mass M_{ms} , the input force F_{in} , the height of the coupling block h_0 and the width of the interstice w_s of the loudspeaker are determined by varying the thickness of the elastic part of the actuators and the surface of the device, in order to reach the desired performance. Equation 2.27 shows that the radiated pressure is proportional to the radiating surface S_d and the input force F_{in} . For a bending piezoelectric cantilever and according to Equations 2.8 and 2.9, the input force F_{in} is proportional to geometric dimensions and linked to the apparent stiffness C_{ms} of the system. To find the best compromise of radiated sound pressure level at the resonance frequency f_s , multiple frequency responses are calculated with random pairs of parameters S_d and t_m . The directivity term is set to 1, and Equation 2.27 becomes

$$p(r, \omega_s) = -j\rho_0 c_0 S_d \frac{F_{in}}{R_{ms} + j\omega_s M_{ms} + \frac{1}{j\omega_s C_{ms}} + Z_r(\omega_s) S_d^2} \frac{e^{j\frac{\omega_s}{c_0} r}}{2\pi r}. \quad (2.49)$$

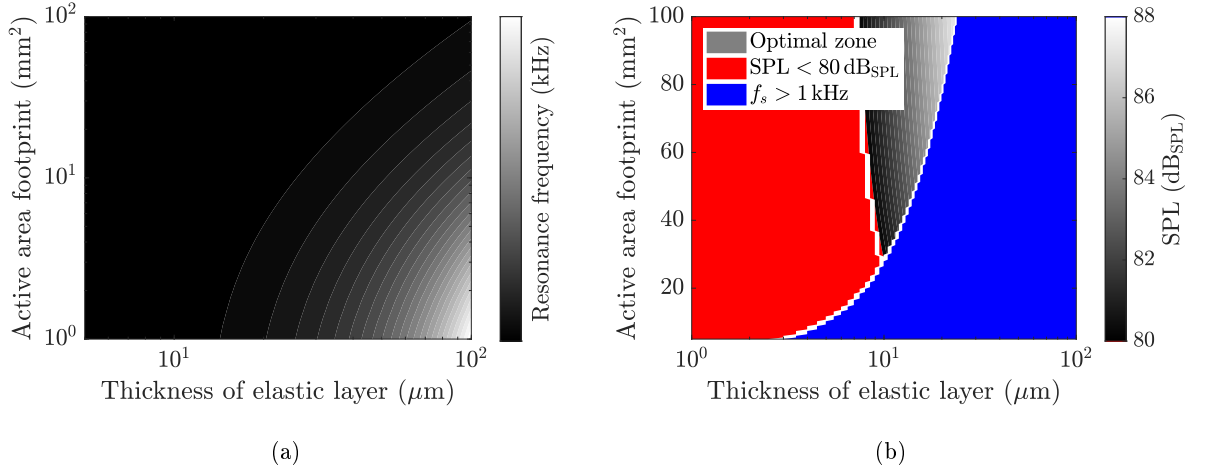


Figure 2.23: Resonance frequency of the loudspeaker as a function of the thickness of the elastic layer t_m and the active area footprint of the device S_d (a) and sound pressure level generated by the loudspeaker as a function of the same parameters (b). The sound pressure level is depicted only for devices whose resonance frequency f_s is equal or lower than 1 kHz and a sound pressure level equal or higher than 80 dB_{SPL} .

Figure 2.23(a) shows that the resonance frequency f_s increases with an increase of the thickness t_m and with a decrease of the active area S_d . Figure 2.23(b) shows the ideal parameters to place the loudspeaker into the target performance of Figure 1.34. It corresponds to a thickness t_m from 8 μm to 22 μm , and to a surface S_d of at least 25 mm^2 and leads to pressures from 80 dB_{SPL} to 88 dB_{SPL} .

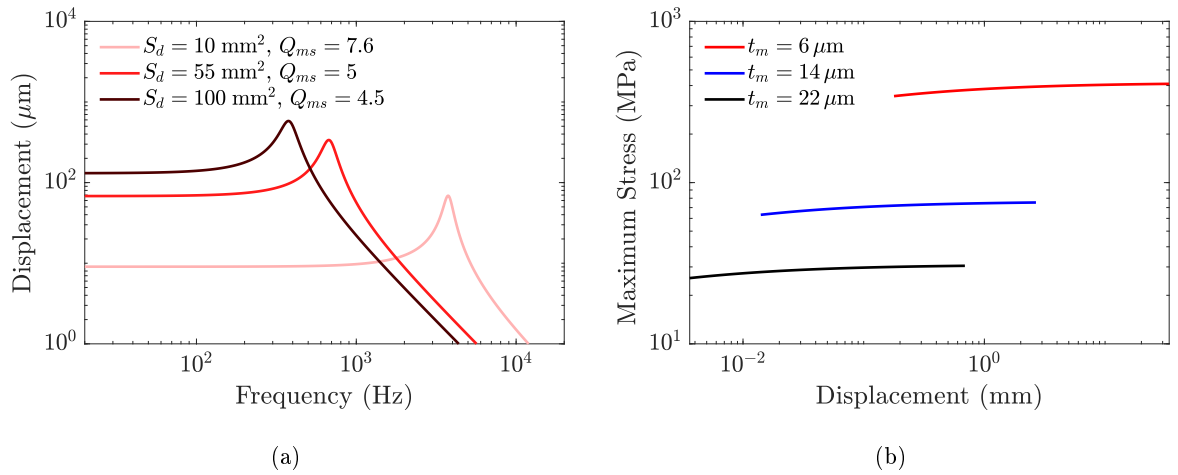


Figure 2.24: Displacement of the moving plate for different loudspeaker dimensions S_d (a) and maximum stress in a clamped-guided beam as a function of the displacement of the guided end for different beam thicknesses t_m (b)

Although an increase of the active area would lead to higher pressures, the surface of the main design is set to $S_d = 36 \text{ mm}^2$ due to concentration of stress in the mechanical structure. The concentration of stress is linked to the maximum displacement of the structure, and the maximum displacement of the structure is linked to the input force F_{in} , the apparent compliance C_{ms} , the mechanical quality factor

Q_{ms} and the resonance frequency f_s . The displacement as a function of frequency is depicted in Figure 2.24(a) for three different dimensions of the loudspeaker. It shows that for resonance frequencies below 1 kHz, and with a quality factor $Q_{ms} = 2$, the displacement can approach 1 mm. The maximum stress in a clamped-guided beam σ_{max} can be expressed as a function of the displacement of the guided end of the beam using

$$\sigma_{max} = \frac{3E_m t_m \delta_0}{L^2} \quad (2.50)$$

by considering a static behavior, by neglecting the effect of the piezoelectric layer and by considering that the input force F_{in} is constant. The maximum stress as a function of the displacement is depicted in Figure 2.24(b) for different thicknesses t_m . It shows that the maximum stress can reach 500 MPa for smaller thicknesses t_m and for large displacements. The maximum stress in the beam needs to be k times smaller than the known maximum tensile stress of monocrystalline silicon, with k a safety factor set to 2.5. This maximum tensile stress is known to vary from 1 GPa to 7 GPa depending on the direction of the crystalline structure of silicon [111]. But due to small fabrication defects, this limit could be way lower [112]. A limit of 400 MPa is chosen as this model is based on several assumptions which would lead to a larger real maximum stress. The maximum achievable displacement is evaluated more precisely using finite element models in Section 3.2.

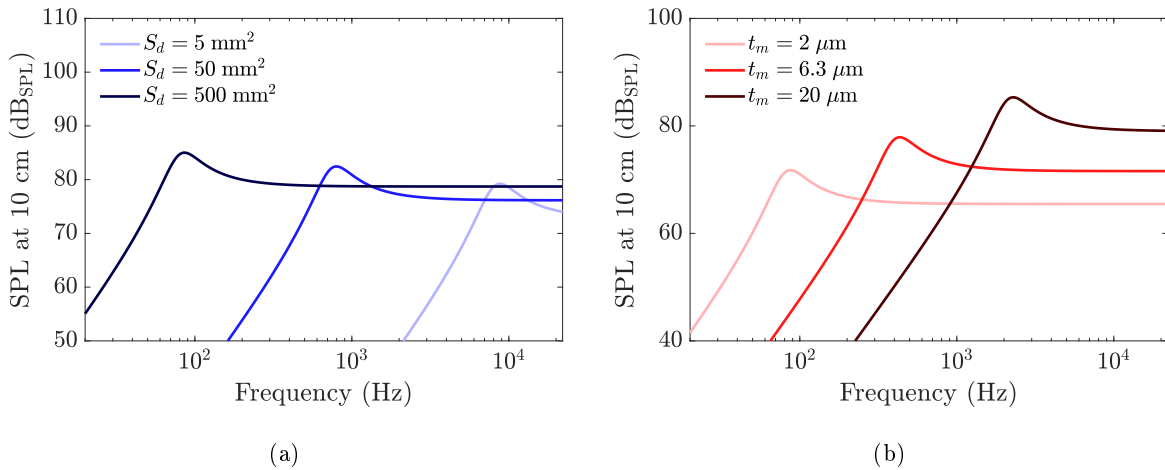


Figure 2.25: Frequency response of the loudspeaker for three different radiating surfaces S_d with a fixed actuator thickness $t_m = 12 \mu\text{m}$ (a) and for three different actuator thicknesses with a fixed surface $S_d = 36 \text{ mm}^2$ (b)

Still using Equation 2.49, Figure 2.25(a) shows the evolution of the frequency response with a change of the radiating area. As the length and the width of actuators is linked through the radiating surface area due to the geometry of the loudspeaker, multiple effects are occurring simultaneously. The increase of the surface S_d increases the radiated sound pressure proportionally, and affects the resonance frequency only slightly by changing the radiating mass. By increasing the length of the actuators, the resonance frequency decreases, as well as the generated force. Figure 2.25(b) shows the evolution of the frequency response with an increase of the thickness of the elastic layer of the loudspeaker. As the thickness of the passive layers of the actuators directly affects the apparent stiffness of the system, it changes the resonance frequency. Since the input force F_{in} is inversely proportional to the thickness of the actuators, the level is affected as well. For the main design, S_d is chosen to be 36 mm^2 and t_m is chosen to be $12 \mu\text{m}$.

Other dimensions are chosen for different designs, in order to either improve the performance with a higher concentration of stress (riskier design) or in order to have safer designs with a higher safety factor k . Dimensions of the other designs are recalled in Table 3.2 and their frequency responses are depicted in Figure 3.36(a) in Section 3.4.3.

2.3.2 Height of the Coupling Blocks

The squeeze film damping of Equation 2.23 can be integrated into the equivalent electrical circuit of Figure 2.5 as the squeeze film damping behind the moving plate is acting as a radiation impedance on the plate. The impedance Z_m can be calculated using

$$Z_m = R_{ms} + j\omega M_{ms} + \frac{1}{j\omega C_{ms}} + Z_{sf} + Z_r S_d^2. \quad (2.51)$$

From the impedance, the sound pressure level is calculated for different heights h_0 and depicted in Figure 2.26(a). The height h_0 changes the quality factor at the resonance. The height h_0 should also be large enough in order to allow a large displacement of the structure, as it can be deduced from Figure 2.3.

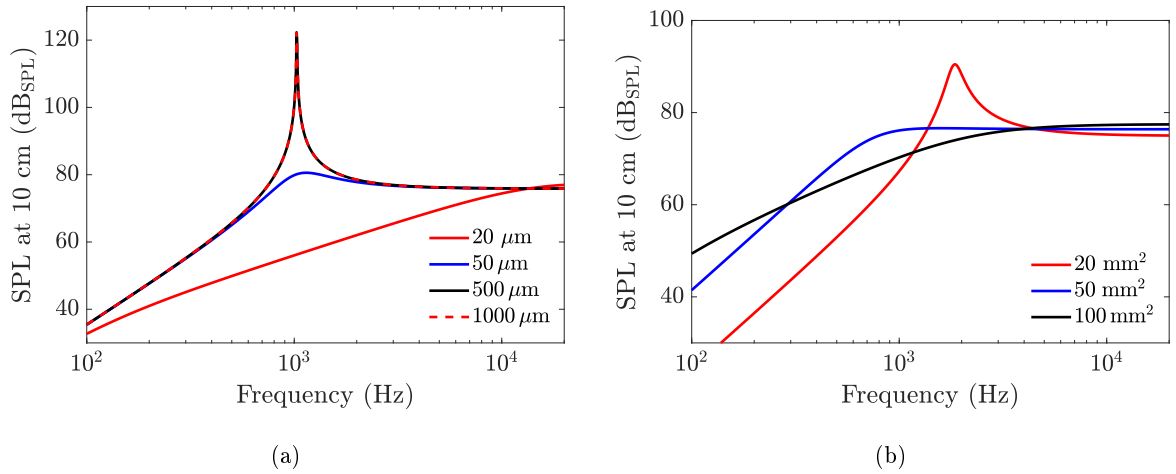


Figure 2.26: Pressure response for different heights h_0 with $R_{ms} = 0$ and $S_d = 36 \text{ mm}^2$ (a) and pressure response for different radiating surfaces S_d (b)

The height h_0 is set to 500 μm as there is no significant effect on the quality factor at the resonance of the loudspeaker for larger dimensions. By changing the surface S_d , the behavior of the loudspeaker changes similarly to what is observed in Figure 2.25, with a significant change of the quality factor due to the squeeze film effect. The height h_0 is also involved in the optimization of the linearization spring described in Section 3.3.

2.3.3 Width of the Air Interstice

The thin air interstice between the moving plate and the frame is mainly used to avoid the acoustic short-cut between the front and back acoustic waves. As discussed in Section 2.2.6, the interstice needs to be smaller than 15 μm wide in order to avoid an acoustic short-cut in the whole audio range. The interstice is also responsible for the damping and frequency responses of a loudspeaker with $S_d = 36 \text{ mm}^2$ and $t_m = 12 \mu\text{m}$ for three different interstice widths are depicted in Figure 2.27(a). It shows that a significant damping effect occurs only for an interstice smaller than 1 μm and that a critical damping is reached for

an unrealistic interstice of 1 nm. The interstice dimension is also limited by the manufacturing process, as described in Section 4.2. As the viscous damping created by the thin air interstice is proportional to the contact surface created by the thickness of the plate and the perimeter, the change of quality factor can also be observed with an increase of the thickness of the plate. As the weight of the plate also changes the moving mass M_{ms} , the resonance frequency is affected as well. For an interstice of 9 μm , no significant change on the quality factor is observed with a change of the thickness of the plate t_{pl} , as it is depicted in Figure 2.27(b).

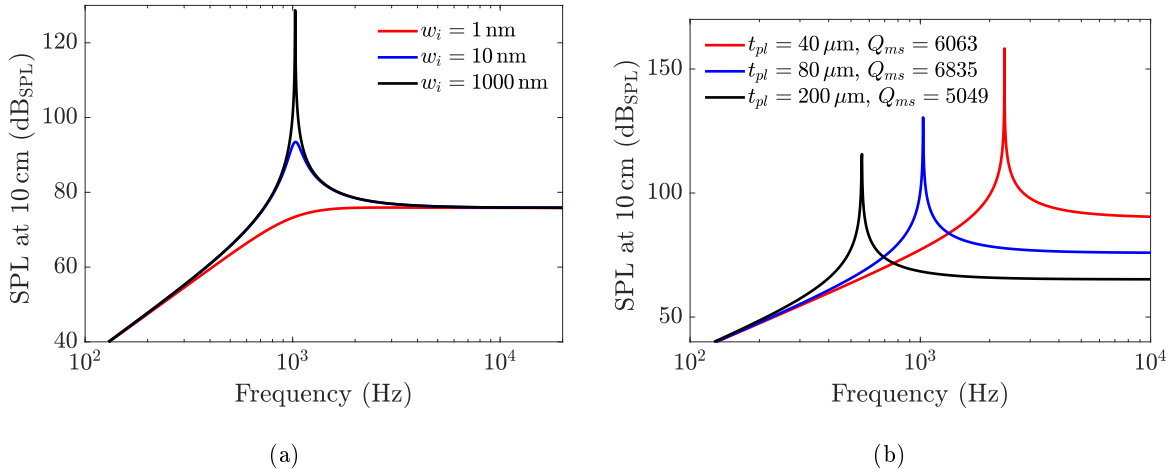


Figure 2.27: Frequency response of the loudspeaker for different interstice widths w_i (a) and for different plate thicknesses t_{pl} , considering the change of moving mass M_{ms} (b)

The air interstice dimensions are more precisely defined in Section 3.2 using finite element model. With the set of parameters C_{ms} , M_{ms} , F_{in} , h_0 and w_i determined, the frequency response matches the required performance determined in Section 1.6, and recalled in Figure 2.1, and the geometry can be more precisely determined using the finite element model described in Section 3.2 as well as the state space model described in Section 3.4. Before designing more precisely the loudspeaker using these models, the amplifier required to power the loudspeaker can be designed based on the previously determined linear parameters.

2.4 Dedicated Driving Board

In this section and based on the parameters determined in Section 2.3, a voltage amplifier able to provide the required voltage of $15\text{V}_{\text{DC}} + 15\text{V}_{\text{AC}}$ to power the loudspeaker is designed. The design is device-based, and starts from the analysis of the expected electrical impedance of the loudspeaker. The amplifier is mainly composed of a buffer, a voltage gain stage and a current gain stage.

2.4.1 Amplifier

The amplifier needs to convert a line level audio signal into a 30 V peak to peak signal and should be able to fulfill the power requirements of the loudspeaker. The impedance of the loudspeaker described in Figure 2.21(a) can be calculated with the previously determined parameters and is depicted in Figure 2.28.

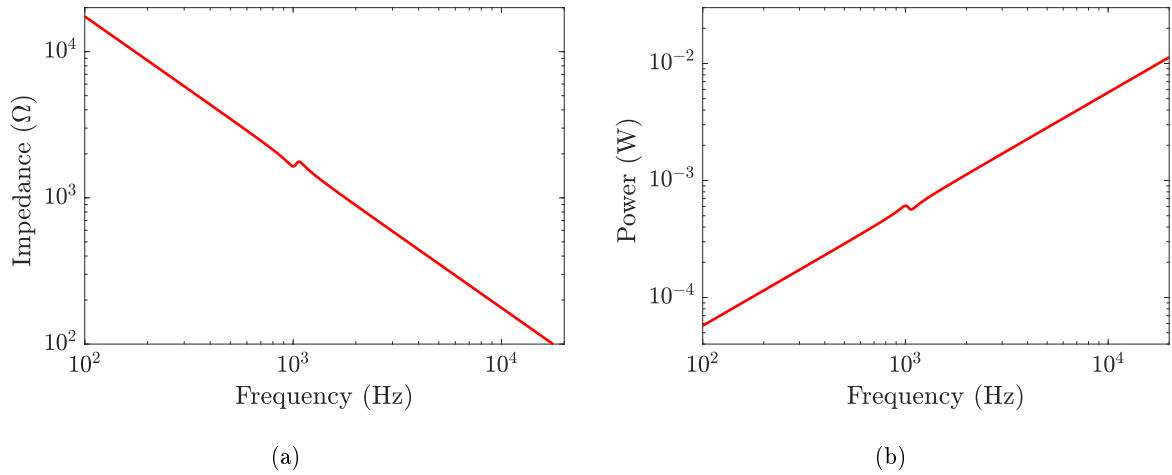


Figure 2.28: Impedance of the loudspeaker (a) and power drawn by the loudspeaker for a 30 V input signal (b)

As it can be seen in Figure 2.28, the impedance of the loudspeaker is mainly capacitive, except for the mechanical resonance of the loudspeaker at approximately 1 kHz. In the low frequencies, the impedance is as high as $10\text{ k}\Omega$ and decreases down to $100\ \Omega$ in the high frequency range. The series and parallel resistors are respectively very small and very big and are not affecting the impedance of the loudspeaker in a significant way for realistic values. The quality factor of the mechanical system affects the electrical impedance of the loudspeaker, but with realistic values of the viscous damping in the loudspeaker, the resonance doesn't create an impedance higher than the low frequency one or lower than the high frequency one around the resonance. Using the impedance and a maximum voltage of 30 V across the piezoelectric actuators, the power dissipated in the loudspeaker can be displayed as a function of frequency, as it is shown in Figure 2.28(b). The amplifier needs to provide 30 V from 20 Hz to 20 kHz with minimal distortion, and needs to have an offset, at the middle of the usable voltage range, in order to have an asymmetric signal. The total harmonic distortion needs to be way below 1 %. The efficiency of the amplifier is not a concern. Using these specifications, the selected topology is a push-pull amplifier, using bipolar transistors and an operational amplifier with a negative feedback to provide the needed current at the output stage. The voltage gain is provided by a simple non-inverting operational amplifier circuit. The variable offset is provided by a simple voltage divider coupled with a capacitor. A push-pull stage is a widely used pair of complementary transistors, that are alternatively turned on and off around a rest point. Also known as a class B amplifier, this topology suffer from crossover distortion, below the needed base to emitter voltage threshold. To circumvent this effect, an operational amplifier with a negative feedback is used to provide the voltage below this threshold. The resulting circuit is presented in Figure 2.29.

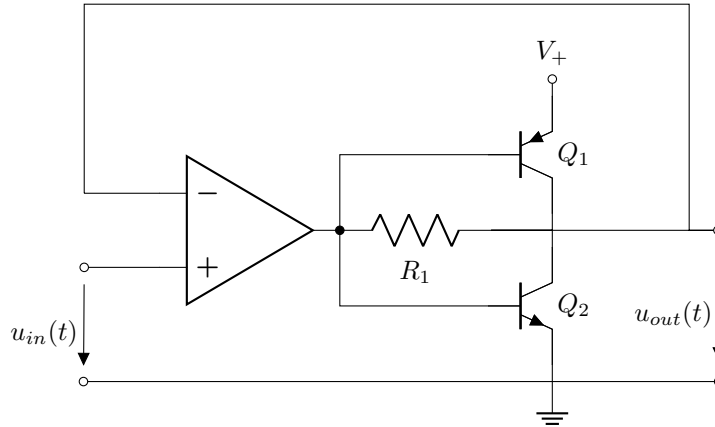


Figure 2.29: Current gain output stage

The amplifier needs to be DC coupled in order to have an offset at the output. The negative feedback ensures that the output voltage $u_{out}(t)$ is equal to the input voltage $u_{in}(t)$, and cancel the crossover distortion for voltage below the diode threshold of the base to emitter junction. The operational amplifier provides the output current for low voltages, when both transistors are off, in the subdiode behavior, though resistor R_1 . Transistors Q_1 and Q_2 are alternatively turned on and off, allowing an output current to flow in the load, for respectively the positive half cycle of the signal and the negative half cycle, around the offset. The input signal is acquired from a sound card, and the amplitude is around 1 V. To obtain the required voltage at the output, before the current gain stage, a simple non inverting operational amplifier circuit is used as a voltage gain, as it is presented in Figure 2.30.

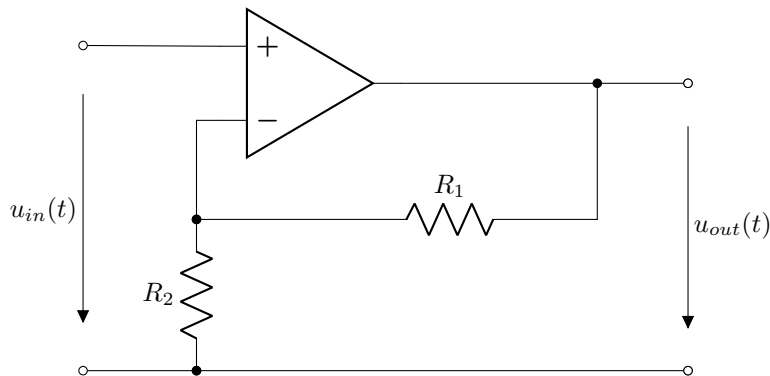


Figure 2.30: Non Inverting Operational Amplifier

To make the gain adjustable, resistor R_1 is replaced by a potentiometer in the implemented design. The selected operational amplifier needs to be able to generate output voltages greater than 30 V. The output voltage can be expressed as

$$u_{out}(t) = \left(1 + \frac{R_1}{R_2}\right) u_{in}(t). \quad (2.52)$$

In order to add an offset to this voltage amplifier, a simple voltage divider is used. To avoid DC voltage to shortcut the output of the source, a coupling capacitor is used in series. The schematic is presented in Figure 2.31.

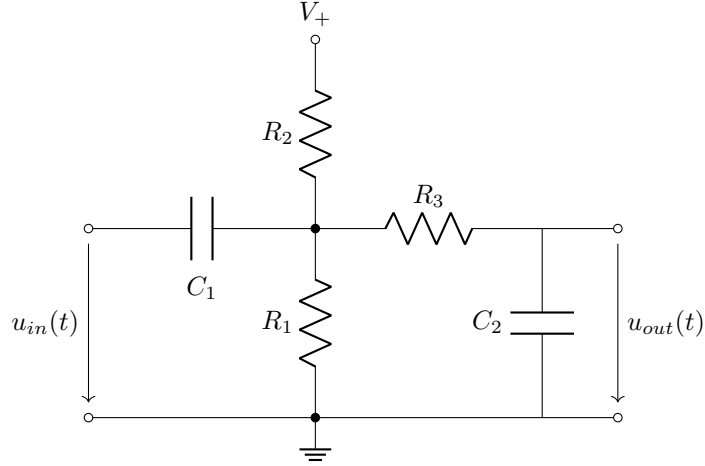


Figure 2.31: Offset adder and low pass filter

The series capacitor with the resistor creates a high pass filter, whose resonance frequency needs to be below the audio frequency range. The resistors R_2 and R_1 need to be large enough to minimize the DC current from V_+ to ground. The ratio of the resistors needs to fulfill the voltage divider criteria to add an offset equal to half of the maximum voltage of the output. As expected, the circuit shows the required high pass behavior, to avoid DC voltages. The other term of Equation 2.53 is the offset. To avoid noise to be amplified, a low pass filter, composed of C_2 and R_3 is used in series with the offset adder. Here the output voltage is composed of the contribution of V_+ , in Equation 2.53 and of u_{in} , in Equation 2.55. In the frequency domain, the contribution of V_+ to the output can be written as

$$u_{outV_+} = \frac{\frac{1}{j\omega C_2}}{\frac{1}{j\omega C_2} + R_3} \frac{Z_{21}}{Z_{21} + R_2} V_+ \quad (2.53)$$

with

$$Z_{21} = \frac{1}{j\omega C_1 + \frac{1}{R_1} + \frac{R_3 j\omega C_2}{R_3 j\omega C_2 + 1}}. \quad (2.54)$$

The circuit is non linear, with a linear part proportional to $u_{in}(t)$ that can be displayed as a function of frequency, as it is presented in Figure 2.32(a).

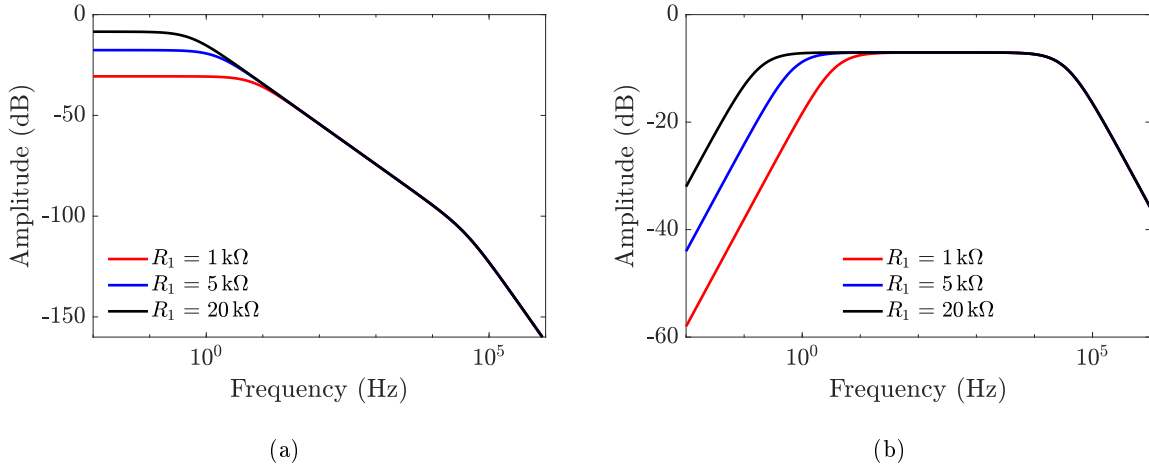


Figure 2.32: Transfer function of the circuit depicted in figure 2.31 from V_+ to u_{out} (a) and from u_{in} to u_{out} (b)

As it can be seen in Figure 2.32(a), only the DC component of the power supply goes into the signal, and the amplitude of this offset is set by changing the value of R_1 . The high frequencies are strongly attenuated, to avoid noise from the power supply to pollute the output signal. The contribution from input signal u_{in} to output signal can be written

$$u_{out u_{in}} = \frac{Z_{31}}{Z_{31} + \frac{1}{j\omega C_1}} \frac{\frac{1}{j\omega C_2}}{R_3 + \frac{1}{j\omega C_2}} u_{in}(t) \quad (2.55)$$

where Z_3 is written

$$Z_{31} = \frac{1}{\frac{1}{R_1} + \frac{1}{R_2} + \frac{R_3 j\omega C_2}{R_3 j\omega C_2 + 1}}. \quad (2.56)$$

Displayed as a function of frequency, the transfer function from u_{in} to u_{out} is shown in Figure 2.32(b). The setting of the resistor for the offset changes the cut-off frequency of the high pass filter, as it can be seen in Figure 2.32(b), but the cut-off frequency is outside of the audio range in the usable range of values of resistors.

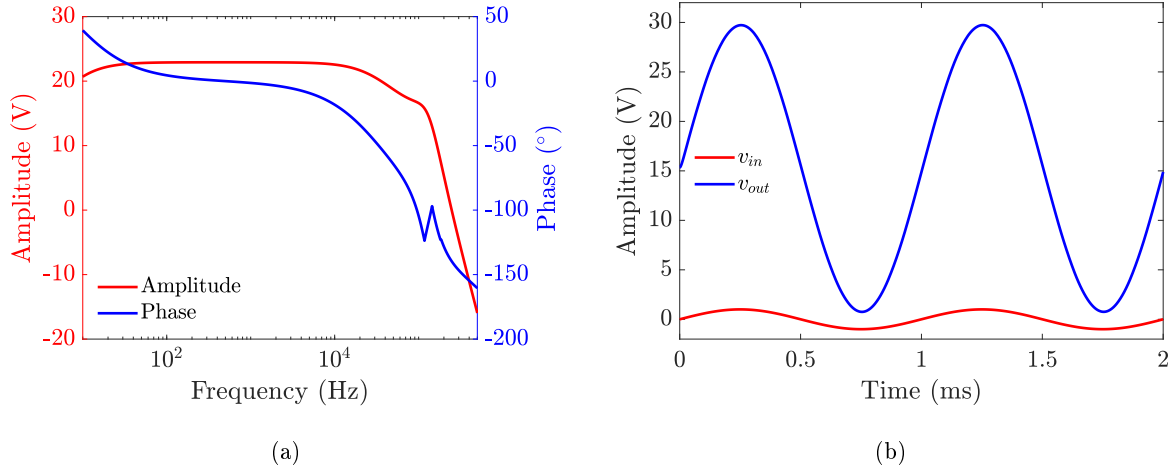


Figure 2.33: Frequency response of the complete circuit simulated using LTspice (a) and input and output time domain signal at 1 kHz of the amplifier at maximum gain (b)

The previously described circuit is connected in series with the amplifier and the complete circuit is simulated using LTspice. A zener diode is used at the output to ensure the output voltage does not exceed 30 V, in order to protect the piezoelectric material of the loudspeaker. A series resistor of small value is used to limit the output current. The frequency response of the obtained circuit is presented in Figure 2.33(a). The amplifier shows the desired bandpass filter characteristic, with the needed gain of about 23 dB. Using LTspice, the time domain signal can be displayed with an input frequency of 1 kHz, as it is presented in Figure 2.33(b).

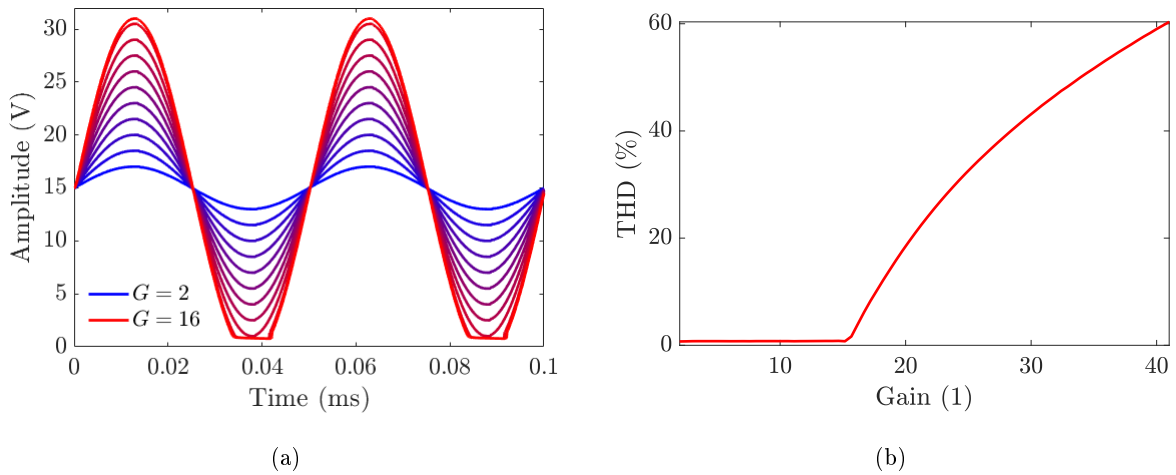


Figure 2.34: Time signal at the output of the amplifier for different amplifier gain simulated with LTspice (a) and THD of the amplifier as a function of gain (b)

The output signal behaves as expected, with the required offset. At the maximum gain of the voltage amplifier, the sine oscillates between nearly 0 V and 30 V. Further analysis can be carried out, such as the total harmonic distortion estimation, as a function of the gain of the amplifier. As it can be seen in Figure 2.34(b), the total harmonic distortion is below 1% for a gain between 1 and 15. Above this value, the output sine starts to clip at the rail voltage of the amplifier, as it is depicted in Figure 2.34(a), and

the total harmonic distortion rises accordingly. After ensuring the correct frequency response and the low distortion of the amplifier the power dissipated by the output transistors is computed and presented in Figure 2.35(a).

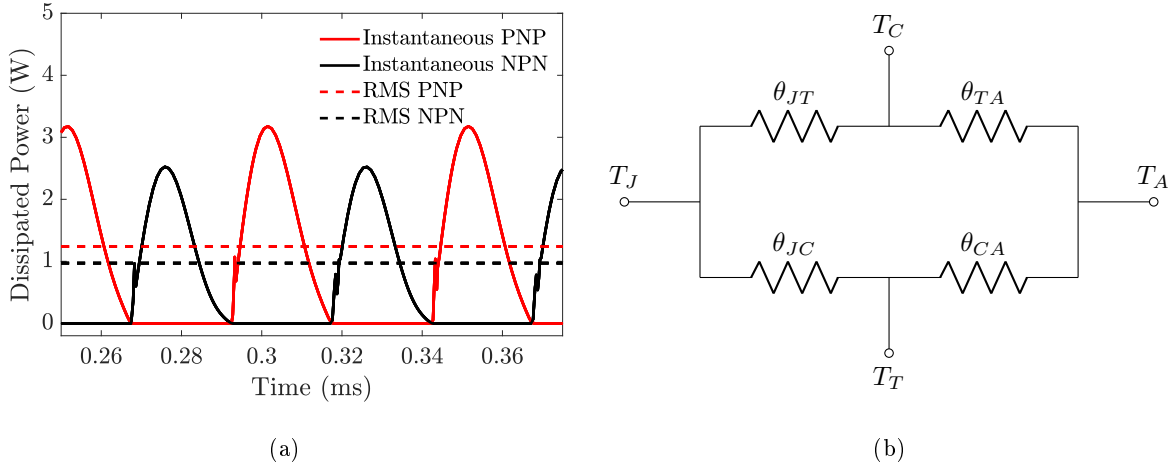


Figure 2.35: Instantaneous and RMS power dissipated in the NPN and the PNP transistors (a) and equivalent thermal circuit of the transistor junction to ambient air (b)

The amplitude of the power is different for the PNP and the NPN transistors due to the slight shift of the offset compared to the dynamic of the signal, and due to the differences of resistance in the transistors. The maximum value is reached at 20 kHz, when the loudspeaker load is minimum. The value of the dissipated power in the transistors is essential to design the dissipators, in order to keep the PN junction of transistors below the maximum temperature of 150 °C. The thermal resistances and the temperatures of the different elements are usually represented with an equivalent electrical circuit, as presented in Figure 2.35(b). As it can be deduced from the equivalent circuit, the thermal power, coming from the PN junction of the transistors, is either dissipated by the IC to an exposed pad through θ_{JC} (thermal resistance from junction to exposed pad) and θ_{CA} (thermal resistance from the PCB to ambient air by convection), or dissipated directly from the die to the air through θ_{JT} (thermal resistance from junction to top of the case) and θ_{TA} (thermal resistance from top of the case to ambient air). The total equivalent thermal resistance is the equivalent resistor of the electrical circuit. From the parameters of the chosen transistors and the average value of the thermal resistance from copper on printed circuit board to air, known to be 1000 °C W⁻¹ cm⁻², the surface of the dissipators can be calculated using

$$T_j = P_t \frac{\theta_{JC} + \theta_{CA} + \theta_{JT} + \theta_{TA}}{(\theta_{JC} + \theta_{CA})(\theta_{JT} + \theta_{TA})} \quad (2.57)$$

where T_j is the temperature of the junction and P_t is the power dissipated by the transistors. Considering that the most important factor is the dimension of the dissipation pads, the needed surface is approximately 300 mm² per transistor. In the final design, these pads are placed on the top layer and on the bottom layer of the PCB, and connected thermally together with vias.

2.4.2 Notch Filter

To avoid a too large displacement of the moving plate at the resonance of the loudspeaker, a parametric notch filter is added to the loudspeaker driving board. The notch filter needs to have a tunable resonant

frequency in order to be adapted to the different variants of the loudspeaker. The notch filter needs to have a variable gain, in order to be adjusted to the different variants and also because the viscous damping of the loudspeaker is difficult to evaluate before measurements. The notch filter is based on a well known schematic used in parametric equalizers. Only one band is used. The schematic is presented in Figure 2.36.

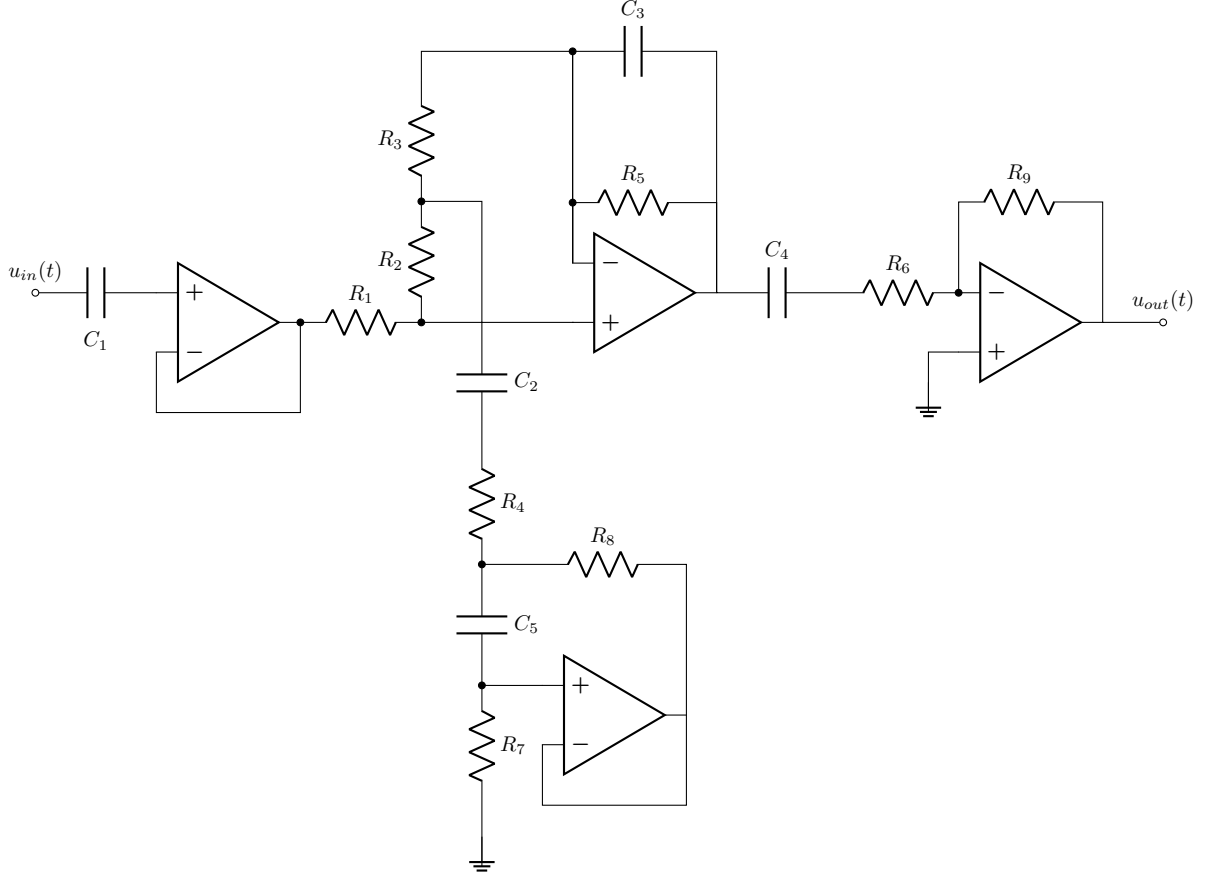


Figure 2.36: Schematic of the notch filter circuit

The circuit is composed of a first input stage, a voltage follower, in order to make the input impedance of the circuit high, to match with the output of the sound card. Ignoring the input coupling capacitor C_1 , the total transfer function of the circuit can be written

$$H = \frac{G(R_3R_2 + R_2Z_1 + R_2Z_2 + R_3Z_1)}{G(R_1R_3 + R_2R_3 + R_2Z_1 + R_3Z_1) - (R_1R_2 + R_1Z_1 + R_1Z_2 + R_3R_2 + R_2Z_1 + R_2Z_2 + R_3Z_1 + Z_1Z_2)} \quad (2.58)$$

with

$$Z_1 = \frac{1 - \omega^2 C_2 C_4 R_8 (R_4 + R_7) + j\omega((R_4 + R_8)C_2 + C_4 R_8)}{j\omega C_2 (j\omega R_8 C_4 + 1)}, \quad (2.59)$$

$$Z_2 = \frac{R_5 \frac{1}{j\omega C_3}}{R_5 + \frac{1}{j\omega C_3}} \quad (2.60)$$

and G the gain of the top operational amplifier. Using the assumption that an operational amplifier gain is infinite, the equation can be written

$$\lim_{G \rightarrow \infty} H = \frac{R_3 R_2 + R_2 Z_1 + R_2 Z_2 + R_3 Z_1}{R_1 R_3 + R_2 R_3 + R_2 Z_1 + R_3 Z_1}. \quad (2.61)$$

The input operational amplifier is a voltage buffer and can be neglected. The last stage of the circuit is an inverting amplifier and the transfer function is the negative ratio of the feedback impedance R_9 over the input impedance and the transfer function H_o writes

$$H_o = -\frac{R_9}{R_6 + \frac{1}{j\omega C_4}}. \quad (2.62)$$

The total transfer function is displayed for different values of resistors R_2 and R_3 , in order to show the variable attenuation, the variable frequency and the variable quality factor, in Figures 2.37(a), 2.37(b) and 2.38(a) respectively.

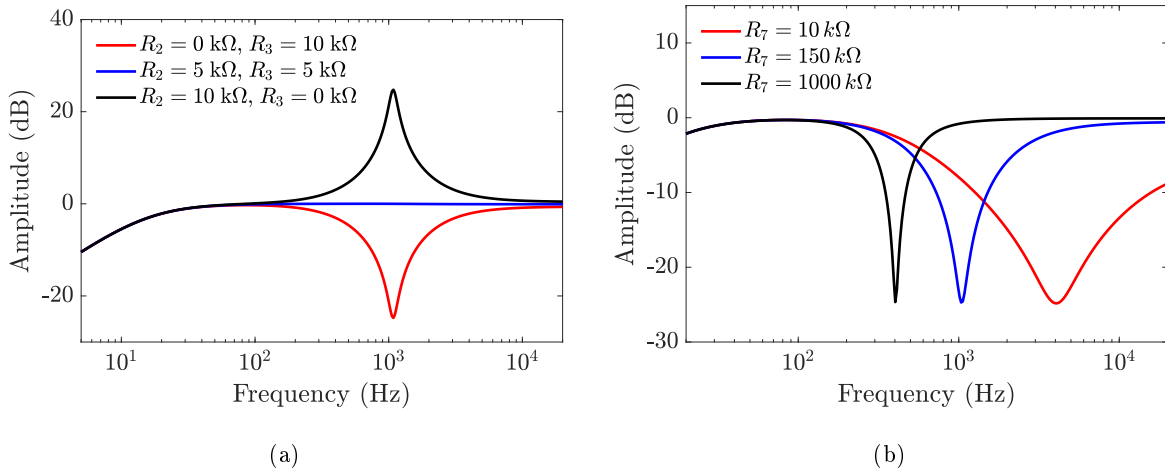


Figure 2.37: Frequency responses of the notch filter for different values of R_2 and R_3 (a) and for different values of R_7 (b)

The circuit behaves as expected, and allows an attenuation down to -25 dB, a wide variation of the resonance frequency, from 400 Hz to 4 kHz and a wide variation of the quality factor, from 0 to 20. The quality factor can be changed by changing the value of R_4 , as presented in Figure 2.38(a).

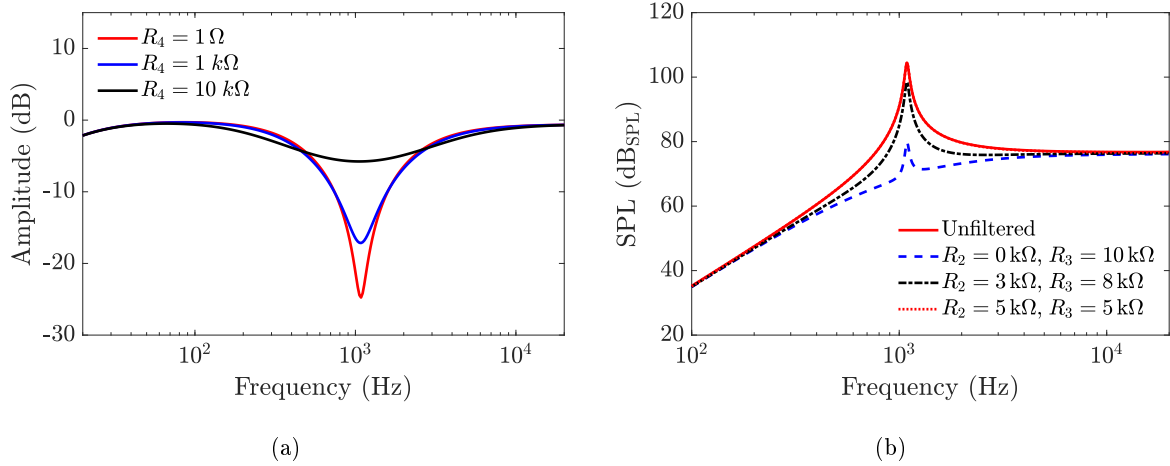


Figure 2.38: Frequency response of the notch filter for different values of R_4 (a) and frequency response of the loudspeaker corrected by the notch filter (b)

Using the transfer function calculated with the model of the loudspeaker, the expected frequency response of the loudspeaker can be simulated by multiplying the notch filter transfer function with the loudspeaker transfer function. The result for a correctly tuned notch filter is compared to the raw response of the loudspeaker and shown in Figure 2.38(b). The limitation of the quality factor of the notch filter is due to the operational amplifier circuit that simulates the inductor. The inductor is imperfect and has a series resistor of value R_8 . This limits the quality factor to about 10. Depending on the resonance of the manufactured loudspeaker, the notch filter allows for a complete compensation of the resonance.

2.4.3 Printed Circuit Board

Once the complete circuit of the driving board is simulated and designed, and after adding some usual electronic parts (AC coupling capacitors, test points, connectors and power supply filters) the printed circuit board is routed. The circuit is routed on a double sided PCB with ground planes on both sides. Dissipators for the output transistors are rooted on a separated potential, and connected together with vias through the PCB. Input and output connectors are placed on the left and right side of the PCB. 0Ω resistors are placed at the input and output of each circuit in order to be able to disconnect them and to test them separately. The full circuits, drawn into Altium Designer with the real components are presented in Appendix G. The routing of all layers of the board is presented in Figure 2.39, and the top and bottom layers are presented separately respectively in Appendix F.1 and F.2.

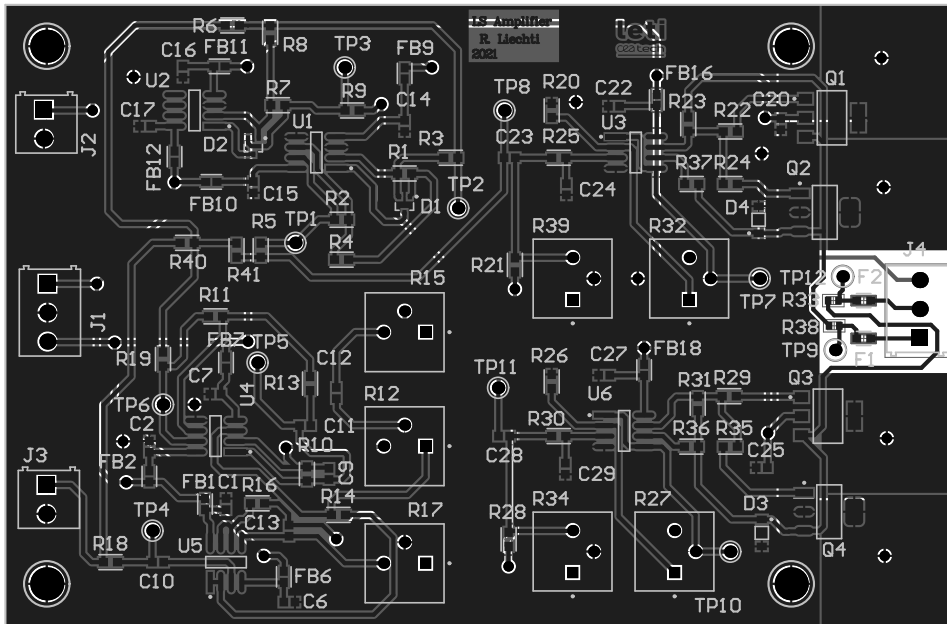
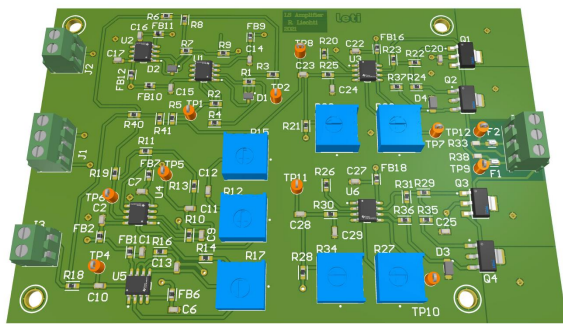
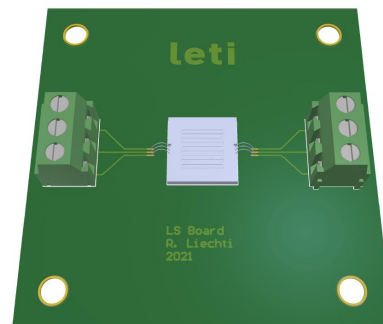


Figure 2.39: Routing of the Printed Circuit Board

Using Altium Designer, the components and their 3D model can be visualized on the PCB, and a 3D view of the printed circuit board is presented in Figure 2.40(a). To make the measurements of the loudspeaker easier, a simple loudspeaker board is designed. The loudspeaker is glued on the PCB and the actuation pads are bonded on the PCB. Screw terminals are used in order to make the connections easier. A hole is cut through the PCB so as not to affect the acoustic load behind the loudspeaker. With this hole, the PCB can also be used as a baffle to avoid acoustic shortcut, in a limited range of frequencies. A 3D view of the designed PCB is presented in Figure 2.40(b). More details on the power supply filters are given in Appendix E.



(a)



(b)

Figure 2.40: 3D view of the loudspeaker amplifier printed circuit board (a) and 3D view of the loudspeaker printed circuit board (b)

2.5 Chapter Conclusion

In this chapter, the linear non dimensional parameters F_{in} , C_{ms} , M_{ms} , h_0 and w_s of the loudspeaker were determined in order to reach the performance identified in the first chapter. This set of parameters gives a sound pressure level of approximately 78 dB_{SPL} and a resonance frequency of approximately 1 kHz, with quality factor of approximately 10. With these linear parameters, the electrical impedance of the loudspeaker was determined, in order to design the required amplifier to actuate the loudspeaker. This amplifier is able to power the loudspeaker with a signal between 0 V and 30 V, from 20 Hz and 20 kHz, in a impedance down to 100 Ω . In the next chapter, the complete three dimensional loudspeaker is simulated with finite element method, and nonlinear effects are investigated with finite element method as well as with a state space model.

Chapter 3

Advanced Design

Contents

3.1	Chapter Introduction	70
3.2	Finite Element Modeling	70
3.2.1	Physics and Geometry	70
3.2.2	Mesh	73
3.2.3	Static Simulation	74
3.2.4	Modal Analysis	75
3.2.5	Perfectly Matched Layer	79
3.2.6	Acoustic Pressure	79
3.2.7	In-Ear	82
3.2.8	Stress	83
3.2.9	Geometric Nonlinearities	84
3.3	Linearization Spring	86
3.3.1	General Structure	86
3.3.2	Static Modeling	86
3.3.3	Dynamic Modeling	89
3.4	State Space Modeling	90
3.4.1	Free Field	91
3.4.2	In-Ear	95
3.4.3	Loudspeaker Design Summary	98
3.5	Chapter Conclusion	101

3.1 Chapter Introduction

After having defined the lumped parameters required for the loudspeaker to reach the performance determined in Chapter 2, this chapter mainly describes the finite element model and the state space model of the loudspeaker, from the step highlighted in red in the design loop depicted in Figure 2.1. This part of the design starts with a three dimension finite element model of the loudspeaker in order to simulate more advanced linear characteristics of the loudspeaker. After confirming the linear performance of the loudspeaker using the finite element model, nonlinear aspects are investigated, using first the same finite element model, and then a nonlinear state space model.

3.2 Finite Element Modeling

This section describes the finite element model built into COMSOL® multiphysics, in order to simulate the loudspeaker frequency response, and other quantities that cannot easily be computed by hand, such as the stress concentration in the actuators at maximum deflection, the guiding coefficient of the loudspeaker, the modal shape and some nonlinearities. Firstly, the physics and geometry involved into the complete finite element simulations of the loudspeaker are described, then the Perfectly Matched Layer (PML) and the mesh, two important aspects of the simulations are detailed. Then the static behavior and the frequency responses of the loudspeaker computed with the finite element model are compared to the ones calculated with the analytical model presented in Section 2.2. Finally, geometric nonlinearities are evaluated.

3.2.1 Physics and Geometry

From the CAD drawings in Appendix D, a complete 3D parametric model of the loudspeaker is implemented into COMSOL®. The complete mechanical geometry in COMSOL® is depicted in Figure 3.1(a), where the piezoelectric layer is represented in purple and where the passive mechanical structure of the loudspeaker, composed of the different layers of oxide and silicon is represented in gray. The loudspeaker is composed of three main physics. The electrostatic physics is used to simulate the piezoelectric layer, and is coupled with a multiphysics coupling to the structural mechanics physics, used to simulated the structure of the loudspeaker. The piezoelectric material is assumed to be linear, as ferroelectric effects are difficult to simulate using finite element method. Then, a hemispherical domain of air, which is represented in blue in Figure 3.1(b), is used to simulate the propagation of acoustic waves, and a structural mechanics to acoustics multiphysics coupling is used on the surface of the plate to couple both domains.

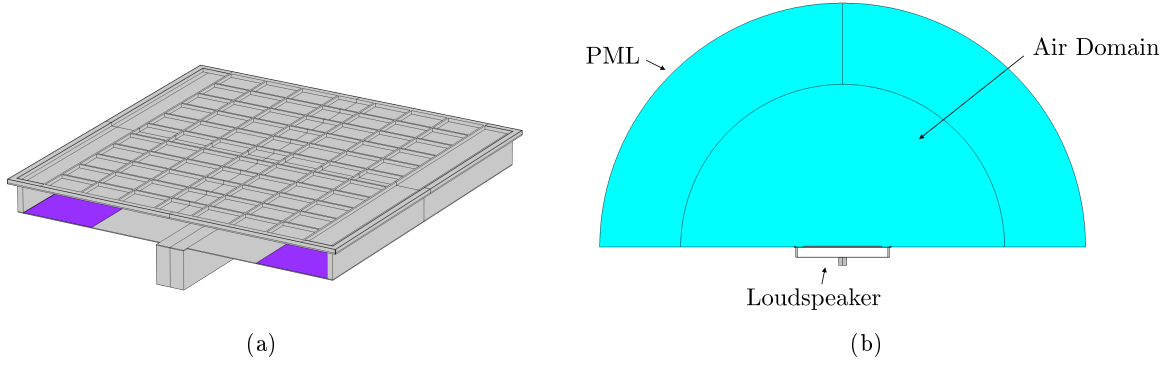


Figure 3.1: 3D mechanical part of the loudspeaker (a) and same loudspeaker coupled to a hemispherical air domain (b) in COMSOL®

To simulate the thermoviscous behavior of the loudspeaker, a thermoviscous domain is used on the periphery of the plate, representing the thin layer of air between the moving plate and the frame of the loudspeaker. The thermoviscous domain is represented in red in Figure 3.2(a). This thermoviscous domain is coupled to the plate via a thermoviscous to structural mechanics coupling, and is coupled to the acoustic domain via a thermoviscous acoustics to acoustics coupling. As the thermoviscous domain has more degrees of freedom, it needs to be kept to a small number of elements in order to reduce the computational cost of the model.

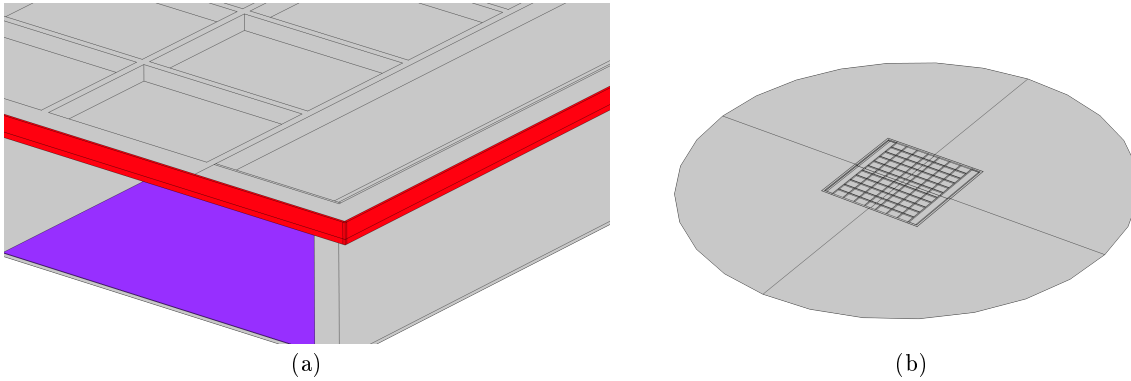


Figure 3.2: Thermoacoustics domain around the moving plate of the loudspeaker (a) and view of the circular hard boundary wall disc around the loudspeaker (b) in COMSOL®

Then a hard circular boundary is used around the plate of the loudspeaker in order to simulate the baffle, as depicted in Figure 3.2(b). The hard boundary wall condition sets the normal acceleration and velocity on the boundary to 0, such as

$$\frac{\partial p}{\partial \mathbf{n}} = 0. \quad (3.1)$$

Materials properties are taken from the COMSOL® library, except the piezoelectric material, whose compliance matrix is extracted from previous measurement at CEA-Leti and writes

$$\mathbf{c}^{\mathbf{E}} = \begin{bmatrix} 6.25 \cdot 10^{-12} & -4.78 \cdot 10^{-12} & -8.45 \cdot 10^{-12} & 0 & 0 & 0 \\ -4.78 \cdot 10^{-12} & 1.65 \cdot 10^{-11} & -8.45 \cdot 10^{-12} & 0 & 0 & 0 \\ -8.45 \cdot 10^{-12} & -8.45 \cdot 10^{-12} & 2.07 \cdot 10^{-11} & 0 & 0 & 0 \\ 0 & 0 & 0 & 4.35 \cdot 10^{-11} & 0 & 0 \\ 0 & 0 & 0 & 0 & 4.35 \cdot 10^{-11} & 0 \\ 0 & 0 & 0 & 0 & 0 & 4.26 \cdot 10^{-11} \end{bmatrix} \text{Pa}^{-1}, \quad (3.2)$$

whose piezoelectric tensor is

$$\mathbf{d} = \begin{bmatrix} 0 & 0 & 0 & 0 & 17.034 & 0 \\ 0 & 0 & 0 & 17.034 & 0 & 0 \\ -6.623 & -6.623 & 23.24 & 0 & 0 & 0 \end{bmatrix} \text{C m}^{-2}. \quad (3.3)$$

and whose mechanical parameters, as well as parameters for air, silicon and silicon oxide are recalled in Table 3.1.

Table 3.1: Main linear and isotropic parameters of the materials used in the COMSOL[®] model

Material	E (GPa)	ν (1)	ρ (kg m ⁻³)	ε_r^T (1)
PZT	82	0.39	7500	—
SiO ₂	70	0.17	2200	4.2
Si	160	0.28	2329	11.7
Air	—	—	—	1

The rear part of the loudspeaker is not coupled to air, in order to reduce the computational cost of the model. The amplifier is assumed to be a perfect voltage amplifier, with no series output resistor and an unlimited output current. This means that the electrical behavior of the piezoelectric actuators can be ignored. The input voltage is then directly applied to the upper and lower boundaries of both piezoelectric actuators. For the structure to acoustic interaction, COMSOL[®] solves the Navier-Stokes equations, that describes the coupling between the velocity field \mathbf{u} and the force exerted by the fluid on the solid \mathbf{F} such as

$$\mathbf{F} = \mathbf{n} \cdot \left(-p\mathbf{I} + (\mu(\nabla\mathbf{u} + \nabla\mathbf{u}^T)) - \frac{2}{3}\mu\nabla\mathbf{u}\mathbf{I} \right). \quad (3.4)$$

For the electrostatic to structure coupling, COMSOL[®] solves the equation described in Section 1.4.2 coupled with the equation of the solid equilibrium given by Newton's second law written as

$$\rho_0 \frac{\partial^2 \mathbf{u}}{\partial t^2} = \nabla_X(FS) + \mathbf{F}_V \quad (3.5)$$

with F the deformation gradient, \mathbf{F}_V a body force with components in the configuration of the underformed volume and S the Piola-Kirchoff stress tensor. The resulting coupled equation is solved using the virtual work formulation.

3.2.2 Mesh

The mesh is an important parameter to consider when using finite element simulation. It needs to have enough elements to be precise, but as little as possible in order to keep the computation time reasonable. In order to have the least elements possible, the mesh of the mechanical part of the loudspeaker is built with mapped meshes, that are swept along the thickness of the structure, as it is shown in Figure 3.3(a). It results in a perfect mesh quality, and a decently low number of elements. The mesh quality is characterized by a dimensionless quantity between 0 and 1, where 1 is a perfectly rectangular element, and where 0 represents a degenerated element. The skewness is calculated as follow

$$s_k = 1 - \max\left(\frac{\theta - \theta_i}{180 - \theta_i}, \frac{\theta_i - \theta}{\theta_i}\right) \quad (3.6)$$

where θ is the angle between two vertex of an element, and θ_i is the same angle for a perfect element.

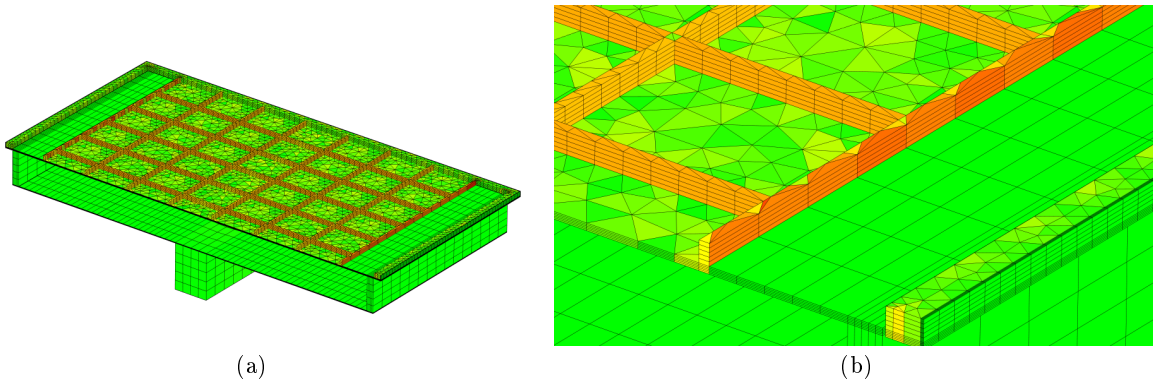


Figure 3.3: 3D view of the skewness of the mechanical part of the model (a) and zoom on the linearization spring (b) represented from red (poor quality) to green (good quality)

As a rule of thumb, it's advised to keep elements quality above a skewness of 0.1. As it can be seen in Figure 3.4(a), a few elements are below this critical limit, and are mostly coming from the poor geometric compatibility between the tetrahedral elements meshing the hemispherical air domain and the quad elements, meshing the mechanical structure. The perfectly matched layer is then meshed with a swept function, in order to have a defined number of elements in the thickness, and a good quality of elements, as it is presented in Figure 3.4.

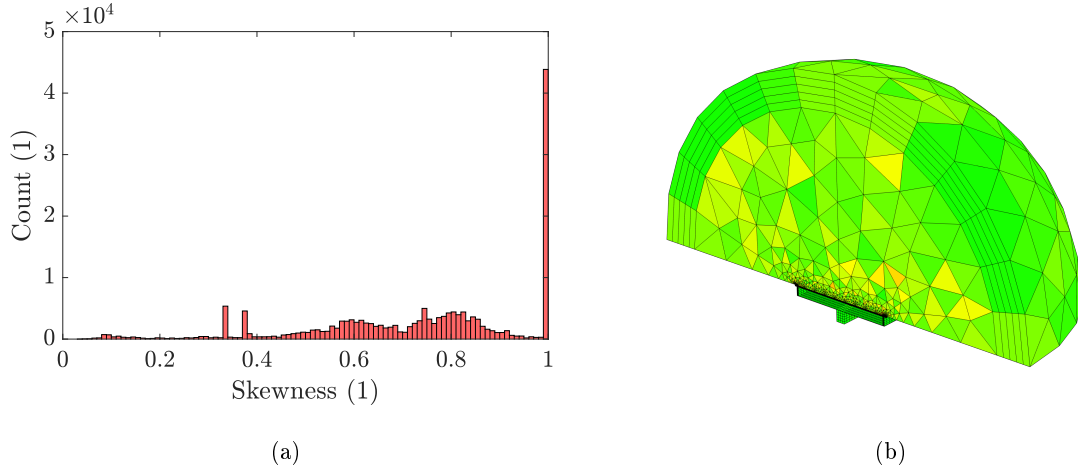


Figure 3.4: Histogram of the skewness for the total number of elements of the model (a) and skewness of elements in a cross section of the complete model represented as red (poor quality) to green (good quality) (b)

The skewness of the mesh can also be depicted as a histogram to observe the distribution of the quality as presented in Figure 3.4(a). It shows that most element quality is equal to 1, but also shows a significant number of elements whose quality is around 0.4, mainly due to the incompatibility between the rectangular elements of the plate and the tetrahedral elements of the air domain. A very few elements have a quality inferior to 0.1. The acoustical domain is entirely meshed with tetrahedral elements, and the perfectly matched layer, at the surface of the hemispherical domain is meshed with a swept, as it is shown in Figure 3.12(b). Due to the complexity of the loudspeaker geometry, the mesh used in our model is perfectly acceptable.

3.2.3 Static Simulation

Once correctly defined and meshed, the model can then be solved for a constant input voltage of 30 V. Assuming a critical damping at the resonance, the static displacement of the loudspeaker is the maximum displacement achieved by the loudspeaker, as discussed in Section 1.2. Static simulations are also used to characterize the stress and the linearity of the loudspeaker. For the simulation, the input voltage is set to $u_{in} = 30$ V, and a stationary study is used. During a stationary study, the acoustic and thermoviscous acoustic domains are turned off. The shape of the loudspeaker, whose displacement field is depicted in Figure 3.12(a), corresponds to a pistonic motion of the plate in the z direction, with a maximum displacement of 108.9 μm at the center of the stiffened plate.

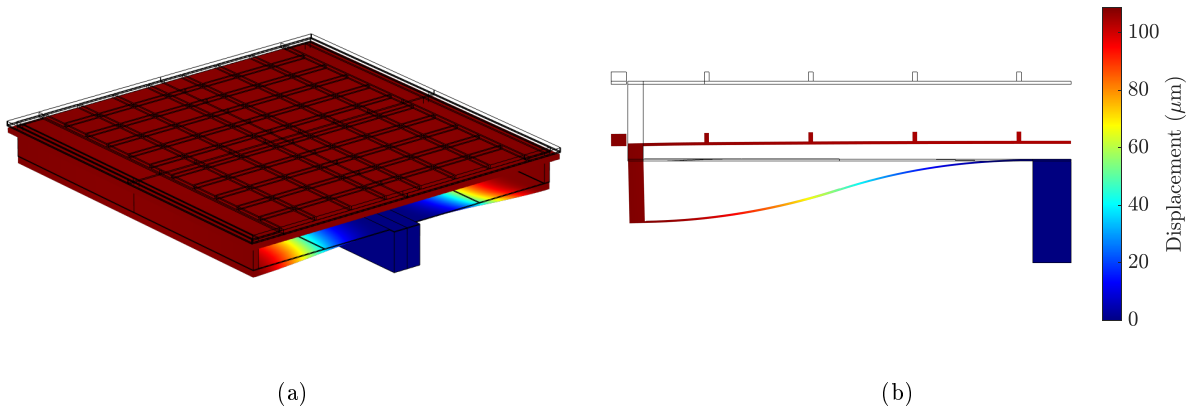


Figure 3.5: 3D view (on scale) (a) and cross section view (not on scale) (b) of the loudspeaker deformed under an input voltage $u_{in} = 30$ V

The profile of deflection of the flexible part of the actuators is then displayed as a function of the length on the actuator in the finite element model and is compared with the deflection calculated using Equations 2.5 and 2.6. The deflection, depicted in Figure 3.6(a), is very similar in both cases, but the finite element model gives a lower displacement of the flexible part of the actuator, of about $-109 \mu\text{m}$, while the analytical model gives a displacement of $-139 \mu\text{m}$.

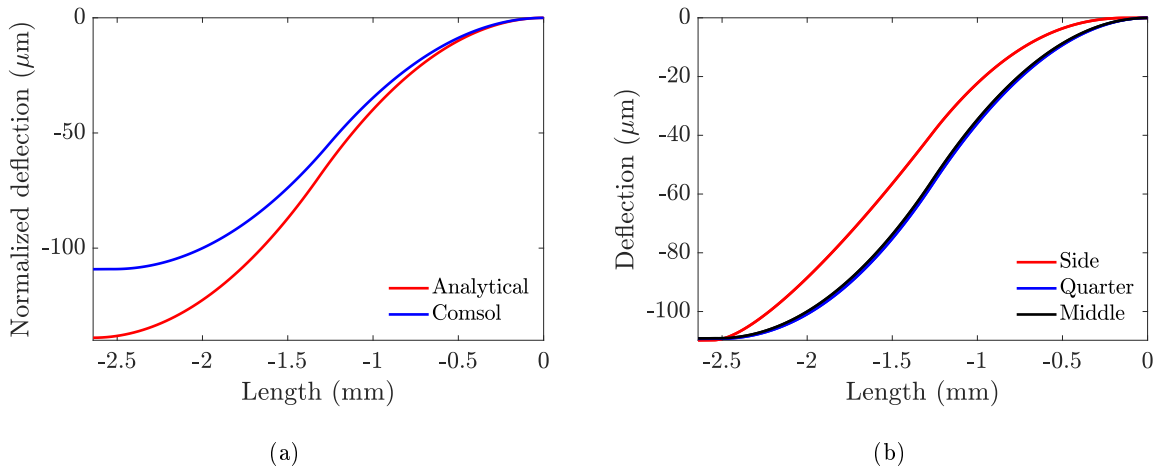


Figure 3.6: Deflection profile of the actuators calculated with the finite element model and with the analytical model (a) and deflection profile calculated along the width of the actuator (b)

The deflection is very similar at a quarter of the width and in the middle of the width, as it is depicted in Figure 3.6(b). It changes only for the side of the actuator, but remain similar at the tip of the actuator, due to the rigid coupling block, attached to the complete width of the actuators.

3.2.4 Modal Analysis

Modal analysis is an important study for every vibrating devices, and is not always easy to calculate analytically for complex structures, such as this loudspeaker. Modes of the mechanical structure could affect the radiated pressure. The modal analysis is first carried out on the plate alone, in order to

determine the number of stiffeners to add on the plate, in order to increase the apparent stiffness of the plate, to push the first mode as high as possible in frequency while reducing the mass in order to improve the sensitivity. The structure is implemented as a parametric structure into COMSOL[®], and the first mode of the plate is depicted as function of the number of stiffeners with n_x the number of stiffeners in the x direction equal to n_y the number of stiffeners in the y direction. The width of the stiffeners is determined in another study and the height of the stiffeners is limited by the manufacturing process.

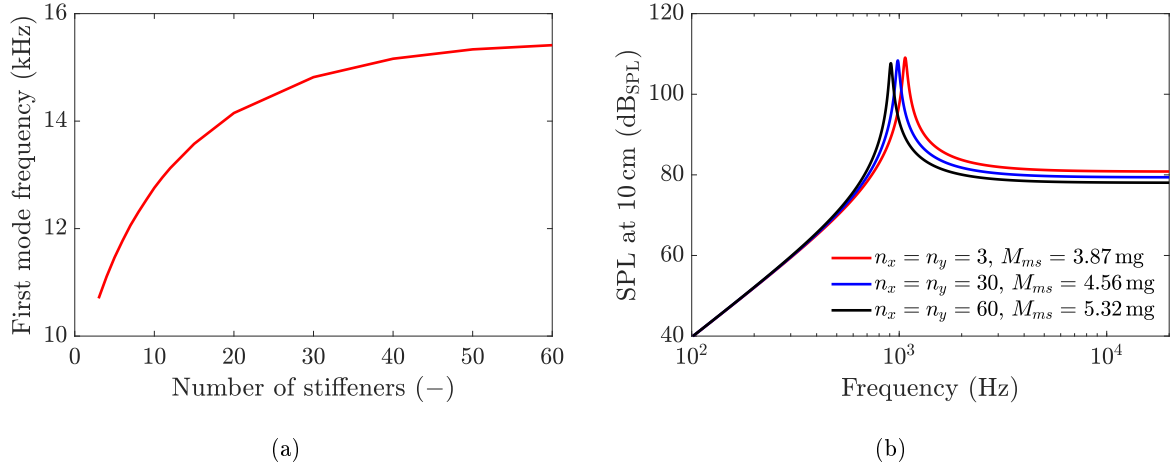


Figure 3.7: First eigenmode of the moving plate as a function of the number of stiffeners (a) and pressure response of the loudspeaker for different number of stiffeners (b)

In order to compute more rapidly the effect of the change of mass due to the number of stiffeners on the frequency response of the loudspeaker, the lumped element model of Section 2.2 is used. The change of mass of the moving plate M_{ms} due to the addition of stiffeners is then determined using the density of silicon and using the volume of the moving plate such as

$$M_{ms} = (W_p L_p t_{pl} - 2W_{ls} L_{ls} (t_{pl} - t_{pp}) - L_{rr} W_{rr} n_x n_y (t_{pl} t_{pp})) \rho_s + M_a / 2 + 2M_{cb} \quad (3.7)$$

with the width and the length of the rectangles created by the stiffeners determined by

$$W_{rr} = \frac{W_p - 2L_{fpx} - (n_x - 1)w_r}{n_x} \quad (3.8)$$

and

$$L_{rr} = \frac{L_p - 2(L_{fpy} + L_{ls} + w_s) - (n_y + 1)w_r}{n_y} \quad (3.9)$$

with L_p , W_p and t_{pl} the external length, width and thickness of the plate, W_{ls} and L_{ls} the width and length of the linearization spring, L_{fp} the width of the plain frame around the plate, w_r the width of the stiffeners, t_{pp} the thickness of the bottom plain plate and L_{rr} and W_{rr} the length and width of the rectangles created by the stiffeners. All dimensions are depicted on a 3D view of the plate in Figure 3.8(a) and on a partial cross section view, not to scale of the plate in Figure 3.8(b). The effect on the pressure response is then calculated with the calculated mass M_{ms} using the lumped element model and is depicted in Figure 3.7(b). The change of mass M_{ms} shifts the resonance of the loudspeaker and affects the radiated sound pressure level in the bandwidth of about 3 dB.

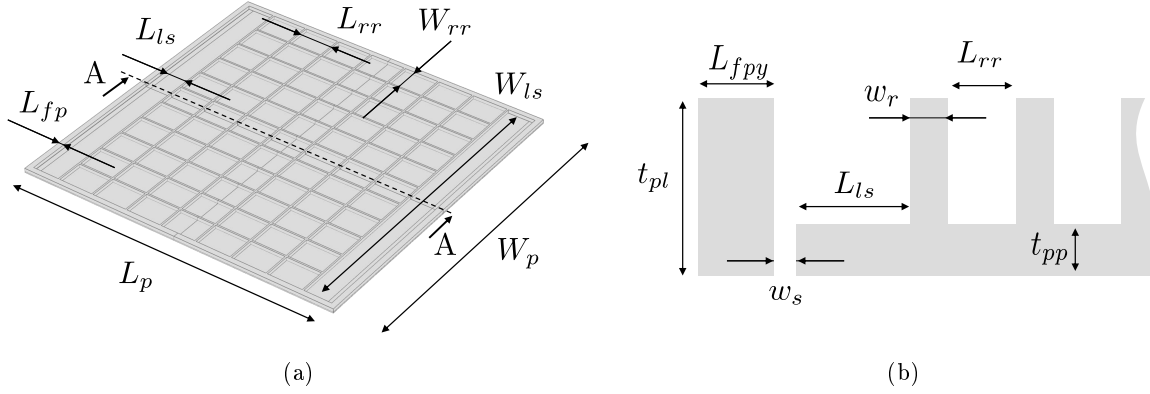


Figure 3.8: Dimensions of the moving plate on a 3D view (a) and dimensions of the plate on a partial cross section of the plate (cross section A) not on scale (b)

The modal study of the plate is performed with the plate clamped on both opposite end, as it is closer to the actual working principle of the loudspeaker. Figure 3.9(a) depicts the geometry of the plate for $n_x = n_y = 3$ and Figure 3.9(b) depicts the displacement field of the plate at its first resonance at 10 864 Hz. Figure 3.9(c) depicts the geometry of the plate for $n_x = n_y = 10$ and Figure 3.9(d) depicts the displacement field of the plate at its first mode at 12 658 Hz. The displacement field is affected by the stiffeners, and for $n_x = n_y = 3$, the shape is more circular than for the deformation for $n_x = n_y = 10$.

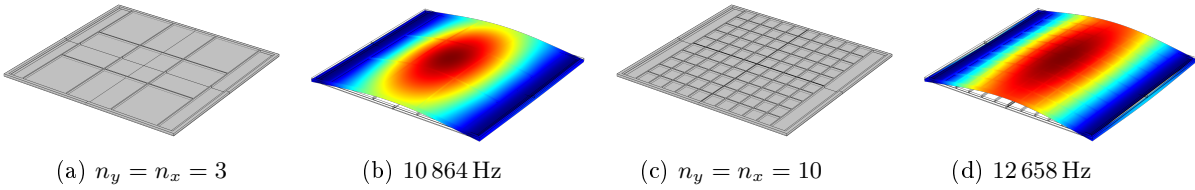


Figure 3.9: Geometry of the plate with $n_x = n_y = 3$ (a), modal shape of the plate with $n_x = n_y = 3$ (b), geometry of the plate with $n_x = n_y = 10$ (c) and modal shape of the plate with $n_x = n_y = 10$ (d)

From Figure 3.7(a) it can be deduced that the shift of the first eigenmode of the plate is decreasing for a bigger number of stiffeners, which is not worth the loss of sensitivity. Supported by further studies that are not detailed in this document, the number of stiffeners in the x direction n_x is set to 11 and the number of stiffeners n_y in the y direction is set to 7. The thickness of the plain plate t_{pp} is set to 20 μm , as well as the height of the stiffeners $t_{pl} - t_{pp}$ to 60 μm . The modal analysis is then carried out using an eigenfrequency study on the complete mechanical structure of the loudspeaker and 16 modes are found in the audio bandwidth.

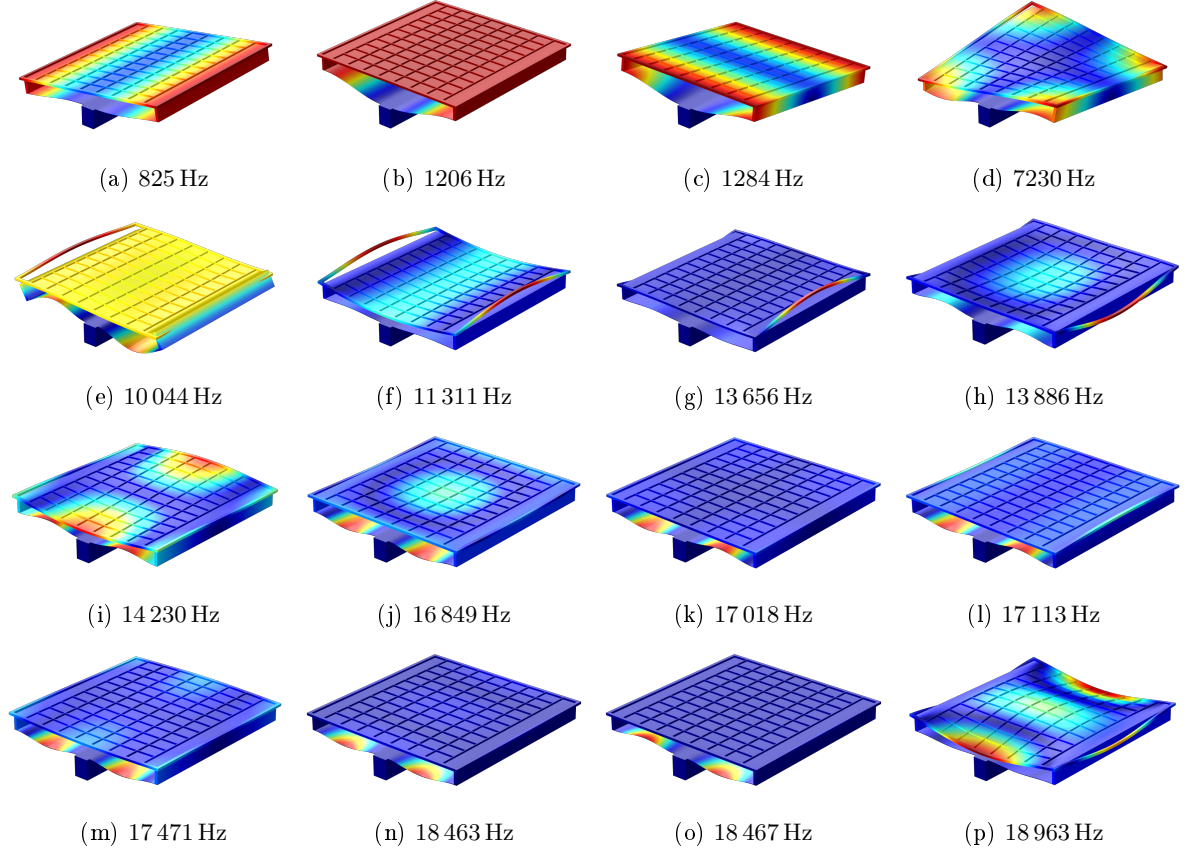


Figure 3.10: Modal shape of the mechanical part in the loudspeaker for the 16 modes in the audio bandwidth

The first mode in Figure 3.10(a) is a rocking mode, and could be triggered by applying an external vibration to the loudspeaker, but it does not occur during operation, as it requires an asymmetric actuation of both actuators. The second mode in Figure 3.10(b) corresponds approximately to the fundamental mode of the loudspeaker at f_s , when the effect of the moving mass M_{ms} is equal and opposed to the effect of the apparent compliance C_{ms} . In Figure 3.10(c), a second rocking mode is depicted. Similarly to the first mode, this mode does not appear during operation of the loudspeaker due to the asymmetry of the deformation of the elastic layers of the actuators. In Figure 3.10(d), an oblique rocking mode composed of a combination of the first mode and the third mode is depicted. From this analysis, it can be deduced that the loudspeaker is operating as a piston from 0 Hz to 11 311 Hz, and is then reproducing a flat frequency response from the first eigenmode to 11 311 Hz. The first mode composed of a deformation of the plate appears at 11 311 Hz in Figure 3.10(f). This mode is strongly interacting with the radiated sound pressure level. The modes depicted in Figures 3.10(e), 3.10(g), 3.10(i), 3.10(k), 3.10(l) and 3.10(o) correspond to asymmetric modes of the actuators or the plate, and should not appear during the operation of the loudspeaker, except if a strong asymmetry in the stiffness or the mass of the structure due to a problem in the manufacturing process is observed. Modes of the plate in Figure 3.10(h), 3.10(j), 3.10(m) and 3.10(p) are affecting significantly the radiated sound pressure in the audio bandwidth. Modes of the actuators, such as the one depicted in Figure 3.10(n), directly affect the velocity of the plate, while not deforming it, creating a peak or a dip in the frequency response.

3.2.5 Perfectly Matched Layer

To meet the Sommerfeld condition on the outside boundary of the acoustics domain, a perfectly matched layer is used. The Sommerfeld condition is a radiation condition that states that the outgoing waves of a radiating source must scatter to infinity, and it can be translated to

$$\lim_{|x| \rightarrow \infty} |x|^{\frac{n-1}{2}} \left(\frac{\partial}{\partial |x|} - ik \right) u(x) = 0. \quad (3.10)$$

The PML applies the Sommerfeld condition by creating a domain, outside of the domain of interest, with a complex dissipative impedance. This can be seen as a virtual anechoic chamber. Figure 3.11 shows a PML bounding a hemispherical domain in 2D. The intensity of the outgoing waves rapidly decreases along r , the radius of the hemisphere.

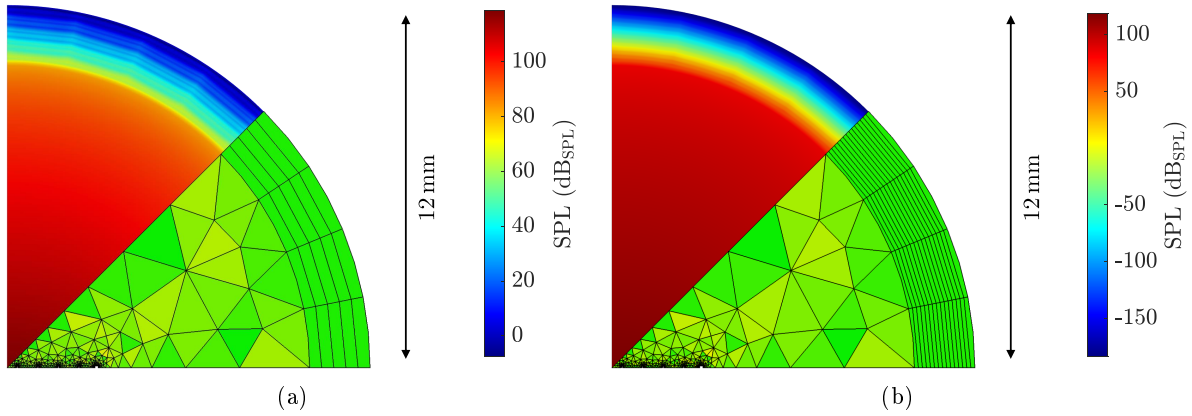


Figure 3.11: Sound pressure level in the air domain and in the PML for a PML with 5 elements of mesh (a) and for a PML with 15 elements of mesh (b)

In Figure 3.11 the effectiveness of the perfectly matched layer is depicted for two different meshes. In Figure 3.11(a) the perfectly matched layer attenuates the incoming acoustic waves from approximately 100 dB_{SPL} to 0 dB_{SPL} in a few millimeters, for a thickness of five elements. In Figure 3.11(b), the same study is carried out with a PML composed of 15 elements in its thickness, and the sound pressure level decreases from 100 dB_{SPL} to -150 dB_{SPL}. In both cases, the ratio between the pressure in the domain and at the hard boundary surrounding the PML is sufficiently large, and reflected waves are not significantly affecting the pressure field inside the air domain. By considering that the outgoing acoustic waves generated by the loudspeaker are hemispherical, a spherical radiation condition could be used on the sphere to reduce the computational cost of the model.

3.2.6 Acoustic Pressure

Once the model is set-up, the frequency response of the loudspeaker can be computed for one hundred frequencies, by placing an evaluation point at 10 mm from the surface of the moving plate of the loudspeaker in the hemisphere of air. It has to be noted that although the loudspeaker uses an asymmetrical signal due to the ferroelectric properties of thin-film PZT, as discussed in Section 2.2.1, the simulation is carried out with a symmetrical signal, making the assumption that the behavior is equivalent in both directions, which is the case if the geometric nonlinearities are not considered. Frequency responses of the different loudspeakers are then compared with the one calculated with the lumped element model in Section 2.3.1 in Figure 3.12.

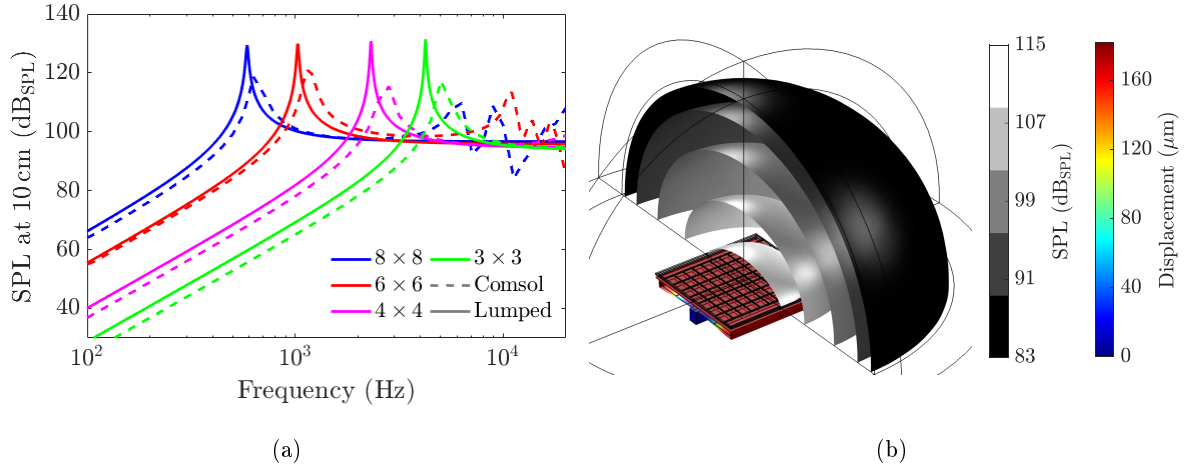


Figure 3.12: Comparison of the sound pressure level computed with the finite element and lumped element models for different loudspeakers dimensions (a) and 3D view of the loudspeaker radiating in air in COMSOL® (b)

There is a good match between the pressure calculated with the finite element and the lumped element models, except higher in frequencies, where peaks and dips appear due to the modal behavior of the loudspeaker, that is not considered with the lumped element model. A shift of the resonance frequency is observed between both models, but seems to not vary with the change of dimensions of the loudspeaker. This can be due to the assumptions made for the actuators, especially the 1D assumption, that doesn't consider the lateral stresses and strains of the beam.

In the thin interstice surrounding the plate, the thermoviscous losses can be visualized and are depicted in Figure 3.13.

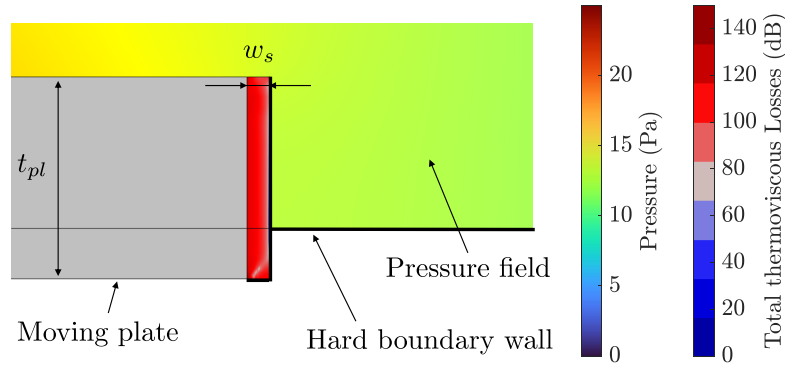


Figure 3.13: Total thermoviscous losses in the interstice surrounding the plate and acoustic pressure in the air domain

To determine the influence of the thermoviscous losses on the mechanical structure, the reaction force experienced by the moving plate is integrated around the plate. To find the impedance, the resulting force is divided by the velocity of the plate. This leads to a viscous resistance $R_v = 7 \mu\text{N s m}^{-1}$ which does not significantly influence the mechanical quality factor of the loudspeaker. The viscosity of the fluid also adds a mass to the plate.

Using a simpler model, only composed of a rigid plate actuated with a constant velocity v , moving along z and flush mounted in a baffle, the influence of the width of the interstice on the pressure can be calculated. The model is composed of a shell, whose surface is equal to S_d . The stiffness of the shell is set to be very large, in order to not have eigenmodes in the audio frequency range. The shell is attached to the hard boundary wall with a spring foundation, whose value is equivalent to the compliance C_{ms} . Figure 3.14(a) depicts the sound pressure level radiated by the simplified loudspeaker for different interstice widths, from $2\ \mu\text{m}$ to $200\ \mu\text{m}$. The pressure is constant from $2\ \mu\text{m}$ to approximately $20\ \mu\text{m}$ and then starts to decrease. For an interstice of $200\ \mu\text{m}$, 10 dB of sound pressure level are lost, due to the acoustic short-cut. It has to be noted that the width of the interstice also sets the maximum thickness of the plate t_{pl} , due to the maximum aspect ratio achievable via etching techniques.

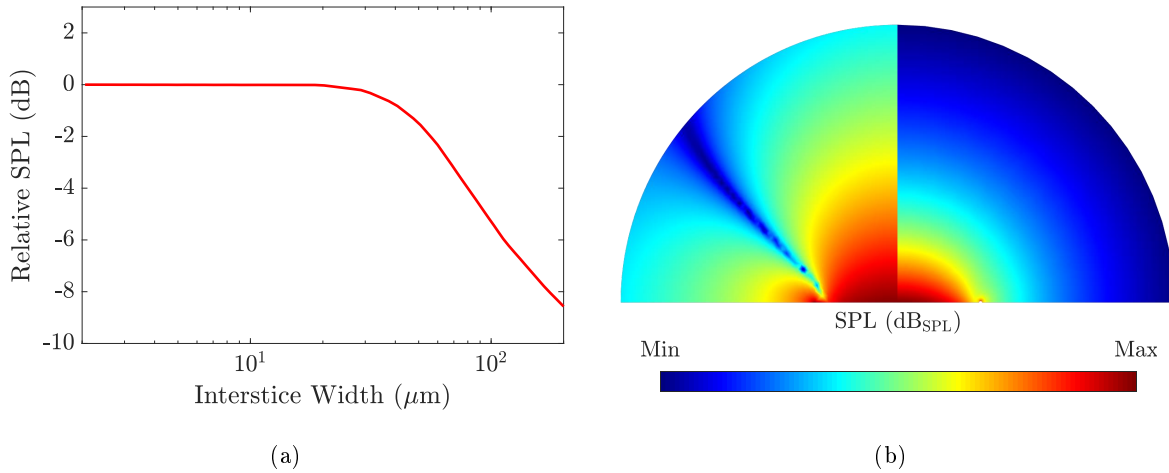


Figure 3.14: Sound pressure level on axis as a function of the width of the air interstice w_s around the moving plate (a) and pressure field simulated with a simple moving plate with a simple acoustic domain around the plate (on the left) and with a thermoviscous domain around the plate (on the right) with an arbitrary scale (b)

Figure 3.14(b) depicts the SPL field around the moving plate, with and without thermoviscous domain. Without considering the thermoviscous losses, a sharp null of pressure appears, following an oblique line from the plate. This null is due to destructive interference between the back acoustic waves and the front acoustic waves. This creates a directive behavior, even for low frequencies, and reduces the on-axis pressure radiated by the loudspeaker. The width of the air interstice around the moving plate w_s is set to $9\ \mu\text{m}$. From the same model, the directivity of the loudspeaker can be evaluated for different frequencies. To be able to compare the directivity with the one calculated analytically in Section 2.2.8, the plate is assumed to be rigid. The sound pressure level is evaluated at the perimeter of the air domain, and the resulting pressure is depicted for four frequencies in Figure 3.15(a).

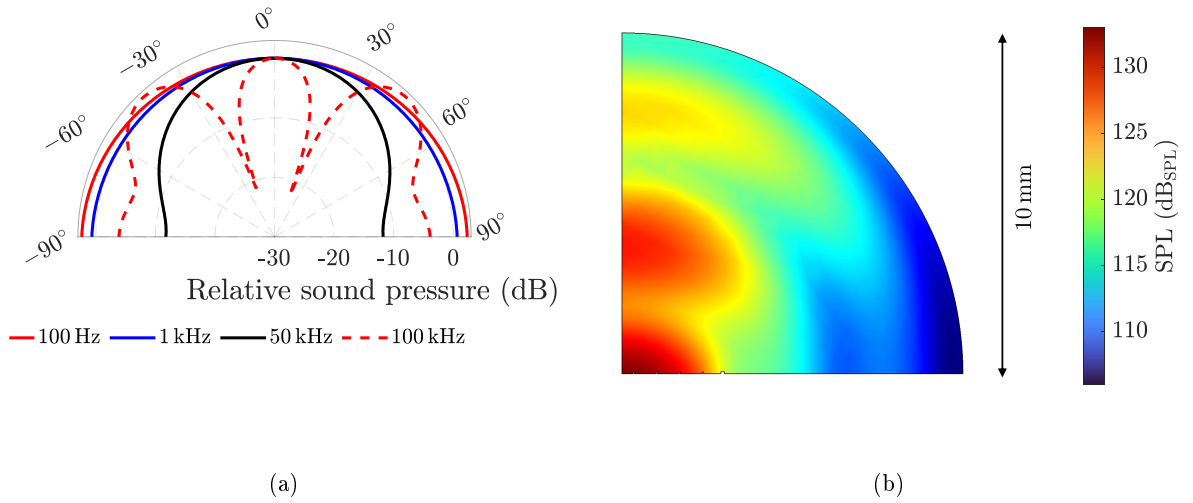


Figure 3.15: Directivity normalized to the pressure at $\theta = 0$ of the loudspeaker for four frequencies (a) and SPL field radiated by the loudspeaker at $f = 50$ kHz

In low frequencies and as simulated in Section 2.2.8, the loudspeaker behaves as a monopole and the radiated sound pressure is hemispherical. A difference of about 1 dB can be observed between the on-axis and the pressure at $\theta = 90^\circ$ at 1 kHz. For a frequency of 50 kHz, the pressure radiated in the normal axis to the plate is 10 dB higher, and the shape of the directivity is similar to the one simulated analytically. For a frequency of 100 kHz, a center lobe and two wide side lobes appear. The angle of the null and the overall shape of the directivity is different from the one simulated analytically. The slight asymmetry is due to the asymmetry in the mesh (limited refinement in order to save computation time), as the loudspeaker is symmetric. In Figure 3.15(b), the complete sound pressure field radiated by the loudspeaker at 50 kHz is depicted.

3.2.7 In-Ear

The COMSOL[®] model of the loudspeaker can also be used with a model of the IEC 60318-4 ear-occluded coupler, in order to predict the frequency response of the loudspeaker in this device. The model of the IEC 60318-4 is available in the COMSOL[®] examples.

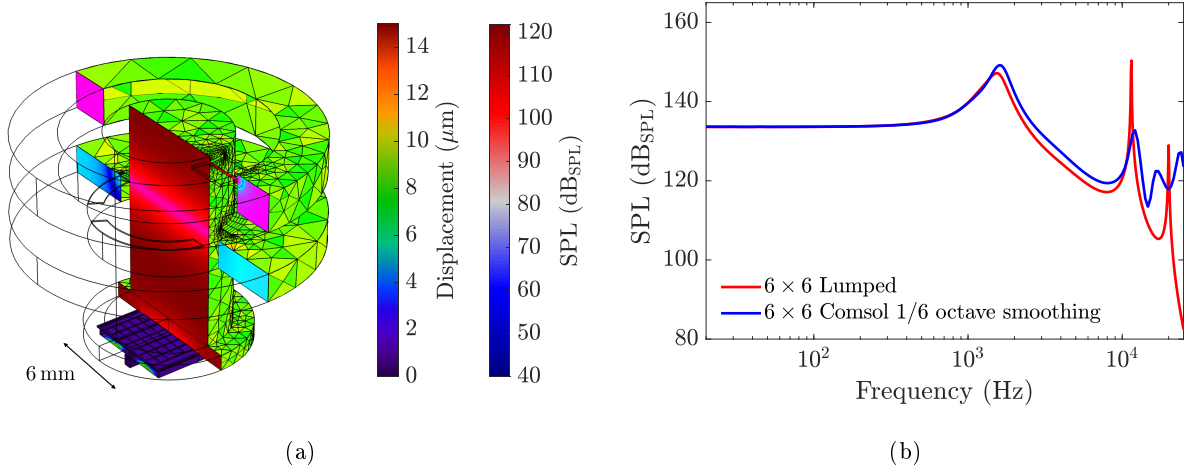


Figure 3.16: 3D view of the loudspeaker inside the coupler at 17 kHz with the displacement field and the deformation of the loudspeaker, as well as the pressure field inside the coupler and the mesh quality on the surface of the coupler, from poor quality (red) to good quality (green) (a) and frequency response calculated with the model, smoothed to a 1/6 of an octave and compared to the frequency response calculated with the lumped element model (b)

The ear-occluded coupler, as well as the adapter used to adapt the surface of the moving membrane of the loudspeaker to the opening of the coupler is depicted in Figure 3.16(a). The additional volume created by the adapter is added as a capacitor in the equivalent circuit of the coupler. Only half of the coupler is shown. The displacement field of the loudspeaker is depicted as well, and is very small on the plate (approximately 2 μm), as the frequency is an order of magnitude higher than the resonance of the loudspeaker. The comparison between the frequency responses calculated with the lumped element model, derived in Section 2.2.9 and with the one calculated with the finite element model is depicted in Figure 3.16(b). There is a very good agreement between both model in level in the low frequency range and around the resonance frequency of the loudspeaker inside the coupler, at around 1.8 kHz. The first mode of the coupler corresponds in frequency, at approximately 10 kHz, but the quality factor is different. Below the second resonance of the coupler, at approximately 20 kHz, a peak in the frequency response calculated with the finite element model appears, and is due to the second eigenmode of the cantilevers, not simulated with the lumped element model. The frequency of the second eigenmode of the coupler is different in both simulations.

3.2.8 Stress

The previously described static simulation is also used to have a first evaluation of the stress in the mechanical structure of the loudspeaker. The stress is determinant in the design of the loudspeakers, as it often limits the maximum displacement of the structure. The large displacement reached by the actuators creates high stress concentration at the tip of the cantilevers and could damage the loudspeaker in use. Because the resonant behavior of the loudspeaker is corrected externally using an active peak filter, the maximum displacement of the loudspeaker is assumed to be the displacement below the resonance frequency, that can be approximated by the static displacement. To ensure the stress is below the maximum admissible stress, a stress study is carried out on the model, in the stationary domain, with a finer mesh. The model uses an input voltage of 30 V, which is assumed to be the maximum admissible

across the piezoelectric layer. The stress is displayed as the Von Mises stress on the surfaces of the actuators. This stress is described with the following equation

$$\sigma_v^2 = \frac{1}{2} ((\sigma_{11} - \sigma_{22})^2 + (\sigma_{22} - \sigma_{33})^2 + (\sigma_{33} - \sigma_{11})^2 + 6(\sigma_{23}^2 + \sigma_{31}^2 + \sigma_{12}^2)), \quad (3.11)$$

with σ_{ij} the components of the Cauchy stress tensor, describing the nine stresses in the nine dimensions of the solid, written as

$$\boldsymbol{\sigma} = \begin{bmatrix} \sigma_{11} & \sigma_{12} & \sigma_{13} \\ \sigma_{21} & \sigma_{22} & \sigma_{23} \\ \sigma_{31} & \sigma_{32} & \sigma_{33} \end{bmatrix}. \quad (3.12)$$

The stress is then depicted on the surface of the actuators. The plate is hidden, as most of the stress is concentrated into the flexible part of the actuators. The Von Mises stress of the structure is shown in Figure 3.17(a), and a zoom on the highest stress is shown in Figure 3.17(b). The highest Von Mises stress is located at the tip of the elastic layer of the actuators, under the coupling bloc. The longitudinal stress in the piezoelectric actuators is also observed, with a value ranging from 100 MPa to 150 MPa for a piezoelectric layer of 2 μm .

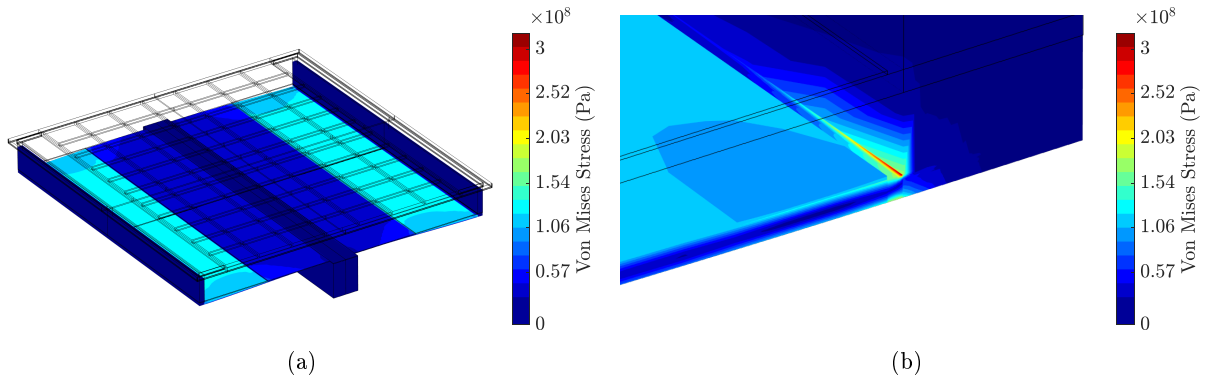


Figure 3.17: 3D view of Von Mises stress in the actuators (a) and zoomed around the location of the maximum Von Mises stress (b)

For the designed micro-loudspeaker with an elastic layer $t_m = 12 \mu\text{m}$, the maximum Von Mises stress observed for a maximum static deflection is around 300 MPa, which is way below the admitted yield stress for silicon [111].

3.2.9 Geometric Nonlinearities

The stationary study of the model can also be used to evaluate the linearity of the loudspeaker. When turning the evaluation of the geometric nonlinearities on, the result of the simulations drastically changes for the clamped-guided case. Due to the difference of curvilinear abscissa ΔL between the deformed and the undeformed actuator, a longitudinal stress appears in the flexible part of the actuator. This stress stiffens the actuator as a function of the displacement, which reduces the performance and increases the THD. Figure 3.18(a) depicts a schematic of a beam subjected to a deformation δ_0 in the z axis and of ΔL in the x axis. The displacement of the end of the actuator is prescribed along x and the deflection is computed with and without the geometrical nonlinearities. The comparison is depicted in Figure 3.18(b). In the finite element model, the piezoelectric material is considered linear, and the nonlinearity only comes from the stiffening effect.

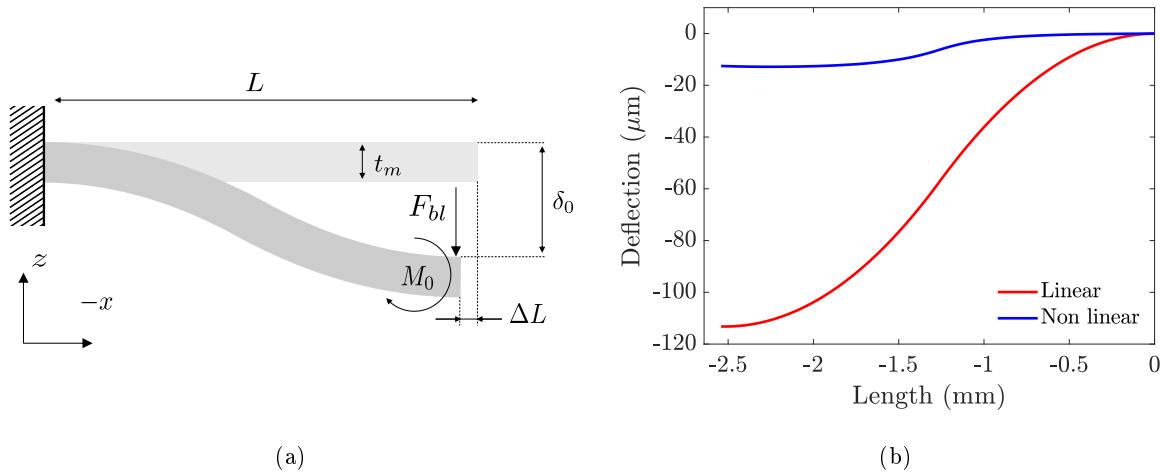


Figure 3.18: Schematic cross section of a clamped-rotation locked cantilever, highlighting the change of projected length ΔL (a) and deflection of the actuators, with and without considering the geometrical nonlinearities in the finite element model (b)

Due to the stiffening effect of the flexible part of the actuators, the displacement taking into account the geometrical nonlinearities is nine times smaller than what is simulated without the geometrical nonlinearities. This would result into a higher resonance frequency, and in a much lower sound pressure level. The displacement can also be depicted as a function of the input voltage, and the result for the linear and nonlinear cases is presented in Figure 3.19(a).

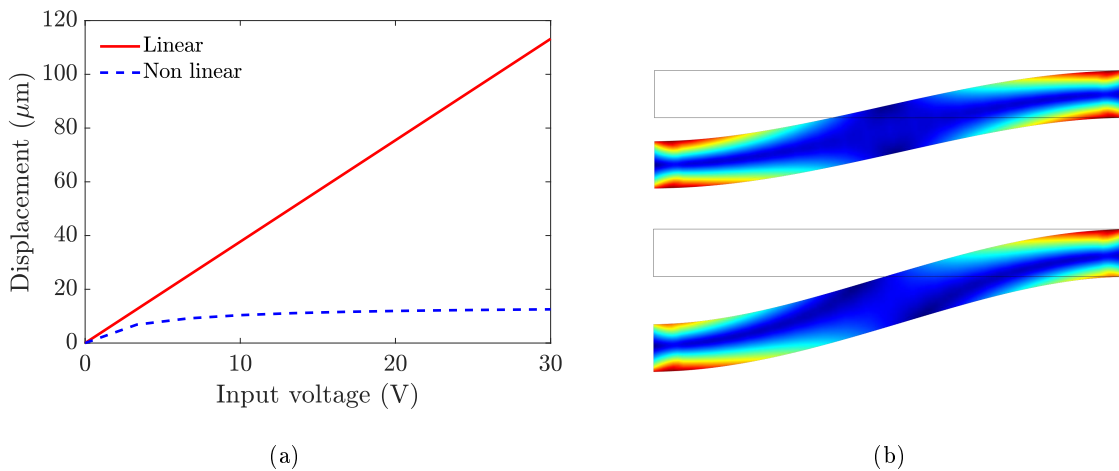


Figure 3.19: Linear and nonlinear stiffness of a clamped-guided silicon beam with a thickness of $12\ \mu\text{m}$, a width W of $5.8\ \text{mm}$ and a length L of $2.641\ \text{mm}$ (a) and Von Mises stress in a clamped-guided cantilever without (on top) and with (on bottom) nonlinearities considered (b) in COMSOL[®] (not on scale)

By forcing a displacement on a simple beam, the difference of the distribution of the stress, taking into account the nonlinearities or not can be observed as well in the finite element model. In the linear case, the concentration of stress is symmetrical on the top and the bottom of the beams, in the compressive and tensile parts. Similarly to what is depicted in Figure 3.18(b), the deflection shape is different as well.

To circumvent this problem, the end of the flexible part of the actuators should be free to move along x .

3.3 Linearization Spring

3.3.1 General Structure

The linearization spring is a deformable structure, placed between the flexible part of the actuators and the moving plate. The structure appear in red in Figure 3.20, where a deformed half cross section of the loudspeaker is represented as a rigid body model with hinges. When the flexible part of the actuators of thickness t_m bends under the stress created by the piezoelectric layer, it adopts a pseudo-clamped-guided deflection shape, as the end of the beam can rotate of an angle ϕ_0 , as well as the coupling block of height h_0 . This rotation, due to the bending of the linearization spring in red in Figure 3.20, experiencing a moment M_{ls} , allows a displacement δL along x of the end of the flexible part of the actuator to diminish the stress in this direction.

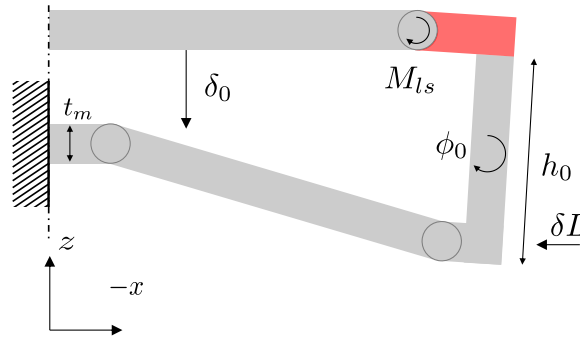


Figure 3.20: Working principle of the linearization spring represented as hinges and rigid bodies

3.3.2 Static Modeling

The linearization spring is designed using a static and a dynamic model. The nonlinear stiffness of a clamped guided beam considering the stiffening due to the elongation of the neutral line can be calculated using [113]

$$F_{bl} = \delta_0 k_0 \left(1 + \frac{1}{2} \left(\frac{\delta_0}{t_m} \right)^2 \right) \quad (3.13)$$

with

$$k_0 = \frac{12EI}{L^3} \quad (3.14)$$

the linear apparent stiffness of the beam and δ_0 the displacement at the guided end. The analytical nonlinear stiffness can be compared to the linear stiffness in Figure 3.21(a). It shows a similar behavior as what is depicted in Figure 3.19(a), with a displacement saturating at a higher force (or higher input voltage, converted into a force by the piezoelectric layer).

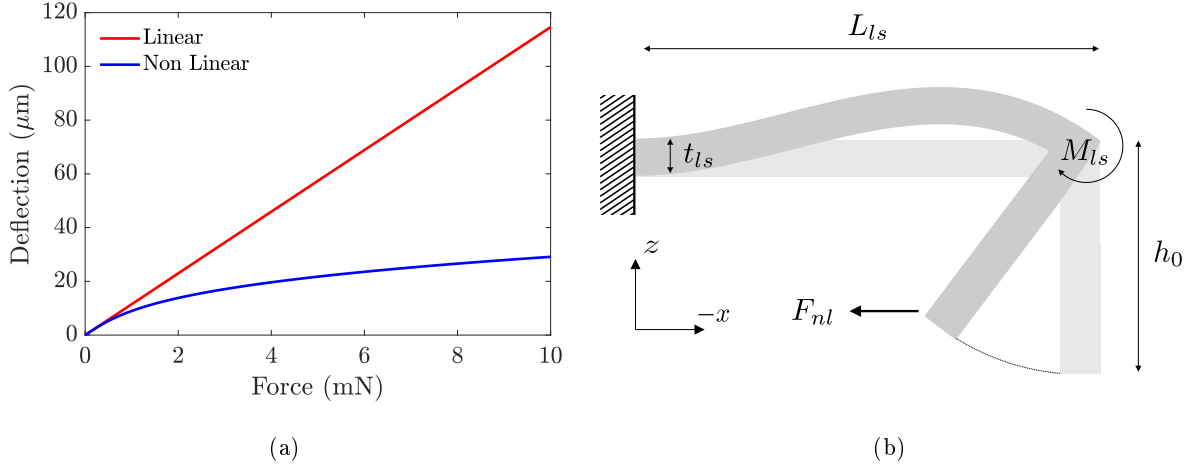


Figure 3.21: Linear and nonlinear stiffnesses of a clamped-guided silicon beam with a thickness of $12\ \mu\text{m}$, a width W of $5.8\ \text{mm}$ and a length L of $2.641\ \text{mm}$ (a) and cross section schematic of the coupling block of height h_0 attached to a linearization spring (b)

To do this, the structure depicted in Figure 3.21(b) is added between the tip of the beam and the moving plate, as it is represented with a rigid body model in red in Figure 3.20. This structure is a deformable plate of silicon one end of which is solidly attached to the plate, and the other end is solidly attached to a rigid part of height h_0 (the coupling block), which is connected to the tip of the actuator. The stiffness along x of the structure depicted in Figure 3.21(b) can be derived using Bernoulli's equation for the beam to calculate the bending torque M_{ls} at the ending tip. The tip of the linearization spring is assumed to not move along y , and so, only the rotation is taken into account. The moment at each point x along the beam is equal to the second derivative of the deflection profile of the beam $\delta_{ls}(x)$ times the moment of inertia and the Young's modulus of the material such as

$$M(x) = -EI \frac{\partial^2 w_{ls}^2}{\partial x^2}. \quad (3.15)$$

Solving Equation 3.15 with the boundary conditions, clamped at $x = 0$ and simply supported at $x = -L$, the bending torque is

$$k_r = \frac{4EI_{ls}}{L_{ls}}. \quad (3.16)$$

To convert this bending torque into a stiffness along x , we use that $k_{ls} = k_r/h_0^2$, with k_{ls} the apparent linear stiffness of the structure along x . The height h_0 behaves as a lever and affects greatly the apparent stiffness seen by the actuator. The resulting equivalent stiffness of the beam can be added in series to the stiffness of the actuators along x , and the equivalent total stiffness along x becomes

$$k_{tot} = \frac{k_{ls}k_{ac}}{k_{ac} + k_{ls}}. \quad (3.17)$$

By using α as the ratio between the linearization spring stiffness and the actuator longitudinal stiffness, Equation 3.13 is modified taking the linearization spring into account and writes [113]

$$F_z = k_0 \delta_0 \left(1 + \frac{\alpha}{2} \left(\frac{\delta_0}{t_m} \right)^2 \right). \quad (3.18)$$

As it can be deduced from Equation 3.18, the stiffness of the linearization spring needs to be small compared to the longitudinal stiffness of the beam in order to improve their linearity. The displacement as a function of the input forces for different dimensions of the linearization spring is depicted in Figure 3.22(a). As it can be deduced from Figure 3.22(a), the linearization spring greatly improves the linearity of the displacement of the loudspeaker and should significantly reduce the THD in the low frequency range.

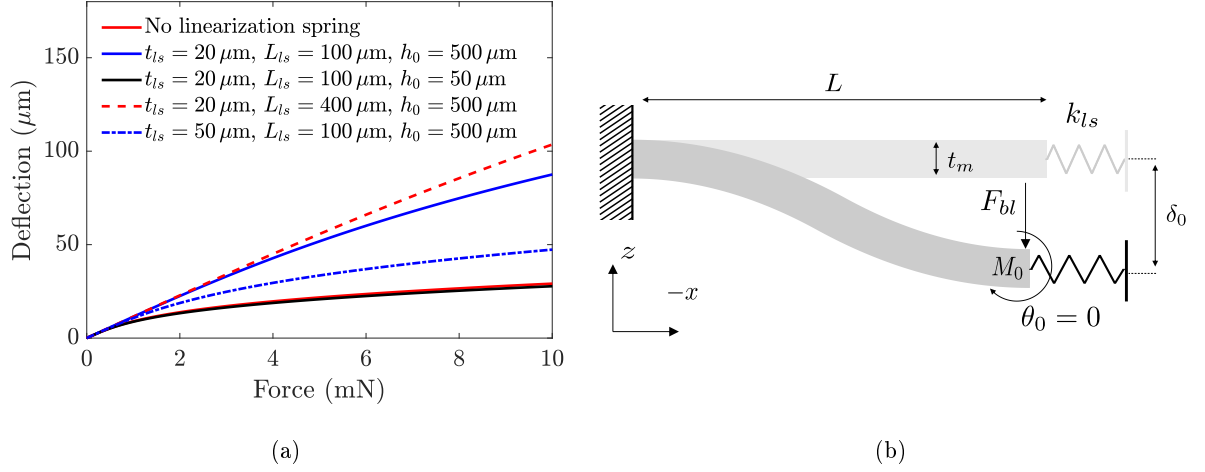


Figure 3.22: Analytical nonlinear stiffness without and with the linearization spring for different parameters t_{ls} , L_{ls} and h_0 (a) and simplified semi lumped cross section view of a nonlinear beam attached to the linearization spring (b)

Knowing that the stiffness is proportional to the cube of the thickness t_{ls} of the linearization spring, inversely proportional to the square of the height h_0 and proportional to the length L_{ls} , an optimal working point can be chosen in order to reduce the nonlinearities, and this corresponds to a thickness t_{ls} of 20 μm, a length L_{ls} of 400 μm and a coupling block height h_0 of 500 μm.

To not affect the working principle of the loudspeaker, the linearization spring needs to be stiff enough in the z direction, in order to transmit the complete force generated by the actuators to the plate. In order to evaluate the influence of the stiffness of the linearization spring along z , a third model is derived. This model considers the linearization spring as a clamped-free cantilever in the z direction, and the apparent stiffness then writes

$$k_{l_{sz}} = \frac{EW_{ls}t_{ls}^3}{L_{ls}^3} \quad (3.19)$$

with E the Young's modulus of silicon and W_{ls} , t_{ls} and L_{ls} respectively the width, thickness and length of the coupling spring. The blocked force at the working point then writes

$$F_{ls} = F_{bl} \frac{1 - k_a}{k_a + k_{l_{sz}}} \quad (3.20)$$

with F_{bl} the blocked force and k_a the apparent stiffness of the actuator both derived from Equation 2.8. The working point, the force displacement curve and the stiffness of the linearization spring are displayed in Figure 3.23(b).

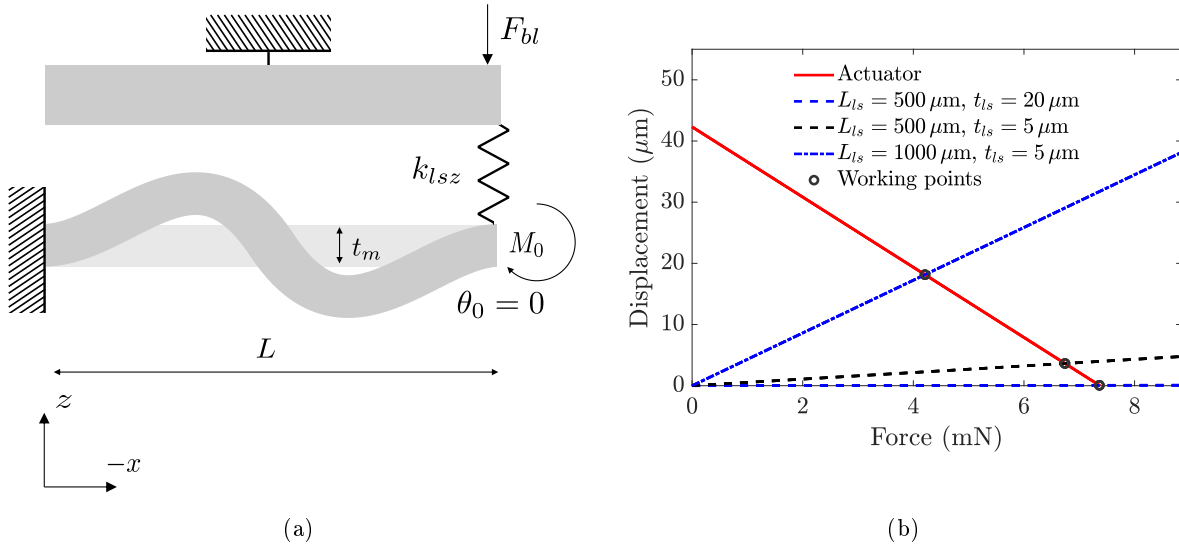


Figure 3.23: Cross section schematic of the piezoelectric actuator linked to the plate of the loudspeaker by an apparent stiffness k_{lsz} (a) and working curves of the actuators crossing the different stiffnesses at different working points (b)

By choosing a stiffer linearization spring, the actuators can fully transfer their force to the plate. It means that the linearization spring doesn't change the blocked force of the actuators, and won't influence the radiated sound pressure level.

3.3.3 Dynamic Modeling

To ensure the linearization spring is not creating an additional modal behavior in the frequency range of interest, the system is simulated by a two degrees of freedom system. The linearization spring is the spring linking the mass of the actuators and the mass of the plate. The equivalent circuit presented in Figure 2.5, neglecting the radiation impedance, is adapted to take into account the linearization spring and is presented in Figure 3.24.

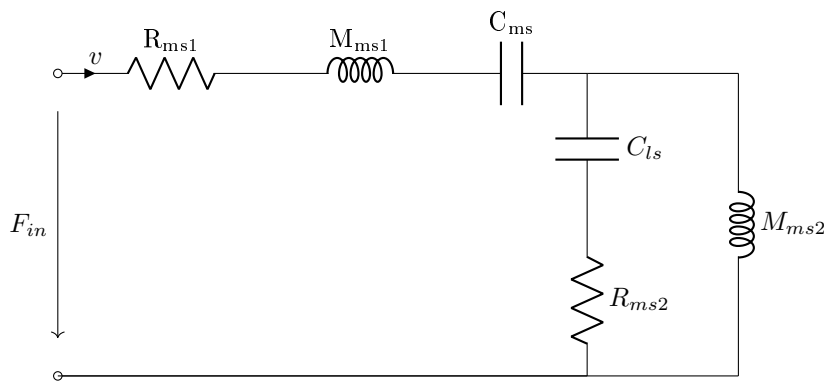


Figure 3.24: Lumped equivalent network of the loudspeaker with a linearization spring

Using the previously derived parameters for the actuators and the linearization spring, the expected pressure response is calculated using

$$p(\mathbf{r}) = j\omega\rho S_d \frac{F_{in}}{Z_{ls} + R_{ms1} + j\omega M_{ms1} + \frac{1}{j\omega C_{ms}}} \frac{e^{jk_0 r}}{2\pi r} \quad (3.21)$$

with

$$Z_{ls} = \frac{-\omega^2 C_{lsz} R_{ms2} M_{ms2} + j\omega M_{ms2}}{-\omega^2 C_{lsz} M_{ms2} + j\omega C_{lsz} R_{ms2} + 1} \quad (3.22)$$

and M_{ms1} the mass of the actuators and the coupling block, C_{lsz} the compliance of the linearization spring in the z direction, C_{ms} the compliance of the actuators, M_{ms2} the mass of the plate and R_{ms1} and R_{ms2} the mechanical losses in the bending elements.

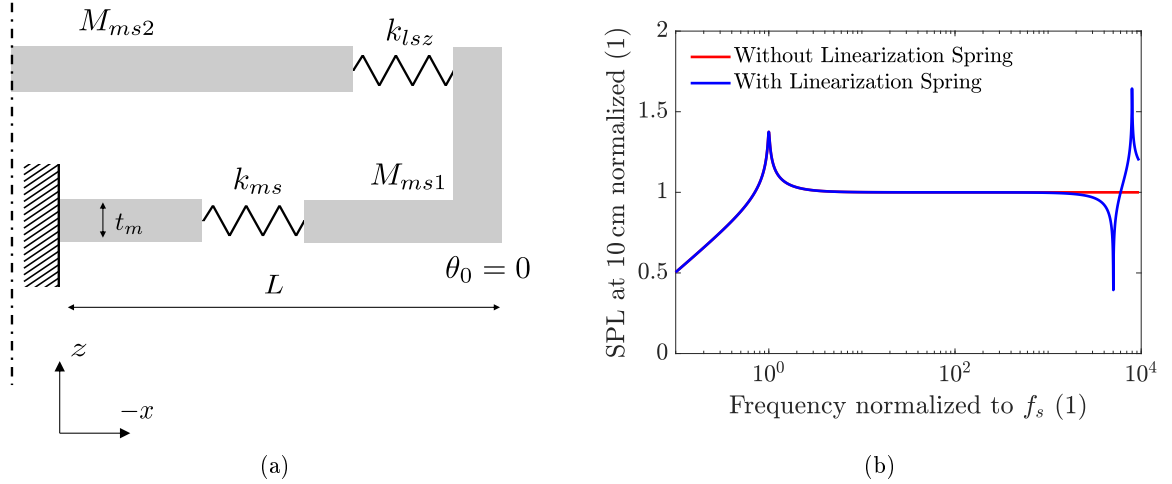


Figure 3.25: Pseudo rigid half cross section of the loudspeaker (a) and pressure radiated by this model in free field (b)

As it is presented in Figure 3.25(b), the linearization spring with the chosen dimensions does not affect the approximated pressure response in the frequency range of interest. From these models, a state space model is derived in the next section in order to see the influence of the nonlinearities on the dynamic response of the loudspeaker.

3.4 State Space Modeling

After using the lumped element model of the loudspeaker to optimize the linear performance, and a finite element model to evaluate the three dimensional behavior of the loudspeaker, as well as the geometrical nonlinearities, a nonlinear model is derived in order to evaluate the linearity of the loudspeaker in the frequency domain. To model the nonlinearities of classical electrodynamic loudspeakers, state space models, port-Hamiltonian systems, Hammerstein models and power series have been extensively used [114–120]. State space models are the most commonly used models to simulate nonlinear effects in electrodynamic loudspeaker, and have shown accurate results. A state space representation is a representation of a system in the time domain. State space modeling mainly consists in entirely describing a system with state variables, that can be any quantities that can be described by differential equations, and expressing the derivative of these quantities as a function of the quantities. The general form of the state space model is written

$$\begin{aligned}\dot{\mathbf{x}} &= \mathbf{A}\mathbf{x} + \mathbf{B}\mathbf{u} \\ \mathbf{y} &= \mathbf{C}\mathbf{x} + \mathbf{D}\mathbf{u}\end{aligned}\quad (3.23)$$

The second equation is not needed for our problem, and the first equation could be detailed as

$$\frac{\partial}{\partial t} \begin{bmatrix} x_1 \\ x_2 \\ \vdots \\ x_n \end{bmatrix} = \begin{bmatrix} a_{11} & a_{12} & \dots & a_{1n} \\ a_{21} & a_{22} & \dots & a_{2n} \\ \vdots & & & \vdots \\ a_{n1} & a_{n2} & \dots & a_{nn} \end{bmatrix} \begin{bmatrix} x_1 \\ x_2 \\ \vdots \\ x_n \end{bmatrix} + \begin{bmatrix} b_{11} & \dots & b_{1r} \\ b_{21} & & b_{2r} \\ \vdots & & \vdots \\ b_{n1} & \dots & b_{nr} \end{bmatrix} \begin{bmatrix} u_1 \\ u_2 \\ \vdots \\ u_r \end{bmatrix}. \quad (3.24)$$

where \mathbf{x} is the state vector, containing n variables, \mathbf{A} is the state matrix, linking the state vector to its derivative, \mathbf{B} is the input matrix and \mathbf{u} contains the input signals. A state space system is usually represented as a block schematic, as shown in Figure 3.26.

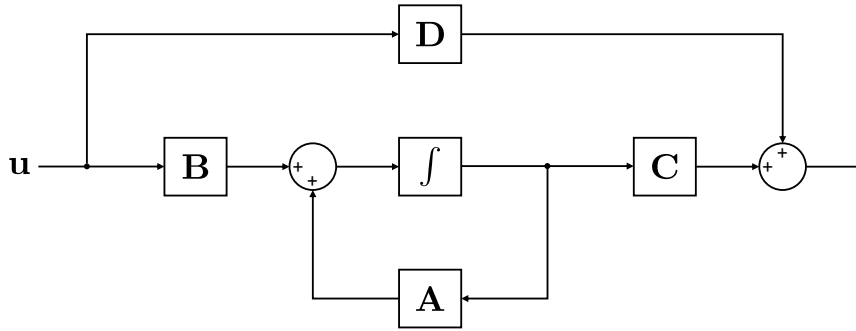


Figure 3.26: Block schematic representation of a state space model

Using a bilinear transform to approximate the derivatives, the discrete matrices can be written as

$$\mathbf{A}_d = \left(\mathbf{I} - \frac{1}{2}\mathbf{A}T_s \right)^{-1} \left(\mathbf{I} + \frac{1}{2}\mathbf{A}T_s \right) \quad (3.25)$$

and

$$\mathbf{B}_d = \left(\mathbf{I} - \frac{1}{2}\mathbf{A}T_s \right)^{-1} \mathbf{B}T_s. \quad (3.26)$$

The system can then be solved iteratively by using

$$\mathbf{x}(k+1) = \mathbf{A}_d\mathbf{x}(k) + \mathbf{B}_d\mathbf{u}(k) \quad (3.27)$$

with k the iteration and T_s the sampling time.

3.4.1 Free Field

From the equivalent electrical circuit of the piezoelectric loudspeaker, whose parameters are amplitude dependent, as it presented in Figure 3.27, the governing equations can be derived.

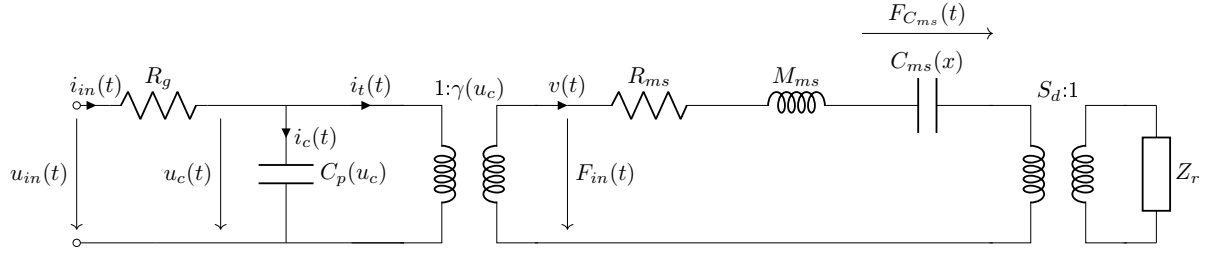


Figure 3.27: Linear lumped equivalent network of the loudspeaker

As in classical bigger electrodynamic loudspeakers, the expected main nonlinearities are expected to be the transduction γ , that depends on the input voltage, the compliance C_{ms} , that depends on the displacement and the capacitance C_p that depends on the voltage u_c . All other parameters are considered constant. The effect of the radiation impedance Z_{rad} on the behavior of the loudspeaker is considered as very small in the frequency range of interest, and the circuit can be simplified to the electrical and the mechanical parts only. The system contains three elements that store energy, the electrical capacitor C_p , that stores an electric charge, the compliance C_{ms} , that stores potential energy, and the mass M_{ms} that stores kinetic energy. The displacement is needed to simulate displacement dependent nonlinear effects, but is not required to fully define the system. The circuit can be described by the following equations

$$\frac{\partial u_c(t)}{\partial t} = -\frac{\gamma(u_t)}{C_p(u_c)}v(t) - \frac{1}{R_g C_p(u_c)}u_c(t) + \frac{1}{R_g C_p(u_c)}u_{in}(t), \quad (3.28)$$

$$\frac{\partial v(t)}{\partial t} = \frac{\gamma(u_t)}{M_{ms}}u_t(t) - \frac{R_{ms}}{M_{ms}}v(t) - \frac{1}{M_{ms}}F_{C_{ms}}(t), \quad (3.29)$$

$$\frac{\partial x(t)}{\partial t} = v(t) \text{ and} \quad (3.30)$$

$$\frac{\partial F_{C_{ms}}(t)}{\partial t} = \frac{1}{C_{ms}(x)}v(t). \quad (3.31)$$

By defining the state vector as the voltage $u_c(t)$ across the capacitor C_p , the velocity $v(t)$ inside the mechanical circuit, the displacement $x(t)$ and $F_{C_{ms}}(t)$ the force generating the bending of the actuator, the matrix **A** and **B** can then be derived from Equations 3.28 to 3.31 and write

$$\frac{\partial}{\partial t} \begin{bmatrix} u_c(t) \\ v(t) \\ x(t) \\ F_{C_{ms}}(t) \end{bmatrix} = \begin{bmatrix} -\frac{1}{R_g C_p(u_c)} & -\frac{\gamma(u_c)}{C_p(u_c)} & 0 & 0 \\ \frac{\gamma(u_t)}{M_{ms}} & -\frac{R_{ms}}{M_{ms}} & 0 & -\frac{1}{M_{ms}} \\ 0 & 0 & 1 & 0 \\ 0 & \frac{1}{C_{ms}(x)} & 0 & 0 \end{bmatrix} \begin{bmatrix} u_c(t) \\ v(t) \\ x(t) \\ F_{C_{ms}}(t) \end{bmatrix} + \begin{bmatrix} \frac{1}{R_g C_p(u_c)} \\ 0 \\ 0 \\ 0 \end{bmatrix} u_{in}(t). \quad (3.32)$$

Using Equation 3.27, the system is solved numerically. The sampling frequency is chosen high enough in order to avoid unwanted distortion in the audio range. The velocity of the system $v(t)$ resulting from an input dirac voltage is calculated and used to calculate the frequency response using the Hyugens integral. The radiated pressure at 10 cm can then be displayed as a function of frequency, as it is shown in Figure 3.28(a). Using a multitone signal, the absolute amplitude of the state space model can be compared with the amplitude simulated using a lumped element method. There is a perfect agreement between the two models, as it is presented in Figure 3.28(a).

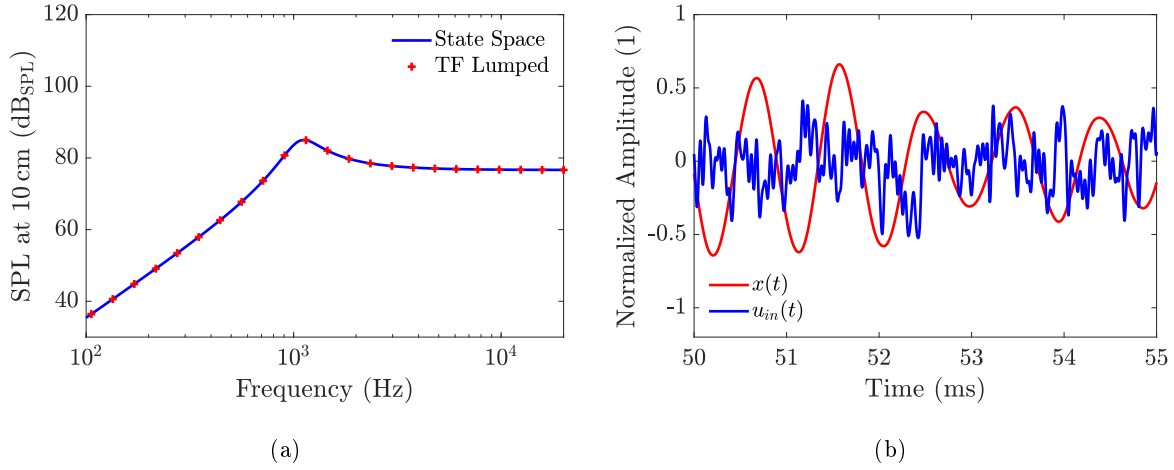


Figure 3.28: Pressure response calculated with the state space model and with the lumped model (a) and input multitone signal and the resulting displacement $x(t)$ computed with the State Space model (b)

In addition to the simulated frequency response of the loudspeaker, the time input signal $u_{in}(t)$ and the displacement $x(t)$ of the loudspeaker are displayed in Figure 3.28(b). As expected, the displacement of the loudspeaker is delayed compared to the input signal, and the high frequencies are filtered, due to the low pass filter shape of the frequency response of the displacement. Using this model, the value of the linear parameters, such as the compliance C_{ms} , the transduction factor γ and the capacitance C_p can be set to be level dependent, in order to introduce nonlinearities in the model, such as discussed in Section 1.3. The nonlinear parameters can be determined from analytical models, finite element simulations or measurements. To evaluate the total harmonic distortion of the loudspeaker in free field, the geometric nonlinearity $C_{ms}(x)$ is expressed with Equation 3.18. The nonlinearity of the transduction factor $\gamma(u_c)$ is expressed from an electromechanical measurement of the piezoelectric material presented in Section 4.2.

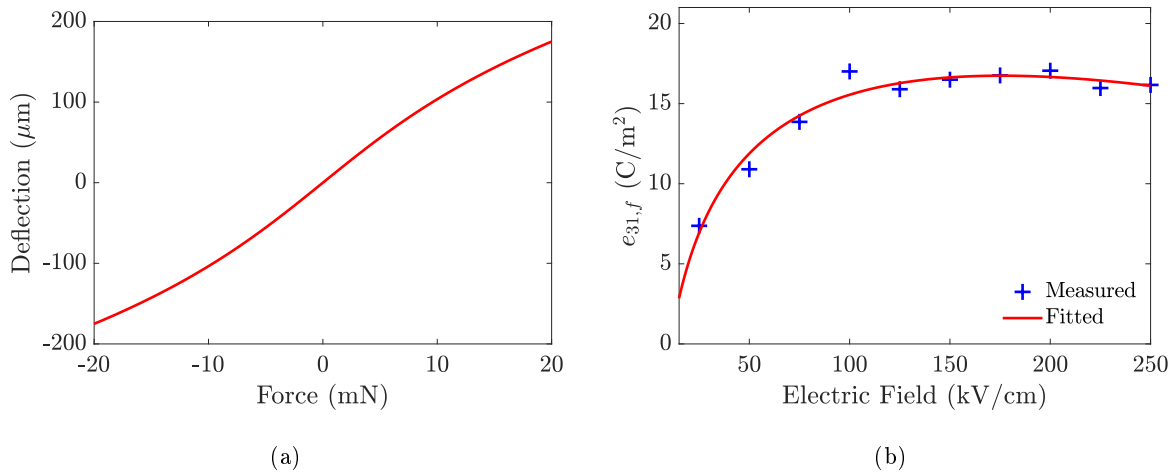


Figure 3.29: Nonlinear theoretical $C_{ms}(x)$ function (a) and nonlinear $\gamma(u_c)$ fitted from measurements (b)

Figure 3.29(a) depicts the nonlinear stiffness of the loudspeaker. It shows that the increase of displacement is smaller for larger forces. Although the loudspeaker is not symmetric along z , the nonlinear stiffness

is assumed to be identical for positive and negative values of force and displacement. The transduction factor $\gamma(u_c)$ is estimated using Equation 3.33 and a fit of the measurement of the piezoelectric coefficient $e_{31,f}$ as a function of the input voltage. The fitted function is of the form

$$f(x) = a \ln (bx) - cx + d \quad (3.33)$$

with a , b , c and d determined using a nonlinear fitting algorithm. The measurement and the fitted function are depicted in Figure 3.29(b). For the nonlinear capacitance, the hysteresis is neglected and a Lorentz function is used on a measurement of the capacitance as a function of the input voltage. Using Equation 1.6 and the nonlinear functions, the THD of the loudspeaker can be computed for different input voltages u_{in} and independently for each parameters, as presented respectively in Figure 3.31(a) and 3.31(b).

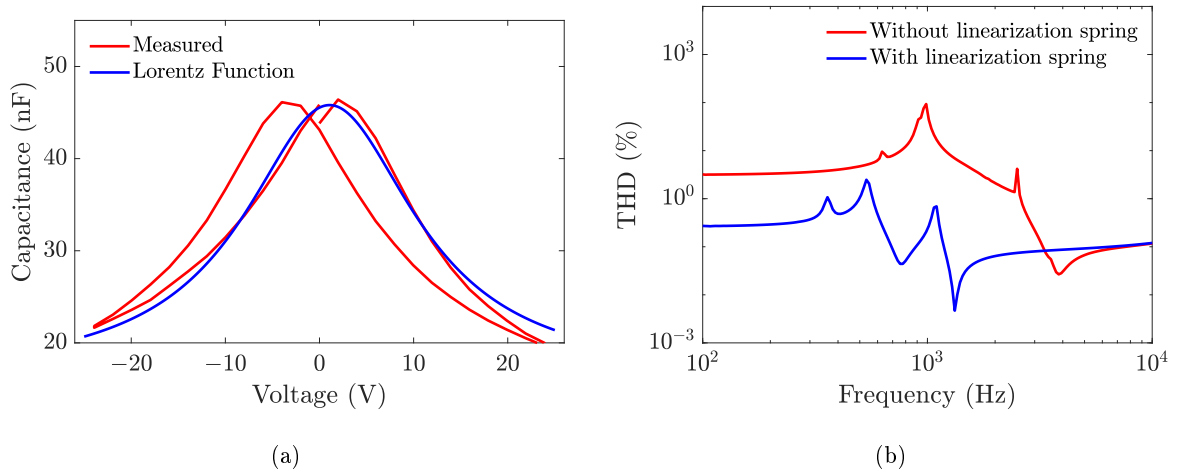


Figure 3.30: Nonlinear capacitance $C_p(u_c)$ fitted to a measurement (a) and total harmonic distortion calculated with the nonlinear model for the loudspeaker with and without linearization spring (b)

Figure 3.30(b) shows the advantage of the linearization spring on the linearity of the loudspeaker. Without linearization spring, the total harmonic distortion rises above 90% at the resonance. With the linearization spring, the THD is around 1% in the whole audio frequency range, with an actuation of 1 V.

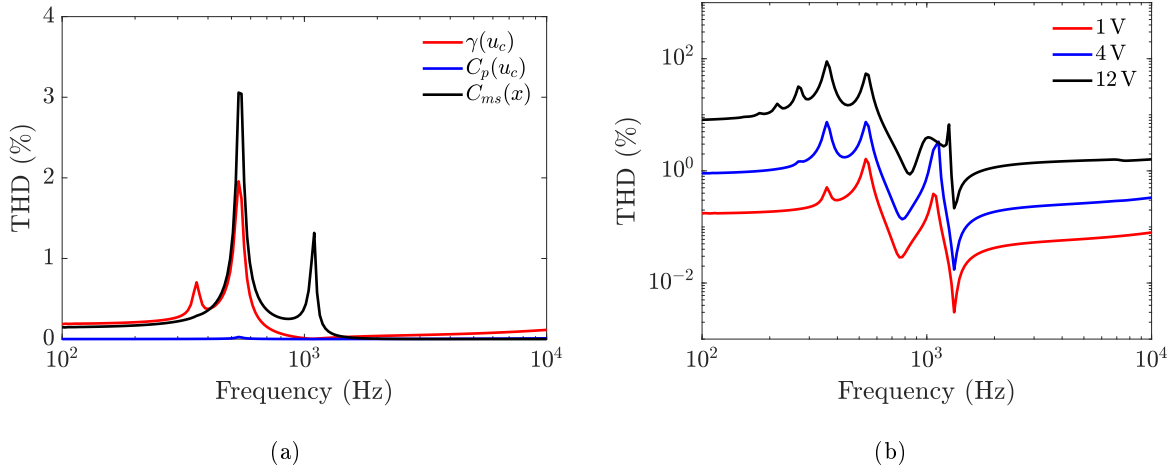


Figure 3.31: Total harmonic distortion at $u_{in} = 1.5$ V independently for each parameters (a) and for different input levels u_{in} (b)

In Figure 3.31(a) the THD is depicted independently for the three nonlinear parameters. The variation of the capacitance C_p with the input voltage creates a negligible distortion in the entire frequency range. The distortion due to the transduction factor γ is constant up to a third of the resonance frequency of the loudspeaker, where the second harmonic is amplified by the frequency response of the loudspeaker. At half the resonance frequency, a second peak of THD is observed. The THD then decreases up to the resonance frequency and starts to increase in the higher frequency range. The variation of the compliance C_{ms} being dependent on the displacement, the distortion generated is at a constant level below the resonance frequency. A peak appears at half the resonance frequency, similarly than for the transduction factor. As the displacement increases at the resonance frequency, a peak of distortion is also observed at the resonance frequency of the loudspeaker. Figure 3.31(b) shows the THD on a logarithmic scale for different input voltages u_{in} . The THD increases with the level and the general shape remains. But the effect of subharmonics is amplified and peaks of distortion down to a sixth of the resonance frequency can be observed for the highest input voltage. For an input level of 12 V, the THD is expected to be as high as 100% below the resonance frequency, which is in line with what is observed for commercial non-MEMS loudspeaker.

3.4.2 In-Ear

Similarly to what is presented for free field applications, the model can be extended to in-ear applications. The electrical equivalent circuit of the loudspeaker radiating inside an IEC 60318-4 coupler is shown in Figure 3.32. The equivalent circuit is written in its nonlinear form, including the parameters $C_{ms}(x)$, varying with the displacement and the parameters $\gamma(u_c)$ and $C_p(u_c)$ varying with the voltage $u_c(t)$ across the piezoelectric layer. Equations 1 to 13 in the appendix A are derived from the equivalent circuit, and the state matrix is also derived from these equations once a state vector is chosen and presented in Equation 3.34.

Firstly and similarly to what is presented for the free field case, the frequency response of the main loudspeaker inside a coupler is compared with the one computed with the lumped element model. The comparison is presented in Figure 3.33(a).

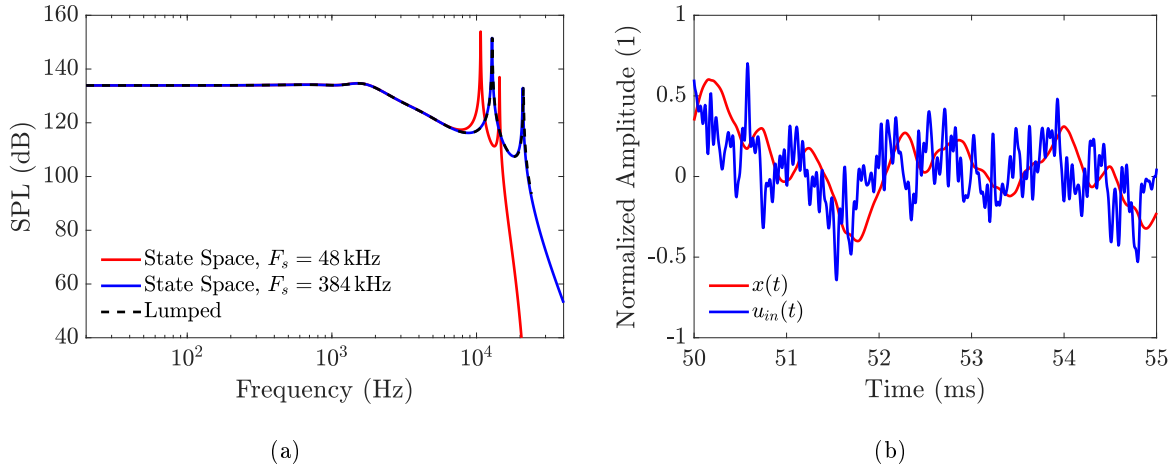


Figure 3.33: Pressure response calculated with the state space model for different sampling frequencies F_s and with the lumped model (a) and input multitone signal and the displacement $x(t)$ computed with the state space model (b)

Both frequency responses are identical, except for the small discrepancies in high frequencies for a sampling frequency of 384 kHz. For a sampling frequency of 48 kHz, the discrepancies are too large, and are more critical in the case of the in-ear simulation, compared to the free field case, where the frequency response is constant in the higher frequency range. The difference being small and as an increase of the sampling frequency increases the computation time, the sampling frequency is chosen to be $F_s = 384$ kHz. Similarly as for the free field case, nonlinear parameters are programmed to be level-dependent and the THD is computed for different input levels and independently for each parameter. In the time domain and as it is depicted in Figure 3.33(b), the low pass filter behavior of the transducer inside the coupler is observable when a multitone signal is used.

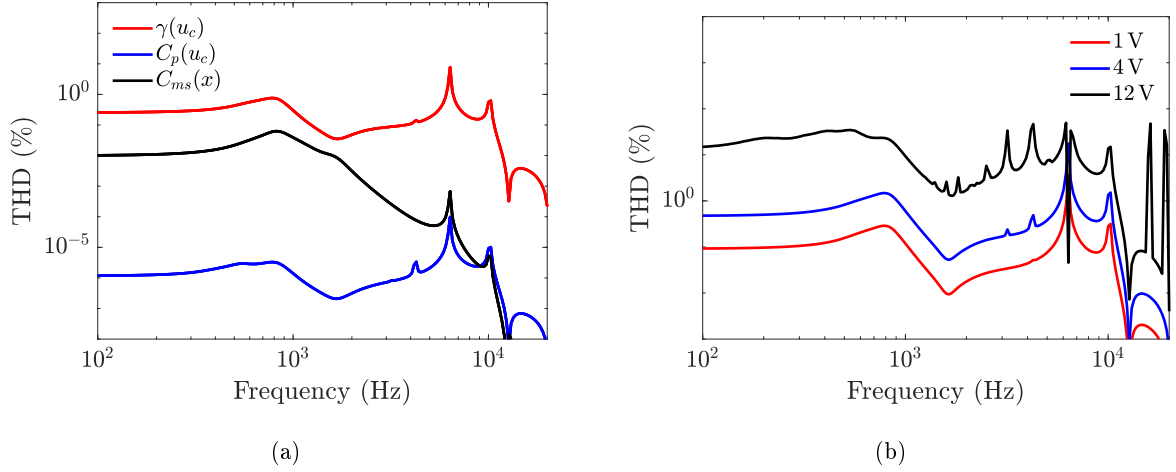


Figure 3.34: Total harmonic distortion at $u_{in} = 1.5$ V independently for each parameters (a) and for different input levels u_{in} (b)

Similarly to what is observed for the free field case, the variation of the capacitance C_p with the voltage u_c creates a negligible harmonic distortion, a few orders of magnitude lower than the one generated by the two other nonlinear parameters as it is depicted in Figure 3.34(a). The THD due to the variation of the compliance C_{ms} is maximum around the mechanical resonance of the loudspeaker inside the coupler, at approximately 1 kHz. It remains high in lower frequencies. The distortion due to the transduction factor is the biggest contribution to the total harmonic distortion and is similar to the frequency response of the loudspeaker, but shifted one octave lower in frequency. Figure 3.34(b) depicts the evolution of the THD with the level on the input voltage u_{in} . The overall shape of the THD is similar and increases with the input voltage. Subharmonics peaks appear for lower levels due to the resonances of the coupler. At an input voltage of 12 V, which corresponds to a pressure inside the coupler of more than 120 dB_{SPL}, the THD is as high as 10% for most frequencies.

3.4.3 Loudspeaker Design Summary

From the previously described studies, the final dimensions of the loudspeaker are set and the loudspeaker is declined into different variants. The main variant is the 6×6 variant, as a reference to the dimensions of the moving plate. The main dimensions of the actuators of the loudspeakers are recalled in Figures 3.35(a) and 3.35(b) for the bottom wafer, and are depicted in Figures 3.8(a) and 3.8(b) for the top wafer.

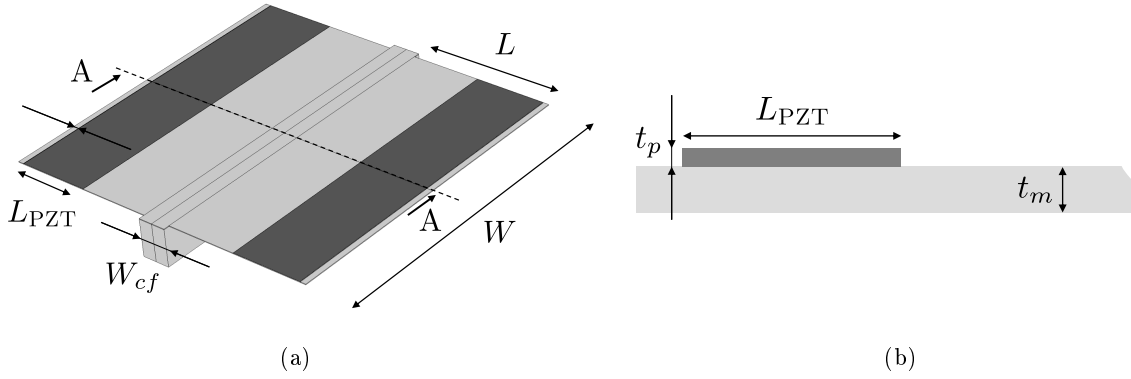


Figure 3.35: 3D CAD view of the actuators of the loudspeaker (a) and partial cross section of the actuators of the loudspeaker (not to scale) (b)

Table 3.2 recalls the varying dimensions of the variants of the loudspeaker. Parameters related to the thicknesses are fixed by the manufacturing process and are not modified. A few parameters are not variant dependent, such as h_0 the height of the coupling block that is set to $500 \mu\text{m}$, L_{fpx} the width of the plain frame around the plate in the x direction that is set to $100 \mu\text{m}$, L_{fpy} the width of the plain frame around the plate in the y direction that is set to $99 \mu\text{m}$, L_{ls} the length of the coupling spring determined in Section 3.3 that is set to $500 \mu\text{m}$, t_{pl} the total thickness of the plate that is set to $80 \mu\text{m}$, t_{pp} the thickness of the plain plate that is set to $20 \mu\text{m}$, w_s the width of the air interstice between the moving plate and the frame, determined in Section 3.2.6 and set to $9 \mu\text{m}$, t_m the thickness of the flexible part of the actuators that is set to $12 \mu\text{m}$, t_p the thickness of the piezoelectric material is set to $2 \mu\text{m}$ and W_{cf} the width of the center frame that is set to $500 \mu\text{m}$.

Table 3.2: Main dimensions of the nine different variants of the loudspeaker (mm)

Parameter	6×6 (1)	8×8 (2)	8×6 (3)	6×8 (4)	5×5 (5)	4×4 (6)	4×3 (7)	3×4 (8)	3×3 (9)
S_d (mm ²)	36	64	48	48	25	16	12	12	9
W	5.8	7.8	5.8	7.8	4.8	3.8	2.8	3.8	2.8
L	2.641	3.641	3.641	2.641	2.641	1.641	1.641	1.641	1.641
W_p	6	8	6	8	5	4	3	4	3
L_p	6	8	8	6	5	4	4	3	3
L_{PZT}	1.2255	1.7255	1.7255	1.2255	0.9755	0.7255	0.7255	0.4755	0.4755
W_{ls}	5.782	7.782	5.782	7.782	4.782	3.782	2.782	3.782	2.782
L_{rr}	0.6491	0.9349	0.9349	0.6491	0.5063	0.3634	0.3634	0.2206	0.2206
W_{rr}	0.5	0.6818	0.5	0.6818	0.409	0.3182	0.2273	0.3182	0.2273

Frequency responses of the nine designs are depicted in Figure 3.36(a). The smaller designs are safer in terms of maximum stress, because their resonance frequency are higher, leading to a smaller displacement of the moving plate below the resonance frequency. The larger designs are displaying better performance, with a lower resonance frequency and a similar sound pressure level, leading to a wider bandwidth, but the maximum stress in the actuators is higher than the recommended one for silicon.

Also, larger designs are softer in the z direction but also in the x and y directions, leading to a poorer guiding of the moving structure. As the resonance frequency of the loudspeaker depends mainly on the length of the actuators, the rectangular design have a similar resonance frequency as the square loudspeaker of same length.

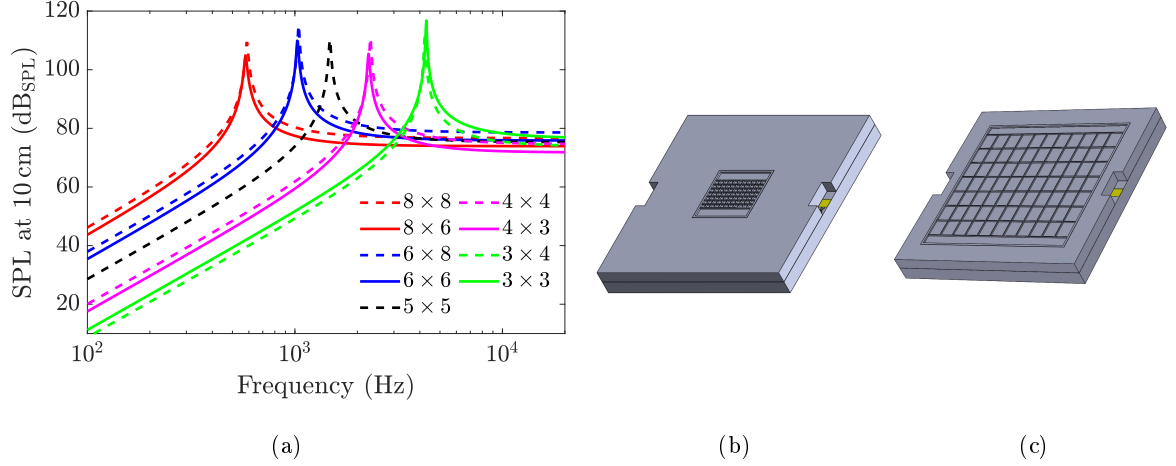


Figure 3.36: Frequency responses of the different variants of the loudspeaker simulated using the lumped element circuit of Section 2.2 (a), 3D CAD view of the 3 × 3 variant (b) and of the 8 × 8 variant (c)

The loudspeakers are then equally distributed on the wafer, in order to make them more independent of the etching inhomogeneity across the radius of the wafer. The mapping of the cell in which the loudspeakers are manufactured is presented in Figure 3.37 and the variants correspond to the number given in Table 3.2. The external size of the frame does not vary with the dimensions of the loudspeaker, as it is depicted in Figure 3.36(b) and 3.36(c). Each cell measures 10 × 10 mm² and 137 cells are distributed on the 200 mm wafer, as depicted in Figure 3.37.

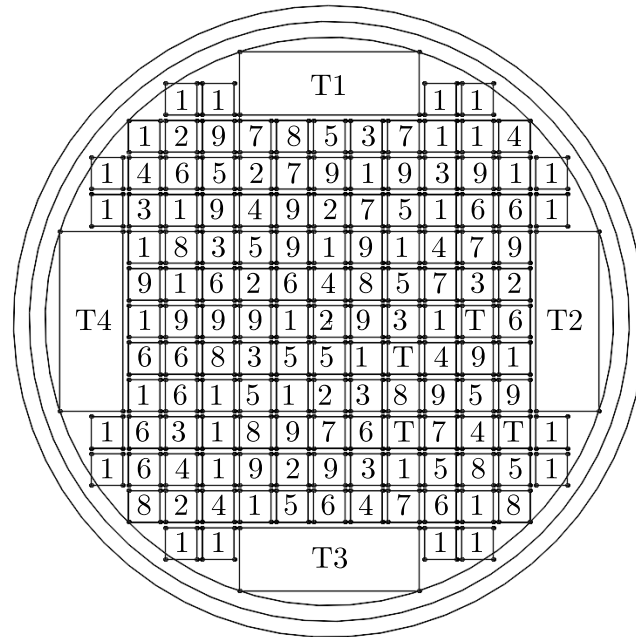


Figure 3.37: Mapping of the loudspeakers on the wafer

Test zones, providing standardized capacitors and other devices related to testing of the correct manufacturing of the piezoelectric layer for example are also distributed on the wafer and are identified with a T in Figure 3.37. Four larger zones are reserved for electromechanical tests devices in cells T1, T2, T3 and T4. Loudspeakers are then manufactured using the process flow detailed in Section 4.2.

3.5 Chapter Conclusion

In this chapter and from the parameters derived in Chapter 2, two more advanced models were derived, in order to simulate three-dimensional aspects of the loudspeaker, as well as evaluating the nonlinear performance of the loudspeaker. In the next chapter, the manufacturing process that was designed concurrently with the finite element model is detailed, as well as the characterization results.

Chapter 4

Technological Realization & Characterization

Contents

4.1	Chapter Introduction	104
4.2	Technological Realization	104
4.2.1	Bottom Wafer (Electromechanical Wafer)	104
4.2.2	Top Wafer (Mechanoacoustical Wafer)	111
4.2.3	Wafer Bonding	114
4.3	Mechanical Characterization	117
4.3.1	Stiffness	117
4.4	Electrical Characterization	118
4.4.1	Impedance	118
4.4.2	Amplifier	119
4.5	Acoustical Characterization	120
4.5.1	Pressure Response on Wafer	120
4.5.2	Pressure Response in Anechoic Chamber	122
4.5.3	Directivity	124
4.6	Non Linearities	124
4.6.1	Frequency Response	124
4.6.2	Transduction Factor	125
4.6.3	Total Harmonic Distortion	126
4.7	Chapter Conclusion	127

4.1 Chapter Introduction

In the first part of this chapter the manufacturing process is detailed step by step, and pictures of the devices are presented at the same time. In the second part, electrical, mechanical and acoustical measurements of the devices and of the amplifier are presented and compared to the modeled ones.

4.2 Technological Realization

4.2.1 Bottom Wafer (Electromechanical Wafer)

Oxide on Device Layer

The first wafer is a thick silicon film on insulator wafer. After being polished and oxidized, the device wafer is bonded on the handle wafer by an automated wafer bonder. The device layer is then grinded down to the desired thickness [121]. The process starts with the wafer with the needed dimensions, a $12\ \mu\text{m}$ thick device layer, and a $675\ \mu\text{m}$ thick handle wafer, separated by a $1\ \mu\text{m}$ thick oxide layer.



Figure 4.1: Bottom wafer

A $500\ \text{nm}$ thick layer of oxide is then deposited on the device layer, and this oxide is thermally strengthened at 800°C , in a $\text{N}_2 + \text{O}_2$ vapour, as it is presented in Figure 4.1.

Piezoelectric Stack Deposition

Then a layer of $10\ \text{nm}$ of Ti is deposited on the top of the SiO_2 layer, and oxidized to a $20\ \text{nm}$ TiO_2 layer. The bottom electrode, a layer of $100\ \text{nm}$ of platinum is deposited by chemical vapor deposition. The PZT is then deposited by spin coating by a successive deposition of layers of $50\ \text{nm}$, until the total thickness of $2\ \mu\text{m}$ is achieved. The top electrode, similarly to the bottom electrode, is deposited by chemical vapor deposition on the top of the PZT and is $100\ \text{nm}$ thick. The resulting technology stack is presented in Figure 4.2.

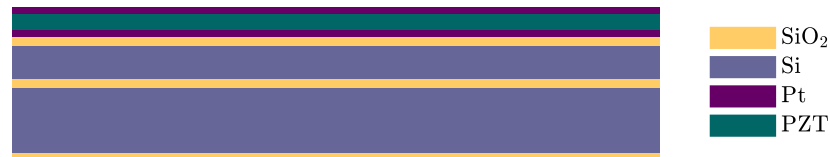


Figure 4.2: Bottom wafer after deposition and etching of the PZT stack layers

After being deposited, the crystalline structure orientation of the PZT can be measured using a X-ray diffractometry (XRD). The result on one wafer is presented in Figure 4.3(a). The required orientation to maximize the piezoelectric effect are the planes (100), (010) and (001), where the outside planes of the tetragonal structure are normal to the electric field. On the measurement, the first peak corresponds to

this orientation, at $2\theta = 22^\circ$. At $2\theta = 31^\circ$, the proportion of crystalline structure in the (110) orientation appears, but they only represent approximately 3% of the total. The orientation (111) appears at $2\theta = 38^\circ$ in a similar proportion as the (110) orientation. The largest peak at $2\theta = 40^\circ$ is due to the crystalline structure of the platinum electrodes, schematically represented in Figure 4.3(b), as well as the three orientations of the PZT.

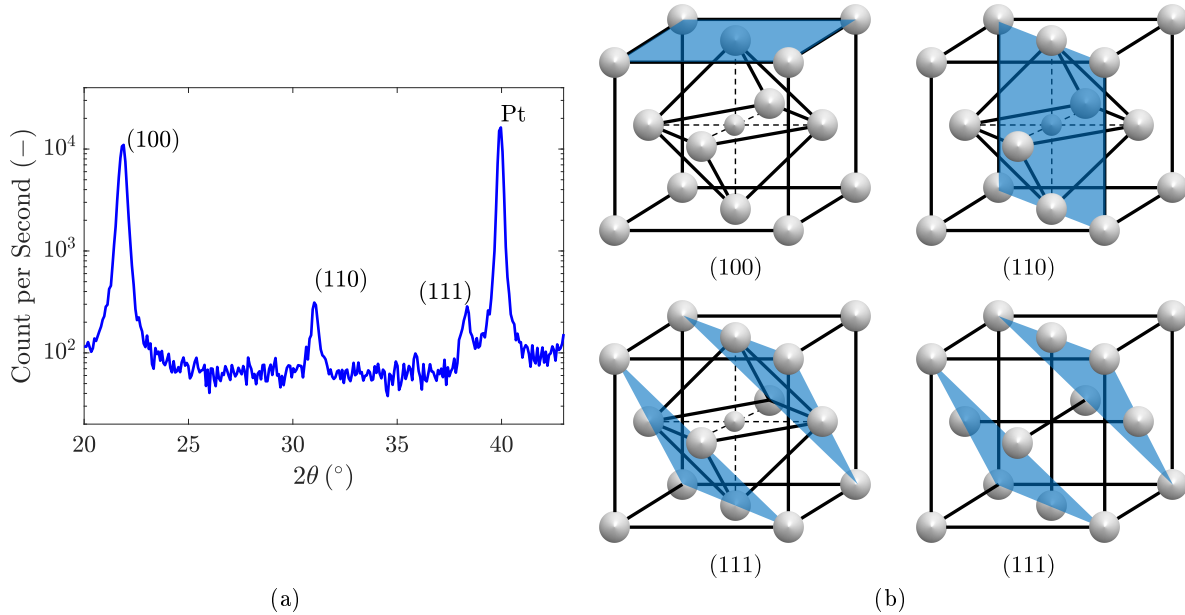


Figure 4.3: XRD measurement of the piezoelectric stack showing the desired orientation (100) of the PZT lattice (a) and planes (100), (110) and (111) for a tetragonal structure (PZT) and plane (111) for a face-centered cubic structure such as the one of platinum (b)

Hard Mask Back Cavity

A hard mask is then etched on the back side of the wafer, in the thermal oxide layer, using a plasma etching. This hard mask is used at the end of the process to release the structure and remains only on the peripheral and on the center frame of the backside of the loudspeakers. The resulting technology stack is presented in Figure 4.4.

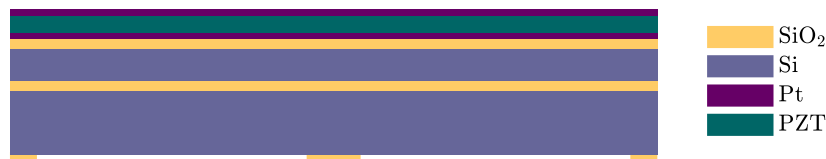


Figure 4.4: Bottom wafer after etching of the hard mask on the handle wafer side

Piezoelectric Stack Etching

The top electrode, the PZT layer and the bottom electrodes are then etched by plasma etching to meet the designed shapes.



Figure 4.5: Bottom wafer after etching of the PZT stack

At this step, the piezoelectric characteristics of the devices are evaluated using an AixACCT TF Analyzer 2000. The polarization loop is evaluated on a 1 mm^2 test capacitor using a triangular signal of 100 Hz, after a prepolarization pulse. No average is used and the polarization loop for three different input voltages is depicted in Figure 4.6(a). At a polarization voltage of 50 V, corresponding to an electric field of 25 MV m^{-1} for a thickness of $2 \mu\text{m}$ of piezoelectric layer, the material seems to not be completely saturated, as it can be deduced from the tangential slope at the maximum electric field.

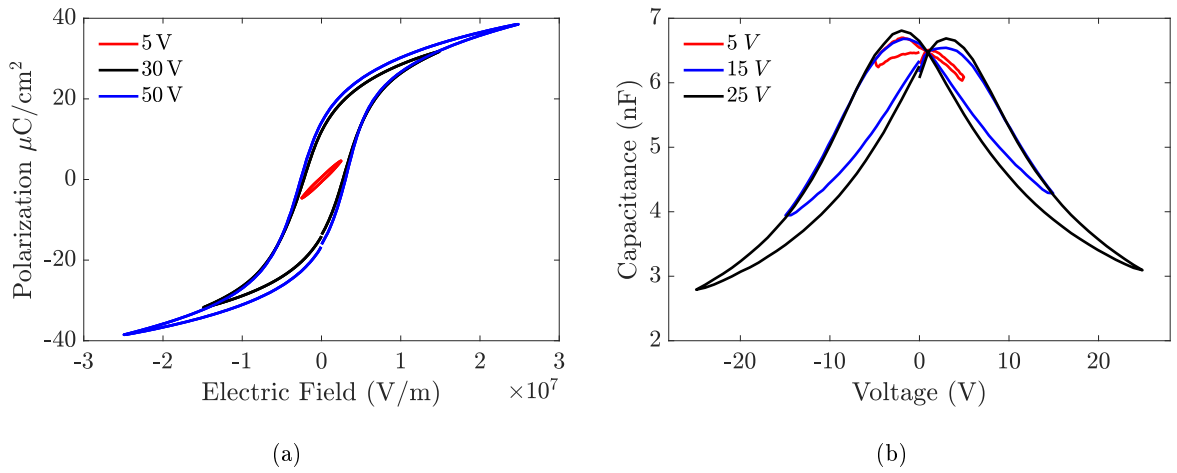


Figure 4.6: Polarization as a function of the electric field (a) and capacitance as a function of the input voltage (b) on test devices on the manufactured PZT

The variation of the capacitance of the piezoelectric layer is then measured using various constant voltage signals on which a smaller sine is added. The capacitance is then estimated with the sine for different offsets, and this gives the curve depicted in Figure 4.6(b). For a maximum voltage of 25 V, the capacitance is as low as 2.8 nF, which is two times lower than the nominal value with no offset. Using the Double Laser Interferometer (DBLI) and the procedure described in [122] and [123], the electromechanical transverse piezoelectric coefficient $e_{31,f}$ can be estimated from the measurement of the longitudinal piezoelectric coefficient $d_{33,f}$. Values ranging from 15 C m^{-2} to 17 C m^{-2} were estimated from the measurements which are in line with the expected values. Using the lumped element model, the minimum and the maximum pressure responses can be calculated using the estimation of the transverse piezoelectric coefficient and the response calculated in Chapter 2 are presented in Figure 4.7(b).

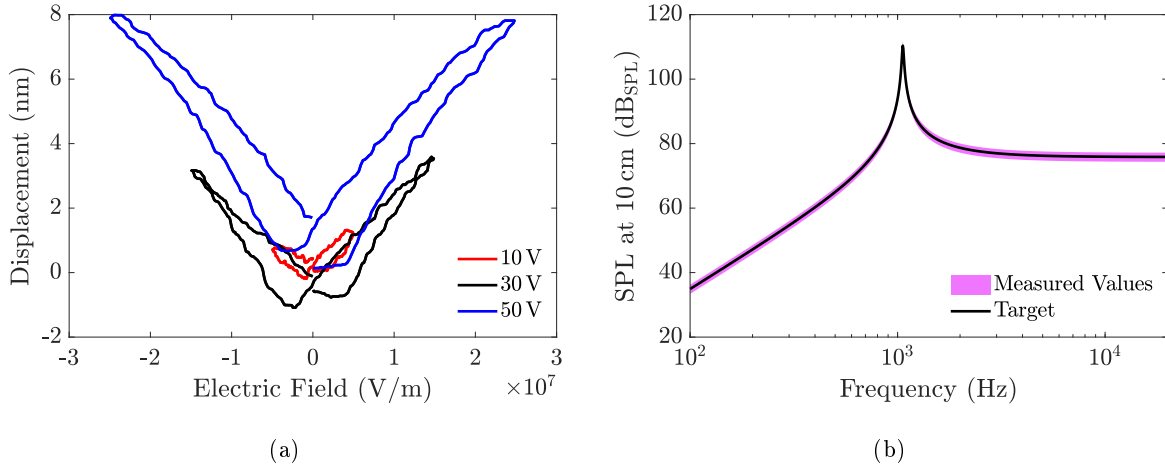


Figure 4.7: Displacement as a function of the electric field on a test device (a) and expected pressure response of the loudspeaker with the $e_{31,f}$ estimated from the electromechanical measurements (b)

As it can be seen in pink in Figure 4.7(b), the variation of the transverse piezoelectric coefficient only changes the expected radiated pressure by less than 3 dB, and the resonance frequency is not affected, as $e_{31,f}$ is only affecting the input force F_{in} . From these measurements, the variation of the piezoelectric transverse coefficient with the input electric field can also be estimated, in order to be used in the model presented in Section 3.4.1. These electrical and electromechanical measurements validate the adequate functioning of the piezoelectric actuators.

Passivation Deposition and Etching

A SiO_2 TEOS layer is then deposited by plasma enhanced chemical vapor deposition and is then etched to open the access to the bottom and top electrodes. This layer, called the passivation, is used as a protective layer for the PZT. The resulting technology stack is presented in Figure 4.8.



Figure 4.8: Bottom wafer after deposition and etching of the passivation layer

Metal Pads Deposition and Etching

A 500 nm thick layer of Au is deposited by electron beam physical vapor deposition on an adhesive 20 nm thick layer of Ti, deposited with the same process. Both layers are then etched with a wet etching process to meet the desired shape. The resulting technology stack is presented in Figure 4.9. Microscope pictures of the devices at this stage of the manufacturing process are presented in Figures 4.10(a) and 4.10(b).



Figure 4.9: Bottom wafer after deposition and etching of the metal pads

The gold conductors are used to connect separately the top and bottom electrodes, in order to apply the electric field to the piezoelectric layer. As the loudspeaker needs a significant amount of power compared to smaller MEMS devices, the gold connectors width is set to $500\ \mu\text{m}$. In order to simplify the characterization of the loudspeaker on wafer, the spacing and the dimensions of the connectors on the other end is not varying with the different variants of the design.

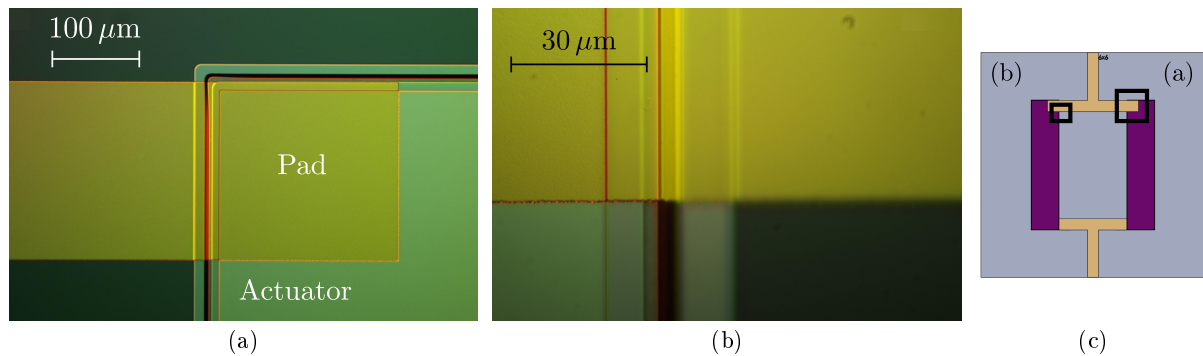


Figure 4.10: Microscope picture of the connection between the top electrode and the gold conductor (a), zoom on the gold connector connecting the top electrode (b) after the etching of the gold pads and location of the pictures on a 2D view of a loudspeaker (c)

In Figure 4.10(a), the connection between the top electrode of a loudspeaker with the gold conductor (in dark yellow) is depicted. The bottom right light green rectangular shape is the complete piezoelectric stack, on which the top electrode appears through the opening of the passivation layer to receive the gold connector. In Figure 4.10(b), a zoom on the gold conductor deposited on the edge of the piezoelectric stack is depicted. It shows the difference of focus between the bottom of the stack (on the left) and the top of the stack (on the right). This perspective emphasizes the topography of $2.2\ \mu\text{m}$ of the piezoelectric stack, and the good continuity of the electrical path between the top and the bottom of the stack. The vertical black line which is crossed by the gold conductor is the slope of the PZT. Figure 4.10(c) depicts the locations at which the pictures from Figure 4.10(a) and Figure 4.10(b) are taken on the loudspeaker. At this stage, Scanning Electron Microscope (SEM) is used on the wafer to verify the thickness of the layers. The SEM picture of the device layer and of the PZT is depicted in Figure 4.11(a) and shows the typical slope of the PZT after the etching, and a zoom on the piezoelectric layer, showing the bottom and top platinum electrodes is depicted in Figure 4.11(b).

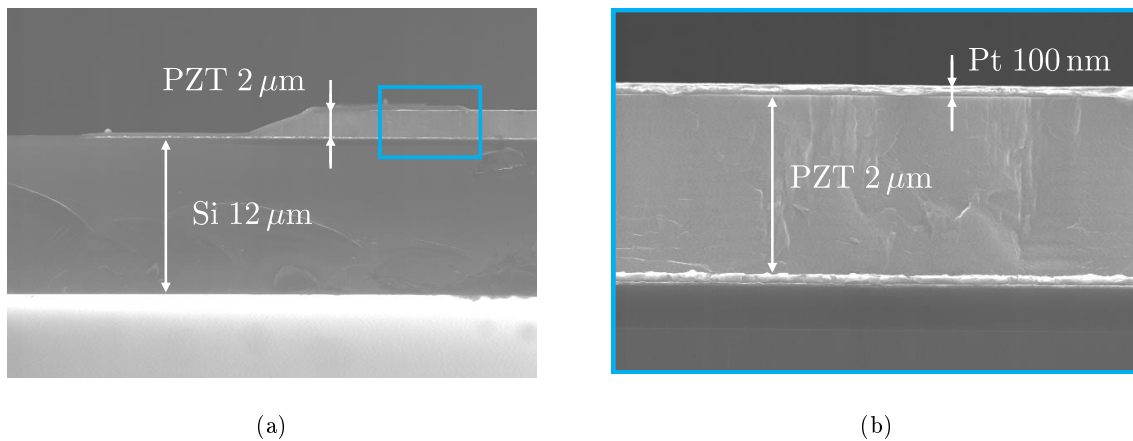


Figure 4.11: SEM picture of the device layer of the bottom wafer (a) and zoom on the PZT stack (b)

Etching of the Device Layer

Dry etching processes are then used on the passivation layer, the thermal oxide and the device layer around the actuators in order to pre-etch the shape of the actuators. The resulting technology stack is schematically represented in Figure 4.12.

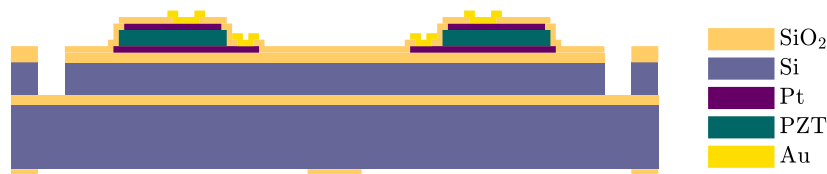


Figure 4.12: Bottom wafer after the pre-release of the structure in the device layer

The etching is first performed on the SiO₂ layer of 800 nm and is then performed on the 12 μm of the device layer, with a stop in the SiO₂ box layer. During this operation, the periphery of the rigid frame of the loudspeaker is also etched in order to separate them later in the process. A picture of one side of one device is depicted in Figure 4.13(a) at this stage of the manufacturing process. In this figure, the periphery etch of the actuators appears in dark green, and the denomination of the device, etched in the gold layer is depicted at the top of the figure. In Figure 4.13(b), a zoom on the edge of the piezoelectric stack, close to the partial etch of the actuators is depicted. It shows a shadow due to the 12 μm of topography on the device.

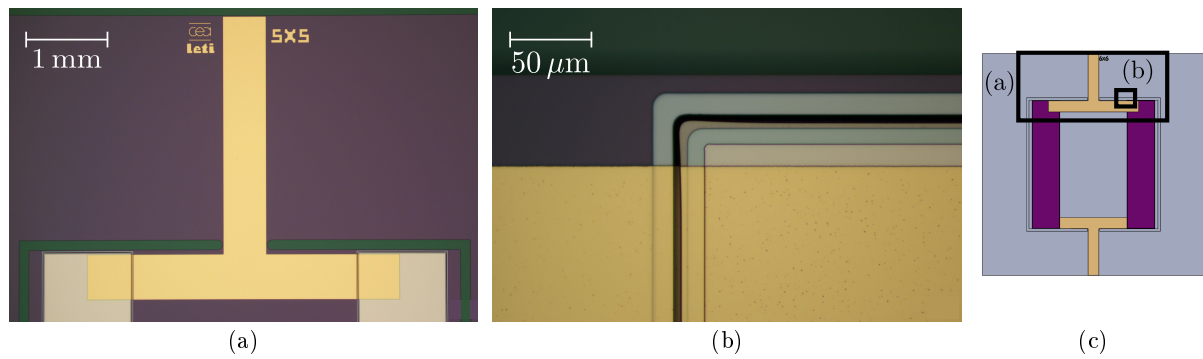


Figure 4.13: Microscope picture of the connection between the top electrode and the gold conductor (a), zoom on the gold connector connecting the top electrode (b) after the etching of the gold pads and locations of the pictures on a 2D view of a loudspeaker (c)

In Figure 4.14(a), a picture of a wafer at this step of the manufacturing process is depicted. The iridescent color of the wafer is due to the passivation layer. In the zoom in Figure 4.14(b), the different variants of the loudspeaker are recognizable, and are distributed as described in Figure 3.37. The partial etching around the devices appears in green.

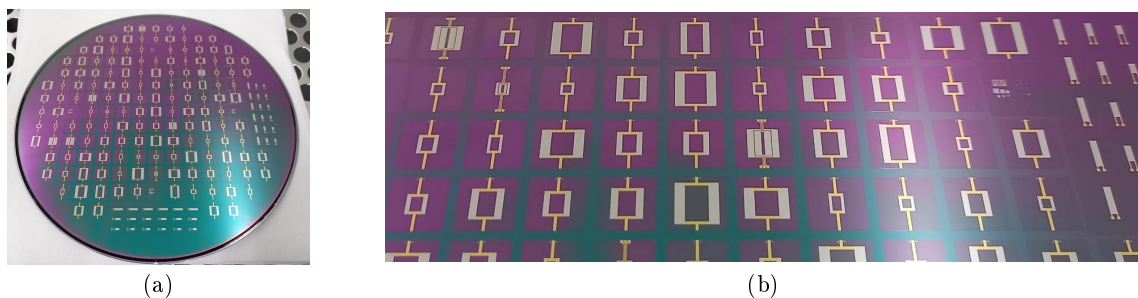


Figure 4.14: Picture of the bottom wafer after the etching of the device layer (a) and zoom on the wafer (b)

Deposition and Patterning of the SINR

In order to bond this wafer with the second one, a layer of $7\ \mu\text{m}$ of SINR is spin coated and patterned to meet the desired shape, at the tip of the actuators and on the frame of the device. The resulting technology stack is presented in Figure 4.15. The SINR remains only at the tip of the flexible part of the actuators, corresponding to the coupling block on the top wafer, and on the rigid frame around the loudspeaker. During the bonding, wafers are aligned with a tolerance of $\pm 10\ \mu\text{m}$, and the structure is designed to not be influenced by this uncertainty.



Figure 4.15: Bottom wafer after the deposition and patterning of the SINR glue

4.2.2 Top Wafer (Mechanoacoustical Wafer)

Hard Mask Back Cavity Deposition

The second wafer is a thick film on insulator wafer, whose dimensions are $80\ \mu\text{m}$ thick for the device layer and $500\ \mu\text{m}$ thick for the handle wafer. The device layer of $80\ \mu\text{m}$ is used for the moving plate of the loudspeaker, and the handle wafer is used for the coupling blocks and the outside frame. The process on the second wafer starts with a $4\ \mu\text{m}$ deposition of SiO_2 on the back side of the wafer by plasma enhanced chemical vapor deposition. The top wafer after the hard mask deposition is presented in Figure 4.16.

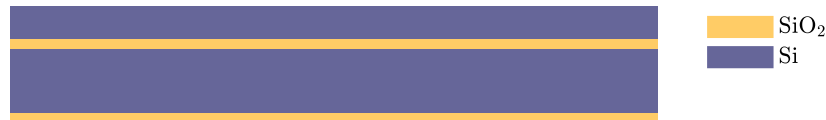


Figure 4.16: Top wafer after hard mask deposition on the handle wafer side

Hard Mask for the Back Cavity

Analogously to the first wafer, the $4\ \mu\text{m}$ hard mask is etched on the back side using a plasma etching process. The resulting technology stack is presented in Figure 4.17. This hard mask is used for the full sheet etching of the handle wafer later in the manufacturing process. The hard mask remains only on the surrounding frame and on the coupling blocks of the loudspeaker.



Figure 4.17: Schematic technology stack after the etching of the back hard mask

Hard Mask Stiffeners

On the device layer side of the wafer, a $2\ \mu\text{m}$ thick hard mask is deposited and etched in order to etch the stiffeners of the plate later on. The resulting technology stack is depicted in Figure 4.18. Two pictures of the device layer after this step are depicted in Figure 4.19. The first picture depicts the complete moving plate of a device, with the linearization spring highlighted in blue and the stiffeners rectangles in a light shade of brown. The periphery of the plate, whose width is $9\ \mu\text{m}$ is hardly visible. In Figure 4.19(b) a zoom on the peripheral etching is depicted where the interstice of the plate is highlighted in blue.

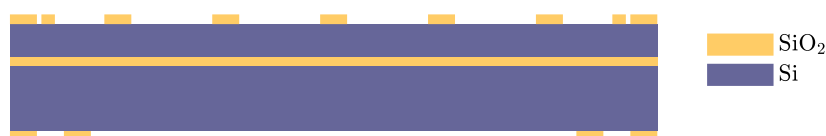


Figure 4.18: Top wafer after etching of the hard mask on the device layer

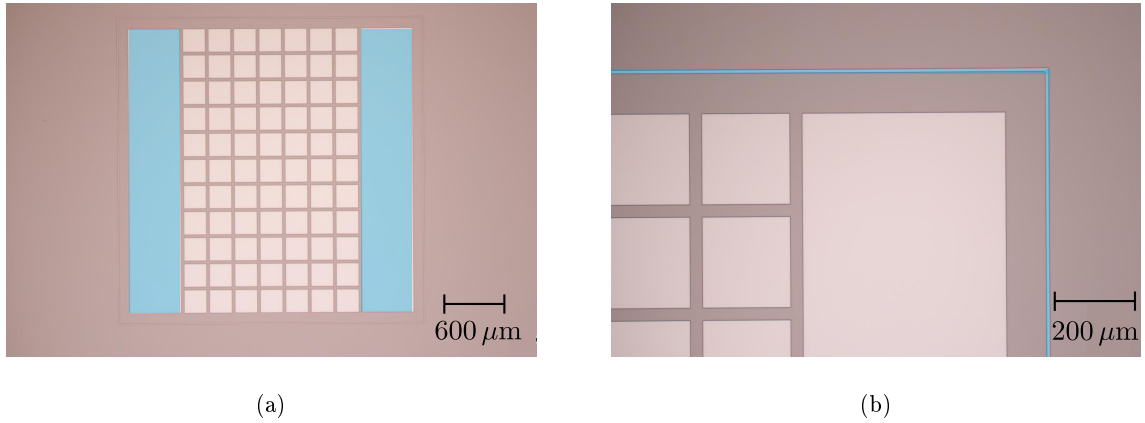


Figure 4.19: Microscope picture of the hard mask of the device layer on the top wafer after etching on a complete moving plate (a) and zoom on the interstice (b)

Calibration of the Partial Etch

In parallel to the manufacturing process, the two next etches are first calibrated on test wafers, as they need to be time stopped. The same lithography masks are used, but on a classical silicon wafer, without device and buried oxide layers. The objective is to obtain a $80\ \mu\text{m}$ deep etch on the periphery of the plate, a plain plate of $20\ \mu\text{m}$ and stiffeners with a height of $60\ \mu\text{m}$. The first etch of depth t_{pe} depicted in Figure 4.20(b) is stopped by time counting, aiming at a depth of approximately $50\ \mu\text{m}$. The second etch is stopped by the buried oxide layer on the real devices, leading to $t_{pe} + t_{fe}$ equal to $80\ \mu\text{m}$. The plain plate is then defined by t_{pp} , as depicted in Figure 4.20(c), which is not necessarily equal to $80\ \mu\text{m} - t_{fe}$ on real devices. On the real devices and due to the difference of opening between both slots, the etch rate of the left slot of Figures 4.20(c) is slower than the etch rate on the right.

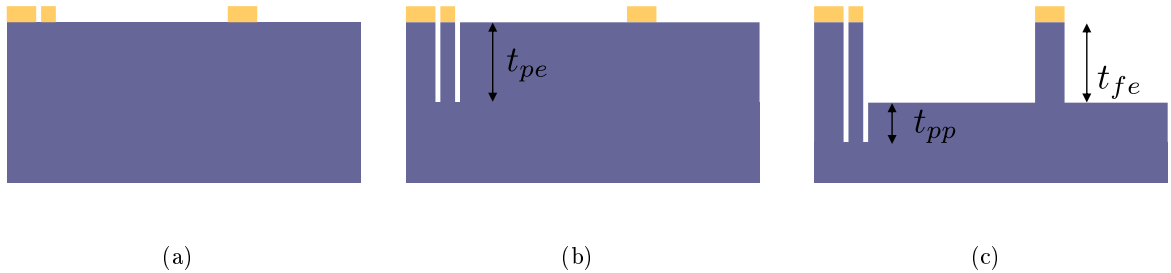


Figure 4.20: Test silicon wafer with a hard mask for the frame and the stiffeners (a), after the partial etch of the interstice around the plate and the linearization spring (b) and after the second etch (c)

In Figure 4.21, two SEM pictures of a test device used for the calibration of the partial etch are shown. Measurement in Figure 4.21(a) shows that the etch in the larger opening, corresponding to the periphery of the linearization spring is deeper than the slot corresponding to the periphery of the plate. Measurement in Figure 4.21(b), shows the correct depth for a stiffener in the center of the plate. The partial etch is finally set to a depth of approximately $55\ \mu\text{m}$, depending on the location of the wafer.

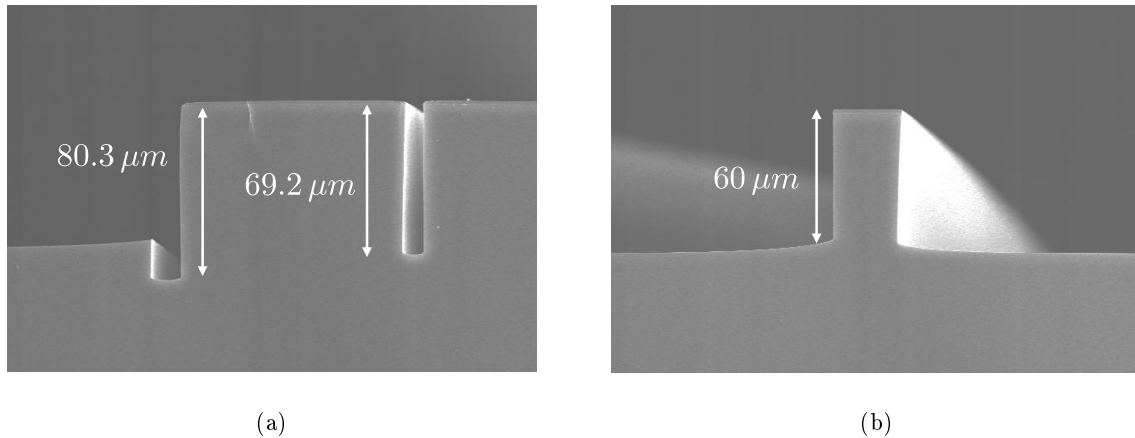


Figure 4.21: SEM picture of the calibration of the partial etching in the device layer of the top wafer at the periphery of the plate (a) and on a stiffener (b)

Partial Etch

From the calibration defined previously, a $55 \mu\text{m}$ deep dry etching is performed using a $5 \mu\text{m}$ mask. The resulting technology stack is presented in Figure 4.22. In Figure 4.23(a), a microscope picture of one plate after the partial etching and the stripping of the mask is depicted. The hard mask is depicted in darker brown. The partial etch slot is done with a larger mask, in order to circumvent possible misalignment issues.

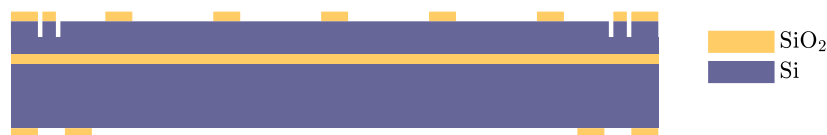


Figure 4.22: Top wafer after the partial etching around the linearization spring and the moving plate

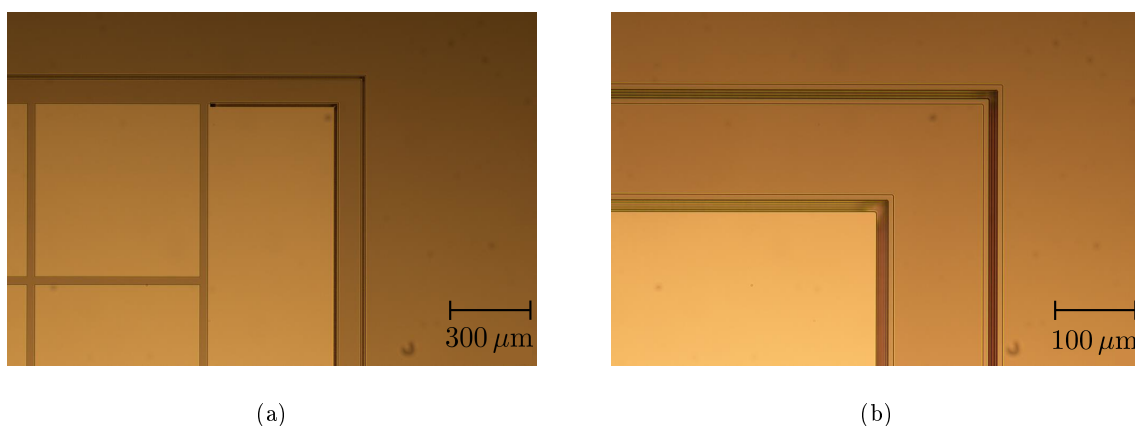


Figure 4.23: Microscope picture of a device after the partial etching of the periphery of the plate (a) and zoom around the periphery of the plate (b)

Back Cavity Etching

The last manufacturing step on the top wafer is the full sheet Deep Reactive Ion Etching (DRIE) of $500\ \mu\text{m}$ for the back cavity on the top wafer, using the previously deposited and etched hard mask. This etching defines the coupling blocks and the rigid frame of the loudspeaker and the resulting technology stack is depicted in Figure 4.24.



Figure 4.24: Top wafer after the back cavity etching

4.2.3 Wafer Bonding

Bonding

Wafers are aligned using an automated wafer aligner and a picture of both wafers is shown in Figure 4.26(a). Figure 4.26(b) depicts a similar view as the microscope picture from the CAD model in Solidworks®. Accordingly to the designed masks, wafer needs to be aligned within $\pm 10\ \mu\text{m}$ in the x and y direction in order for the loudspeakers to operate correctly. Using a dedicated wafer bonding machine, the back side of the top wafer is bounded on the front side of the bottom wafer by slightly heating the SINR. The resulting technology stack is presented in Figure 4.25.

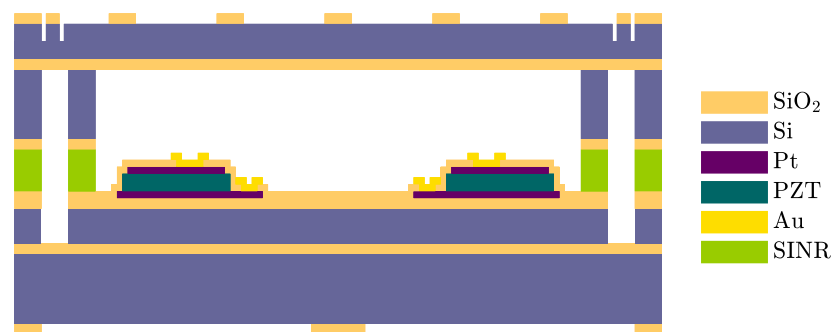


Figure 4.25: Top and bottom wafers after bonding

For the bonding, a partial vacuum of 500 mbar is used, because at this stage of the manufacturing process the center cavity is sealed, and differences of pressure would result in the deformation of the moving plate. A low bonding pressure is used as well, of only 2 kN, due to the fragility of the structure, especially on the top wafer, where surfaces of approximately $80\ \text{mm}^2$ are only $80\ \mu\text{m}$ thick.

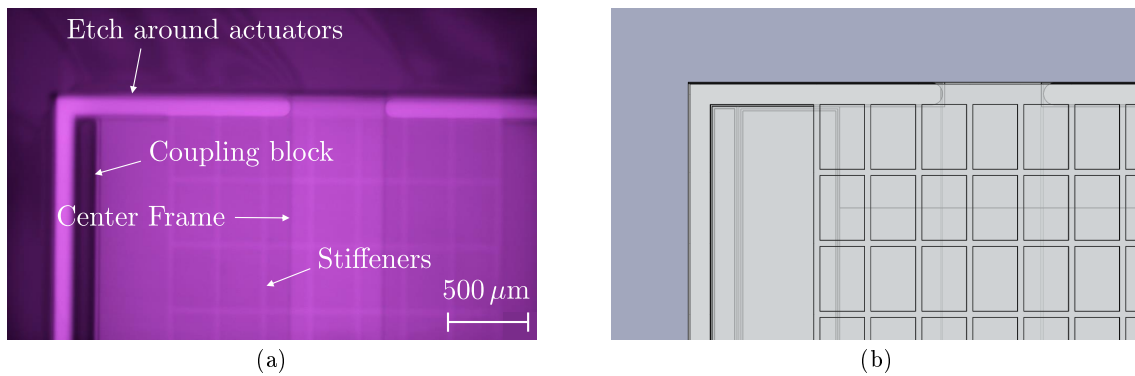


Figure 4.26: Infrared microscope picture of a 3×4 device after bonding (a) and same device as designed in Solidworks® (b)

Etching of the Stiffeners

Using the previously defined hard masks, the stiffeners are dry etched on the front side of the second wafer, with a stop on the buried oxide layer of the top wafer. The resulting technology stack is depicted in Figure 4.27. Then, the 1 μm thick remaining oxide layer in the interstice of the plate and around the linearization spring is etched.

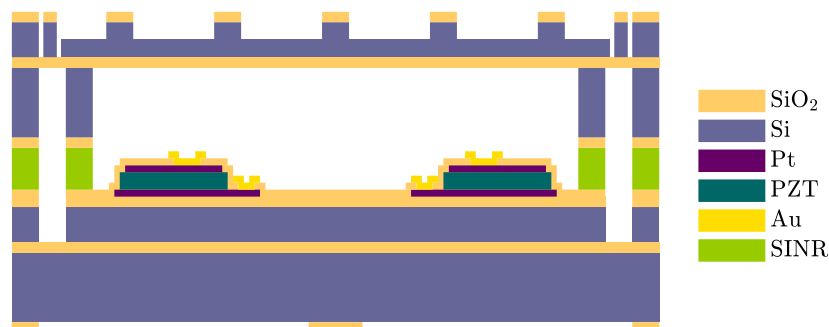


Figure 4.27: Wafer 1 and 2 after etching of the stiffeners on the device side of the top wafer

In Figure 4.28(a) the top wafer after the etching of the stiffeners is depicted. In Figure 4.28(b), a zoom around the linearization spring shows the iridescent layer of oxide, 80 μm below the top of the plate.



Figure 4.28: Microscope picture of the top wafer after the etching of the stiffeners (a) and zoom around the linearization spring (b)

Full Sheet Etching of the Back Cavity and Remaining Oxides

For the release of the structures, wafers are flipped and a full sheet DRIE of $675\mu\text{m}$ is performed on the handle wafer side. The etch is stopped on the buried oxide layer of the bottom wafer. Finally, the remaining oxide layers are removed. The resulting technology stack, flipped again is depicted in Figure 4.29.

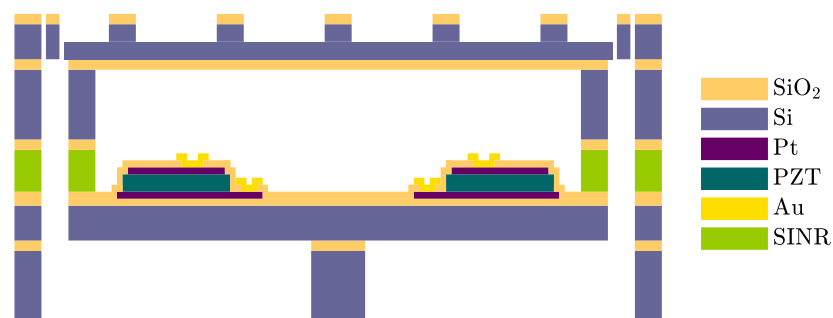


Figure 4.29: Wafer 1 and 2 after full sheet etching of the back cavity on back side 1 and etching of remaining oxides

At the end of the process, wafers are diced using a laser dicing process. A laser is focused inside the silicon, and this amorphizes the silicon in a vertical plane. The devices are then separated mechanically using an expended tape, on which the wafer was previously attached [124]. A picture of the diced loudspeakers is depicted in Figure 4.30(b), as well as a picture of a diced loudspeaker on a one euro coin, taken with a binocular magnifier in Figure 4.30(a).

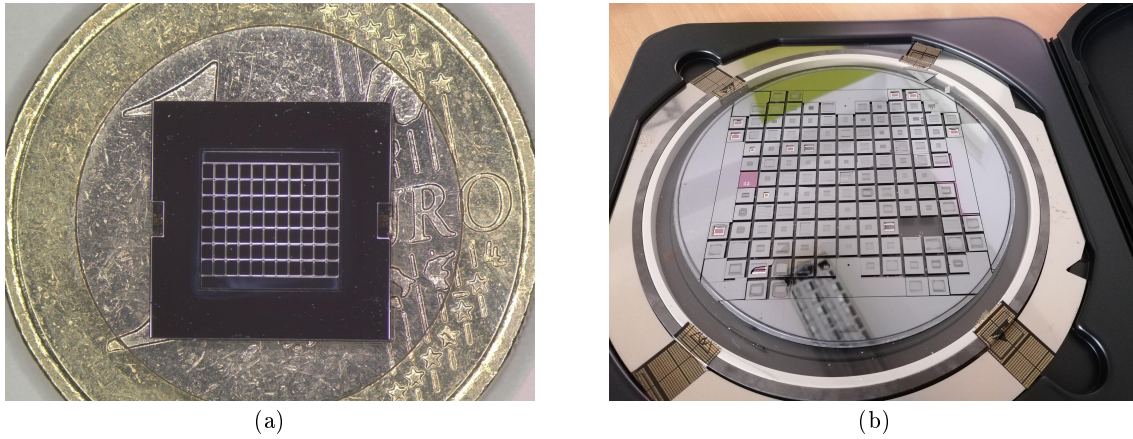


Figure 4.30: Picture of a diced 6×6 loudspeaker on a one euro coin (a) and picture of a wafer after the dicing process (b)

4.3 Mechanical Characterization

4.3.1 Stiffness

The stiffness of the loudspeaker is measured using a nanoindenter (MTS Nanoindenter XP) with the technique presented in [125]. The nanoindenter is mainly composed of a shaft, guided along z and able to move in this direction using an electromagnetic actuator. The force applied to the shaft is calculated using the current supplied to the coil of the electromagnetic actuator and gives a resolution below 1 nN. The displacement of the shaft is measured using a capacitive sensor, giving a resolution in the subnanometer range. A schematic of the nanoindenter is depicted in Figure 4.31(a). The loudspeaker is glued on a flat hard surface, with the moving plate facing the indenter tip. The indenter tip is a rounded cone tip with a radius of $50 \mu\text{m}$. The nanoindenter is then set to measure the resulting force while applying a fixed displacement of approximately $20 \mu\text{m}$ on the center of the moving plate. The resulting curves, measured on a 5×5 and on a 4×4 loudspeaker are depicted in Figure 4.31(b).

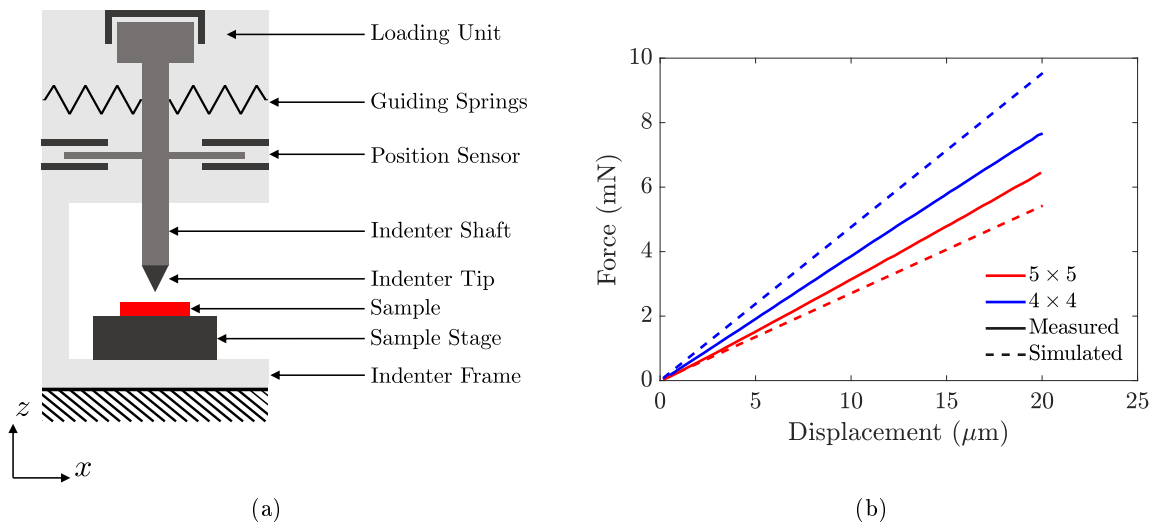


Figure 4.31: Schematic cross section of a nanoindenter (a) and stiffness measured and simulated on two loudspeakers (b)

The apparent stiffness simulated is about 24 % higher than the one measured for the 4×4 variant, and the stiffness simulated is approximately 18 % smaller than the one measured for the 5×5 variant. Due to the manufacturing process and the uncertainty on the thickness of the device layer of the bottom wafer, the uncertainty on the value of the stiffness is quite large. The equation for the uncertainty on the apparent compliance is derived in appendix C and this lead to $C_{ms} = 2.1 \pm 0.4 \text{ mN}^{-1}$ for the 4×4 variant and to $C_{ms} = 3.60 \pm 0.74 \text{ mN}^{-1}$ for the 5×5 variant. Considering these rather large uncertainties, the simulation predicted correctly the measurement. Unfortunately, no measurement were made on the other variants of the loudspeaker.

4.4 Electrical Characterization

4.4.1 Impedance

The electrical impedance of the loudspeaker is measured using a E4990A Impedance Analyzer and is compared to the electrical impedance calculated in Section 2.2.11.

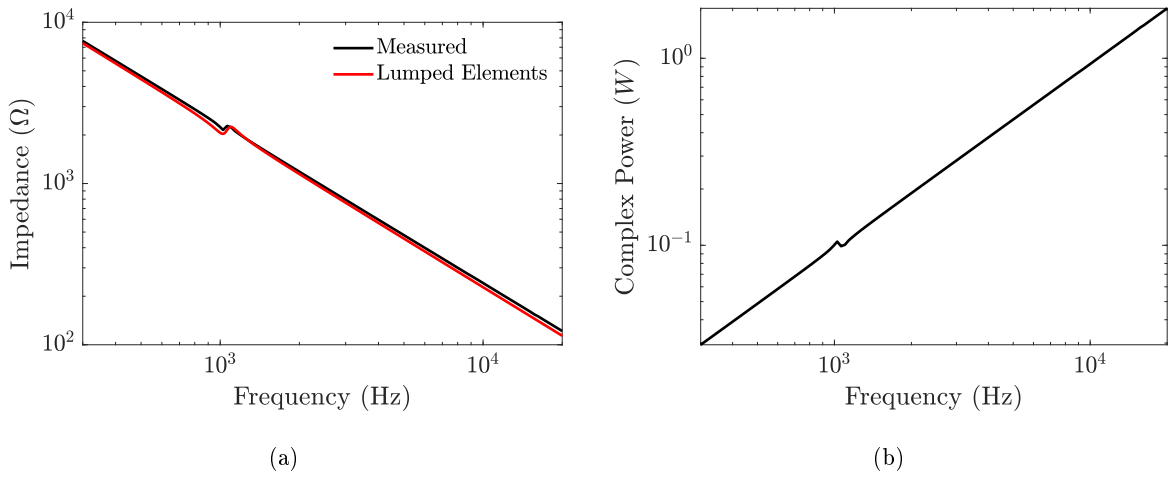


Figure 4.32: Impedance of the loudspeaker (a) and reactive power of the loudspeaker calculated using the measured impedance (b)

The comparison of the model and of the measurement is presented in Figure 4.32(a). The value of the capacitor C_p is adjusted to 70 nF to fit the measurement. This leads to a PZT relative permittivity of 1115, which is in agreement with the literature. The value of R_s and R_p are respectively too small and too large to be measured with this technique, and can be assumed to be infinitely small and infinitely large. Using a multimeter, the measured value is 73 nF. By assuming the amplifier gives a constant voltage of 30 V in the entire frequency range, the complex power drawn by the loudspeaker can be calculated and is depicted in Figure 4.32(b). The loudspeaker being mainly capacitive, the power drawn by the loudspeaker is mainly reactive. The power is inversely proportional to the impedance, and is approximately 30 mW at 300 Hz and increases linearly with frequency, up to approximately 1.8 W at 20 kHz. Despite the rough frequency response of the loudspeaker higher in frequency in the pressure response, the impedance remains flat.

4.4.2 Amplifier

After being assembled, the amplifier and the signal processing circuits are measured. A picture of the amplifier is depicted in Figure 4.33.

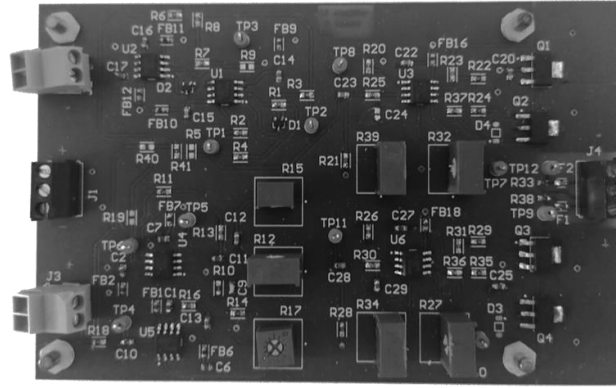


Figure 4.33: Picture of the amplifier

The amplifier is first measured using a probe with the setup presented in Section 4.5.2, and the frequency response is compared to the response simulated with LTSpice in Section 2.4.1 in Figure 4.34(a), and the input and output signals of the amplifier at a frequency of 1 kHz are depicted in Figure 4.34(b).

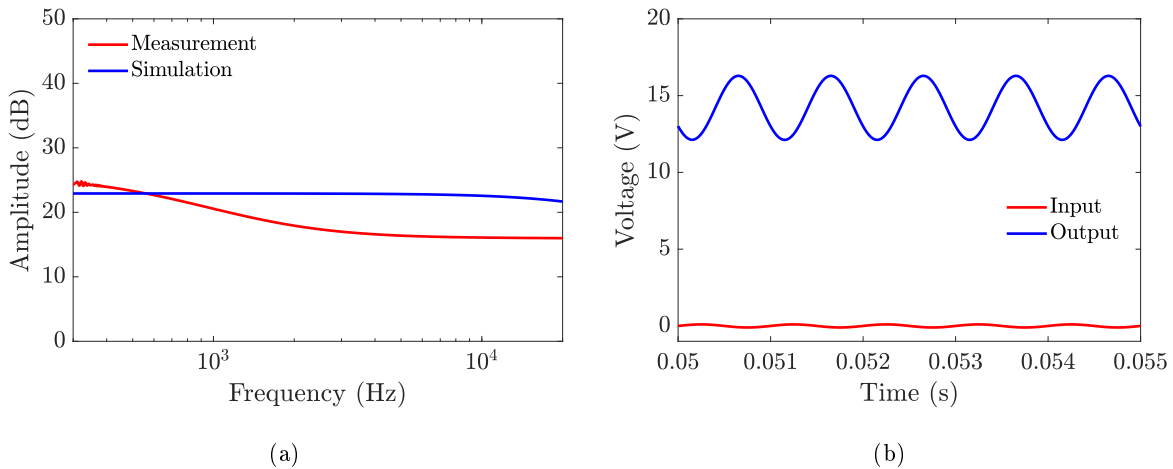


Figure 4.34: Frequency response measured and simulated (a) and input and output time domain signals (b) of the amplifier

The measured frequency response is slightly different from the simulated one in the lower frequencies. The amplifier displays a low shelf filtering effect in the low frequency range, with a cut-off frequency at approximately 1 kHz. In Figure 4.34(b), the time domain signal shows a gain slightly lower than 15, with the output signal oscillating around 14 V. As the value of the potentiometer cannot be measured easily without removing them from the printed circuit board, it is difficult to depict the gain and the offset as a function of their respective values. The total harmonic distortion of the amplifier can then be measured using the same measurement setup and for different input levels.

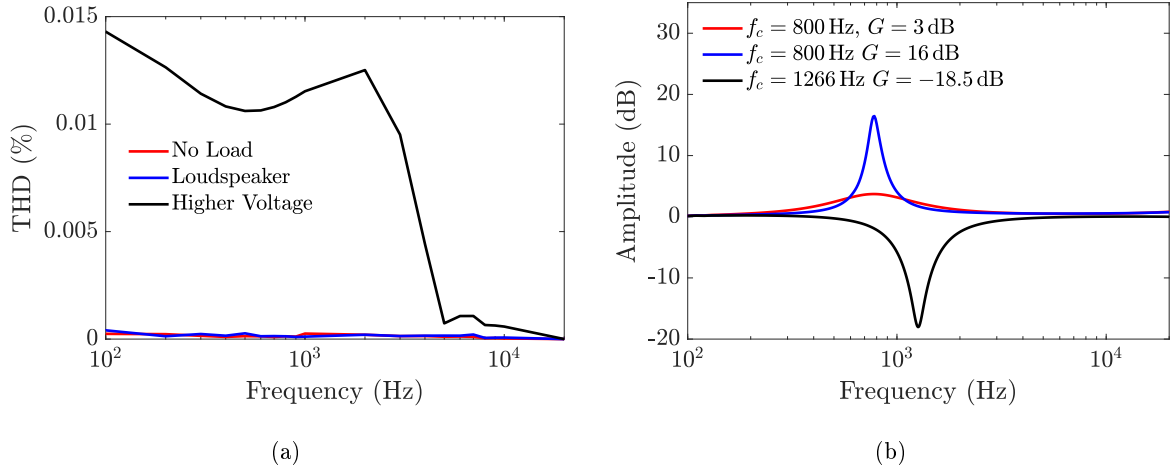


Figure 4.35: Total harmonic distortion as a function of frequency (a) and transfer function of the active peak filter for different settings of R_{12} , R_{15} and R_{17} (b)

In Figure 4.35(a), the total harmonic distortion at the output of the amplifier is depicted for an input voltage of 100 mV with a gain of 15 from 100 Hz to 20 kHz with no load, with the loudspeaker connected and with an input voltage of 1 V without load. The THD is very low in the entire frequency range, and does not seem to be affected by the load. For an input voltage of 1 V, corresponding roughly to an output voltage of 30 V, the THD is below 0.02%. The low distortion is due to the feedback and the operational amplifier, that avoids any difference between the input and the output voltages. The peak filter is then measured for different quality factors, different gains and different frequencies as it is depicted in Figure 4.35(b). As it is difficult to measure the value of the potentiometer while in use, the peak filter is set for one frequency with two different gains, and is then set to approximately the resonance frequency of the loudspeaker with a negative gain. The active peak filter allows an attenuation of a sharp frequency band down to -18.5 dB.

4.5 Acoustical Characterization

4.5.1 Pressure Response on Wafer

The first acoustical characterization is performed on wafer, before dicing. The wafer is placed on a Cascade PM8 prober, and the loudspeaker are actuated using the designed amplifier. The vacuum system is turned off, as it would damage the moving structure of the loudspeaker. Due to the construction of the wafer, and the influence of the back cavity on the response of the loudspeakers, only a part of the loudspeakers can be measured on this setup. The measurement setup, using the DC coupled amplifier, an acquisition card, a G.R.A.S. 46BE microphone as well as a G.R.A.S. 12AL microphone preamplifier is depicted in Figure 4.36.

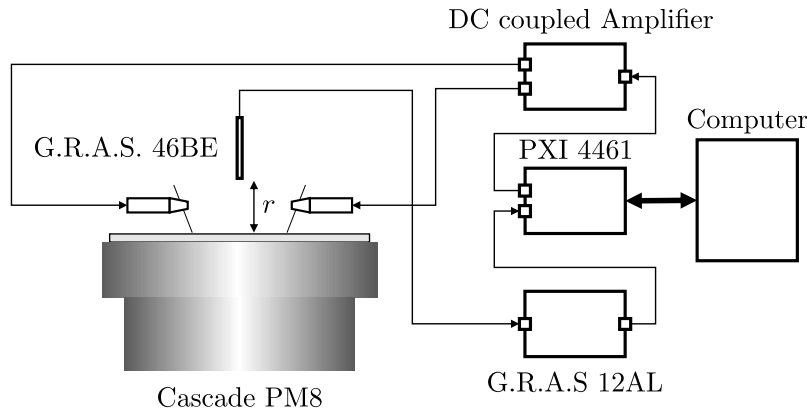


Figure 4.36: Measurement setup of the wafer on the prober

Measurements are performed on twelve loudspeakers of the 6×6 variant (see Table 3.2), at the periphery of the wafer, whose positions on the wafer are depicted in Figure 4.37(b). The average frequency response of the loudspeaker, as well as the standard deviation is depicted in Figure 4.37(a). Loudspeakers show a very similar behavior in the low frequency range, around the resonance frequency with a standard deviation of only 1.5 dB. Higher in frequency, the standard deviation is as high as 12 dB. At these frequencies, a small difference in the structure of the loudspeaker could trigger different modes and leads to a highly different frequency responses. Also, due to the setup, loudspeakers are not exactly measured at the same location, and the differences could be attributed to reflections on the setup. There is a good agreement between the simulated and measured frequency responses, in terms of resonant frequency and level. The uncertainty of the simulated curve appears in transparent blue. Propagation of errors are derived in Appendix C.

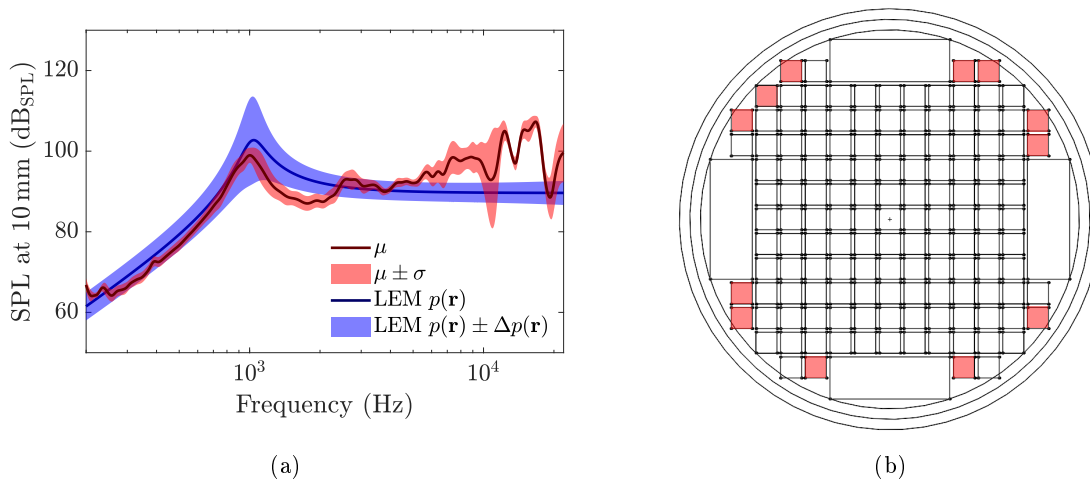


Figure 4.37: Frequency response of the loudspeaker calculated with the lumped element model and compared to the one measured on twelve loudspeakers (a) and position of the twelve loudspeakers on the wafer (b)

4.5.2 Pressure Response in Anechoic Chamber

In order to avoid interference on the measurement, the loudspeaker is bonded onto the PCB designed in Section 2.4.3, and this PCB is attached to a larger baffle designed to avoid an acoustic short-circuit between the front and the back acoustic waves. This baffle is then used inside an AL003 anechoic chamber from G.R.A.S (Fig. 4.38). The effect of the PCB and of the baffle on the behavior of the loudspeaker, due to the added mass as well as the diffraction effect due to the finite baffle is neglected in the model for the comparison.

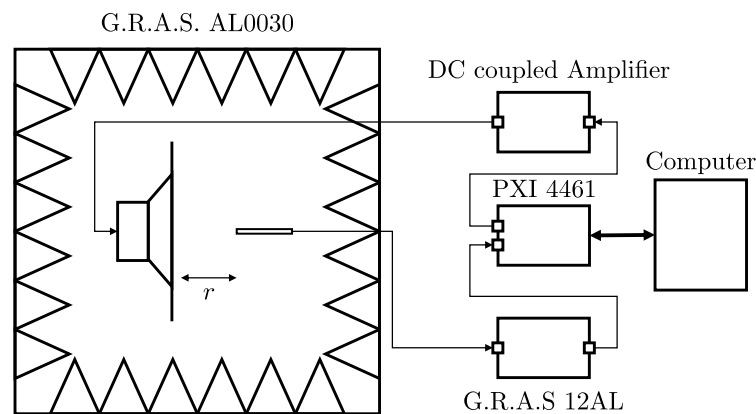


Figure 4.38: Schematic of the measurement setup

A cross section of a 3D drawing of the baffle on which the PCB and the loudspeaker are attached is depicted in Figure 4.39(a). A picture of the loudspeaker mounted and bonded on the PCB taken with a binocular magnifier is depicted in Figure 4.39(b).

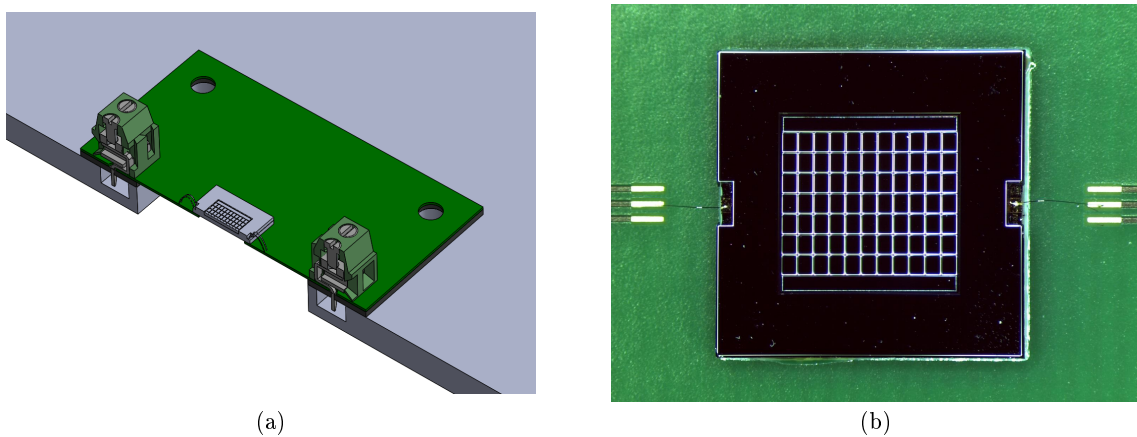


Figure 4.39: Cross section of a 3D drawing of the loudspeaker mounted on the PCB and on the baffle (a) and binocular magnifier picture of a 6×6 loudspeaker mounted on the PCB (b)

The loudspeaker on the baffle is placed with the moving plate facing the bottom, using the drawer of the anechoic chamber. To avoid leaks between the baffle and the PCB, although the pressure involved is not extremely high, a soft gasket is used and is depicted in dark gray in Figure 4.39(a) and appears in dark red in Figure 4.40(a). The microphone is placed in front of the moving plate of the loudspeaker, at 10 mm of the moving plate.

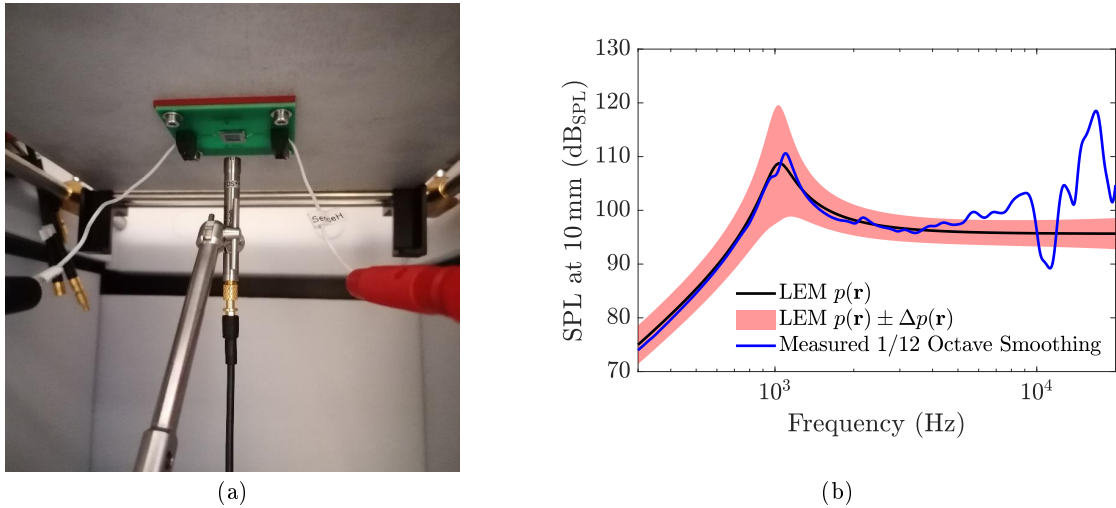


Figure 4.40: Picture of the measurement setup inside the anechoic chamber (a) and measured pressure response smoothed at 1/12 octave compared to the frequency response calculated with the lumped element model (b)

The comparison between the measured pressure, smoothed at 1/12 octave, and the calculated one is depicted in Figure 4.40(b). The quality factor Q_{ms} of the model is adjusted manually to fit the pressure response. The simulation gives a very good estimation of the level and of the resonance frequency of the loudspeaker around the resonance. The measured frequency response is within the uncertainty in a wide frequency range, from 300 Hz to 6 kHz. Above 6 kHz, the modal behavior of the loudspeaker, not taken into account by the lumped element model makes the two curves diverge. The measured pressure response can also be compared to the one calculated using the finite element model, as depicted in Figure 4.41.

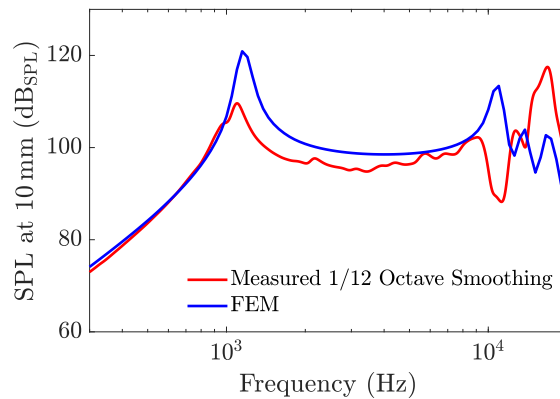


Figure 4.41: Schematic of the measurement setup

Although the resonance frequency and the level are slightly different, the shape of the frequency response is better estimated with the finite element model, due to the mode at approximately 10 kHz, giving a concave shape to the simulated response, similar as the one observed on the measured curve. The mode are not estimated correctly, as the peak simulated with the finite element model corresponds to a dip in the measured frequency response at approximately 10 kHz. Above 15 kHz, the behavior is different as

well.

4.5.3 Directivity

Using a similar setup as the one shown in Figure 4.38, with the loudspeaker mounted on a rotating support, the frequency response of the loudspeaker is measured at different angles from the normal to the moving plate, with a step of 2° .

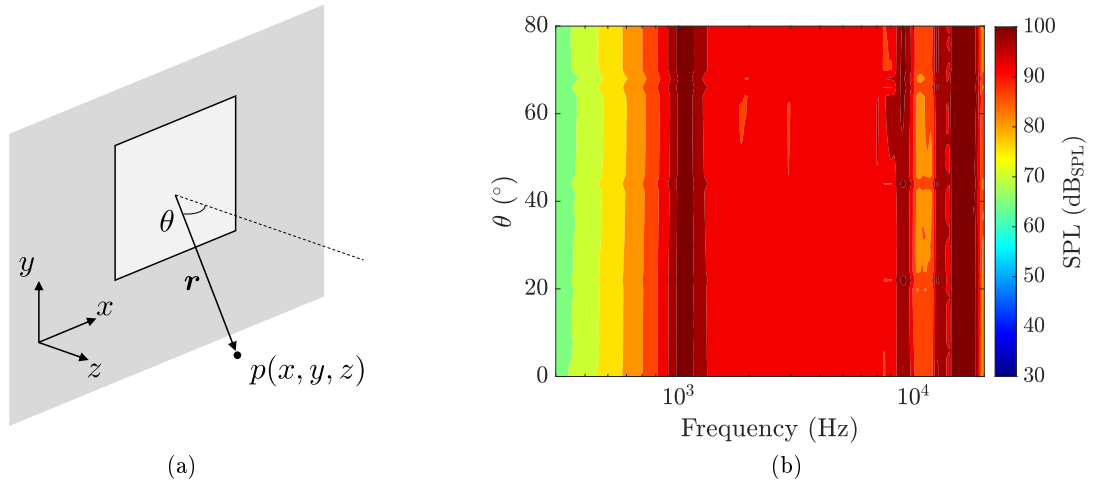


Figure 4.42: Schematic of the measurement setup (a) and measured directivity (b)

The measured directivity is given in Figure 4.42(b) and as expected from the model presented in Section 2.2.8, the loudspeaker is not directive in the audio range, and a similar frequency response can be observed at all the angles, except at approximately 11 kHz, where a different level appears for angles between 35° and 50° , due to the modal behavior of the plate.

4.6 Non Linearities

4.6.1 Frequency Response

The nonlinearities can be observed with an increase of the input level on the frequency response of one 6×6 loudspeaker.

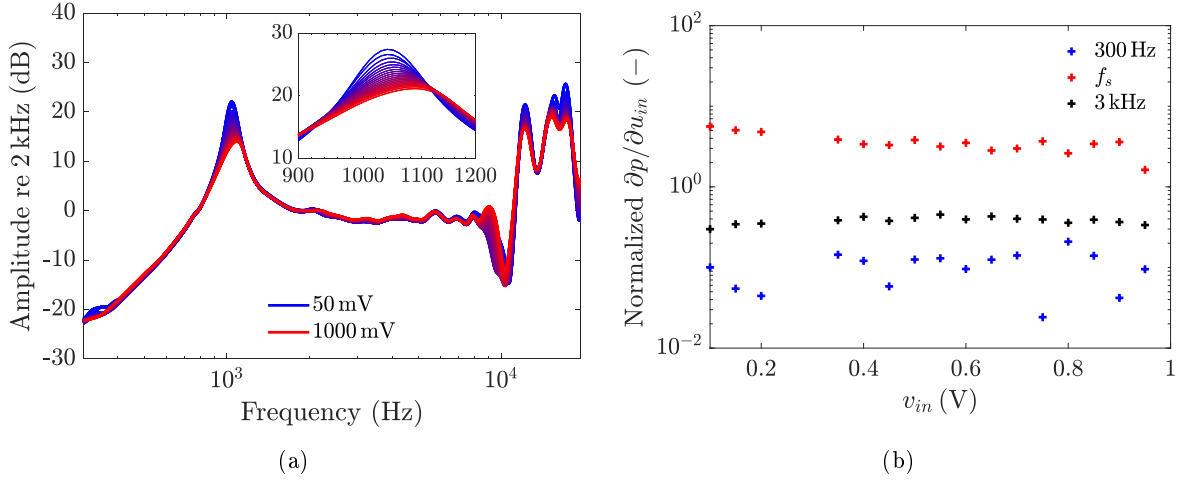


Figure 4.43: Twenty frequency responses of the loudspeaker with an input voltage before the amplifier from 50 mV to 1000 mV referenced to the pressure at 2 kHz (a) and increase of the level of the response for different frequencies (b)

For small signals, the assumption can be made that the loudspeaker is linear. When the level increases, both most significant nonlinearities such as the one of the transduction and the one due to the stiffening effect of the elastic part of the actuators are affecting the frequency response. The effect on the frequency response can be observed in Figure 4.43(a). Both effects are limiting the increase of pressure radiated with a higher input voltage. A shift of the resonance frequency can also be observed in the detail of Figure 4.43(a). Due to the increase of the apparent stiffness C_{ms} with the stiffening effect, the resonance frequency shifts from 1040 Hz to 1080 Hz. The derivative of the pressure radiated by the loudspeaker can be calculated at 300 Hz, at the resonance frequency f_s and at 3 kHz. Figure 4.43(b) depicts the evolution of the increase of the pressure $\partial p/\partial u_{in}$ depending on the input voltage and shows that the increase of pressure at the resonance decreases with the input level. Above the resonance the increase of pressure is mainly constant with an increase of the input voltage. Below the resonance frequency, the trend of the evolution of the increase is approximately flat.

4.6.2 Transduction Factor

Although it is difficult to measure γ the transduction factor directly, it is possible from the time domain pressure signal to visualize the ratio between the measured pressure and the input voltage. The pressure signal is first high pass filtered in order to remove the unwanted oscillation of the main component of the signal. Both voltage and pressure signal are then phase shifted in order to be in phase. Then the pressure is displayed as a function of the input voltage, for a few hundred periods. The result is depicted in Figure 4.44(a) for different frequencies, and in Figure 4.44(b) for different input levels.

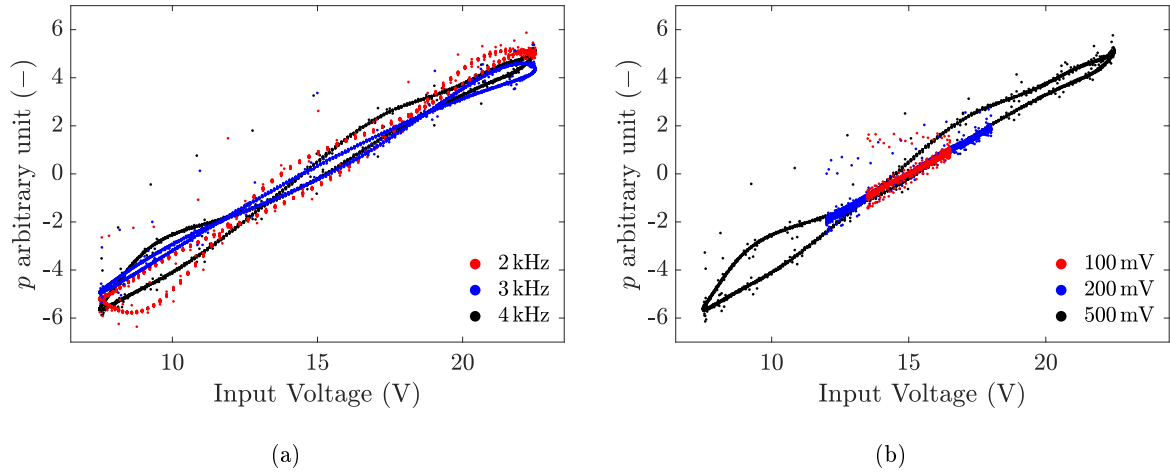


Figure 4.44: Acoustic pressure as a function of the input voltage for different frequencies (a) and for different input voltages (b)

In Figure 4.44(a), the input voltage is equal to 500 mV, which results into a sine oscillating between 7.5 V and 22.5 V after the amplifier. The transduction appears to be mainly linear except for some points outside of the main shape, due to the transient part of the signal and of the filter. Although the shape is mainly linear, an hysteresis appears and the shape seems to be curved at a higher voltage. This complex behavior can be attributed to the contribution of both the nonlinear transduction factor, and the nonlinear stiffness of the loudspeaker. The shape seems to change with frequency, but the main three loops appear for all three frequencies. In Figure 4.44(b), the hysteresis is not clear for an input voltage of 100 mV and 200 mV but clearly appears for an input voltage of 500 mV. It means that the transduction factor is involved into a significant amount of nonlinearities above 200 mV.

4.6.3 Total Harmonic Distortion

The total harmonic distortion of the loudspeaker is measured using the same setup and the same loudspeaker depicted in Figure 4.38 and with pure tones at different frequencies. The total harmonic distortion is measured for an input voltage of 100 mV which corresponds to a sine oscillating between 13.5 V and 16.5 V at the output of the amplifier. The quality factor of the model is first adjusted to precisely match the quality factor of the measurement, as depicted in Figure 4.45(a). This leads to a quality factor of $Q_{ms} = 18.5$ with a mechanical resistance of $R_{ms} = 1.5 \text{ mNs m}^{-1}$. There is a good fit in level and shape between the measured frequency response and the calculated one from 300 Hz to 7.5 kHz. From this comparison of frequency responses, the calculation of the THD can be assumed to be valid an octave below the upper limit. Above this limit, the modal behavior of the loudspeaker is affecting significantly the measured THD.

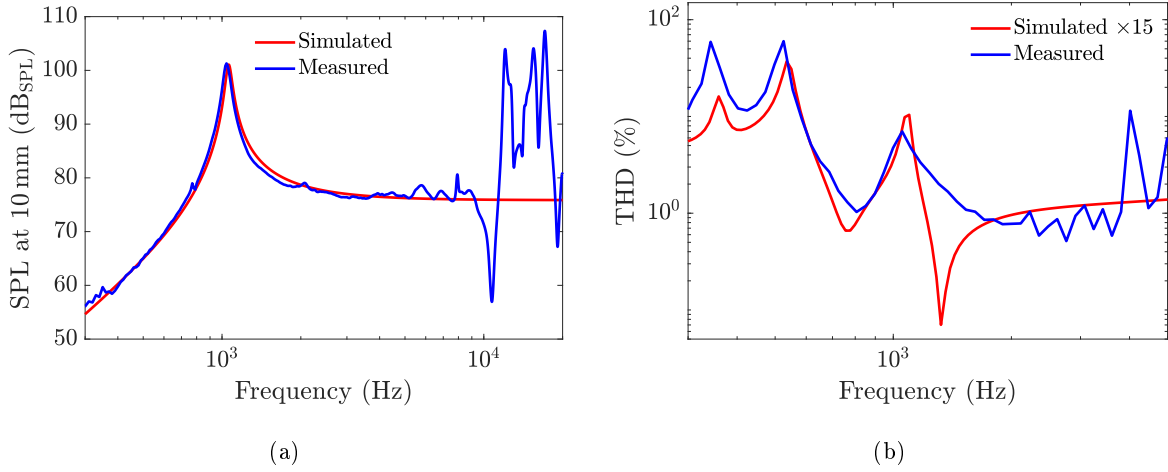


Figure 4.45: Simulated and measured frequency response of the loudspeaker at $u_{in} = 100 \text{ mV}$ (a) and simulated and measured THD (b)

Using the model described in Section 3.4.1, the measured THD can be compared with the calculated one, using theoretical nonlinear functions for the input nonlinear functions. The comparison is depicted in Figure 4.44(b). Despite an agreement in the shape of the calculated and measured THD, the level is not well estimated, and the curve sits approximately 15 times below the measured one. The level is adjusted in the figure in order to compare the shape of the curves. The shape is well estimated, and both peaks due to the first and second harmonics, reaching a THD of 59 % and 60 % two times and three times below the resonance frequency at 340 Hz and 525 Hz do appear in the simulated curve. At the resonance, the THD increases up to 7 % due to the large displacement of the loudspeaker. Above the resonance frequency, the THD is as low as 1 % in a wide frequency range, from 1450 Hz to 3800 Hz. Higher in frequencies, the modal behavior of the loudspeaker affects the THD of the loudspeaker, which is not simulated into the model. The difference of level could be due to the hysteresis of the piezoelectric actuators which is not taken into account in the model.

4.7 Chapter Conclusion

In this chapter, the manufacturing process was detailed step by step and the mechanical, electrical and acoustical characterizations of the 6×6 variant of the loudspeaker were successively presented. The lumped element model, as well as the finite element model are correctly predicting the behavior of the loudspeaker, within $\pm 5\%$ around the resonance frequency. Typical stiffening and hysteresis effects were observed as well. For demonstration purposes, a horn was designed and 3D printed and the conception is described in Appendix B.

Conclusion

In this thesis, the models, the design, the manufacturing process and the characterization of a new high performance MEMS loudspeaker based on an innovative manufacturing process are presented. Built into two separated wafers, the loudspeaker radiates up to $110 \text{ dB}_{\text{SPL}}$ at 1 kHz which is the highest reported pressure at this frequency for a loudspeaker of these dimensions. More than featuring a high pressure, the frequency response of this loudspeaker is closer to the ideal one, as it radiates a similar pressure in a wider frequency range than what was reported recently. Considering the uncertainties on the different mechanical components of the loudspeaker, the lumped element model shows a good agreement with the acoustical measurement of the loudspeakers in anechoic conditions.

For the nonlinear aspect, the model predicted correctly the shape of the THD harmonic distortion, but is unable to predict correctly the level. This is firstly due to the lack of measurement on the direct nonlinearities and this could also be due to the hysteresis behavior of the piezoelectric material, not taken into account into the nonlinear model.

The good performance of the loudspeaker could be attributed to the separation of the electromechanical transducer and the mechanoacoustical transducer, similarly to what is usually done with larger loudspeakers. Despite the limitation of piezoelectric bending actuators, whose output force is inversely proportional to their stiffness, linking inevitably the resonance frequency and the amplitude of the system, the additional design lever created by the separation of the transducer allows to reach a different optimization.

This proof of concept also shows that the designed loudspeaker is mechanically able to withstand displacements as large as $\pm 190 \mu\text{m}$, which validates the possibility to radiate a even higher acoustic pressure in the bandwidth of the loudspeaker, by increasing the electric field in the piezoelectric layer, while correcting the resonant behavior of the loudspeaker with the use of digital signal processing or other active control techniques. For the integration, a dedicated acoustic packaging using a Helmholtz resonator could increase the sound pressure level in a specific frequency band. Active or digital filtering and more advanced electronic systems could improve the performance and protect the loudspeaker as well. These loudspeakers are also easily scalable, and could be used for in-ear application, using the packaging to precisely tune their frequency response.

Aside from the loudspeaker, a dedicated low THD direct coupled amplifier with variable offset as well as a parametric peak filter were designed, built and tested successfully.

In its current form and despite the good acoustic performance, the loudspeaker would not be able to advantageously replace non-MEMS loudspeakers, due to the high manufacturing cost, as a result of a high number of manufacturing steps and due to the geometry of the loudspeaker, composed of two non standard SOI wafers. Even on a dedicated line, the cost of manufacturing of such loudspeakers would still be higher than non-MEMS ones. In terms of reliability and although the loudspeakers are able to withstand extremely high displacements for a short period of time, they might be damaged after longer period of high input voltages.

The next step into trying to adapt loudspeaker to micro-manufacturing processes would be to reach similar performance while simplifying the manufacturing process, but as it was described in the modeling chapters, the good performance of the loudspeaker is reached due to the complexity of the geometry. Also, due to European regulations the PZT might be restricted due to the presence of lead, and research should be carried on in order to find a piezoelectric material with similar performance and manufacturability without lead.

Bibliography

- [1] *Loudspeaker 16x9 mm rectangular 0.8w 6ohm 600hz*, CMS-160916A-SP, Rev. D, CUI Devices, 2019 (cit. on pp. iv, 9).
- [2] M. Kleiner, *Electroacoustics*. CRC Press, 2013 (cit. on p. 4).
- [3] L. D. Fielder and E. M. Benjamin, “Subwoofer performance for accurate reproduction of music,” *Journal of the Audio Engineering Society*, vol. 36, no. 6, pp. 443–456, 1988 (cit. on p. 7).
- [4] J. Vanderkooy and K. B. Krauel, “Another view of distortion perception,” in *Audio Engineering Society Convention 133*, Audio Engineering Society, 2012 (cit. on p. 7).
- [5] J. Larson, G. DellaSaia, and D. Keele Jr, “A tutorial on the audibility of loudspeaker distortion at bass frequencies,” in *Audio Engineering Society Convention 143*, Audio Engineering Society, 2017 (cit. on p. 7).
- [6] S. Temme, P. Brunet, and P. Qarabaqi, “Measurement of harmonic distortion audibility using a simplified psychoacoustic model,” in *Audio Engineering Society Convention 133*, Audio Engineering Society, 2012 (cit. on p. 7).
- [7] J.-H. Kwon, S.-M. Hwang, and K.-S. Kim, “Development of slim rectangular microspeaker used for minimultimedia phones,” *IEEE Transactions on Magnetics*, vol. 43, no. 6, pp. 2704–2706, 2007 (cit. on p. 9).
- [8] C.-M. Lee, J.-H. Kwon, K.-S. Kim, J.-H. Park, and S.-M. Hwang, “Design and analysis of microspeakers to improve sound characteristics in a low frequency range,” *IEEE Transactions on Magnetics*, vol. 46, no. 6, pp. 2048–2051, 2010 (cit. on p. 9).
- [9] J.-R. Chang and C. Wang, “Acoustical analysis of enclosure design parameters for microspeaker system,” *Journal of Mechanics*, vol. 35, no. 1, pp. 1–12, 2019 (cit. on p. 9).
- [10] S.-M. Hwang, H.-J. Lee, J.-H. Kim, J.-H. Kwon, K.-S. Hong, and G.-Y. Hwang, “Development of hi-fi microspeakers with a woofer and a tweeter used for mobile phones,” *Journal of applied physics*, vol. 97, no. 10, 10R512, 2005 (cit. on p. 9).
- [11] Y. Nakashima, T. Ohya, and T. Yoshimura, “Prototype of parametric array loudspeaker on mobile phone and its acoustical characteristics,” in *Audio Engineering Society Convention 118*, Audio Engineering Society, 2005 (cit. on p. 9).
- [12] T. Matsumura, S. Saiki, K. Sano, and S. Usuki, “Ultra-thin micro-loudspeaker using oblique magnetic circuit,” in *Audio Engineering Society Convention 124*, Audio Engineering Society, 2008 (cit. on p. 9).

- [13] J. H. Huang, H.-C. Her, Y. Shiah, and S.-J. Shin, “Electroacoustic simulation and experiment on a miniature loudspeaker for cellular phones,” *Journal of Applied Physics*, vol. 103, no. 3, p. 033 502, 2008 (cit. on p. 9).
- [14] S.-M. Hwang, H.-J. Lee, K.-S. Hong, B.-S. Kang, and G.-Y. Hwang, “New development of combined permanent-magnet type microspeakers used for cellular phones,” *IEEE Transactions on Magnetics*, vol. 41, no. 5, pp. 2000–2003, 2005 (cit. on p. 9).
- [15] I. Shahosseini, E. Lefeuvre, J. Moulin, E. Martincic, M. Woytasik, and G. Lemarquand, “Optimization and microfabrication of high performance silicon-based mems microspeaker,” *IEEE Sensors Journal*, vol. 13, no. 1, pp. 273–284, 2012 (cit. on pp. 9, 10, 29).
- [16] I. Shahosseini, E. Lefeuvre, M. Woytasik, J. Moulin, X. Leroux, S. Edmond, E. Dufour-Gergam, A. Bosseboeuf, G. Lemarquand, and V. Lemarquand, “Towards high fidelity high efficiency mems microspeakers,” in *SENSORS, 2010 IEEE*, IEEE, 2010, pp. 2426–2430 (cit. on p. 9).
- [17] I. Shahosseini, E. Lefeuvre, E. Martincic, M. Woytasik, J. Moulin, S. Megherbi, R. Ravaud, and G. Lemarquand, “Microstructured silicon membrane with soft suspension beams for a high performance mems microspeaker,” *Microsystem Technologies*, vol. 18, no. 11, pp. 1791–1799, 2012 (cit. on p. 9).
- [18] G. Lemarquand, R. Ravaud, I. Shahosseini, V. Lemarquand, J. Moulin, and E. Lefeuvre, “Mems electrodynamic loudspeakers for mobile phones,” *Applied Acoustics*, vol. 73, no. 4, pp. 379–385, 2012 (cit. on p. 9).
- [19] E. Sturtzer, I. Shahosseini, G. Pillonnet, E. Lefeuvre, and G. Lemarquand, “High fidelity microelectromechanical system electrodynamic micro-speaker characterization,” *Journal of Applied Physics*, vol. 113, no. 21, p. 214 905, 2013 (cit. on p. 9).
- [20] M. Brissaud, *Matériaux piézoélectriques: caractérisation, modélisation et vibration*. PPUR presses polytechniques, 2007 (cit. on p. 11).
- [21] A. Erturk and D. J. Inman, *Piezoelectric energy harvesting*. John Wiley & Sons, 2011 (cit. on p. 12).
- [22] S. Trolier-McKinstry and P. Muralt, “Thin film piezoelectrics for mems,” *Journal of Electroceramics*, vol. 12, no. 1, pp. 7–17, 2004 (cit. on p. 12).
- [23] J.-F. Li, D. Viehland, T. Tani, C. Lakeman, and D. Payne, “Piezoelectric properties of sol-gel-derived ferroelectric and antiferroelectric thin layers,” *Journal of Applied Physics*, vol. 75, no. 1, pp. 442–448, 1994 (cit. on p. 12).
- [24] L. Cross and R. Newnham, “History of ferroelectrics,” *Ceramics and civilization*, vol. 3, pp. 289–305, 1987 (cit. on p. 12).
- [25] D. Damjanovic, “Hysteresis in piezoelectric and ferroelectric materials,” Academic Press, Tech. Rep., 2006 (cit. on p. 13).
- [26] L. Lian and N. R. Sottos, “Effects of thickness on the piezoelectric and dielectric properties of lead zirconate titanate thin films,” *Journal of Applied Physics*, vol. 87, no. 8, pp. 3941–3949, 2000 (cit. on p. 13).
- [27] D. Damjanovic, “Stress and frequency dependence of the direct piezoelectric effect in ferroelectric ceramics,” *Journal of Applied Physics*, vol. 82, no. 4, pp. 1788–1797, 1997 (cit. on p. 13).
- [28] —, “Ferroelectric, dielectric and piezoelectric properties of ferroelectric thin films and ceramics,” *Reports on Progress in Physics*, vol. 61, no. 9, p. 1267, 1998 (cit. on p. 13).

- [29] D. L. Polla, P. Schiller, and L. Francis, "Microelectromechanical systems using piezoelectric thin films," in *Integrated Optics and Microstructures II*, International Society for Optics and Photonics, vol. 2291, 1994, pp. 108–124 (cit. on p. 14).
- [30] W. P. Robbins, D. L. Polla, and D. E. Glumac, "Compact, high-displacement piezoelectric actuator with potential micromechanical applications," in *IEEE Symposium on Ultrasonics*, IEEE, 1990, pp. 1191–1195 (cit. on p. 14).
- [31] W. Tjhen, T. Tamagawa, C.-P. Ye, C.-C. Hsueh, P. Schiller, and D. L. Polla, "Properties of piezoelectric thin films for micromechanical devices and systems," in *[1991] Proceedings. IEEE Micro Electro Mechanical Systems*, IEEE, 1991, pp. 114–119 (cit. on p. 14).
- [32] S. S. Lee and R. M. White, "Piezoelectric cantilever voltage-to-frequency converter," *Sensors and Actuators A: Physical*, vol. 71, no. 1-2, pp. 153–157, 1998 (cit. on p. 14).
- [33] H. Wang, Z. Chen, and H. Xie, "A high-spl piezoelectric mems loud speaker based on thin ceramic pzt," *Sensors and Actuators A: Physical*, vol. 309, p. 112 018, 2020 (cit. on pp. 14, 29).
- [34] Q. Wang, Z. Yi, T. Ruan, Q. Xu, B. Yang, and J. Liu, "Obtaining high spl piezoelectric mems speaker via a rigid-flexible vibration coupling mechanism," *Journal of Microelectromechanical Systems*, vol. 30, no. 5, pp. 725–732, 2021 (cit. on pp. 14, 30).
- [35] H. Wang, P. X.-L. Feng, and H. Xie, "A dual-electrode mems speaker based on ceramic pzt with improved sound pressure level by phase tuning," in *2021 IEEE 34th International Conference on Micro Electro Mechanical Systems (MEMS)*, IEEE, 2021, pp. 701–704 (cit. on pp. 14, 29).
- [36] H. Wang, M. Li, Y. Yu, Z. Chen, Y. Ding, H. Jiang, and H. Xie, "A piezoelectric mems loud speaker based on ceramic pzt," in *2019 20th International Conference on Solid-State Sensors, Actuators and Microsystems & Eurosensors XXXIII (TRANSDUCERS & EUROSENSORS XXXIII)*, IEEE, 2019, pp. 857–860 (cit. on pp. 14, 29).
- [37] Y.-J. Wang, S.-C. Lo, M.-L. Hsieh, S.-D. Wang, Y.-C. Chen, M. Wu, and W. Fang, "Multi-way in-phase/out-of-phase driving cantilever array for performance enhancement of pzt mems microspeaker," in *2021 IEEE 34th International Conference on Micro Electro Mechanical Systems (MEMS)*, IEEE, 2021, pp. 83–84 (cit. on pp. 14, 30).
- [38] M. V. Garud and R. Pratap, "A novel mems speaker with peripheral electrostatic actuation," *Journal of Microelectromechanical Systems*, vol. 29, no. 4, pp. 592–599, 2020 (cit. on pp. 14, 16, 17, 29).
- [39] A. R. Clerici, "Mems speaker modeling," in *MikroSystemTechnik Congress 2021; Congress*, VDE, 2021, pp. 1–5 (cit. on p. 14).
- [40] Usound, *Adap UT-P 2019 Datasheet*, 2020. [Online]. Available: https://www.usound.com/wp-content/uploads/2020/01/2001_Adap-UT-P-2019-Datasheet.pdf (cit. on p. 15).
- [41] S. H. Yi and E. S. Kim, "Micromachined piezoelectric microspeaker," *Japanese journal of applied physics*, vol. 44, no. 6R, p. 3836, 2005 (cit. on pp. 15, 29).
- [42] I.-J. Cho, S. Jang, and H.-J. Nam, "A piezoelectrically actuated mems speaker with polyimide membrane and thin film pb (zr, ti) o3 (pzt) actuator," *Integrated Ferroelectrics*, vol. 105, no. 1, pp. 27–36, 2009 (cit. on pp. 15, 29).
- [43] H. J. Kim, K. Koo, S. Q. Lee, K.-H. Park, and J. Kim, "High performance piezoelectric microspeakers and thin speaker array system," *ETRI journal*, vol. 31, no. 6, pp. 680–687, 2009 (cit. on pp. 15, 29).

- [44] W. Liu, J. Huang, Y. Shen, and J. Cheng, “Theoretical modeling of piezoelectric cantilever mems loudspeakers,” *Applied Sciences*, vol. 11, no. 14, p. 6323, 2021 (cit. on p. 15).
- [45] F. Stoppel, C. Eisermann, S. Gu-Stoppel, D. Kaden, T. Giese, and B. Wagner, “Novel membraneless two-way mems loudspeaker based on piezoelectric dual-concentric actuators,” in *2017 19th International Conference on Solid-State Sensors, Actuators and Microsystems (TRANSDUCERS)*, IEEE, 2017, pp. 2047–2050 (cit. on p. 15).
- [46] K. Seo, J. Park, H. Kim, D. Kim, S. Ur, and S. Yi, “Micromachined piezoelectric microspeakers fabricated with high quality aln thin film,” *Integrated Ferroelectrics*, vol. 95, no. 1, pp. 74–82, 2007 (cit. on p. 15).
- [47] H. Nathanson and R. Wickstrom, “A resonant-gate silicon surface transistor with high-q band-pass properties,” *Applied physics letters*, vol. 7, no. 4, pp. 84–86, 1965 (cit. on p. 15).
- [48] M. R. Bai, R.-L. Chen, and C.-J. Wang, “Electroacoustic analysis of an electret loudspeaker using combined finite-element and lumped-parameter models,” *The Journal of the Acoustical Society of America*, vol. 125, no. 6, pp. 3632–3640, 2009 (cit. on p. 16).
- [49] H. Kim, A. A. Astle, K. Najafi, L. P. Bernal, P. D. Washabaugh, and F. Cheng, “Bi-directional electrostatic microspeakers with two large-deflection flexible membranes actuated by single/dual electrodes,” in *SENSORS, 2005 IEEE*, IEEE, 2005, 4–pp (cit. on pp. 17, 29).
- [50] C. Sano, M. Ataka, G. Hashiguchi, and H. Toshiyoshi, “An electret-augmented low-voltage mems electrostatic out-of-plane actuator for acoustic transducer applications,” *Micromachines*, vol. 11, no. 3, p. 267, 2020 (cit. on p. 17).
- [51] C. Glacer, A. Dehé, D. Tumpold, and R. Laur, “Silicon microspeakers with out-of-plane displacement,” in *The 9th IEEE International Conference on Nano/Micro Engineered and Molecular Systems (NEMS)*, IEEE, 2014, pp. 12–16 (cit. on pp. 17, 29).
- [52] R. C. Roberts, J. Du, A. O. Ong, D. Li, C. A. Zorman, and N. C. Tien, “Electrostatically driven touch-mode poly-sic microspeakers,” in *SENSORS, 2007 IEEE*, IEEE, 2007, pp. 284–287 (cit. on pp. 17, 29).
- [53] A. Murarka, J. H. Lang, and V. Bulovic, “Printed membrane electrostatic mems microspeakers,” in *2016 IEEE 29th International Conference on Micro Electro Mechanical Systems (MEMS)*, IEEE, 2016, pp. 1118–1121 (cit. on p. 17).
- [54] R. Dejaeger, “Modélisations multiphysiques, réalisation et expérimentations d’un haut-parleur digital matriciel piézoélectrique mems,” Ph.D. dissertation, INSA de Lyon, 2014 (cit. on p. 18).
- [55] R. Dejaeger, F. Casset, B. Desloges, G. Le Rhun, P. Robert, S. Fanget, Q. Leclère, K. Ege, and J.-L. Guyader, “Development and characterization of a piezoelectrically actuated mems digital loudspeaker,” *Procedia Engineering*, vol. 47, pp. 184–187, 2012 (cit. on p. 18).
- [56] F. Casset, R. Dejaeger, B. Laroche, B. Desloges, Q. Leclere, R. Morisson, Y. Bohard, J. Goglio, J. Escato, and S. Fanget, “A 256 mems membrane digital loudspeaker array based on pzt actuators,” *Procedia Engineering*, vol. 120, pp. 49–52, 2015 (cit. on pp. 18, 19, 29).
- [57] A. Arevalo, D. Castro, D. Conchouso, J. Kosel, and I. G. Foulds, “Digital electrostatic acoustic transducer array,” in *2016 IEEE 11th Annual International Conference on Nano/Micro Engineered and Molecular Systems (NEMS)*, IEEE, 2016, pp. 225–228 (cit. on p. 18).
- [58] —, “Mems digital parametric loudspeaker,” in *2016 IEEE 29th International Conference on Micro Electro Mechanical Systems (MEMS)*, IEEE, 2016, pp. 1098–1101 (cit. on p. 18).

- [59] S. Monkronthong, N. White, and N. Harris, "A study of efficient speaklet driving mechanisms for use in a digital loudspeaker array based on pzt actuators," in *2016 IEEE Sensors Applications Symposium (SAS)*, IEEE, 2016, pp. 1–5 (cit. on p. 19).
- [60] M. Hänslér and M. Auer, "Design considerations for a digital input mems speaker audio amplifier with energy recovery," in *2019 15th Conference on Ph. D Research in Microelectronics and Electronics (PRIME)*, IEEE, 2019, pp. 297–300 (cit. on p. 19).
- [61] D. Mayrhofer and M. Kaltenbacher, "Investigation of a new method for sound generation—advanced digital sound reconstruction," *e & i Elektrotechnik und Informationstechnik*, vol. 138, no. 3, pp. 148–154, 2021 (cit. on p. 19).
- [62] P. Guiraud, S. Giordano, O. Bou Matar, P. Pernod, and R. Lardat, "Thermoacoustic wave generation in multilayered thermophones with cylindrical and spherical geometries," *Journal of Applied Physics*, vol. 129, no. 11, p. 115 103, 2021 (cit. on p. 19).
- [63] W. Fei, J. Zhou, and W. Guo, "Low-voltage driven graphene foam thermoacoustic speaker," *Small*, vol. 11, no. 19, pp. 2252–2256, 2015 (cit. on pp. 20, 29).
- [64] Q. Zhou and A. Zettl, "Electrostatic graphene loudspeaker," *Applied physics letters*, vol. 102, no. 22, p. 223 109, 2013 (cit. on p. 20).
- [65] L. Xiao, Z. Chen, C. Feng, L. Liu, Z.-Q. Bai, Y. Wang, L. Qian, Y. Zhang, Q. Li, K. Jiang, *et al.*, "Flexible, stretchable, transparent carbon nanotube thin film loudspeakers," *Nano letters*, vol. 8, no. 12, pp. 4539–4545, 2008 (cit. on p. 20).
- [66] H. Tian, T.-L. Ren, D. Xie, Y.-F. Wang, C.-J. Zhou, T.-T. Feng, D. Fu, Y. Yang, P.-G. Peng, L.-G. Wang, *et al.*, "Graphene-on-paper sound source devices," *ACS nano*, vol. 5, no. 6, pp. 4878–4885, 2011 (cit. on p. 20).
- [67] T. Snaidero, F. Jacobsen, and J. Buchholz, "Measuring hrtfs of Brüel & Kjær type 4128-c, Gras kemar type 45bm, and head acoustics hms ii. 3 head and torso simulators," *Lyngby, Denmark: Technical University of Denmark, Department of Electrical Engineering*, 2011 (cit. on p. 21).
- [68] S. Olive and T. Welti, "The relationship between perception and measurement of headphone sound quality," in *Audio Engineering Society Convention 133*, Audio Engineering Society, 2012 (cit. on pp. 21, 23).
- [69] M. Hiipakka, "Measurement apparatus and modelling techniques of ear canal acoustics," *Espoo: Helsinki University of Technology*, 2008 (cit. on p. 21).
- [70] M.-C. Cheng, W.-S. Huang, and S. R.-S. Huang, "A silicon microspeaker for hearing instruments," *Journal of Micromechanics and Microengineering*, vol. 14, no. 7, p. 859, 2004 (cit. on p. 24).
- [71] Y. Chen, W.-T. Liu, T.-Y. Chao, and Y.-T. Cheng, "An optimized cu-ni nanocomposite coil for low-power electromagnetic microspeaker fabrication," in *TRANSDUCERS 2009-2009 International Solid-State Sensors, Actuators and Microsystems Conference*, IEEE, 2009, pp. 25–28 (cit. on p. 24).
- [72] S.-S. Je, N. Wang, H. C. Brown, D. P. Arnold, and J. Chae, "An electromagnetically actuated microspeaker with fully-integrated wax-bonded nd-fe-b micromagnets for hearing aid applications," in *TRANSDUCERS 2009-2009 International Solid-State Sensors, Actuators and Microsystems Conference*, IEEE, 2009, pp. 885–888 (cit. on p. 24).
- [73] B. Y. Majlis, G. Sugandi, and M. M. Noor, "Compact electrodynamic mems-speaker," in *2017 China Semiconductor Technology International Conference (CSTIC)*, IEEE, 2017, pp. 1–3 (cit. on pp. 24, 30).

- [74] S.-S. Je, F. Rivas, R. E. Diaz, J. Kwon, J. Kim, B. Bakkaloglu, S. Kiaei, and J. Chae, “A compact and low-cost mems loudspeaker for digital hearing aids,” *IEEE Transactions on Biomedical Circuits and Systems*, vol. 3, no. 5, pp. 348–358, 2009 (cit. on p. 24).
- [75] Y. Chen and Y.-T. Cheng, “A low-power milliwatt electromagnetic microspeaker using a pdms membrane for hearing aids application,” in *2011 IEEE 24th International Conference on Micro Electro Mechanical Systems*, IEEE, 2011, pp. 1213–1216 (cit. on pp. 24, 30).
- [76] B. Kaiser, S. Langa, L. Ehrig, M. Stolz, H. Schenk, H. Conrad, H. Schenk, K. Schimmanz, and D. Schuffenhauer, “Concept and proof for an all-silicon mems micro speaker utilizing air chambers,” *Microsystems & Nanoengineering*, vol. 5, no. 1, pp. 1–11, 2019 (cit. on pp. 24, 25, 30).
- [77] H. Conrad, H. Schenk, B. Kaiser, S. Langa, M. Gaudet, K. Schimmanz, M. Stolz, and M. Lenz, “A small-gap electrostatic micro-actuator for large deflections,” *Nature communications*, vol. 6, no. 1, pp. 1–7, 2015 (cit. on p. 24).
- [78] B. Spitz, F. Wall, H. Schenk, A. Melnikov, L. Ehrig, S. Langa, M. Stolz, B. Kaiser, H. Conrad, and H. Schenk, “Audio-transducer for in-ear-applications based on cmos-compatible electrostatic actuators,” in *MikroSystemTechnik 2019; Congress*, VDE, 2019, pp. 1–4 (cit. on p. 24).
- [79] A. Melnikov, H. A. Schenk, J. M. Monsalve, F. Wall, M. Stolz, A. Mrosk, S. Langa, and B. Kaiser, “Coulomb-actuated microbeams revisited: experimental and numerical modal decomposition of the saddle-node bifurcation,” *Microsystems & nanoengineering*, vol. 7, no. 1, pp. 1–13, 2021 (cit. on p. 25).
- [80] J. M. Monsalve, A. Melnikov, B. Kaiser, D. Schuffenhauer, M. Stolz, L. Ehrig, H. A. Schenk, H. Conrad, and H. Schenk, “Large-signal equivalent-circuit model of asymmetric electrostatic transducers,” *IEEE/ASME Transactions on Mechatronics*, 2021 (cit. on p. 25).
- [81] J. J. Neumann Jr and K. J. Gabriel, “Cmos-mems membrane for audio-frequency acoustic actuation,” *Sensors and Actuators A: Physical*, vol. 95, no. 2-3, pp. 175–182, 2002 (cit. on p. 25).
- [82] F. Stoppel, A. Männchen, F. Niekiel, D. Beer, T. Giese, and B. Wagner, “New integrated full-range mems speaker for in-ear applications,” in *2018 IEEE Micro Electro Mechanical Systems (MEMS)*, IEEE, 2018, pp. 1068–1071 (cit. on pp. 26, 30).
- [83] A. Fawzy, Y. Lang, and M. Zhang, “Design and analysis of piezoelectric mems micro-speaker based on scandium-doped aln thin film,” *Micro & Nano Letters*, vol. 16, no. 3, pp. 227–231, 2021 (cit. on p. 26).
- [84] G. Massimino, C. Gazzola, V. Zega, S. Adorno, and A. Corigliano, “Ultrasonic piezoelectric mems speakers for in-ear applications: bubbles-like and pistons-like innovative designs,” in *2022 23rd International Conference on Thermal, Mechanical and Multi-Physics Simulation and Experiments in Microelectronics and Microsystems (EuroSimE)*, IEEE, 2022, pp. 1–4 (cit. on p. 26).
- [85] Q. Wang, T. Ruan, Q. Xu, B. Yang, and J. Liu, “Wearable multifunctional piezoelectric mems device for motion monitoring, health warning, and earphone,” *Nano Energy*, vol. 89, p. 106324, 2021 (cit. on p. 26).
- [86] H.-H. Cheng, Z.-R. Huang, M. Wu, and W. Fang, “Low frequency sound pressure level improvement of piezoelectric mems microspeaker using novel spiral spring with dual electrode,” in *2019 20th International Conference on Solid-State Sensors, Actuators and Microsystems & Eurosensors XXXIII (TRANSDUCERS & EUROSENSORS XXXIII)*, IEEE, 2019, pp. 2013–2016 (cit. on p. 26).

- [87] Y. Hirano, Y. Suzuki, N. Fujita, C.-M. Li, H. Chiba, and S. Tanaka, "Pzt mems speaker integrated with silicon-parylene composite corrugated diaphragm," in *2022 IEEE 35th International Conference on Micro Electro Mechanical Systems Conference (MEMS)*, IEEE, 2022, pp. 255–258 (cit. on p. 26).
- [88] H.-H. Cheng, S.-C. Lo, Z.-R. Huang, Y.-J. Wang, M. Wu, and W. Fang, "On the design of piezoelectric mems microspeaker for the sound pressure level enhancement," *Sensors and Actuators A: Physical*, vol. 306, p. 111 960, 2020 (cit. on pp. 26, 30).
- [89] S.-H. Tseng, S.-C. Lo, Y.-J. Wang, S.-W. Lin, M. Wu, and W. Fang, "Sound pressure and low frequency enhancement using novel pzt mems microspeaker design," in *2020 IEEE 33rd international conference on micro electro mechanical systems (MEMS)*, IEEE, 2020, pp. 546–549 (cit. on pp. 26, 30).
- [90] Y.-T. Lin, S.-C. Lo, and W. Fang, "Two-way piezoelectric mems microspeaker with novel structure and electrode design for bandwidth enhancement," in *2021 21st International Conference on Solid-State Sensors, Actuators and Microsystems (Transducers)*, IEEE, 2021, pp. 230–233 (cit. on p. 26).
- [91] S. Yi, S. C. Ur, and E. S. Kim, "Performance of packaged piezoelectric microspeakers depending on the material properties," in *2009 IEEE 22nd International Conference on Micro Electro Mechanical Systems*, IEEE, 2009, pp. 765–768 (cit. on p. 26).
- [92] A. Rusconi, S. Costantini, and C. Prelini, "Micro speakers," in *Silicon Sensors and Actuators*, Springer, 2022, pp. 651–676 (cit. on p. 26).
- [93] Usound, *Achelous UT-P 2018 Datasheet*, 2020. [Online]. Available: https://www.usound.com/wp-content/uploads/2020/01/2001_Achelous-UT-P-2018-Datasheet.pdf (cit. on pp. 27, 29).
- [94] H. Kim and W. Yang, "The effects of electrodes patterned onto the piezoelectric thin film on frequency response characteristics of pmn-pt mems acoustic actuators," *Journal of Electroceramics*, vol. 35, no. 1, pp. 45–52, 2015 (cit. on p. 29).
- [95] S. Yi, M. Yoon, and S. Ur, "Piezoelectric microspeakers with high compressive zno film and floating electrode," *Journal of electroceramics*, vol. 23, no. 2, pp. 295–300, 2009 (cit. on p. 29).
- [96] C.-H. Han and E. S. Kim, "Parylene-diaphragm piezoelectric acoustic transducers," in *Proceedings IEEE Thirteenth Annual International Conference on Micro Electro Mechanical Systems (Cat. No. 00CH36308)*, IEEE, 2000, pp. 148–152 (cit. on p. 29).
- [97] R. Gao, X. Chu, Y. Huan, Y. Sun, J. Liu, X. Wang, and L. Li, "A study on (k, na) nbo3 based multilayer piezoelectric ceramics micro speaker," *Smart materials and structures*, vol. 23, no. 10, p. 105 018, 2014 (cit. on p. 29).
- [98] H. Tian, Y. Yang, D. Xie, T.-L. Ren, Y. Shu, C.-J. Zhou, L.-Q. Tao, and L.-T. Liu, "Flexible and large-area sound-emitting device using reduced graphene oxide," in *2013 IEEE 26th International Conference on Micro Electro Mechanical Systems (MEMS)*, IEEE, 2013, pp. 709–712 (cit. on p. 29).
- [99] H. Fletcher and W. A. Munson, "Loudness, its definition, measurement and calculation," *Bell System Technical Journal*, vol. 12, no. 4, pp. 377–430, 1933 (cit. on p. 29).
- [100] D. Rousseau and M. Melon, "La gestion des sons de très basses fréquences dans le domaine de l'audio," *Acoustique & techniques (Neuilly-sur-Seine)*, no. 67, pp. 44–49, 2011 (cit. on p. 29).
- [101] Y. Podgorny, K. Vorotilov, and A. Sigov, "Estimation of steady-state leakage current in polycrystalline pzt thin films," *AIP Advances*, vol. 6, no. 9, p. 095 025, 2016 (cit. on p. 41).

- [102] W. Ye, X. Wang, W. Hemmert, D. Freeman, and J. White, “Air damping in laterally oscillating microresonators: a numerical and experimental study,” *Journal of Microelectromechanical Systems*, vol. 12, no. 5, pp. 557–566, 2003 (cit. on p. 43).
- [103] S. W. Rienstra and A. Hirschberg, “An introduction to acoustics,” *Eindhoven University of Technology*, vol. 18, p. 19, 2004 (cit. on p. 43).
- [104] M. Bao and H. Yang, “Squeeze film air damping in mems,” *Sensors and Actuators A: Physical*, vol. 136, no. 1, pp. 3–27, 2007 (cit. on p. 44).
- [105] R. B. Darling, C. Hivick, and J. Xu, “Compact analytical modeling of squeeze film damping with arbitrary venting conditions using a green’s function approach,” *Sensors and Actuators A: Physical*, vol. 70, no. 1-2, pp. 32–41, 1998 (cit. on p. 44).
- [106] E. G. Williams, *Fourier acoustics: sound radiation and nearfield acoustical holography*. Academic press, 1999 (cit. on p. 46).
- [107] N. Akkaya, “Acoustic radiation from baffled planar sources: a series approach,” Ph.D. dissertation, Texas Tech University, 1999 (cit. on p. 46).
- [108] F. P. Mechel, *Formulas of acoustics*. Acoustical Society of America, 2004 (cit. on p. 46).
- [109] P. M. Morse and K. U. Ingard, *Theoretical acoustics*. Princeton university press, 1986 (cit. on p. 48).
- [110] B. E. Anderson, “Understanding radiation impedance through animations,” in *Proceedings of Meetings on Acoustics 175ASA*, Acoustical Society of America, vol. 33, 2018, p. 025 003 (cit. on p. 48).
- [111] S. Franssila, *Introduction to microfabrication*. John Wiley & Sons, 2010 (cit. on pp. 55, 84).
- [112] I. Shahosseini, “Vers des micro-haut-parleurs à hautes performances électroacoustiques en technologie silicium,” Ph.D. dissertation, Paris 11, 2012 (cit. on p. 55).
- [113] S. Boisseau, G. Despesse, and B. A. Seddik, “Adjustable nonlinear springs to improve efficiency of vibration energy harvesters,” *arXiv preprint arXiv:1207.4559*, 2012 (cit. on pp. 86, 87).
- [114] M. Rébillat, R. Hennequin, E. Corteel, and B. F. Katz, “Identification of cascade of hammerstein models for the description of nonlinearities in vibrating devices,” *Journal of sound and vibration*, vol. 330, no. 5, pp. 1018–1038, 2011 (cit. on p. 90).
- [115] A. Falaize and T. Hélie, “Passive modelling of the electrodynamic loudspeaker: from the thiele-small model to nonlinear port-hamiltonian systems,” *Acta Acustica*, vol. 4, no. 1, p. 1, 2020 (cit. on p. 90).
- [116] A. Falaize, N. Papazoglou, T. Hélie, and N. Lopes, “Compensation of loudspeaker’s nonlinearities based on flatness and port-hamiltonian approach,” in *22ème Congrès Français de Mécanique*, 2015 (cit. on p. 90).
- [117] A. Novak, L. Simon, P. Lotton, B. Merit, and J. Gilbert, “Nonlinear analysis and modeling of electrodynamic loudspeakers,” in *10ème Congrès Français d’Acoustique*, 2010 (cit. on p. 90).
- [118] W. Klippel, “Large signal performance of tweeters, micro speakers and horn drivers,” in *Audio Engineering Society Convention*, vol. 118, 2005, p. 19 (cit. on p. 90).
- [119] —, “Loudspeaker nonlinearities—causes, parameters, symptoms,” in *Audio Engineering Society Convention 119*, Audio Engineering Society, 2005 (cit. on p. 90).

- [120] A. King and F. Agerkvist, "Fractional derivative loudspeaker models for nonlinear suspensions and voice coils," *Journal of the Audio Engineering Society*, vol. 66, no. 7/8, pp. 525–536, 2018 (cit. on p. 90).
- [121] M. Tilli, M. Paulasto-Krockel, M. Petzold, H. Theuss, T. Motooka, and V. Lindroos, *Handbook of silicon based MEMS materials and technologies*. Elsevier, 2020 (cit. on p. 104).
- [122] S. Sivaramakrishnan, P. Mardilovich, T. Schmitz-Kempen, and S. Tiedke, "Concurrent wafer-level measurement of longitudinal and transverse effective piezoelectric coefficients (d 33, f and e 31, f) by double beam laser interferometry," *Journal of Applied Physics*, vol. 123, no. 1, p. 014 103, 2018 (cit. on p. 106).
- [123] S. Sivaramakrishnan, P. Mardilovich, A. Mason, A. Roelofs, T. Schmitz-Kempen, and S. Tiedke, "Electrode size dependence of piezoelectric response of lead zirconate titanate thin films measured by double beam laser interferometry," *Applied Physics Letters*, vol. 103, no. 13, p. 132 904, 2013 (cit. on p. 106).
- [124] S. Takyu, Y. Fumita, D. Yamamoto, S. Yamashita, K. Furuta, Y. Yamashita, K. Tanaka, N. Uchiyama, T. Ogiwara, and Y. Kondo, "A novel dicing technologies for wlcsps using stealth dicing through dicing tape and back side protection-film," in *2016 IEEE 66th Electronic Components and Technology Conference (ECTC)*, IEEE, 2016, pp. 1241–1246 (cit. on p. 116).
- [125] R. Liechti, S. Durand, T. Hilt, F. Casset, C. Poulain, G. Le Rhun, F. Pavageau, H. Kuentz, and M. Colin, "Total harmonic distortion of a piezoelectric mems loudspeaker in an iec 60318-4 coupler estimation using static measurements and a nonlinear state space model," *Micromachines*, vol. 12, no. 12, p. 1437, 2021 (cit. on p. 117).
- [126] P. Tinnemans, "Dysco3 thin film substrates: an x-ray diffraction study," Ph.D. dissertation, [Sl: sn], 2012 (cit. on p. 164).

List of Publications

- [1] R. Liechti, S. Durand, T. Hilt, F. Casset, C. Dieppedale, T. Verdot, and M. Colin, “A piezoelectric mems loudspeaker lumped and fem models,” in *2021 22nd International Conference on Thermal, Mechanical and Multi-Physics Simulation and Experiments in Microelectronics and Microsystems (EuroSimE)*, IEEE, 2021, pp. 1–8.
- [2] R. Liechti, S. Durand, T. Hilt, F. Casset, C. Poulain, G. Le Rhun, F. Pavageau, H. Kuentz, and M. Colin, “Total harmonic distortion of a piezoelectric mems loudspeaker in an iec 60318-4 coupler estimation using static measurements and a nonlinear state space model,” *Micromachines*, vol. 12, no. 12, p. 1437, 2021.
- [3] R. Liechti, S. Durand, T. Hilt, F. Casset, C. Dieppedale, T. Verdot, and M. Colin, “A piezoelectric mems loudspeaker for in-ear and free field applications lumped and finite element models,” *Microelectronics Reliability*, vol. 134, p. 114555, 2022.
- [4] F. Pavageau, C. Dieppedale, P. Perreau, R. Liechti, A. Hamelin, C. Licitra, F. Casset, and G. Le Rhun, “Highly transparent piezoelectric pzt membranes for transducer applications,” *Sensors and Actuators A: Physical*, p. 113 866, 2022.
- [5] R. Liechti, S. Durand, T. Hilt, F. Casset, C. Dieppedale, and M. Colin, “High performance piezoelectric mems loudspeaker based on an innovative wafer bonding process,” *Microsystems & Nano-engineering*, vol. 1, no. 1, pp. 1–17, 2015, Under Review.

Appendices

A State Space Modeling

Equations of the state space model of the coupler

$$\frac{\partial u_c(t)}{\partial t} = \frac{1}{R_g C_p(u_c)} u_{in}(t) - \frac{1}{R_g C_p(u_c)} u_c(t) - \frac{\gamma(u_c)}{C_p(u_c)} v(t) \quad (1)$$

$$\frac{\partial v(t)}{\partial t} = \frac{\gamma(u_c)}{M_{ms} + S_d^2 L_1} u_c(t) - \frac{R_{ms}}{M_{ms} + S_d^2 L_1} v(t) - \frac{1}{M_{ms} + S_d^2 L_1} F_{C_{ms}}(t) - \frac{S_d}{M_{ms} + S_d^2 L_1} p_{C_1}(t) \quad (2)$$

$$\frac{\partial F_{C_{ms}}}{\partial t} = \frac{1}{C_{ms}(x)} v(t) \quad (3)$$

$$\frac{\partial x(t)}{\partial t} = v(t) \quad (4)$$

$$\frac{\partial p_{C_1}(t)}{\partial t} = \frac{S_d}{C_1} v(t) - \frac{1}{C_1} Q_2(t) - \frac{1}{C_1} Q_{L_3}(t) \quad (5)$$

$$\frac{\partial Q_2(t)}{\partial t} = \frac{1}{L_2} p_{C_1}(t) - \frac{1}{L_2} p_{C_2}(t) - \frac{R_2}{L_2} Q_2(t) \quad (6)$$

$$\frac{\partial p_{C_2}(t)}{\partial t} = \frac{1}{C_2} Q_2(t) \quad (7)$$

$$\frac{\partial Q_{L_3}(t)}{\partial t} = \frac{1}{L_3} p_{C_1}(t) - \frac{1}{L_3} p_{C_3}(t) \quad (8)$$

$$\frac{\partial p_{C_3}(t)}{\partial t} = \frac{1}{C_3} Q_{L_3}(t) - \frac{1}{C_3} Q_4(t) - \frac{1}{C_3} Q_{out}(t) \quad (9)$$

$$\frac{\partial Q_4(t)}{\partial t} = \frac{1}{L_4} p_{C_3}(t) - \frac{1}{L_4} Q_4(t) - \frac{1}{L_4} p_{C_4}(t) \quad (10)$$

$$\frac{\partial p_{C_4}(t)}{\partial t} = \frac{1}{C_4} Q_4(t) \quad (11)$$

$$\frac{\partial Q_{out}(t)}{\partial t} = \frac{1}{L_5} p_{C_3}(t) - \frac{1}{L_5} p_{out}(t) \quad (12)$$

$$\frac{\partial p_{out}(t)}{\partial t} = \frac{1}{C_5} Q_{out}(t) \quad (13)$$

B Horn

A horn is designed to increase the output level of the loudspeaker for demonstration purposes. The horn is designed analytically by using a two-port model of the loudspeaker, and of the successive sections of tubes. A horn can increase the output level of a loudspeaker by adapting the high acoustical impedance of a loudspeaker to the low acoustical impedance of air. A horn has a cut-off frequency, determined by its size, below which its principle is not working. For the profile of the horn, the famous exponential horn is used. The section of the horn as a function of the length x is given by

$$S(x) = S_0 e^{mx} \quad (14)$$

with $S(x)$ the section at the position x , S_0 the section at the throat of the horn. The mouth area of the horn can be calculated using

$$S_L = S_0 e^{mL} \quad (15)$$

with L the total length of the horn. The lower cut-off frequency can be calculated using:

$$f_c = \frac{mc_0}{4\pi} \quad (16)$$

with c_0 the sound velocity in air at ambient temperature. The throat area is fixed by the radiating surface of the loudspeaker. The horn being circular, the throat area is the circumscribed circle around the squared membrane of the loudspeaker. Following the observations during the measurements, the best design is considered to be the 6×6 design, and so the throat diameter is equal to 56.55 mm^2 . Using a cut-off frequency of $f_c = 850 \text{ Hz}$, the total length and the growing factor m of the horn are determined. The horn is then discretized into small cylindrical sections, as it is depicted in Figure B.1 whose are then simulated using Equation 17.

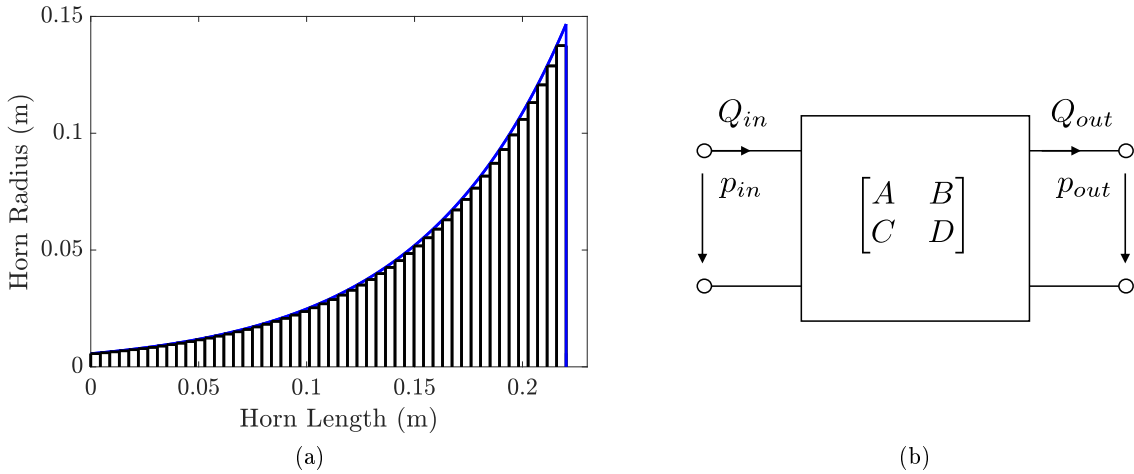


Figure B.1: Horn shape and discretized tubes (a) and simple acoustical quadripole element

Then, the dissipative plane wave assumption is used to simulate each section of the horn, using the transfer matrix of a tube written as

$$\begin{bmatrix} p_{in} \\ Q_{in} \end{bmatrix} = \begin{bmatrix} \cos(k_c L) & jZ_c \sin(k_c L) \\ \frac{j}{Z_c} \sin(k_c L) & \cos(k_c L) \end{bmatrix} \begin{bmatrix} p_{out} \\ Q_{out} \end{bmatrix}. \quad (17)$$

As it is presented in Figure B.1, the total length of the horn is approximately 223 mm and the mouth have a diameter of approximately 286 mm. Using the complete equivalent circuit of the loudspeaker depicted in Figure B.2, the pressure response of the loudspeaker can be calculated, by multiplying all the matrices of the sections of the horn, and by evaluating the transfer impedance of the horn for all audio frequencies.

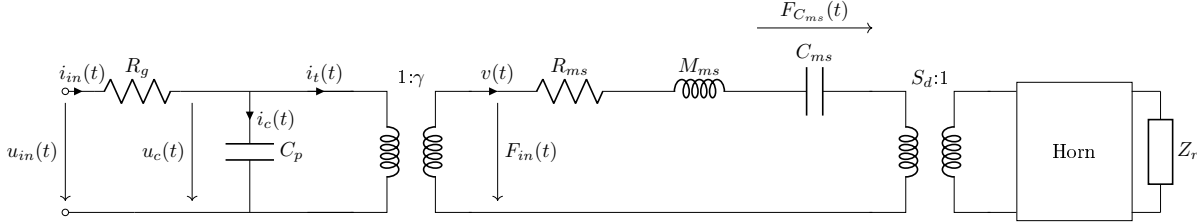


Figure B.2: Linear lumped equivalent network of the loudspeaker radiating into a horn

The complete equation writes

$$\begin{bmatrix} u_{in} \\ i_{in} \end{bmatrix} = \begin{bmatrix} 1 & 0 \\ j\omega C_p & 1 \end{bmatrix} \begin{bmatrix} \frac{1}{\gamma} & 0 \\ 0 & \gamma \end{bmatrix} \begin{bmatrix} 1 & R_{ms} \\ 0 & 1 \end{bmatrix} \begin{bmatrix} 1 & j\omega M_{ms} \\ 0 & 1 \end{bmatrix} \begin{bmatrix} 1 & \frac{1}{j\omega C_{ms}} \\ 0 & 1 \end{bmatrix} \begin{bmatrix} S_d & 0 \\ 0 & \frac{1}{S_d} \end{bmatrix} \prod_{n=1}^N \begin{bmatrix} \cos(k_{c_n} L_d) & jZ_{c_n} \sin(k_{c_n} L_d) \\ \frac{j}{Z_{c_n}} \sin(k_{c_n} L_d) & \cos(k_{c_n} L_d) \end{bmatrix} \begin{bmatrix} p_{out} \\ Q_{out} \end{bmatrix} \quad (18)$$

Using the discretized matrices of the horn, the equation linking the input voltage u_{in} and the input current i_{in} with the output pressure p_{out} and the output volume velocity Q_{out} is written

$$Q_{out} = \frac{A_h \Re(Z_{out}) + B_h}{C_h \Re(Z_{out}) + D_h}. \quad (19)$$

For the acoustics volume velocity Q_{out} at the mouth of the horn, the pressure at 10 cm can be calculated using the reduced Rayleigh integral. From the horn only, the real and imaginary part of the horn can be calculated and are depicted in Figure B.3(a).

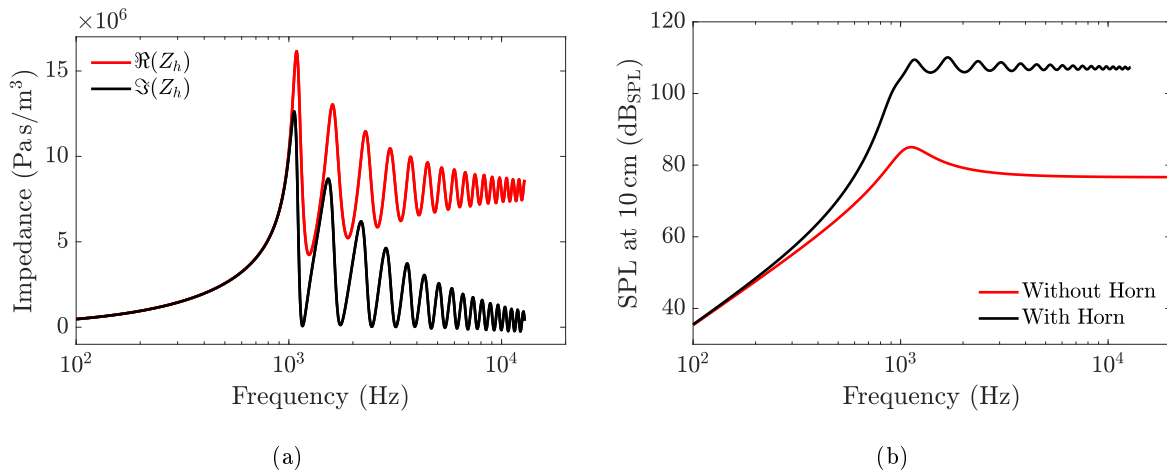


Figure B.3: Imaginary and real part of the acoustical impedance of the horn (a) and pressure radiated by the loudspeaker with and without horn (b)

The horn is then drawn into Solidworks® using the calculated profile. At the throat, the circular section of the horn is adapted to a square to adapt to the moving plate of the loudspeaker. A 3D picture of the

horn is depicted in Figure B.4(a) and a cross section view of the loudspeaker, mounted on the PCB and mounted on the horn is depicted in Figure B.4(b). For printing, the end of the horn is flattened.

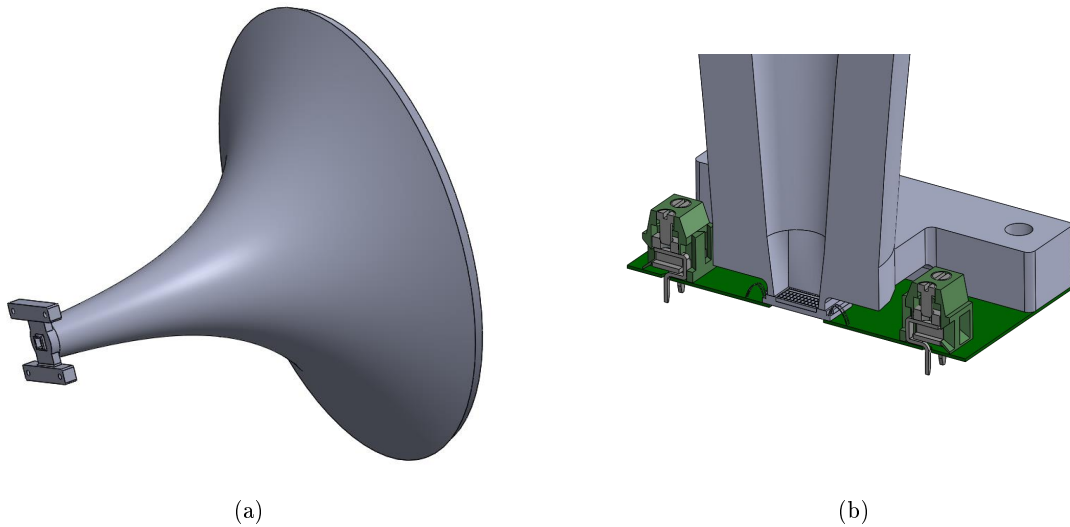


Figure B.4: 3D CAD view of the horn in Solidworks® (a) and cross section 3D view of the horn mounted on the PCB on which the loudspeaker is bonded (b)

From the CAD model, the horn is imported to COMSOL to simulate the acoustic response. A PML is used around a hemispherical domain, and only a quarter of the horn is simulated due to the symmetry. To simulate the loudspeaker, a rigid shell of the same surface as the moving plate of the loudspeaker is used at the throat of the horn. This shell is attached to the horn with a spring, simulating the equivalent compliance C_{ms} of the loudspeaker. The density, the thickness and the stiffness of the shell is set in order to have a mass equal to M_{ms} and no eigenmodes in the audio range.

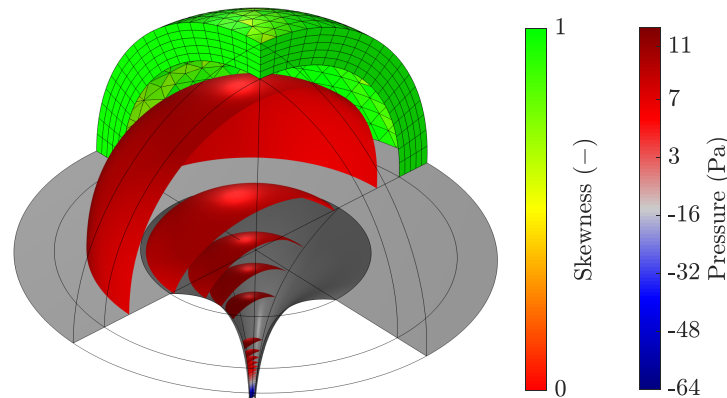


Figure B.5: Acoustic simulation of the horn using COMSOL®

In Figure B.5, the horn as well as the rigid baffle are represented respectively in dark gray and in a lighter gray. The acoustic pressure is represented as isosurfaces, and displays a pressure as high as 64 Pa at the throat of the horn, which is equivalent to 130 dB_{SPL}. The mesh quality whose skewness is depicted from poor quality (red), to good quality (green) for a quarter of the perfectly matched layer domain. The complete frequency response of the horn is calculated, as well as the acoustical impedance and is compared to the one calculated using the two-port formulation. The comparison is depicted in Figures

B.6(a) and B.6(b). Major differences in the shape of the response can be attributed to the acoustical radial modes of the horn, that are not simulated in the two-port model. The cut-off frequency as well as the level is well estimated.

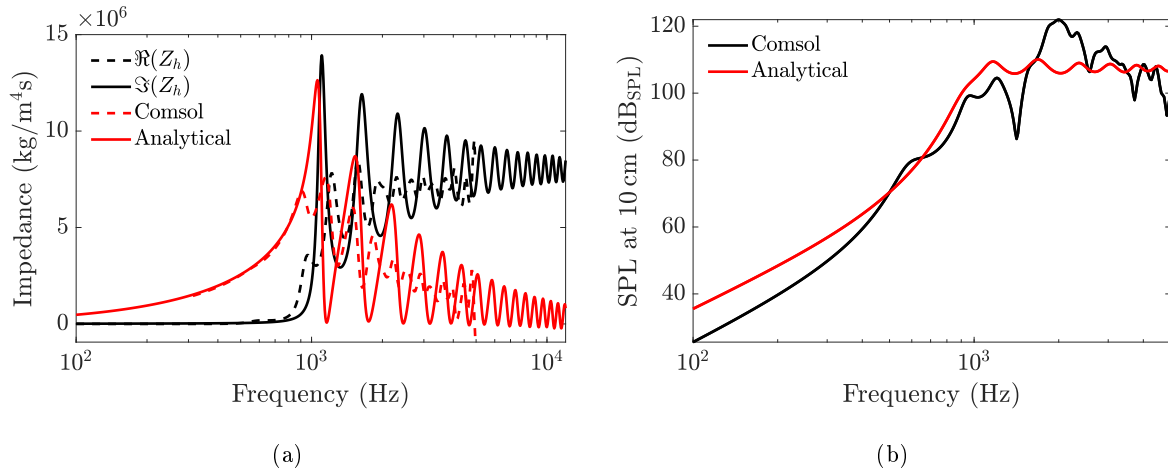


Figure B.6: Real and imaginary part of the acoustical impedance of the horn calculated using the two port model and COMSOL[®] (a) and pressure response of the horn at 10 cm calculated with the two port model and with COMSOL[®] (b)

C Cumulative Error Calculation

Calculation of the cumulative error for estimation of the incertainties on the measurements and simulation.

C.1 Moving Mass

The moving mass is determined using

$$M_{ms} = \rho_s \left(2L_{cb}WW_{cb} + t_pL_pW_p - t_{rp}n_{rl}n_{rw}l_{rr}w_{rr} - 2Wt_{rp}(L_{cs} + w_{it}) + W\frac{L}{2}t_m \right) \quad (20)$$

with ρ_s the density of silicon, L_{cb} the length of the coupling blocks, W the width of the plate, W_{cb} the width of the coupling blocks, t_p the thickness of the plate, t_{rp} the thickness of the reinforcement plates, n_{rl} the number of opening in the plate along L , n_{rw} the number of opening in the plate along W , l_{rr} the length of the opening, w_{rr} the width of the opening, L_{cs} the length of the coupling springs, w_{it} the width of the interstice around the plate and t_m the thickness of the actuators.

Knowing the manufacturing tolerances on W , L , W_{cb} , t_p , l_{rr} , w_{rr} , t_{rp} , L_{cs} , w_{it} and t_m , the error on the mass M_{ms} can be computed using

$$\begin{aligned} \Delta M_{ms} = & \left| \frac{\partial M_{ms}}{\partial W} \right| \Delta W + \left| \frac{\partial M_{ms}}{\partial L_{cb}} \right| \Delta L_{cb} + \left| \frac{\partial M_{ms}}{\partial W_{cb}} \right| \Delta W_{cb} + \left| \frac{\partial M_{ms}}{\partial t_p} \right| \Delta t_p \\ & + \left| \frac{\partial M_{ms}}{\partial L} \right| \Delta L + \left| \frac{\partial M_{ms}}{\partial t_{rp}} \right| \Delta t_{rp} + \left| \frac{\partial M_{ms}}{\partial l_{rr}} \right| \Delta l_{rr} + \left| \frac{\partial M_{ms}}{\partial w_{rr}} \right| \Delta w_{rr} \\ & + \left| \frac{\partial M_{ms}}{\partial l_{cs}} \right| \Delta l_{cs} + \left| \frac{\partial M_{ms}}{\partial w_{it}} \right| \Delta w_{it} + \left| \frac{\partial M_{ms}}{\partial t_m} \right| \Delta t_m, \end{aligned} \quad (21)$$

which leads to

$$\begin{aligned} \Delta M_{ms} = & |2WW_{cb}\rho_s| \Delta L_{cb} + \left| \rho_s \left(2L_{cb}W_{cb} + t_pL + \frac{L}{2} - 2t_{rp}(L_{cs} + w_{it}) \right) \right| \Delta W \\ & + |2L_{cb}W\rho_s| \Delta W_{cb} + |WL\rho_s| \Delta t_p + \left| \frac{1}{2}W\rho_s(2t_p + t_m) \right| \Delta L \\ & + |-\rho_s(2W(L_{cs} + w_{it}) - n_{rl}n_{rw}l_{rr}w_{rr})| \Delta t_{rp} + |-t_{rp}n_{rl}n_{rw}w_{rr}\rho_s| \Delta l_{rr} \\ & + |-t_{rp}n_{rl}n_{rw}l_{rr}\rho_s| \Delta w_{rr} + |-2Wt_{rp}\rho_s| w_{it} + \left| \frac{1}{2}WL\rho_s \right| \Delta t_m. \end{aligned} \quad (22)$$

Using the uncertainties formula and the desired values of the moving mass, the manufactured value gives

$$M_{ms} = 4.18 \pm 0.193 \text{ mg}. \quad (23)$$

C.2 Compliance

The compliance is derived from the bernoulli beam's model and can be written

$$C_{ms} = \frac{L^3(1 + 14\tau + \tau^2)}{16Wt_m^3E_m\tau(1 + \tau)} \quad (24)$$

The bending torque of the piezoelectric layer being very small compared to the bending torque of the silicon, the uncertainty on τ is assumed to be null. The uncertainty on the computed value of the compliance then writes

$$\Delta C_{ms} = \left| \frac{\partial C_{ms}}{\partial L} \right| \Delta L + \left| \frac{\partial C_{ms}}{\partial E_m} \right| \Delta E_m + \left| \frac{\partial C_{ms}}{\partial t_m} \right| \Delta t_m + \left| \frac{\partial C_{ms}}{\partial W} \right| \Delta W, \quad (25)$$

which leads to

$$\Delta C_{ms} = \left| \frac{3L^2(1+14\tau+\tau^2)}{16E_m t_m^3 W \tau(1+\tau)} \right| \Delta L + \left| -\frac{L^3(1+14\tau+\tau^2)}{16E_m^2 W t_m^3 \tau(1+\tau)} \right| \Delta E_m + \left| \frac{3L^3(1+14\tau+\tau^2)}{16E_m W t_m^4 \tau(1+\tau)} \right| \Delta t_m + \left| \frac{L^3(1+14\tau+\tau^2)}{16E_m W^2 t_m^3 \tau(1+\tau)} \right| \Delta W. \quad (26)$$

Using the uncertainties from the different values leads to

$$C_{ms} = 5.7 \pm 1.1 \text{ mm/N} \quad (27)$$

C.3 Blocked Force

The transduction factor is the blocked force divided by the actuation voltage, and is derived from the beam model. The transduction factor γ writes

$$\gamma = \frac{24e_{31,f}W(t_m + t_p)}{L(1 + \tau + \tau^2)} \quad (28)$$

As for the compliance, the ratio τ is assumed to have no uncertainty to simplify substantially the calculation, and the sum of the partial derivatives writes:

$$\Delta\gamma = \left| \frac{\partial\gamma}{\partial e_{31,f}} \right| \Delta e_{31,f} + \left| \frac{\partial\gamma}{\partial W} \right| \Delta W + \left| \frac{\partial\gamma}{\partial t_m} \right| \Delta t_m + \left| \frac{\partial\gamma}{\partial t_p} \right| \Delta t_p + \left| \frac{\partial\gamma}{\partial L} \right| \Delta L \quad (29)$$

which leads to.

$$\Delta\gamma = \left| \frac{24W(t_m + t_p)}{L(1 + 14\tau + \tau^2)} \right| \Delta e_{31,f} + \left| \frac{24e_{31,f}(t_m + t_p)}{L(1 + 14\tau + \tau^2)} \right| \Delta W + \left| \frac{24We_{31,f}}{L(1 + 14\tau + \tau^2)} \right| \Delta t_m + \left| \frac{24We_{31,f}}{L(1 + 14\tau + \tau^2)} \right| \Delta t_p + \left| \frac{24We_{31,f}(t_m + t_p)}{L^2(1 + 14\tau + \tau^2)} \right| \Delta L \quad (30)$$

Using the uncertainties from the different values leads to

$$\gamma = 2.6 \pm 0.081 \text{ mN/V}. \quad (31)$$

C.4 Radiating Surface

$$S_d = L_p W_p \quad (32)$$

The uncertainty simply writes:

$$\Delta S_d = L_p \Delta W_p + W_p \Delta L_p \quad (33)$$

which lead to

$$S_d = 36 \pm 0.012 \text{ mm}^2 \quad (34)$$

C.5 Total

Using all the previously determined uncertainties, the total uncertainty on the radiated sound pressure level can be evaluated. The radiated sound pressure, as a function of the transduction factor and the impedance of the loudspeaker can be written as

$$p(\mathbf{r}) = j\omega\rho S_d \frac{\gamma u_{in}}{R_{ms} + j\omega M_{ms} + \frac{1}{j\omega C_{ms}} + (Z_{front} + Z_{back})S_d^2} \frac{e^{jkr}}{2\pi r}. \quad (35)$$

The contribution of the radiation impedance being small for a loudspeaker this size, it can be neglected to simplify the calculation. The equation of the pressure is rewritten for the evaluation of the uncertainties at each frequencies as

$$p(\mathbf{r}) = j2\pi f_e \rho S_d \frac{\gamma u_{in}}{R_{ms} + j2\pi f_e M_{ms} + \frac{1}{j2\pi f_e C_{ms}}} \frac{e^{jkr}}{2\pi r}. \quad (36)$$

The uncertainty on the radiated pressure then writes

$$\begin{aligned} \Delta p(\mathbf{r}) = & \left| \frac{\partial p(\mathbf{r})}{\partial \rho} \right| \Delta \rho + \left| \frac{\partial p(\mathbf{r})}{\partial S_d} \right| \Delta S_d + \left| \frac{\partial p(\mathbf{r})}{\partial \gamma} \right| \Delta \gamma + \left| \frac{\partial p(\mathbf{r})}{\partial u_{in}} \right| \Delta u_{in} \\ & + \left| \frac{\partial p(\mathbf{r})}{\partial M_{ms}} \right| \Delta M_{ms} + \left| \frac{\partial p(\mathbf{r})}{\partial C_{ms}} \right| \Delta C_{ms} + \left| \frac{\partial p(\mathbf{r})}{\partial r} \right| \Delta r, \end{aligned} \quad (37)$$

which leads to

$$\begin{aligned} \Delta p(\mathbf{r}) = & \left| j2\pi f_e \rho \frac{\gamma u_{in}}{R_{ms} + j2\pi f_e M_{ms} + \frac{1}{j2\pi f_e C_{ms}}} \frac{e^{\frac{j2\pi f_e}{c_0}}}{2\pi r} \right| \Delta S_d \\ & + \left| j2\pi f_e S_d \frac{\gamma u_{in}}{R_{ms} + j2\pi f_e M_{ms} + \frac{1}{j2\pi f_e C_{ms}}} \frac{e^{\frac{j2\pi f_e}{c_0}}}{2\pi r} \right| \Delta \rho \\ & + \left| j2\pi f_e \rho S_d \frac{u_{in}}{R_{ms} + j2\pi f_e M_{ms} + \frac{1}{j2\pi f_e C_{ms}}} \frac{e^{\frac{j2\pi f_e}{c_0}}}{2\pi r} \right| \Delta \gamma \\ & + \left| j2\pi f_e \rho S_d \frac{\gamma}{R_{ms} + j2\pi f_e M_{ms} + \frac{1}{j2\pi f_e C_{ms}}} \frac{e^{\frac{j2\pi f_e}{c_0}}}{2\pi r} \right| \Delta u_{in} \\ & + \left| \frac{8\gamma\pi^3 C_{ms}^2 f_e^4 \rho S_d u_{in} e^{\frac{j2\pi f_e}{c_0}}}{r(1 + 2\pi C_{ms} f_e (-2\pi f_e M_{ms} + jR_{ms}))^2} \right| \Delta M_{ms} \\ & + \left| \frac{2\gamma\pi f_e^2 \rho S_d u_{in} e^{\frac{j2\pi f_e}{c_0}}}{r(1 + 2\pi C_{ms} f_e (-2\pi f_e M_{ms} + jR_{ms}))^2} \right| \Delta C_{ms} \\ & + \left| \frac{2j\gamma\pi C_{ms} f_e^2 \rho S_d u_{in} e^{\frac{-2j\pi f_e r}{c_0}} (2\pi f_e r - jc_0)}{c_0 r^2 (-1 + 2\pi C_{ms} f_e M_{ms} - jR_{ms})} \right| \Delta r. \end{aligned} \quad (38)$$

The sound pressure is finally calculated with

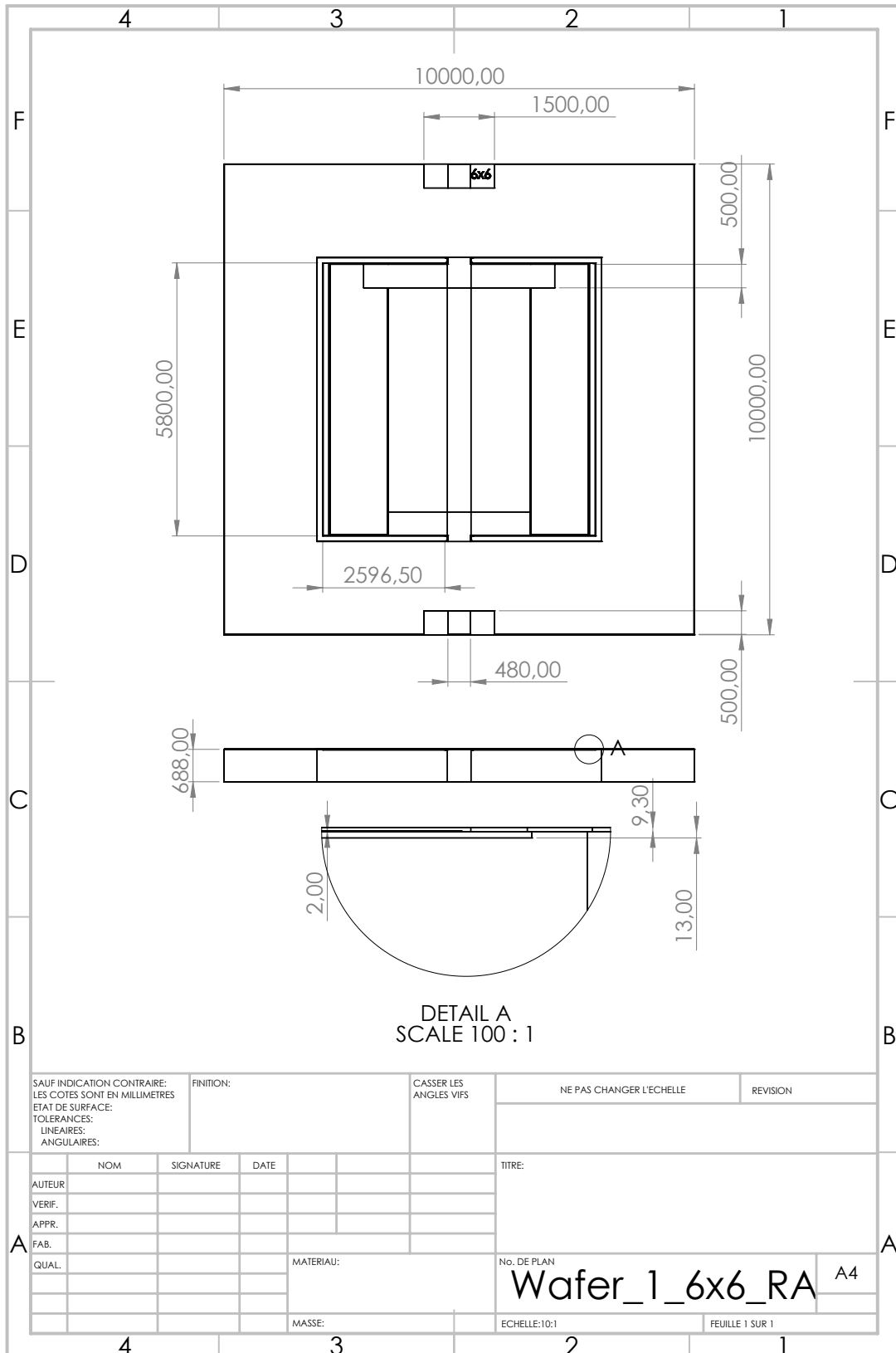
$$p(\mathbf{r})_{SPL} = 20 \log_{10} \left(\frac{p(\mathbf{r})}{p_{ref}} \right), \quad (39)$$

which lead to

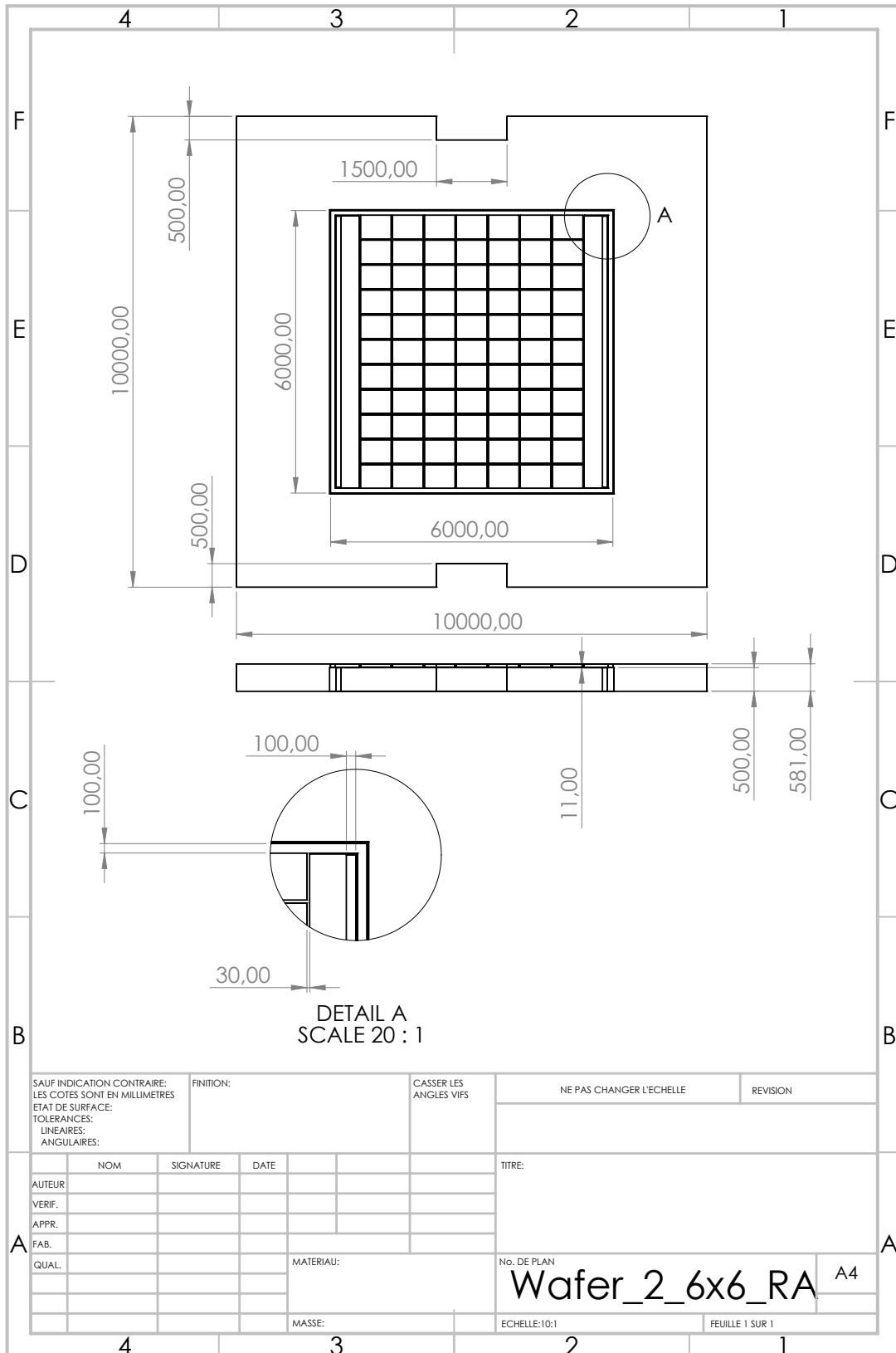
$$\Delta p(\mathbf{r})_{SPL} = \left| \frac{20}{p(\mathbf{r}) \log(10)} \right| \Delta p(\mathbf{r}). \quad (40)$$

D CAD Plans

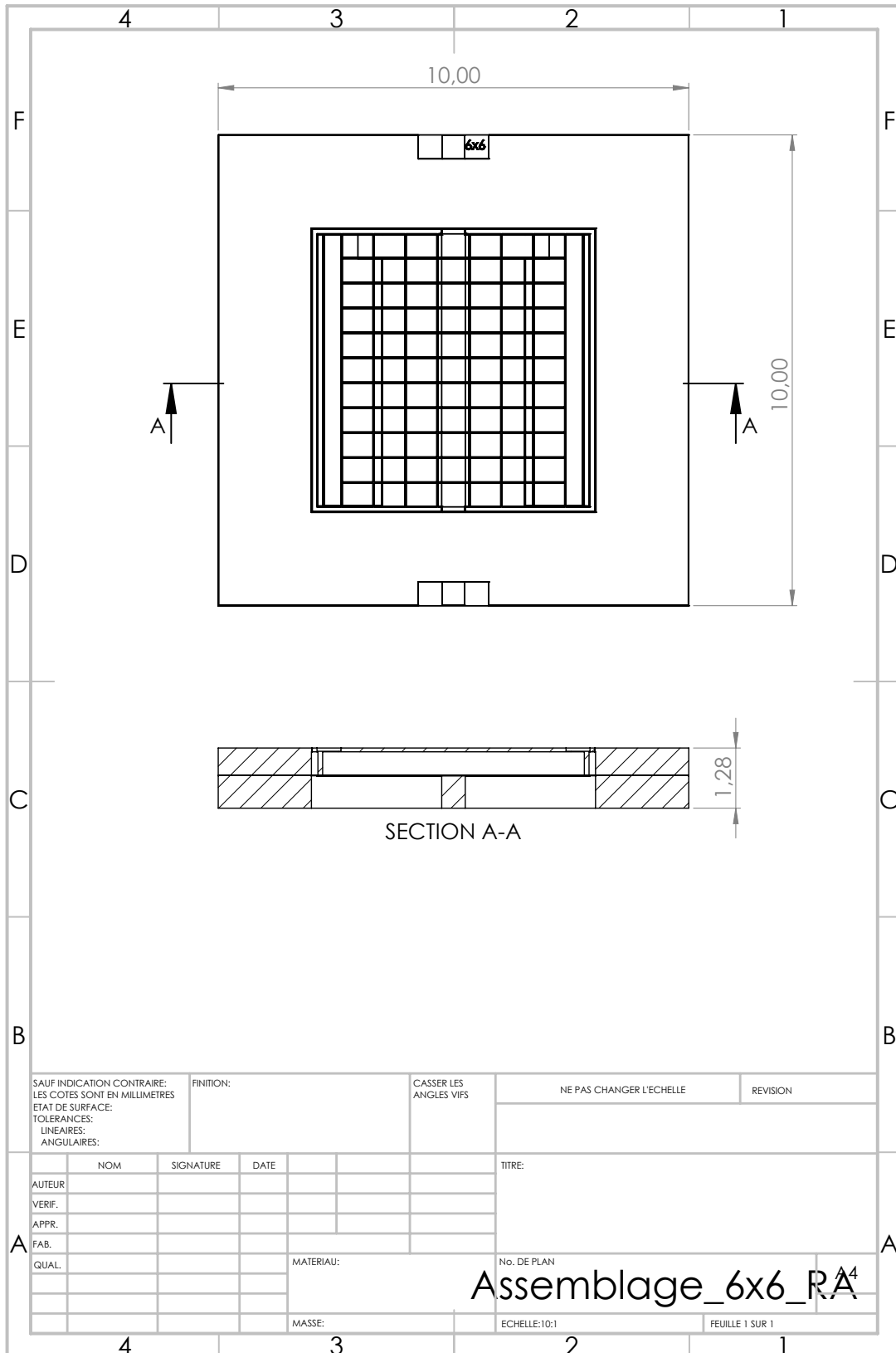
D.1 Wafer 1



D.2 Wafer 2



D.3 Assembly



E Power Supply Filters

This section describes briefly the filters used on the power supplies of the amplifier and the filters. In order to filter the power supply and avoid unwanted electromagnetic interferences to interact with the circuit, ferrite beads are used. Ferrite beads are essentially an inductive conductor element in a ferrite material. Due to magnetic interactions between the current carried by the conductor, the inductive element and the ferrite, the impedance of the ferrite widely depends on the frequency and is very high in a limited frequency range. The equivalent electrical circuit of a ferrite bead is shown in Figure E.1:

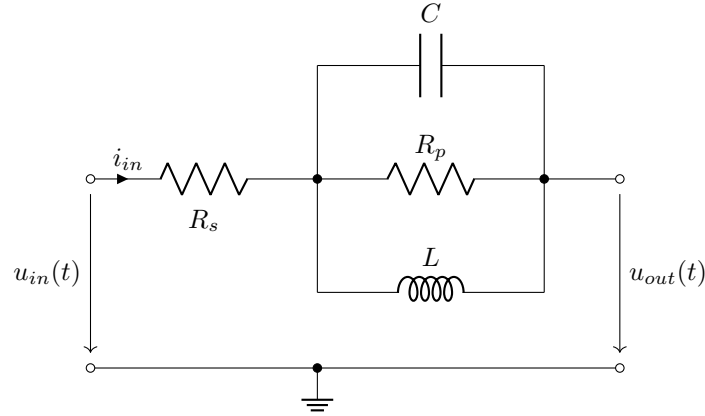


Figure E.1: Equivalent Electrical Circuit of a Ferrite Bead

And the equivalent impedance writes

$$Z_{beam} = \frac{u_{in}}{i_{in}} = R_s + \frac{1}{j\omega C + \frac{1}{j\omega L} + \frac{1}{R_p}}. \quad (41)$$

Ferrite beads are widely used for filtering power supplies and are added independently on each power supply pin of the operational amplifiers and other circuit, with a parallel capacitor, as close as possible to the component pin. This parallel capacitor acts as a low pass filter with the ferrite bead and provide the needed short time current for the component. The impedance curve of the ferrite bead is shown in Figure E.2(a). The transfer function from the power supply to the signal line with a parallel capacitor can be written as

$$T_f = \frac{\frac{1}{j\omega C_f}}{Z_{beam} + \frac{1}{j\omega C_f}} \quad (42)$$

The transfer function of the power supply filters is calculated and depicted in Figure E.2(b).

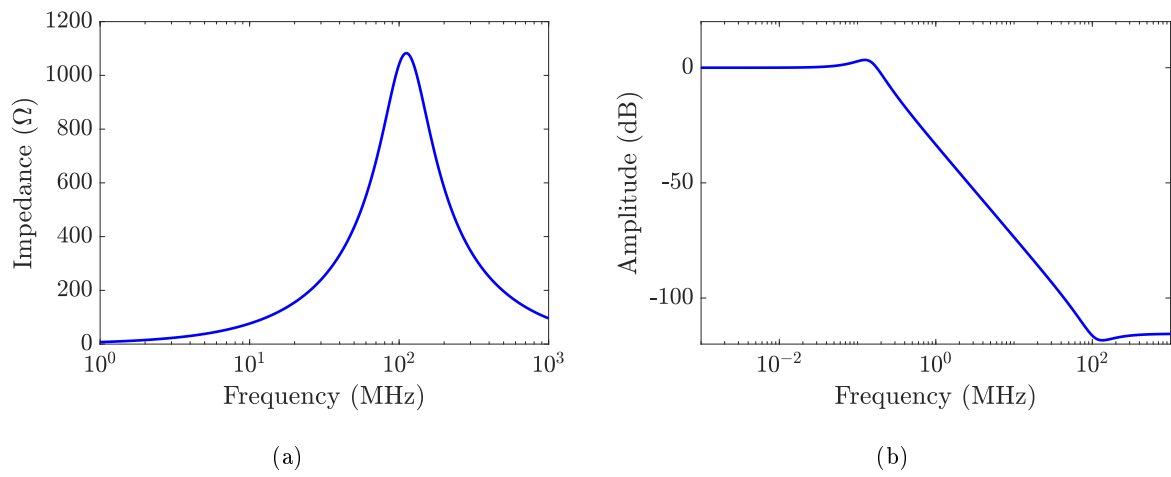
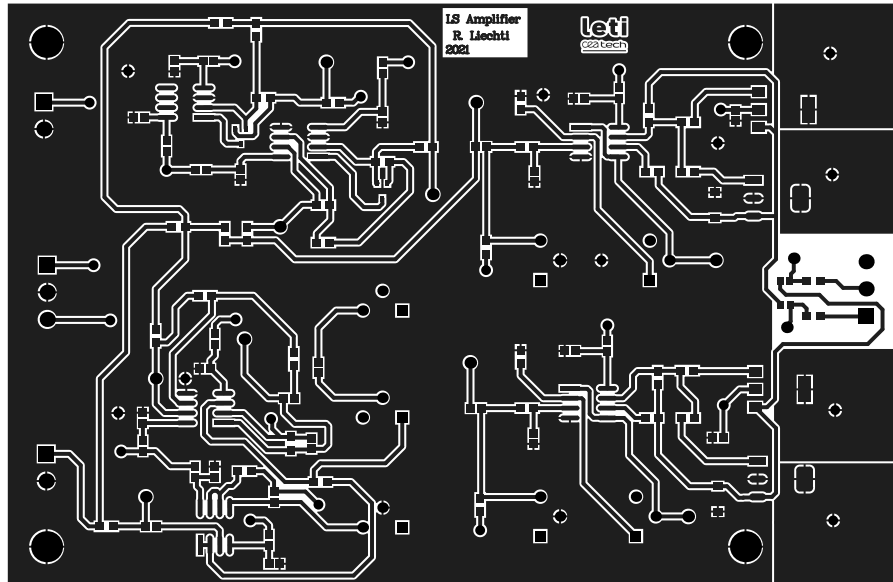


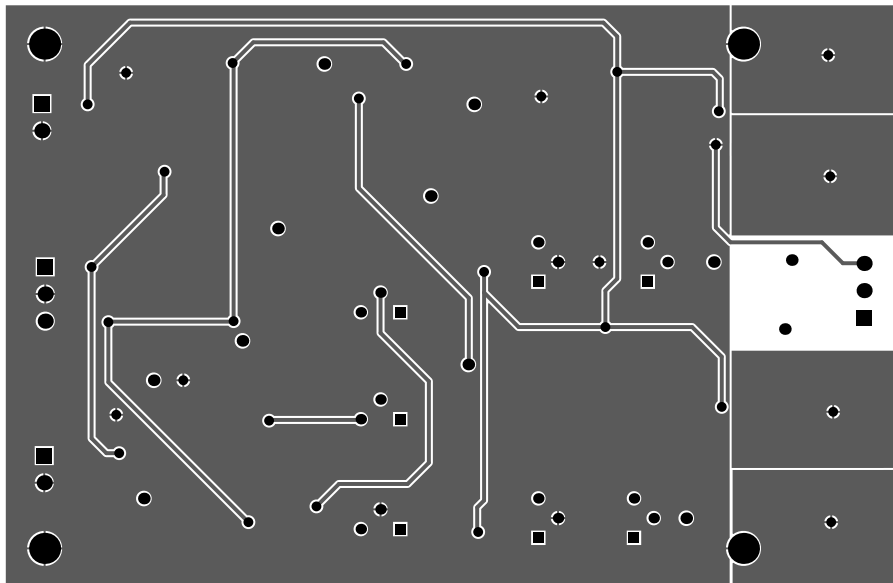
Figure E.2: Electrical impedance of a ferrite beam with a series decoupling capacitor (a) and transfer function of the power supply filter (b)

F Printed Circuit Board

F.1 Top Layer

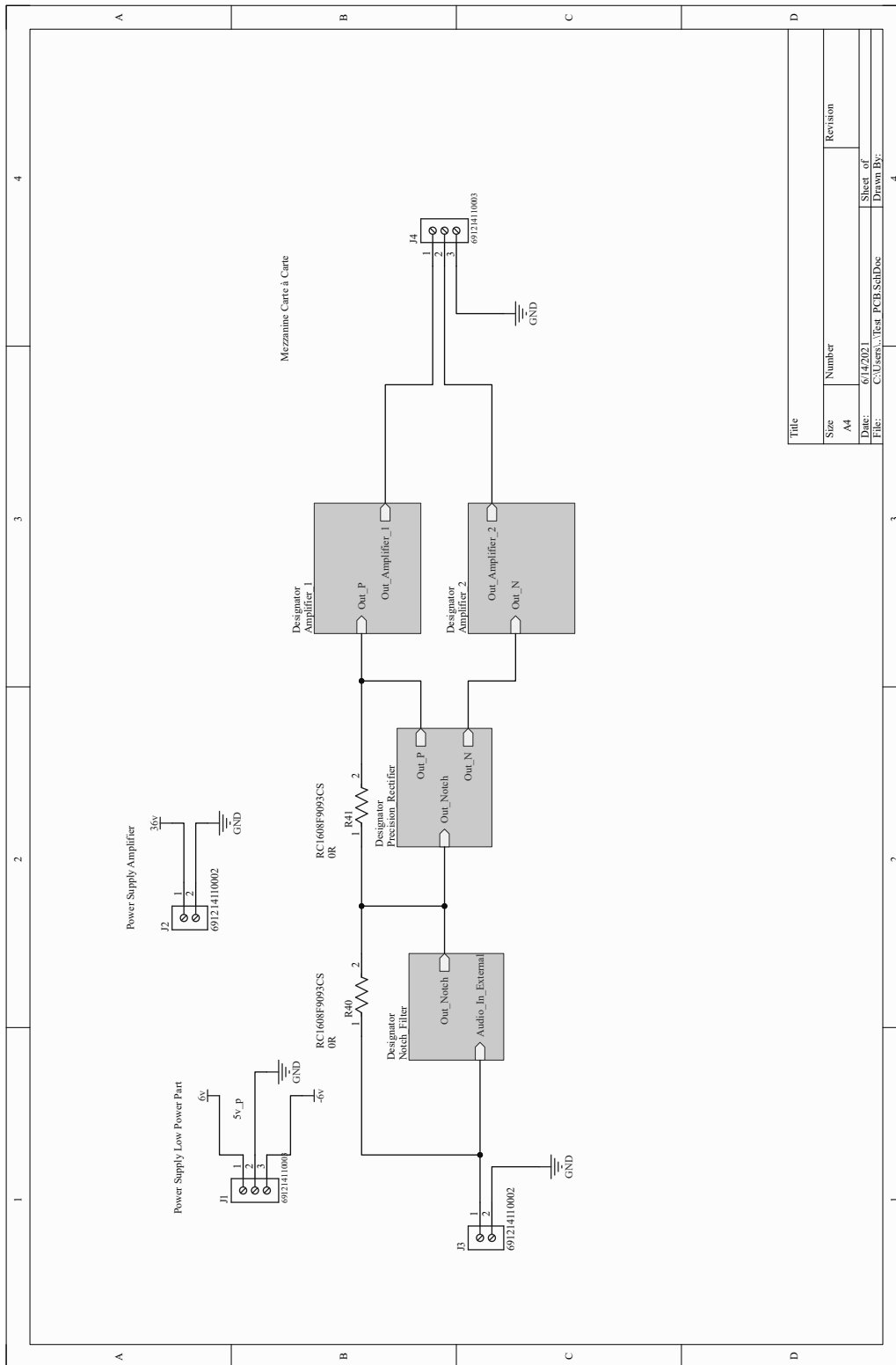


F.2 Bottom Layer

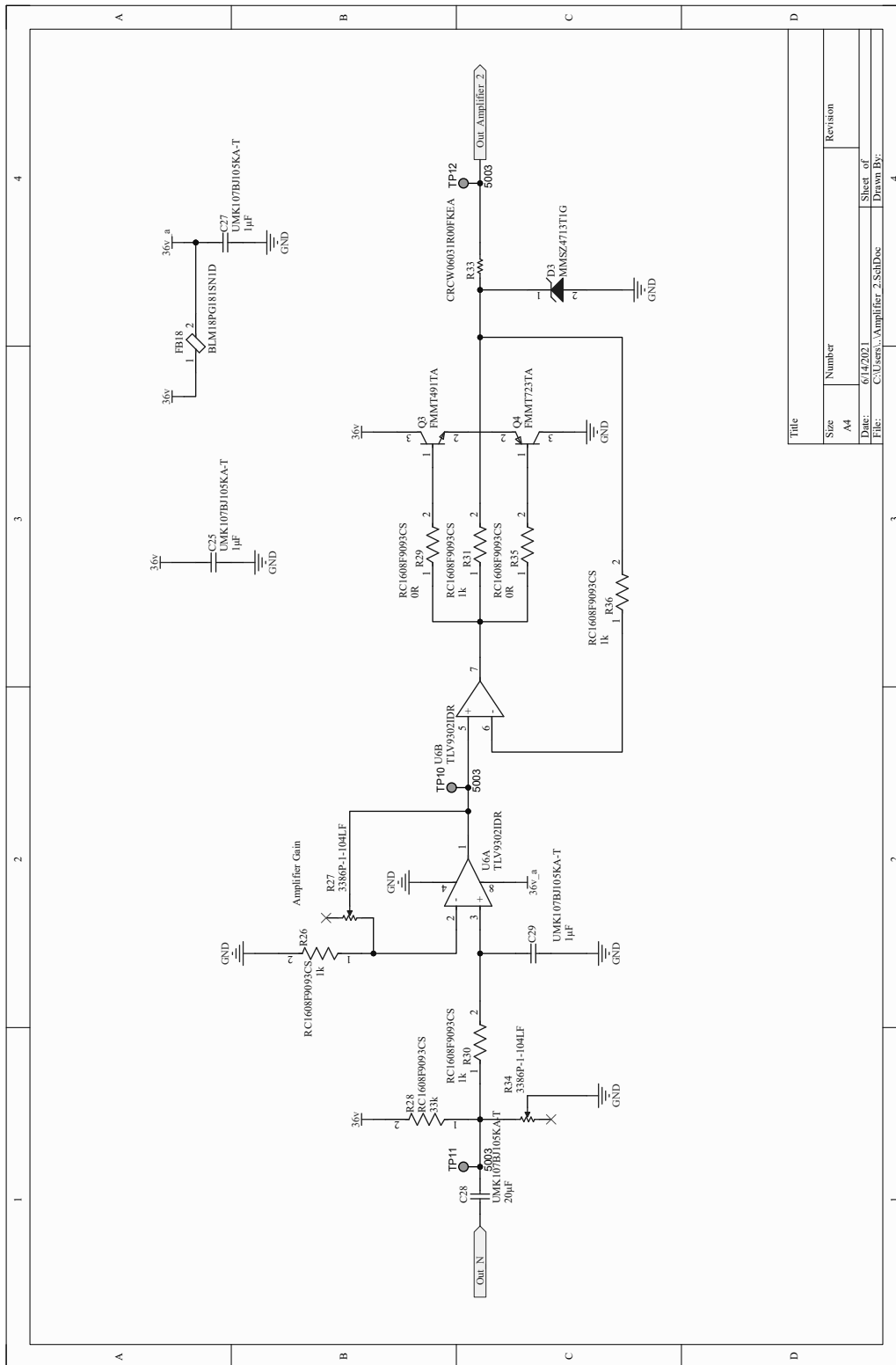


G Altium Circuits

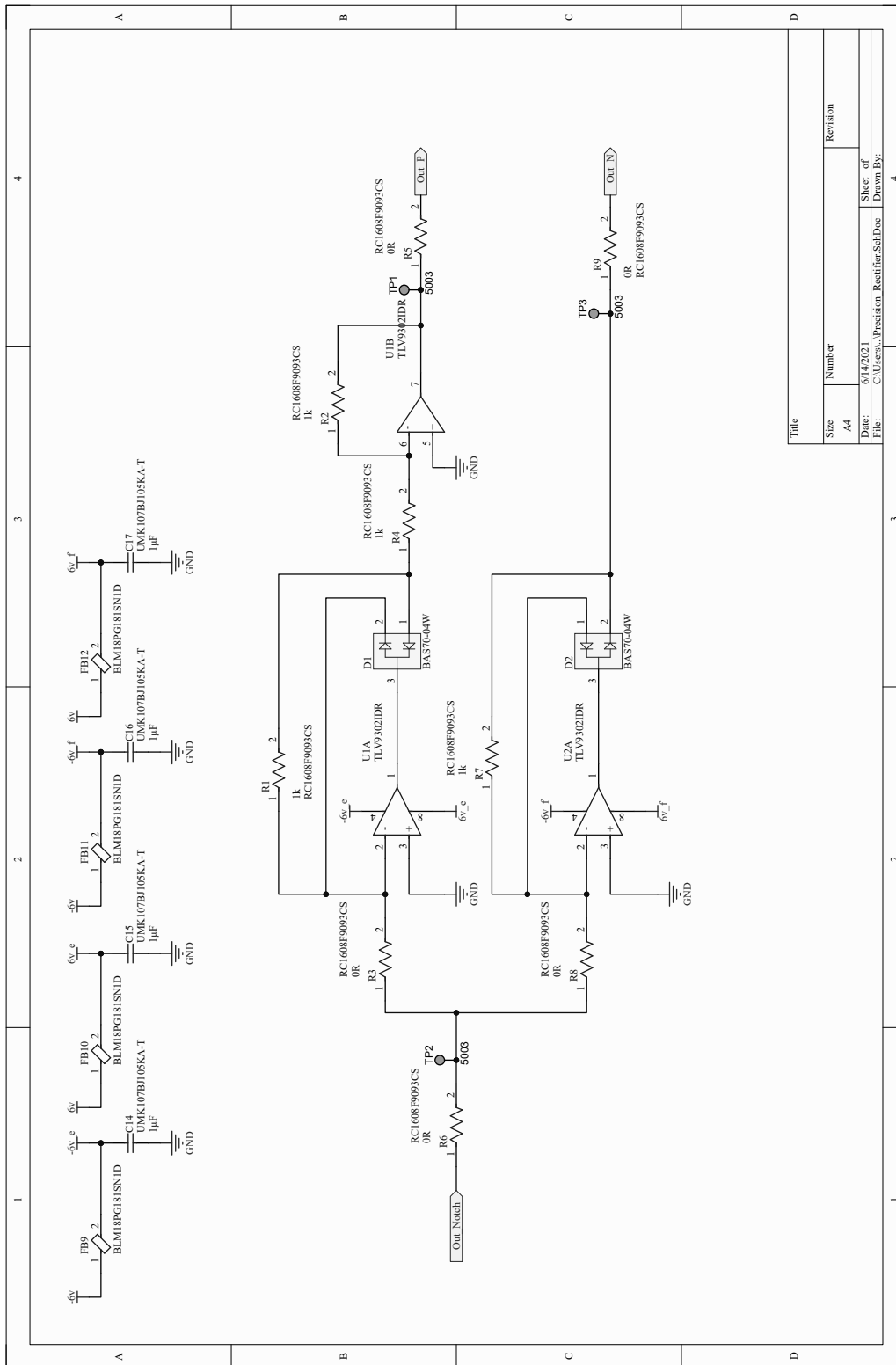
G.1 Top Level



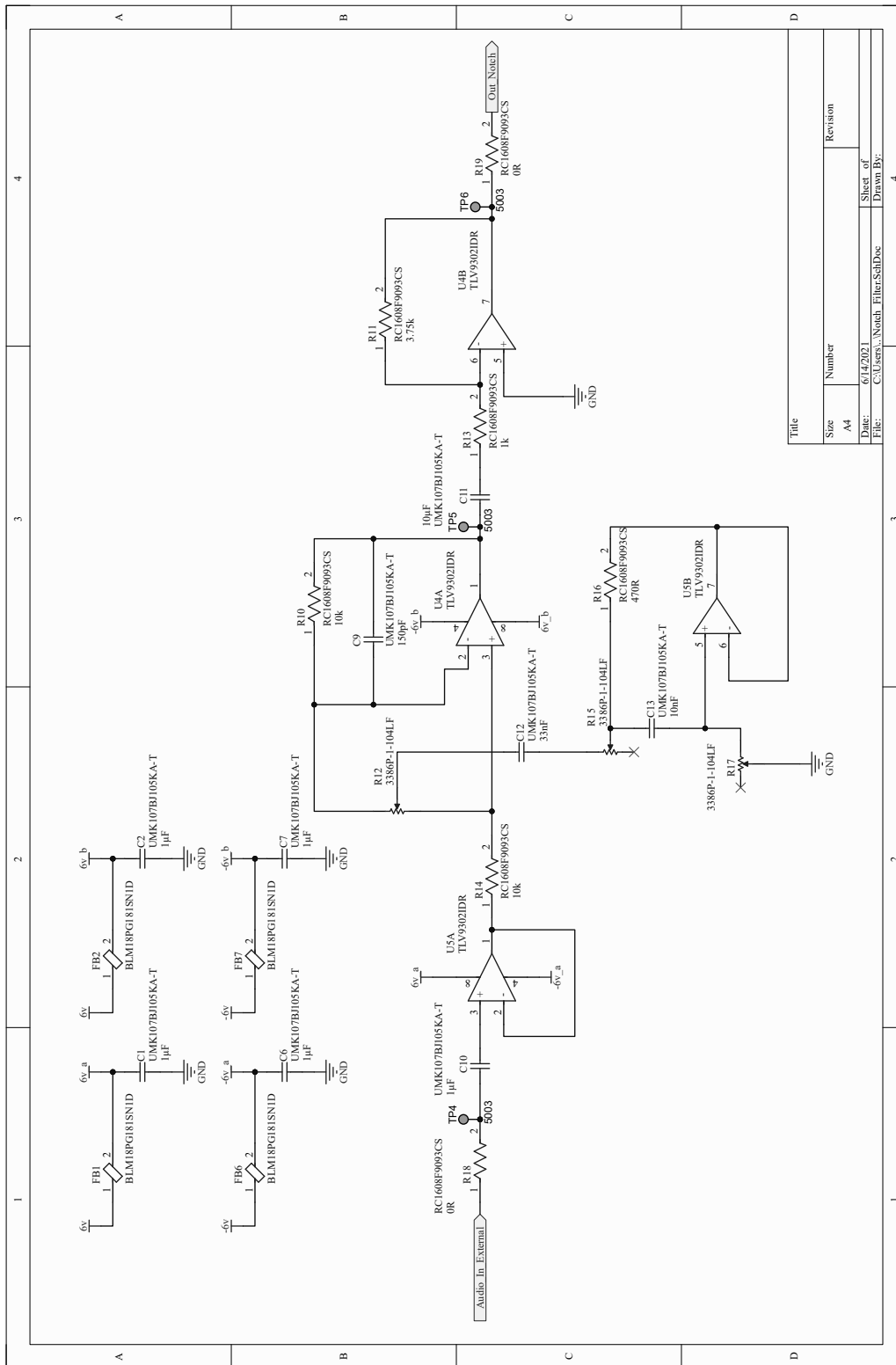
G.3 Amplifier 1



G.4 Precision Rectifier



G.5 Nocth Filter



Title	
Size	Number
A4	
Date:	Revision
6/14/2021	
File:	Sheet of
C:\Users\... \Nocth_Filter.SchDoc	4
	Drawn By:

H Cover

Frequency responses from Figure 4.43 are used for the cover. The frequency responses are truncated from 300 Hz to 8 kHz. They are displayed on a linear axis for the frequency and a black patch is placed under the curve as depicted in Figure H.1(a). The curve and the patch are then mirrored and repeated with a shift along the y axis, as depicted in Figure H.1(b). The frequency response and the patch are then shifted along the x axis at the same time by a step calculated with a sine function, as depicted in Figure H.2(a). For the cover, a noisy sine function composed of a sum of two sines is used. This function is depicted on arbitrary axis in Figure H.2(b). This cover is inspired by Paul Tinnemans' cover in his thesis [126] as well as by the famous album Unknwon Pleasures by Joy Division.

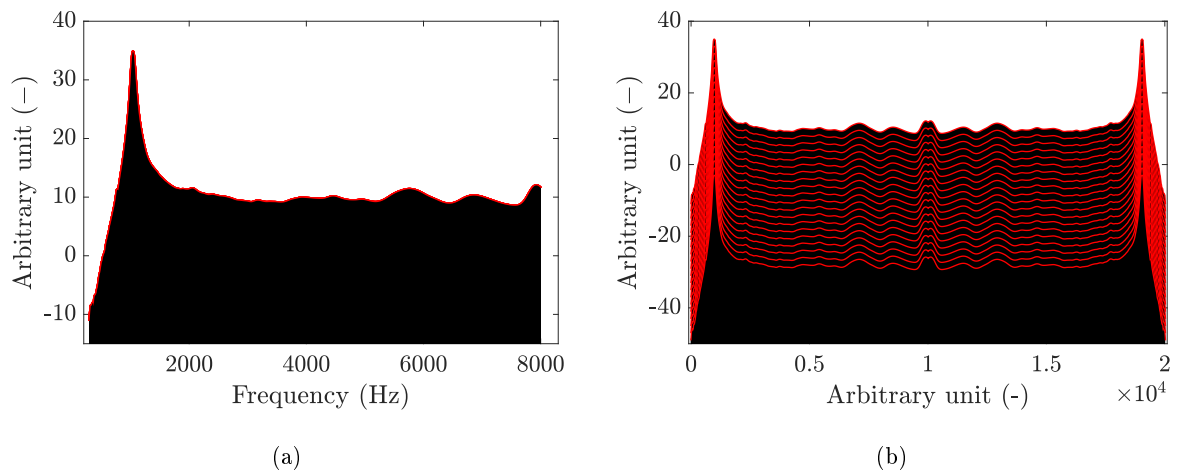


Figure H.1: Frequency response using a patch (a) and mirrored repeated and shifted frequency response (b)

Different settings are then added in order to disable the axis and make the background black, as it is described in the Matlab code. The picture is then printed as an EMF file using the painter figure renderer in order to have a vector file.

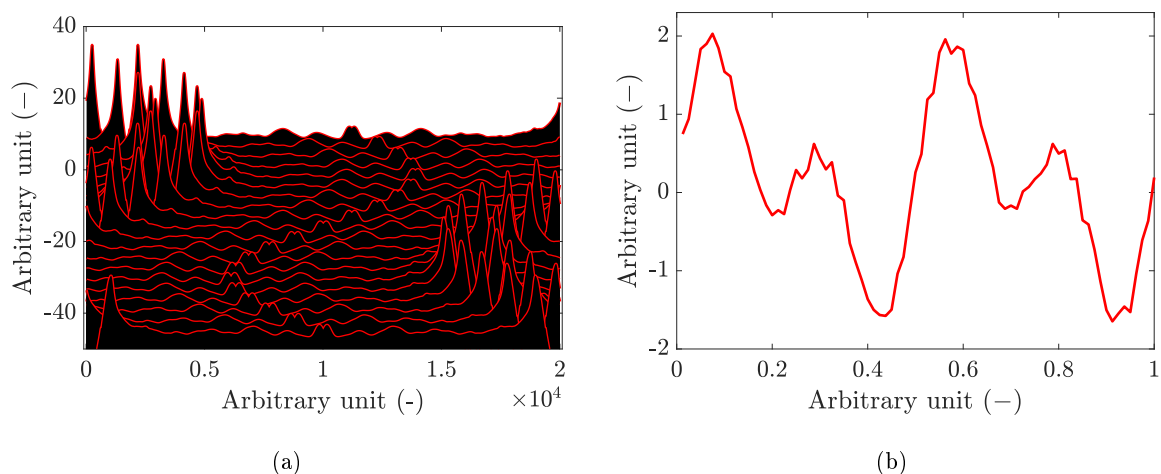


Figure H.2: Frequency responses with patch iteratively shifted by a sine (a) and noisy shifting sum of sine used in the cover (b)

Matlab Code

```

1 %%
2 clc; close all; clearvars
3
4 % Load data
5 load('FR_level_4.mat');
6 num = load('freq.mat');
7 ffrd = num.ffrd;
8 P = ID1;
9 idy = 3;
10
11 % Truncate matrix from 300 to 8e3 Hz
12 [minValue_min,closestIndex_min] = min(abs(ffrd-3e2));
13 [minValue_max,closestIndex_max] = min(abs(ffrd-8e3));
14 ffrd_tr = ffrd(closestIndex_min:closestIndex_max);
15 P1 = P(:,closestIndex_min:closestIndex_max);
16
17 % Mirror the curve
18 P2 = zeros(length(P1(:,1)),2*length(P1(1,:)));
19 P2(:,1:end/2) = P1;
20 P2(:,end/2+1:end) = fliplr(P1);
21
22 % New x axis to matrix dimensions
23 ffrd_trd = linspace(20,2e4,length(P2(1,:)));
24
25 % Shift function
26 yaxe = linspace(1,length(P2(:,1)),length(P2(:,1)));
27 fsin = (1./(yaxe(end)));
28 % sine_shift = sin(2.*pi.*fsin.*yaxe);
29 sine_shift = yaxe.*0;
30
31 P3 = zeros(length(P2(:,1)),length(P2(1,:)));
32
33 for kk = 1:length(yaxe)
34     P3(kk,:) = circshift(P2(kk,:),round(3e2.*sine_shift(kk)));
35 end
36
37 %% Plot simple
38 h1 = figure(1);
39 hold on
40 for kk = 1:length(P3(:,1))
41     plot(ffrd_trd,-(kk-1)*idy+100+20.*log10(abs(P3(kk,:))), 'linewidth',2, 'color',[1 0 0])
42     fill([ffrd_trd';flipud(ffrd_trd')],-(kk-1)*idy+[(-100.*ones(1,length(ffrd_trd)))]';
         flipud((100+20.*log10(abs(P3(kk,:))))'),[0 0 0], 'linestyle','none')
43 end
44 grid off
45 hold on
46 xlim([-100 2.01e4])
47 ylim([-50 40])
48 xlabel('Arbitrary unit  $\mathrm{(-)}$ ');
49 ylabel('Arbitrary unit  $\mathrm{(-)}$ ');
50 box on; grid off;
51 Ax = gca;
52 Ax.Color = 'k';
53 Ax.XColor = 'none';
54 Ax.YColor = 'none';

```

```
55 PrintEmfDouble(h1, 'Cover_Step_4')
```


In pursuance of making loudspeakers compatible with very large scale integration (VLSI) processes, research has been carried out on the development of MEMS loudspeaker, from nearly as early as the first MEMS device and recently arouses a gain of interest due to the thinning of portable multimedia devices. Despite interesting performances for in-ear loudspeaker, where high resonance frequencies and small displacements can generate significant sound pressure level, no solution was found to advantageously replace non-MEMS loudspeakers for free field applications. To widen the frequency range of MEMS loudspeaker, an innovative geometry based on an assembly of two wafers is proposed, in order to separate the electro-mechanical transducer from the mechano-acoustics transducer, with the aim of reaching a better optimization target. In this thesis, the working principle of the loudspeaker, as well as the models used for the design and the optimization are presented and detailed. The innovative custom manufacturing process with which the loudspeaker is manufactured in the CEA Leti clean rooms is then detailed, and the measured frequency response is compared with the simulated ones. The loudspeaker is able to radiate pressures as high as 110 dB_{SPL} at 1 kHz, the resonance frequency of the loudspeaker, which is above the state of the art for MEMS loudspeaker these dimensions. By using digital signal processing, as well as a dedicated packaging with specific acoustical couplings, this loudspeaker could replace the secondary loudspeaker of smartphones.



LAUM
Laboratoire d'Acoustique
Le Mans Université CNRS - UMR 6613



Titre : Développement d'un micro haut-parleur aux performances optimisées

Mot clés : Haut-parleur, MEMS, Audio, Piézoélectrique

Résumé : Dans le but de rendre les haut-parleurs compatibles avec les processus d'intégration à très grande échelle (VLSI), des recherches ont été menées sur le développement de haut-parleur MEMS, depuis le premier MEMS, et suscitent récemment un gain d'intérêt en raison de l'amin-cissement des systèmes multimédias portables. Malgré des performances intéressantes pour les haut-parleurs intra-auriculaires, pour lesquels des fréquences de résonance élevées et de petits déplacements peuvent générer un niveau de pression acoustique important, aucune solution n'a été trouvée pour remplacer avantageusement les haut-parleurs non MEMS pour les applications en champ libre. Pour élargir la gamme de fréquences du haut-parleur MEMS, une géométrie innovante basée sur un assemblage de deux wa-

fers est proposée, afin de séparer le transducteur électro-mécanique du transducteur mécano-acoustique, dans le but d'atteindre une meilleure cible d'optimisation. Dans cette thèse, le principe de fonctionnement du haut-parleur, ainsi que les modèles utilisés pour la conception et l'optimisation sont présentés et décrits. Le procédé innovant de fabrication avec lequel le haut-parleur est fabriqué dans les salles blanches du CEA Leti est ensuite décrit, et la réponse en fréquences mesurée est comparée à celles simulées. Le haut-parleur est capable de rayonner une pression de 110 dB_{SPL} à 1 kHz, la fréquence de résonance du haut-parleur, ce qui est au-dessus de l'état de l'art pour un haut-parleur MEMS de ces dimensions.

Title: Development of a MEMS Loudspeaker with optimized performance

Keywords: Loudspeaker, MEMS, Audio, Piezoelectric

Abstract: In pursuance of making loudspeakers compatible with very large scale integration (VLSI) processes, research has been carried out on the development of MEMS loudspeaker, from nearly as early as the first MEMS device and recently arouses a gain of interest due to the thinning of portable multimedia devices. Despite interesting performances for in-ear loudspeaker, where high resonance frequencies and small displacements can generate significant sound pressure level, no solution was found to advantageously replace non-MEMS loudspeakers for free field applications. To widen the frequency range of MEMS loudspeakers, an innovative geometry based on an assembly of two wafers is proposed, in order to separate the electro-mechanical transducer from the mechano-acoustics one, with the

aim of reaching a better optimization target. In this thesis, the working principle of the loudspeaker, as well as the models used for the design and the optimization are presented and detailed. The innovative custom manufacturing process with which the loudspeaker is manufactured in the CEA Leti clean rooms is then detailed, and the measured frequency response is compared with the simulated ones. The loudspeaker is able to radiate pressures as high as 110 dB_{SPL} at 1 kHz, the resonance frequency of the loudspeaker, which is above the state of the art for MEMS loudspeakers of such dimensions. By using digital signal processing, as well as a dedicated packaging with specific acoustical couplings, this loudspeaker could replace the secondary loudspeaker of smartphones.